

ON THE USE OF RAMAN SPECTROSCOPY AND INSTRUMENTED  
INDENTATION FOR CHARACTERIZING DAMAGE IN MACHINED CARBIDE  
CERAMICS

by

BENJAMIN PETER GROTH

A Dissertation submitted to the  
Graduate School-New Brunswick  
Rutgers, The State University of New Jersey

in partial fulfillment of the requirements

for the degree of

Doctor of Philosophy

Graduate Program in Materials Science and Engineering

written under the direction of

Professor Adrian B. Mann

and approved by

---

---

---

---

---

New Brunswick, New Jersey

January, 2013

## **ABSTRACT OF THE DISSERTATION**

On the Use of Raman Spectroscopy and Instrumented Indentation for Characterizing  
Damage in Machined Carbide Ceramics

By BENJAMIN P. GROTH

Dissertation Advisor: Prof. Adrian B. Mann

Machining is a necessary post-processing step in the manufacturing of many ceramic materials. Parts are machined to meet specific dimensions, with tight tolerances, not attainable from forming alone, as well as to achieve a desired surface finish. However, the machining process is very harsh, often employing the use of high temperatures and pressures to achieve the wanted result. In the case of silicon carbide, a material with extremely high hardness and stiffness, machining is very difficult and requires machining conditions that are highly aggressive. This can leave behind residual stresses in the surface of the material, cause unwanted phase transformations, and produce sub-surface deformation that can lead to failure.

This thesis seeks to determine the effect of various machining conditions on the Raman spectra and elastic properties of sintered silicon carbide materials. Sample sets examined included hot-pressed silicon carbide tiles with four different surface finishes, as well as "ideal" single crystal silicon carbide wafers. The surface finishes studied were as follows: an as-pressed finish; a grit blast finish; a harsh rotary ground finish; and a mirror

polish. Each finish imparts a different amount, as well as type, of deformation to the sample and are each utilized for a specific application.

The sample surfaces were evaluated using a combination of Raman spectroscopy, for phase identification and stress analysis, and nanoindentation, for obtaining elastic properties and imparting uniform controlled deformation to the samples. Raman spectroscopy was performed over each sample surface using 514- and 633-nm wavelength excitation, along with confocal and non-confocal settings to study depth variation. Surface stresses were determined using peak shift information extracted from Raman spectra maps, while other spectral variations were used to compare levels of machining damage. Elastic modulus, hardness, and plastic work of indentation maps were generated from load-depth curves obtained from nanoindentation with a Berkovich tip at 10mN and 30mN maximum loads. The Raman measurements were repeated on indented samples, over the indented regions. Stress-free single crystal silicon carbide wafers were used as a reference for both the Raman and nanoindentation measurements.

The Raman analysis showed that stress gradients could be determined within each machined sample. Additionally, it revealed variations in the magnitude of residual stresses between machining conditions. No correlation was found between elastic properties of samples and Raman stress data. However, it was found that the 30mN indentation caused an increase in the near-surface average stress value for the mirror finish sample. The relative peak width also increased, indicating a plastic deformation resolvable by Raman.

## **Acknowledgements**

I would like to first thank my advisor, Prof. Adrian Mann, for his help and guidance through my time at Rutgers. His ability to provide me with keen insights both in the scientific world and in life helped me make it through. I would like to also extend my thanks to my thesis committee: Prof. Rich Haber, Prof. John Matthewson, Dr. Laura Fabris, and Dr. Douglas Mrotek. Thank you for putting up with me and my work, and for your input throughout the process. An extra thanks to Dr. Mrotek for stepping in at the last minute when needed most.

Thank you to my friends and fellow graduate students at Rutgers for being able to commiserate on the graduate student life and provide an outlet. To Brian and Meg V, Joe Pantina, Jesse Kohl, Doug Slusark, my office mates Stuart and Mahsa who made getting work done a hardship, I want to thank you for the conversations and for being there to bounce ideas off of. To my friends outside of Rutgers and the engineering discipline, thank you for putting up with never being able to understand a thing I talk about.

To my parents, George and Cheryl, thank you for always trying to explain what it is I do but not really knowing yourselves. Thank you for being behind me through all that I do. To my brothers, Dan and Tim, thanks for not causing permanent brain damage when beating me up, it certainly would have made all this much more difficult. To my wonderful girlfriend, Marcellina, thank you for putting up with me being so far away for so long. To my awesome dog Mooch, who taught you how to read!?

Finally, I would like to extend my thanks to the faculty and staff in the Rutgers Materials Science department. Without the aid of Claudia, Michelle and Phyllis, I'm certain that all would be lost.

## **PREFACE**

This thesis is partially based on the following papers:

1. Identifying changes in residual stress using indentation on machined metallic surfaces. B.P. Groth and A.B. Mann; Materials Letters 89 (2012) 287-290
2. Using Raman mapping to determine stress variation in machined silicon carbide ceramics. B.P. Groth and A.B. Mann; submitted to the Journal of the American Ceramic Society 2012
3. Variations in the Raman spectral profile of 6H-silicon carbide ceramics due to machining. B.P Groth and A.B. Mann; submitted to the Journal of the American Ceramic Society 2012

The relevant chapters of this thesis contain these papers as submitted and accepted, along with additional results and discussion where necessary.

## Table of Contents

<b>ABSTRACT OF THE DISSERTATION .....</b>	<b>ii</b>
<b>ACKNOWLEDGEMENTS .....</b>	<b>iv</b>
<b>PREFACE.....</b>	<b>vi</b>
<b>TABLE OF CONTENTS .....</b>	<b>vii</b>
<b>LIST OF FIGURES .....</b>	<b>x</b>
<b>1. INTRODUCTION.....</b>	<b>1</b>
<b>2. BACKGROUND .....</b>	<b>3</b>
2.1 SILICON CARBIDE.....	3
2.1.1 <i>Crystal Structure</i> .....	3
2.1.2 <i>Mechanical Properties</i> .....	5
2.1.3 <i>Thermal and Electrical Properties</i> .....	5
2.1.4 <i>Industrial Uses</i> .....	6
2.2 PROCESSING OF SILICON CARBIDE CERAMICS.....	7
2.2.1 <i>Production of Silicon Carbide Powders</i> .....	8
2.2.2 <i>Growth Methods</i> .....	9
2.2.3 <i>Forming Methods</i> .....	10
2.2.4 <i>Machining of Ceramics</i> .....	13
2.3 RAMAN SPECTROSCOPY .....	17
2.3.1 <i>Theory of Raman</i> .....	19
2.3.2 <i>Simple Model for Stress Analysis</i> .....	21
2.3.4 <i>Spectra Components</i> .....	22

2.3.5 Penetration Depth.....	23
2.3.6 Special Techniques in Raman .....	24
2.3.7 Raman of Silicon Carbide.....	28
2.4 NANOINDENTATION .....	32
2.4.1. Area Function Determination .....	33
2.4.2 Analysis Methods .....	35
<b>3. EXPERIMENTAL PROCEDURES .....</b>	<b>39</b>
3.1 RAMAN SPECTROMETER .....	39
3.1.2 Raman Mapping.....	43
3.1.3 Curve Fitting.....	44
3.2 NANOINDENTATION .....	46
<b>4. STUDY ON STRESS IN METALLIC SAMPLES.....</b>	<b>48</b>
4.1 IDENTIFYING CHANGES IN RESIDUAL STRESS USING INDENTATION ON MACHINED METALLIC SURFACES.....	48
<b>5. STRESS VARIATIONS IN MACHINED SILICON CARBIDE.....</b>	<b>60</b>
5.1 USING RAMAN MAPPING TO DETERMINE STRESS VARIATION IN MACHINED SILICON CARBIDE CERAMICS.....	60
5.2 FURTHER DISCUSSION .....	83
5.2.1 Effects of Indentation on Measured Stress.....	83
<b>6. VARIATIONS IN RAMAN SPECTRA OF SILICON CARBIDE.....</b>	<b>105</b>
6.1 VARIATIONS IN THE RAMAN SPECTRAL PROFILE OF 6H-SILICON CARBIDE CERAMICS DUE TO MACHINING.....	105



<b>7. MECHANICAL PROPERTIES FROM INDENTATION.....</b>	<b>128</b>
7.1 ELASTIC MODULUS .....	130
7.2 HARDNESS .....	131
7.3 PLASTIC WORK OF INDENTATION.....	132
7.4 ELASTIC MODULUS SQUARED DIVIDED BY HARDNESS ( $E^2/H$ ).....	132
<b>8. CONCLUSIONS .....</b>	<b>134</b>
<b>9. FUTURE WORK.....</b>	<b>136</b>
<b>APPENDIX 1 – RAMAN MAPS OF INDENTED SAMPLES.....</b>	<b>138</b>
<b>APPENDIX 2 – MECHANICAL PROPERTIES MAPS.....</b>	<b>154</b>
<b>APPENDIX 3 – ADDITIONAL RAMAN SPECTRA.....</b>	<b>162</b>
<b>APPENDIX 4 – ADDITIONAL LOAD-DEPTH CURVES.....</b>	<b>170</b>
<b>REFERENCES.....</b>	<b>175</b>
<b>CURRICULUM VITAE.....</b>	<b>182</b>

## List of Figures

Figure 1.1: The three most commonly used forms of silicon carbide .....	4
Figure 2.2: Energy interactions in Raman scattering and Rayleigh scattering.....	17
Figure 2.3: Simple visualization of Raman scattering.....	18
Figure 2.4: Accessible reduced wave vectors for common SiC polytypes.....	29
Figure 2.5: Phonon dispersion curves for 3C-, 4H-, and 6H-SiC.....	30
Figure 2.6: Schematic of indenter-sample surface contact during loading and unloading. .....	33
Figure 2.7: Load displacement curve.....	34
Figure 2.8: Schematic of the total and elastic work descriptions. ....	37
Figure 3.1: External Components of the Raman inVia microscope. ....	41
Figure 3.2: Internal Components of the Raman inVia microscope. ....	41
Figure 3.3: Laser path through the Raman spectrometer.....	43
Figure 3.4: Fit parameters for the Raman curve fitting software.....	44
Figure 3.5: Load function used for 10mN maximum load indentation. ....	46
Figure 3.6: Load function used for 30mN maximum load indentation. ....	47
Figure 5.1: Typical indent in single crystal SiC with maximum load of 10mN.....	84
Figure 5.2: Typical indent in single crystal SiC with maximum load of 30mN.....	84
Figure 5.3: Stress maps of the standard surface finish obtained using the confocal setting. .....	85
Figure 5.4: Stress maps of the standard surface finish obtained using the regular scan setting.....	86

Figure 5.5: Stress maps of the grit blast surface finish obtained using the confocal scan setting.....	87
Figure 5.6: Stress maps of the grit blast surface finish obtained using the regular scan setting.....	88
Figure 5.7: Stress maps of the rotary ground surface finish obtained using the confocal scan setting.....	89
Figure 5.8: Stress maps of the rotary ground surface finish obtained using the regular scan setting.....	90
Figure 5.9: Stress maps of the mirror polish surface finish obtained using the confocal scan setting.....	91
Figure 5.10: Stress maps of the mirror polish surface finish obtained using the regular scan setting.....	92
Figure 5.11: Relative width maps of the standard surface finish obtained using the confocal scan setting.....	93
Figure 5.12: Relative width maps of the standard surface finish obtained using the regular scan setting.....	94
Figure 5.13: Relative width maps of the grit blast surface finish obtained using the confocal scan setting.....	95
Figure 5.14: Relative width maps of the grit blast surface finish obtained using the regular scan setting.....	96
Figure 5.15: Relative width maps of the rotary ground surface finish obtained using the confocal scan setting.....	97

Figure 5.16: Relative width maps of the rotary ground surface finish obtained using the regular scan setting. ....	98
Figure 5.17: Relative width maps of the mirror polish surface finish obtained using the confocal scan setting. ....	99
Figure 5.18: Relative width maps of the mirror polish surface finish obtained using the regular scan setting. ....	100
Figure 5.19: Average stress value plots pre- and post-indentation. The increase in average value of the mirror finish is seen at the near surface. ....	102
Figure 5.20: Average relative width value plots pre- and post-indentation. ....	103
Figure 7.1: Mechanical properties obtained from indentation experiments. ....	128
Figure 7.2: Typical load-depth curve obtained from indentation up to a peak load of 10mN. ....	129
Figure 7.3: Load-depth curves obtained at 10mN peak load indentation. ....	130
Figure A1.1: Stress maps of the standard surface finish obtained using the confocal scan setting. ....	138
Figure A1.2: Stress maps of the standard surface finish obtained using the regular scan setting. ....	139
Figure A1.3: Stress maps of the grit blast surface finish obtained using the confocal scan setting. ....	140
Figure A1.4: Stress maps of the grit blast surface finish obtained using the regular scan setting. ....	141
Figure A1.5: Stress maps of the rotary ground surface finish obtained using the confocal scan setting. ....	142

Figure A1.6: Stress maps of the rotary ground surface finish obtained using the regular scan setting.....	143
Figure A1.7: Stress maps of the mirror polish surface finish obtained using the confocal scan setting.....	144
Figure A1.8: Stress maps of the mirror polish surface finish obtained using the regular scan setting.....	145
Figure A1.9: Relative width maps of the standard surface finish obtained using the confocal scan setting. ....	146
Figure A1.10: Relative width maps of the standard surface finish obtained using the regular scan setting. ....	147
Figure A1.11: Relative width maps of the grit blast surface finish obtained using the confocal scan setting. ....	148
Figure A1.12: Relative width maps of the grit blast surface finish obtained using the regular scan setting. ....	149
Figure A1.13: Relative width maps of the rotary ground surface finish obtained using the confocal scan setting. ....	150
Figure A1.14: Relative width maps of the rotary ground surface finish obtained using the regular scan setting. ....	151
Figure A1.15: Relative width maps of the mirror polish surface finish obtained using the regular scan setting. ....	152
Figure A1.16: Relative width maps of the mirror polish surface finish obtained using the regular scan setting. ....	153
Figure A2.1: Indentation data for the standard surface finish sample at 10mN. ....	154

Figure A2.2: Indentation data for the standard surface finish sample at 30mN. ....	155
Figure A2.3: Indentation data for the grit blast surface finish sample at 10mN.....	156
Figure A2.4: Indentation data for the grit blast surface finish sample at 30mN.....	157
Figure A2.5: Indentation data for the rotary ground finish sample at 10mN. ....	158
Figure A2.6: Indentation data for the rotary ground finish sample at 30mN. ....	159
Figure A2.7: Indentation data for mirror polish surface finish sample at 10mN.....	160
Figure A2.8: Indentation data for the mirror polish surface finish sample at 30mN.....	161
Figure A3.1: Typical Raman spectra for standard finish 514nm confocal setting. ....	162
Figure A3.2: Typical Raman spectra for standard finish 633nm confocal setting. ....	162
Figure A3.3: Typical Raman spectra for standard finish 514nm regular setting.....	163
Figure A3.4: Typical Raman spectra for standard finish 633nm regular setting.....	163
Figure A3.5: Typical Raman spectra for grit blast finish 514nm confocal setting.....	164
Figure A3.6: Typical Raman spectra for grit blast finish 633nm confocal setting.....	164
Figure A3.7: Typical Raman spectra for grit blast finish 514 regular setting .....	165
Figure A3.8: Typical Raman spectra for grit blast finish 633nm regular setting. ....	165
Figure A3.9: Typical Raman spectra for rotary ground finish 514nm confocal setting.	166
Figure A3.10: Typical Raman spectra for rotary ground finish 633nm confocal setting. .....	166
Figure A3.11: Typical Raman spectra for rotary ground finish 514nm regular setting.	167
Figure A3.12: Typical Raman spectra for rotary ground finish 633nm regular setting.	167
Figure A3.13: Typical Raman spectra for mirror finish 514nm confocal setting.....	168
Figure A3.14: Typical Raman spectra for mirror finish 633nm confocal setting.....	168
Figure A3.15: Typical Raman spectra for mirror finish 514nm regular setting.. ....	169

Figure A3.16: Typical Raman spectra for mirror finish 633nm regular setting..	169
Figure A4.1: Typical Load-Depth curve for single crystal 6H-SiC at a maximum applied load of 30mN.	170
Figure A4.2: Typical Load-Depth curve for standard finish 6H-SiC at a maximum applied load of 10mN.....	171
Figure A4.3: Typical Load-Depth curve for standard finish 6H-SiC at a maximum applied load of 30mN.....	171
Figure A4.4: Typical Load-Depth curve for grit blast 6H-SiC at a maximum applied load of 10mN. ....	172
Figure A4.5: Typical Load-Depth curve for grit blast 6H-SiC at a maximum applied load of 30mN.. ....	172
Figure A4.6: Typical Load-Depth curve for rotary ground 6H-SiC at a maximum applied load of 10mN.. ....	173
Figure A4.7: Typical Load-Depth curve for rotary ground 6H-SiC at a maximum applied load of 30mN. ....	173
Figure A4.8: Typical Load-Depth curve for mirror finish 6H-SiC at a maximum applied load of 10mN. ....	174
Figure A4.9: Typical Load-Depth curve for mirror finish 6H-SiC at a maximum applied load of 30mN. ....	174

## 1. Introduction

The process of machining hard carbide ceramics has proven to cause damage within the machined component<sup>[1]</sup>. Understanding the effects of this machining damage is of great importance to the materials science community. However, the extents of the machining induced damage, as well as the effects on properties and performance are not easily determined without the use of destructive characterization tools<sup>[2,3]</sup>.

Machining has been shown to introduce residual surface stresses in machined components<sup>[4-6]</sup>, as well as cause subsurface damage that can lead to early failure<sup>[7-9]</sup>. Despite this fact machining is a necessary processing step, especially in hard ceramics, undergone to achieve specific surface finishes that are otherwise unattainable from the forming process alone. Machining techniques have been developed that aim to reduce the introduction of unwanted stresses and damage, yet all have their own disadvantages<sup>[1]</sup>. The samples studied in this work are all machined using common grinding procedures. Machining via grinding is one of the harshest forms of machining that exist, but is also one of the most efficient for harder ceramics.

As an analysis tool, Raman spectroscopy is non-destructive and provides excellent lateral as well as depth resolution. It has also proven effective in detecting subsurface damage in both machined polycrystalline sintered samples and single crystal wafers that have undergone surface treatments<sup>[10-12]</sup>. Similarly, nanoindentation has proven effective in studying machining damage. It has been utilized as an accurate means of detecting residual surface stresses and subsurface damage based on interpretation of the load-depth curves obtained from the experimental procedure<sup>[13-15]</sup>. Nanoindentation



has also proven to be useful in causing damage, such as the amorphization in silicon that has been indented at specific loads and loading rates <sup>[16]</sup>.

This thesis seeks to examine the effect of various machining processes on the Raman spectra of silicon carbide. Raman spectroscopy was used to analyze stress states within machined samples, as well as deformation and subsurface damage caused by the machining process. Machined samples of hot-pressed silicon carbide were used for this study. Each sample was processed and formed from the same starting batch material and differ only in the post-pressing surface treatments received. The samples were all produced commercially to tight tolerances, under specific highly controlled pressing schedules. Nanoindentation was used to obtain mechanical property information of each machined surface, as well as to introduce damage to the surfaces of the samples. Additional Raman was performed over indented regions to study the effects of indentation on the residual stressing, as well as deformation, of the machined samples. It was shown that the type of machining has a significant effect on the amount of residual stress in samples, as well as the perceived deformation and subsurface damage caused by machining.

## **2. Background**

Presented in this section is background information relating to the structure and processing of silicon carbide, as well as the techniques used in this thesis work. Also discussed is previous work in the literature that helped shape the methods and motivations of this project.

### **2.1 Silicon Carbide**

Silicon carbide is one of the hardest materials known, 4<sup>th</sup> behind diamond, boron carbide, and cubic boron nitride<sup>[17]</sup>. Along with extremely high hardness, SiC has a large compressive strength and high elastic modulus, all three of which make it suitable for a broad range of industrial applications. The strong covalent bonding between atoms and interesting crystal structure of silicon carbide are what bestow these beneficial properties to the material.

#### **2.1.1 Crystal Structure**

Over a short range silicon carbide is composed of a diamond-like arrangement of silicon and carbon atoms<sup>[18]</sup>. Tetrahedra containing 4-Si and 1-C, or 4-C and 1-Si depending on the notation make up the base unit of SiC. The long-range order becomes increasingly complicated due to the vast number of what are known as polytypes present in silicon carbide. Polytypes come about as variations in the stacking sequence of the Si-C tetrahedra, where alternating layers are able to stack in such a way as to be either parallel or anti-parallel to the layer below. Three such stacking sequences can be seen in

figure 2.1, and are the most commonly utilized structures of silicon carbide. Successive parallel/anti-parallel stacking of layers within the structure can lead to an almost infinite number of stacking permutations while preserving the stoichiometry of the system.

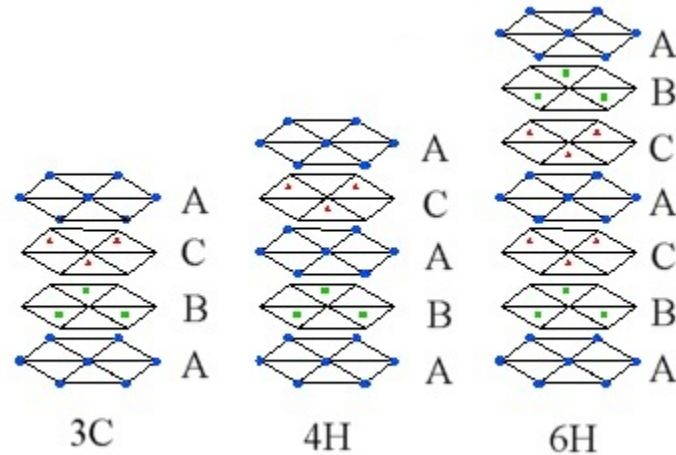


Figure 1.1: The three most commonly used forms of silicon carbide, each varying by the stacking sequence of the Si-C tetrahedra.

More than two-hundred fifty polytypes have been identified in silicon carbide as recently as 2006<sup>[17]</sup>. Multiple notations have been developed to describe the distribution of silicon and carbon atoms in each polytype. The most common notation currently employed, as developed by Ramsdell<sup>[19]</sup>, uses the form  $nL$ , where  $n$  refers to the periodicity of the stacking and  $L$  refers to the general crystallographic symmetry of the lattice. Polytypes considered as having important industrial uses include SiC-3C (also known as  $\beta$ -SiC), SiC-4H, and SiC-6H (also known as  $\alpha$ -SiC).  $\beta$ -SiC is a metastable form that is the most commonly produced polytype at lower temperatures, while  $\alpha$ -SiC is the most stable polytype above 2000°C<sup>[20]</sup>.

### 2.1.2 Mechanical Properties

The theoretical density of SiC is  $3.21 \text{ g/cm}^3$ , and by weight is comprised of 70.05% Si, and 29.95% C. Silicon carbide materials are characterized by high hardness, high compressive strength, and high elastic moduli, and is considered to be the fourth hardest material available. Only diamond, boron carbide, and cubic boron nitride have higher hardness values. Hot pressed 6H-SiC is shown to have an elastic modulus of 410 GPa and an indentation hardness of roughly 31GPa, while also having a compressive strength of 2.82GPa <sup>[21]</sup>. The strong covalent bonds between silicon and carbon are what bring about such high values of these properties. The degree of covalency has been measured at close to 87%, which also contributes to the high melting point and minimal high-temperature induced creep attributed to this material<sup>[21]</sup>.

### 2.1.3 Thermal and Electrical Properties

The thermal conductivity of silicon carbide has been measured at  $150 \text{ W/m}\cdot\text{K}$  at  $20^\circ\text{C}$  and  $54 \text{ W/m}\cdot\text{K}$  at  $1400^\circ\text{C}$ . Silicon carbide has a low coefficient of thermal expansion (CTE) of  $4.7 \times 10^{-6}$  between 20 and  $1400^\circ\text{C}$  <sup>[21]</sup>. These two properties lead to silicon carbide having a high thermal shock resistance.

Silicon carbide is also a semiconductor material. The band gap for various polytypes ranges from 2.4 to 3.3eV. The band gaps for the 4H and 6H polytypes are 3.26 and 3.03eV, respectively <sup>[22]</sup>. For this reason silicon carbide is considered to be a wide band gap material. The electronic structure is stable at temperatures of over  $550^\circ\text{C}$ , making it suitable for high temperature semiconductor devices. The conductivity of SiC-based materials may be increased by doping with any of nitrogen (N), phosphorus (P),

aluminum (Al) and boron (B), which substitute for carbon and silicon in the lattice. The addition of Al and B lead to p-type character, while the addition of N and P leads to n-type character. The resistivity of silicon carbide may be varied between 0.1 and  $10^{12}$  Ohm-cm through the addition of dopants <sup>[22]</sup>.

#### **2.1.4 Industrial Uses**

More than 700,000 tons of silicon carbide is produced every year, half of which solely goes towards use in the abrasives industry <sup>[23]</sup>. Silicon carbides extremely high hardness makes it especially useful for grinding and polishing of a wide range of materials. In a loose particle form, silicon carbide is an excellent lapping agent, and when mixed with a binder can be made into abrasive sticks or applied as a coating for cutoff wheels <sup>[17]</sup>. Many polishing wheels found in university and commercial labs make use of silicon carbide polishing papers, where SiC grit is bonded to a paper pad. Carbide powders are also added to cement agglomerate mixes to increase the wear resistance of concrete <sup>[23]</sup>.

Of the remaining 50%, nearly two-thirds goes towards additives in steel making for the metallurgical industry. When dissolved in a molten iron melt, SiC produces an exothermic reaction. This increases the temperature, which in turn pushes further deoxidization of the metal melt and improves homogeneity within the mix <sup>[23]</sup>. A more homogeneous melt increases the quality of the steel pour and final product.

What's left of the annual production is spread over various industries and applications. Silicon carbide finds its way into many high temperature applications, as it has very good thermal shock resistance and low coefficient of thermal expansion. This

includes use as furnace heating elements, crucibles, kiln furniture, igniter devices, and furnace walls <sup>[24]</sup>. The wear industry takes advantage of the hardness of silicon carbide and wear resistance for the production of sand blast nozzles, pump seals, artificial rollers and ball bearings, rocket nozzles, brake discs, and furnace rollers <sup>[24]</sup>. Silicon carbide powders are used as the starting point for CVD and PVD growth of single crystal SiC used in the semiconductor industry. In the single crystal form, SiC is used in the development of high voltage/current electronic devices <sup>[22]</sup>. Recently, there has been a good deal of research into the feasibility of silicon carbide for use in turbine, diesel, and gasoline engine blocks. By operating at higher temps, these engines offer the promise of increased efficiency.

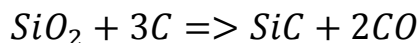
## **2.2 Processing of Silicon Carbide Ceramics**

There are many steps that need to be taken in order to produce fully-dense advanced silicon carbide ceramics. What little natural deposits exist are typically mined, beneficiated, milled, and then sieved <sup>[24]</sup>. What is not found naturally is created in a batch process and differently graded powders are extracted to be used in specific applications. The cleaned and sized raw materials are then heated in a large batch furnace to induce a chemical reaction, forming silicon carbide crystals. These crystals are manually selected from the furnace batch, which are then broken down and undergo further milling and sizing. Regardless of the use of pressure or pressure-less sintering routes, silicon carbide powders must be brought to extremely high temperatures and necessitate sintering aids to become fully dense.

### 2.2.1 Production of Silicon Carbide Powders

As there is little natural silicon carbide, or Moissanite, found in the world, most high-quality powders must be synthesized <sup>[24]</sup>. Silicon carbide powders are obtained via the production method known as the Acheson process. This process, developed by Acheson in 1893<sup>[19]</sup>, utilizes a resistance furnace to carbo-thermally reduce raw starting powders.

A large cylindrical graphite rod, used as the resistively heated element, is covered in a fine mix of silica sand ( $\text{SiO}_2$ ) and some source of carbon, often coke. This is then surrounded by a refractory lining and housed within a steel shell. High current is passed through the graphite rod, heating it up and generating temperatures in excess of  $2500^\circ\text{C}$  <sup>[17]</sup>. Heat is then transferred from the core throughout the silica-coke mix, and as soon as the mix reaches  $1500^\circ\text{C}$  the following main reaction occurs:



This reaction continues over the course of a period of 40 or more hours, over which time as much as possible of the silica-coke mixture that can be reacted is allowed to do so. Once the system is allowed to cool, the sides of the furnace are broken away, exposing any unreacted mixture surrounding what is now a mass of crystalline silicon carbide. As a direct result of the mass being heated from the center, there is a gradient of material purity that defines the end use of the silicon carbide. Powders closest to the electrode are often of the highest purity, and are used solely for advanced ceramics applications. Less reacted material located further from the graphite core are often used in

the abrasives industry. In either case, the harvested silicon carbide must be crushed, milled, and sieved before any further use.

### **2.2.2 Growth Methods**

Semiconductor grade silicon carbide must be grown much like boules of silicon are grown. However, the methods use to produce the SiC boules is quite different from that of silicon production. Given below are the 2 main methods of single crystal silicon carbide production used currently.

#### **2.2.2.1 Lely Method**

Lely's method, developed in 1955, forms the basis of the modern methods of growing SiC crystals <sup>[25]</sup>. A dense graphite crucible, which houses a thin walled cylindrical graphite pipe, is filled with SiC source powder, placed between the outer wall of the cylinder and the crucible walls. The crucible is sealed and heated to temperatures in excess of 2500°C. Upon vaporization, platelets of high quality SiC crystals are deposited on the inside of the cylinder walls. While this method produces some of the highest quality SiC crystals, it has several drawbacks that make it unacceptable for production of electronic devices. Many of the important aspects of growth: the growth surfaces, rates and direction, are entirely random with no means of control. Even the size and thickness of platelets is uncontrollable. The platelets produced tend to be small, on average less than 5 x 8 mm <sup>[25]</sup>, with quite inefficient yields limiting their use in



semiconductor devices. Most importantly, there is no means of selecting the polytype or controlling the impurities.

#### **2.2.2.2 Chemical Vapor Deposition (CVD)**

CVD is a growth process in which gaseous compounds are moved to a substrate surface, where they react to form the desired material. Initially disappointing results in the 1960's and 1970's dulled interest in CVD for bulk SiC growth, but it forms a significant part of the epitaxial growth field in many semiconductor systems as well as for SiC <sup>[26]</sup>. Epitaxial growth is the formation of one crystal layer upon another of the compound on a substrate material. Homoepitaxy, where the substrate is the same polytype as the epitaxial layer, is the most common form for most polytypes of SiC. Often the doping or other properties of the epitaxial layer are designed to be different to the substrate in order to form a junction<sup>[27]</sup>. The reaction of the precursor materials forms the epitaxial layer. One of the most significant choices in CVD is, therefore, that of the precursor materials. The most common choices for SiC growth are SiH<sub>4</sub> and C<sub>3</sub>H<sub>8</sub>, although many others have been reported.

#### **2.2.3 Forming Methods**

There are quite a few methods under which silicon carbide ceramics can be sintered. Like any process, each has its own advantages and disadvantages, but all allow for near fully or fully dense SiC. The samples examined in this thesis were formed and sintered under the aid of pressure and therefore only pressure-assisted sintering methods will be discussed.

### 2.2.3.1 Hot-Pressing

The use of pressure along with heat to form a fully dense material is what identifies a sintering method as being pressure-assisted. One method widely used to help densify covalently bonded ceramics such as silicon carbide is hot pressing, as first demonstrated by Alliegro in 1956<sup>[17]</sup>. In its most basic form a hot-press consists of an hydraulic ram, an induction furnace, and some form of die, often made of graphite, into which a powder compact is placed<sup>[28]</sup>. A uniaxial pressure, applied by the hydraulic ram, is used to introduce additional stresses at the boundaries between particles. This additional stress acts to reduce the required surface energy, the driving force of sintering, needed to produce a dense material.

Unlike the dependence grain growth has on maximum applied temperature, there is no such dependence between applied pressure and the growth of the grains<sup>[29]</sup>. The applied pressure acts against pore pressure and causes transport of vacancies from the neck to the space between particles, an act that helps to remove large pores and promote densification<sup>[28]</sup>. With the application of pressure driving down the required surface energy for densification, the material can densify at a lower temperature than without the applied load. The result is a material which has been sintered to a high density at a low enough temperature and over a short enough time as to avoid inducing significant grain growth. The main disadvantages to this sintering method involve the expense and low production rate of densified product. The process of hot-processing is not a continuous one, and needs to be performed under vacuum conditions or within a controlled atmosphere<sup>[28]</sup>. The shortened lifetime of the forming dies adds to the financial expenditures needed to produce hot-pressed samples. Die lifetimes are decreased by hot-

pressing as they undergo the same heating and thermal stresses as the powder compact sample <sup>[28]</sup>.

#### **2.2.3.2 Spark Plasma Sintering**

A rather new, and decidedly modern, sintering method known as spark plasma sintering (SPS) has become more and more interesting in recent years. This method allows for high-speed densification of both conductive and non-conductive materials <sup>[30]</sup>. As with the hot-press method, densification occurs through the application of high temperatures and uniaxial pressure. The heating however, is thought to be achieved by the generation of spark plasma at the contact points between particles through the “on/off” pulsing of a low-voltage, high-amperage DC current source <sup>[31]</sup>. At the points where this spark is generated, temperatures of greater than 10,000°C have been recorded <sup>[30]</sup>. As the heating is concentrated to the surface of particles, rather than throughout the bulk of the particle, vaporization of the surface layers occurs. This leads to material transport from the surface to interparticle necks. The heating time and the maximum cycle temperature directly influence the resultant density of the sintered work piece <sup>[30]</sup>.

There are a number of mechanisms that occur in SPS that result in sintering and densification. The extreme temperatures generated at the surface of particles causes a large plastic deformation at the contact points <sup>[31]</sup>. The applied electric field causes high-speed transfer of heat and diffusion throughout the entire powder compact. The diffusion rate of atoms is enhanced by the intensity of the pulse current. As the current is passed through the dies and punches, there is resistive Joule heating that occurs, further aiding in the densification of the powder compact <sup>[31]</sup>.

One of the major advantages of spark plasma sintering is the ability to densify materials in shorter times when compared to other densification methods. This acts to control grain growth during the sintering process. Additionally, the high-speed of sintering allows for the sintering of nanocrystalline materials and sintering of materials free from additives and binders <sup>[30]</sup>. There are similar disadvantages to spark plasma sintering as in hot-pressing that prevent SPS from being utilized in low-cost, mass production of sintered materials. While the sintering cycle occurs in a comparatively short period of time, it is still a batch process that requires frequent replacement of graphite punches and dies, which adds to production costs <sup>[30]</sup>.

#### **2.2.4 Machining of Ceramics**

Machining is a necessary step in the production of most advanced ceramics. This is mainly due to the inability to create formed pieces to the extremely tight tolerances often needed in advanced ceramic applications. Along with this, complex shapes are difficult to manufacture efficiently and some form of machining is needed to define the desired shape. However, the machining process has been shown to reduce strength properties and introduce subsurface flaws <sup>[32,33]</sup>. Discussed below are several methods of machining, with a focus on those used on the samples studied in this thesis.

##### **2.2.4.1 Grinding Techniques**

The samples studied in this work have been mechanically machined to different surface finishes. In hard ceramics, the main method of machining has been some form of

grinding<sup>[34]</sup>, where a machining tool often coated with several layers of a hard material is used to remove layers of ceramic. This is often time consuming and expensive, as the machining tools need to be replaced often in order to make precise cuts<sup>[34]</sup>. The grinding process has also been shown to cause performance issues, as will be discussed later in this section.

Grit blasting of a material involves impacting the material surface with hard spheres of either a metal such as steel, or a hard ceramic such as alumina or silicon carbide at a high speed. At the basic level, grit blasting is used to smooth a rough surface, roughen a smooth surface, help shape a material, or remove surface contaminants<sup>[35]</sup>. It is often used as a pre-step to applying some form of coating to a substrate, where the rough surface allows for better coating adhesion<sup>[36,37]</sup>. One effect of the blasting process is the introduction of compressive residual stresses at the surface of the impacting material. This often produces the effect of toughening the material and increasing resistance to crack propagation<sup>[35]</sup>.

Rotary surface grinding is often used as a means of obtaining work piece thicknesses that require very tight tolerances<sup>[38]</sup>. Diamond abrasive cutting wheels are used to remove layers of material at the surface of the sample. Variations in the cutting speed, or turning speed, as well as applied pressure to the cutting wheel are used to control the rate of material removal<sup>[38]</sup>. Depending on the size of the grit on the cutting wheel, the cutting parameters and the angle of grinding, different surface finishes can be obtained<sup>[38]</sup>. These will vary from rough surfaces, similar to those produced by grit blasting, to finer surface finishes that come close to emulating a mirror polish. The

grinding parameters have also been shown to influence the amount of subsurface damage produced within the piece being machined <sup>[39,40]</sup>.

Mechanical mirror polishing is a machining method used to produce a mirror-like finish in the final surface of the ceramic. Typically used in applications where a highly reflective surface is needed, the polishing procedure involves using abrasive grit, most often SiC, alumina, or diamond, to remove material from the surface of a component <sup>[41]</sup>. The abrasive is bonded to polishing pads and samples are turned at a set speed and pressure against the pads. As the machining process continues, finer and finer abrasive grit is used to remove scratches caused by the previous step. This is done until the grit being used is fine enough so as to cause no surface scratches that appear optically, and a mirror-like finish is achieved. Many studies have been performed examining the effects of polishing speeds and times, as well as grit size on the induced damage within the polished sample <sup>[42,43]</sup>. Much of the damage from the polishing process is introduced in the form of subsurface cracking to depths on the order of the grit size, which is not removed subsequently by the finer grit <sup>[44,45]</sup>.

#### **2.2.4.2 Advanced Machining Techniques**

There are many machining techniques that have been developed with the goal of minimizing the induced damage in the machined material <sup>[46-50]</sup>. These range from abrasive techniques that are modifications of some of the above mentioned grinding procedures, to abrasion-less cutting with electricity, to the use of lasers to remove material by vaporization.

Hydrodynamic machining, also known as water-jet machining, uses a high-velocity jet of fluid to erode material. The fluid can act alone, or contain abrasive particles to aid in the erosion of material. Increasing the jet pressure and decreasing the nozzle diameter, distance from the sample, and overall depth of the cut will generally increase the rate at which cutting occurs. The main benefits of the hydrodynamic method include: no heating effects, no large mechanical forces acting on the work piece, very little vibration of the sample and nearly no subsurface damage is introduced <sup>[1]</sup>. However, the biggest disadvantage to this technique is a reduction in the as-fired strength of the material, dependent on the cutting parameters and the size of the abrasive used, as well as the material being machined.

Abrasion-less forms of machining include laser-beam (LBM) and electron-beam (EBM) machining, where in an intense beam is focused onto the material causing it to vaporize. The EBM technique is much faster than the LBM technique, but requires a vacuum chamber which limits the size of the material that can be machined as well as the speed at which work pieces can be swapped out <sup>[1]</sup>. Laser beam machining setups are often less expensive as well, and both can be used to cut any hard material, including diamond. The rate at which machining occurs is dependent on how quickly the material can be vaporized and then removed from the surface. Thermal gradients caused by the beam heating can result in cracking in less thermally resistant ceramics. However, this heating can also impart beneficial residual stresses to the surface of the machined piece. The main disadvantage to this technique is the limited size that can be machined. Laser machining is often reserved for micromachining applications because of low energy efficiency of the cutting laser or electron beam <sup>[1]</sup>.

## 2.3 Raman Spectroscopy

Raman scattering is named after the Indian scientist C.V. Raman who discovered the effect in 1928 <sup>[51]</sup>. If light of a single color (wavelength) is shone on a material, most scatters off elastically, with no change in the color of the light (Rayleigh scattered light). However a tiny fraction of the light (typically on the order of 1 part per 10 million <sup>[51]</sup>) exchanges energy with vibrations in the material and is scattered at a slightly different wavelength because it has changed energy. This is known as Raman scattering, and is an inelastic form of scattering.

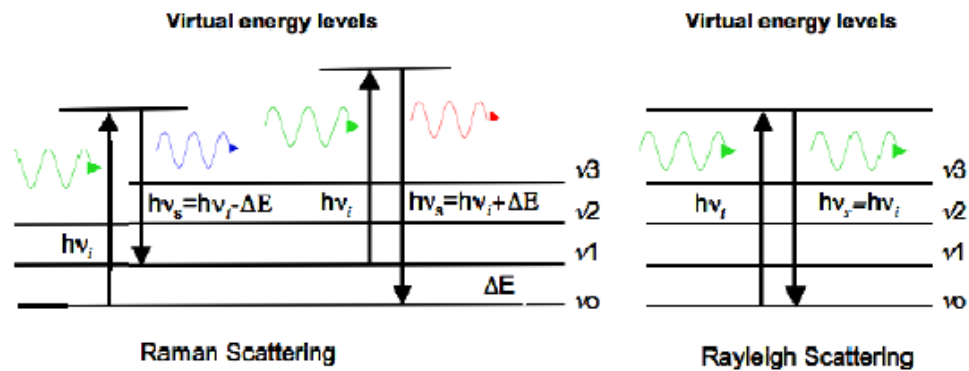


Figure 2.2: Energy interactions in Raman scattering (left) and Rayleigh scattering (right). Energy is shifted in Raman scattering due to interactions with vibrational states causing scattered light to return at a slightly different wavelength.





Figure 2.3: Simple visualization of Raman scattering. Incident light (orange) causes the irradiated molecule to vibrate. This vibration changes the energy of the scattered light to the Raman characteristic energy (blue).

Scattering occurs when an electromagnetic wave encounters a molecule, or passes through a lattice. This shift is characteristic of the chemical bonding present in the sample. The process of this scattering can be visualized in figure 2.2, which shows both the Stokes and anti-Stokes shifts. The general aim of Raman spectroscopy is to analyze the Raman scattered light and infer from it as much as possible about the chemistry and structure of the material. Figure 2.3 depicts a simplification of the Raman effect, showing a beam of incident light at one wavelength (color) as it interacts with a molecule, changing energy and thus the wavelength of the scattered light.

### 2.3.1 Theory of Raman

Raman scattering in molecules is based upon the polarizability of a molecule. In the presence of an electric field, the electrons and nuclei in a molecule can become distorted <sup>[52]</sup>. This distortion will induce a dipole moment within the molecule, and will be considered polarized. In molecules that can become polarized, light can induce this change as photons take the form of electromagnetic waves. The magnitude of any induced dipole can be expressed in the following terms:

$$\mu = \alpha E$$

where  $\mu$  is the size of the dipole,  $\alpha$  is the polarizability of the molecule and  $E$  is the applied electric field. Since the polarizability of the molecule is often anisotropic, it is convenient to express the polarizability in terms of a polarizability ellipsoid, which is a representation of the magnitude of the polarizability in three-dimensional space <sup>[52]</sup>.

When light is incident upon the molecule, it exposes the molecule to an electric field. The electric field oscillates by the following equation:

$$E = E_0 \sin 2\pi \nu \tau$$

This causes the induced dipole to oscillate giving:

$$\mu = \alpha E = \alpha E_0 \sin 2\pi \nu \tau$$

The classical explanation of Rayleigh scattering as a particular, uninteresting form of Raman scattering, follows simply from this equation. The oscillating dipole emits radiation at its own oscillating frequency; i.e. the same frequency as the incident light. Thus the light is elastically scattered.

It is unlikely, however, that the molecule will be completely stationary. To consider the case that the molecule has internal motion, either of a rotational or vibrational kind, any possible effect of this motion on the polarizability must be considered. It is assumed here that a particular vibration with frequency  $\nu_{\text{vibration}}$  will change the polarizability thusly:

$$\alpha = \alpha_0 + \beta \sin 2\pi\nu_{\text{vib}}\tau$$

Where  $\alpha_0$  is the equilibrium polarizability and  $\beta$  is the rate of change of polarizability with motion, proportional to  $\Delta\alpha/\Delta x$ , where  $x$  is a displacement co-ordinate of the motion. This will have the following effect on the induced dipole:

$$\mu = (\alpha_0 + \beta \sin 2\pi\nu_{\text{vib}}\tau)E_0 \sin 2\pi\nu\tau$$

Expanding and simplifying gives:

$$\mu = \alpha_0 E_0 \sin 2\pi\nu\tau + \frac{1}{2}\beta E_0 [\cos 2\pi(\nu - \nu_{\text{vib}})\tau - \cos 2\pi(\nu + \nu_{\text{vib}})\tau]$$

In this case it can be seen that the oscillation of the dipole includes three components. The first term is that of elastically scattered light. The second and third terms, which indicate possible emission from this oscillating dipole that includes light at frequencies  $\nu \pm \nu_{\text{vibration}}$  require that  $\beta$  is non-zero to be non-zero themselves. From this it can be seen that internal motion of the molecule does not necessarily affect the polarizability. A molecular motion can only be Raman active if it modifies the magnitude or the direction of the classical polarizability ellipsoid.

### 2.3.2 Simple Model for Stress Analysis

Often used to describe the atomic/molecular motions in a system, the anharmonic oscillator model can be used to show how Raman peak shift relates to lattice strains. In the simple harmonic model <sup>[53]</sup>, the stiffness of bonds is a constant  $k$ , and bonds have an at rest length  $l_0$ . If a bond is stretched a distance  $\Delta l$  given by  $l - l_0$ , then a diatomic oscillator has a restoring force given by :

$$F = -k \frac{\Delta l}{l_0}$$

And a corresponding potential energy well  $V$ , given by:

$$V = \frac{1}{2} k (l - l_0)^2$$

When anharmonicity is taken into account, the potential energy well looks like:

$$V(l) = \frac{k}{2} (l - l_0)^2 + k' (l - l_0)^3$$

When there is a change in the interatomic distance due to stress, there should also be a change in the force constants of the material <sup>[53]</sup>. The result of this change is a wavenumber shift in the atomic vibrations of the material system. There is an empirical relationship between the strain-induced Raman wavenumber shift ( $\Delta\nu$ ) and the strains ( $\Delta\epsilon$ ) given by:

$$\Delta\nu = S^\epsilon \times \Delta\epsilon$$

Where  $S^\epsilon$  is a parameter known as the Raman strain tensor <sup>[53]</sup>. Applying Hooke's law gives the following relation:

$$\Delta\nu = S^\varepsilon \times \Delta\varepsilon = S^\varepsilon \times \frac{\Delta\sigma}{100 \times E} = S^\sigma \times \Delta\sigma$$

Where  $S^\sigma$  is now a Raman stress tensor that defines a specific wavenumber shift given an applied stress. In the silicon carbide system, this stress tensor is often empirically fit by performing Raman analysis on single crystals under load applied by a diamond anvil cell. There has been significant work done in the field of Raman stress analysis on many of the relevant silicon carbide polytypes <sup>[54-60]</sup>.

#### 2.3.4 Spectra Components

The information acquired from Raman spectroscopy provides a wealth of characterization data on the material studied. When performing a Raman and subsequent spectral analysis, there are certain features that are generally examined based on what they can reveal about the sample. The first component of a Raman spectrum is the characteristic Raman frequencies. These are unique to the bonding between elements in a specific material and give an idea of the composition of the material being investigated. Raman is typically used in a qualitative manner by analyzing the characteristic frequencies; often one is looking for phase information, local composition of the material, or any spurious peaks that would indicate the presence of an unwanted component.

When breaking down the characteristic Raman frequencies into individual peaks, the more quantitative aspects of Raman are allowed. A characteristic peak has a specific wavenumber, or Raman shift. Changes in this peak position are often indicative of stress or strain states within the sample, as will be discussed. In silicon, the standard for most machine calibration, a shift of the characteristic peak at  $520.5\text{cm}^{-1}$  by as little as  $2\text{cm}^{-1}$  is

equivalent to 2GPa of residual stress <sup>[53]</sup>. The so called Raman-stress tensor, the GPa/cm<sup>-1</sup> relation, is typically different from material to material. However, some systems with similar structures and elastic properties can show the same stress dependence on peak shift.

Much like in XRD, the width of a Raman peak can tell the user about the quality of the crystal being analyzed. Wider peaks tend to be indicative of a disruption in order such as amorphization, or some other plastic deformation within the material. Unlike XRD, there is not necessarily a grain size dependence on the peak width. In other words, nano-grained or nano-particle samples will not show broader peaks unless they are disordered.

Of interest to most researchers is the intensity of a Raman peak. Variations in peak intensities are related to the amount of material that is being investigated. In the case of measuring transparent film thicknesses, the larger the characteristic peaks of the substrate, the thinner the film. This is due to the amount of Raman scattered photons from the substrate that can make it back to the detector. Thicker films mean less chance of scattered photons from the substrate reaching the detector. This can also give an indication of the amount of material in a mixture, given unique Raman modes that can be identified for each component. The relative intensity between two peaks can give an indication of the composition, as compared to the pure spectra of the components.

### **2.3.5 Penetration Depth**

The interaction between the sample and laser is such that there is a penetration of incident light into the sample. The depth to which the incident laser light penetrates, unsurprisingly called the Penetration Depth, is dictated by the absorption coefficient of the material being irradiated. In transparent samples, penetration depth is typically not considered, as most light will be transmitted through the sample. However in opaque materials, the penetration depth is necessary to know so that an idea of the volume of sample being investigated can be understood. The following equation estimates the dependence of penetration depth on the absorption coefficient <sup>[61]</sup>:

$$D_p \cong \frac{1.15}{\alpha(\lambda)}$$

This equation is defined as the sample thickness that scatters back 90% of the incident intensity for an infinitely thick sample. It is important to note that the absorption coefficient is dependent on the excitation wavelength, and therefore penetration can vary by varying excitation. This fact is utilized in this study to take advantage of depth analysis. The absorption coefficient of hot-pressed 6H-SiC has been shown to be  $\sim 3800\text{cm}^{-1}$  at 514nm excitation and  $\sim 3300\text{cm}^{-1}$  at 633nm excitation <sup>[62]</sup>. These correspond to a penetration depth of  $3\mu\text{m}$  and  $3.5\mu\text{m}$  respectively.

### **2.3.6 Special Techniques in Raman**

It is important to mention some of the more advanced techniques that take advantage of unique features of Raman spectroscopy and the Raman Effect in certain materials. Each of the techniques mentioned below take advantage of a different

interaction mechanism between the excitation source and the sample, and the resulting Raman scattering. While none of these techniques were employed for this study, their understanding opens up avenues of further experimentation that may prove useful elsewhere or in future work based on this thesis.

### **2.3.6.1 Surface Enhanced Raman Spectroscopy**

One interesting application of Raman spectroscopy is the ability to use nanometer size spheres, often metallic, to enhance the local electromagnetic field under the particle<sup>[63]</sup>. Known as Surface Enhanced Raman Spectroscopy, or SERS, this effect is defined as the enhancement of Raman scattering of molecules physisorbed or chemisorbed onto the surface of metallic particles <sup>[64]</sup>. The large Raman enhancement around the particle allows for analysis of small sample volumes normally overlooked by Raman. This enhancement can increase scattering intensity by several orders of magnitude beyond that of the non-adsorbed molecules. This allows also for the detection of single molecules, as the sensitivity is increased so greatly.

There are two schools of thought in regards to what the mechanisms for enhancement are: one is an increase in the molecular polarizability ( $\alpha$ ) of the molecule, while the other stems from an increase in the local electric field ( $E$ ). The polarizability theory comes from a charge transfer or bond formation between the SERS particle and the adsorbate which can increase the molecular polarizability in both particle and adsorbed molecule <sup>[64]</sup>. Increased polarizability causes stronger scattering and therefore an increased Raman signal. In the enhanced electromagnetic field theory, light incident to



the surface of the SERS particles excites conduction electrons which generate a surface Plasmon resonance. This resonance increases the local electromagnetic field within the particle that in turn increases the incident field around the surface. This stronger field causes an increase in the induced dipole moment of the Raman scattered light, and therefore increases signal intensity <sup>[63]</sup>.

Regardless of which theory is the driving mechanism for the SERS effect, the enhancement would not be possible without the use of metallic substrates or nanoparticles. Gold, silver, and platinum are all used as metals of choice for SERS enhancement. The Plasmon resonance frequencies that are thought to be required fall within the visible and near-infrared energies often used for excitation of Raman active modes of vibration <sup>[63]</sup>. Additionally, these metals are typically chosen for molecular adsorption because of their biocompatibility.

#### **2.3.6.2 Resonance Raman Spectroscopy**

In resonance Raman spectroscopy the excitation energy, and thus wavelength, is chosen such that the energy coincides with an electronic transition of the material of interest <sup>[65]</sup>. Instead of exciting to a virtual energy state, the atom or molecule is excited into one of the electronic states. Since the energy of these transitions differ from one chemical species to the next, this technique did not become applicable until the advent of tunable lasers in the early 1970s. When the frequency of the laser beam is tuned to be near an electronic transition, the resonance frequency, the vibrational modes associated

with that particular transition exhibit a greatly increased Raman scattering intensity. This increase in intensity is such that all other Raman active signals are often overwhelmed.

This aspect of Raman spectroscopy becomes especially useful for large biomolecules, with a vast number of vibrational modes <sup>[65]</sup>. Using Resonance Raman spectroscopy allows for the ability to look at relatively few vibrational modes at a time. This reduces the complexity of the spectrum and allows for easier identification of any unknown constituents. As the resonance effects are intimately related to electronic transition states, Resonance Raman is often used when characterizing semiconductor materials and probing the electronic properties of a system. Utilizing a tunable laser source and a temperature controlled testing stage, electronic band information can be obtained over a wide range of temperatures and wavelengths <sup>[64,65]</sup>.

The true advantage of this technique over traditional Raman spectroscopy is the large increase in intensity of the peaks in question, up to  $10^6$  times as the signal strength. This allows resonance Raman spectra to be generated from organic samples with very low concentrations of components. Also, as mentioned previously in samples with many vibrational states, only a few peaks will appear at one time and different peaks can be accessed by targeting specific electronic transitions. However, the main disadvantage of this technique is the increased risk of fluorescence and photo-degradation of the sample due to the increased energy of the incoming laser light. Both of these factors can be minimized by using an infrared laser instead of visible light for non-resonant Raman scattering, but not in RR where the laser must be tuned to the specific resonance, unless electronic levels of lower energy are available for the system under investigation <sup>[65]</sup>.

### 2.3.7 Raman of Silicon Carbide

The structure of silicon carbide is such that a vast number of long-range stacking sequences can be arranged as the unit cell. The result, as discussed earlier, is the formation of many different polytypes of SiC. Fortunately, based on the phonon interactions in silicon carbide, each polytype shows fairly unique Raman characteristic spectra. The following is a description of how different Raman modes appear in silicon carbide.

#### 2.3.7.1 Polytype Distinctions

The polytype structure of SiC is such that there are a potentially large number of atoms in the unit cell. 4H and 6H-SiC, containing 8 and 12 atoms respectively, will extend the unit cell in the c-direction only <sup>[66]</sup>. Given this the Ramsdell notation for hexagonal (nH) stacking also describes how many more multiples of the Si-C formula unit a polytype has than the basic 3C-polytype. Given that the first Brillouin zone is obtained only from the closest set of reciprocal lattice points in the gamma point, this means that the whole unit cell will not be represented in the Brillouin zone without some modification <sup>[67]</sup>.

To account for this effect, the Brillouin zone in the c-axis direction is reduced to  $1/n$  of the basic zone. The dispersion curves of the phonon modes that propagate outside this range are approximated by folding the dispersion curves back into the reduced first Brillouin zone. The large-zone boundary is described thus by Feldman et al. <sup>[68]</sup>.

$$k_{max} = \frac{n\pi i}{cn}$$

Where  $cn$  is the lattice constant and is approximately equal to  $nxa$ . Since  $n$  is proportional to  $cn$ , the large zone has the same extension into reciprocal space for all polytypes. Therefore, for the comparison of all polytypes using the folded modes, the reduced wave vector  $x = k/k_{max}$  is used. The following table shows the values of  $x$  that result in folded modes at  $k=0$  and therefore Raman peaks for common polytypes <sup>[69,70]</sup>.

Polytype	Atoms per unit cell	Accesible values of X
3C	2	0
4H	8	0, 0.5, 1
6H	12	0, 0.33, 0.67, 1

Figure 2.4: Accessible reduced wave vectors for common SiC polytypes.

The modes at which  $x=0$  are those at the center of the Brillouin zone and are the stronger modes in the Raman spectrum, caused by the Si and C sublattices vibrating against each other.

### 2.3.7.2 Peak Descriptions

Figure 2.5 shows the above mentioned folded phonon dispersion modes for 3C-, 4H-, and 6H-SiC. Raman peaks are determined by this phonon dispersion and are given designations based on the type of peak and whether it is a folded mode. Technically speaking, any peak not associated with the 3C-SiC stacking is a folded mode, and often if the 3C structure is not present, then the peak is assumed to be a folded mode and the “F”

designation is ignored. There are two main phonon branches that are seen, optical (O) and acoustic (A) <sup>[67]</sup>.

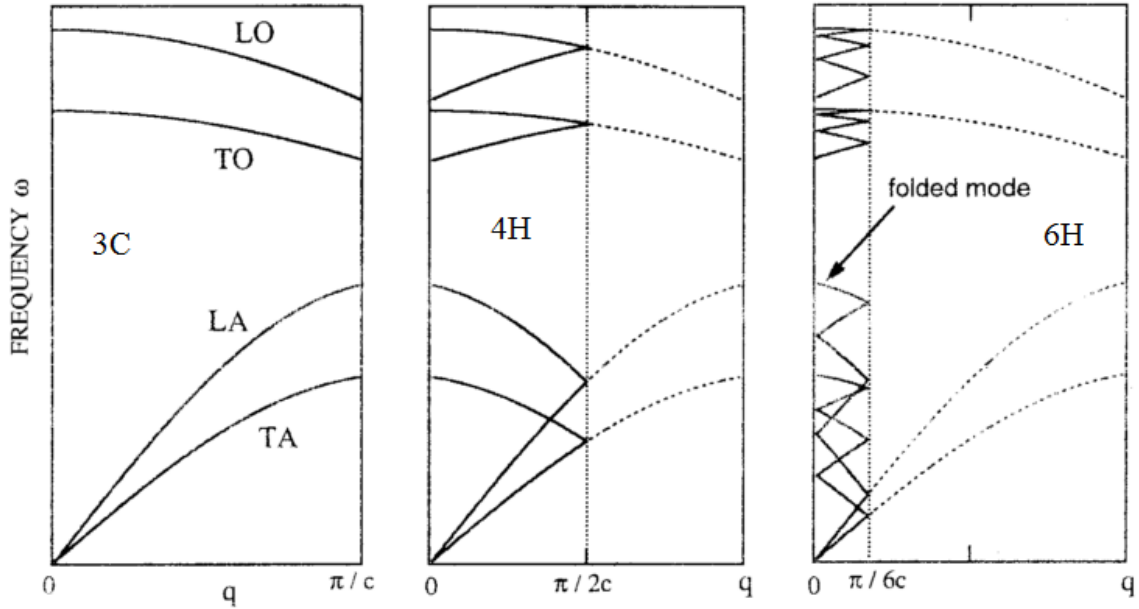


Figure 2.5: Phonon dispersion curves for 3C-, 4H-, and 6H-SiC. The folding of the Brillouin zone allows for unique peaks to develop for each polytype of silicon carbide, making Raman spectroscopy an excellent tool for characterization of SiC.

The optical branch derives its name from the ability to excite optical vibrations using light. The acoustic branch is analogous to long wavelength acoustic vibrations, wherein the amplitudes of the vibrations of the atoms are equal. To go along with the optical and acoustic modes are indications of the propagation direction of the electromagnetic waves (incident laser excitation). Those waves which propagate in the same direction as their motion are known as longitudinal (L) waves, and those which propagate parallel to their motion are known as transverse (T) waves. In looking at the

Raman spectra of SiC, the main phonon mode associated with a reduced wave vector of 0 is the TO (transverse optical) mode, and is the main peak studied in this work for stress and deformation analysis. The TA modes are examined as well, as these are more invariant to short range distortions in the crystal structure.

## 2.4 Nanoindentation

Nanoindentation is an experimental technique used to measure the mechanical properties of a material. Typically in nanoindentation, a spherical or pyramidal shaped diamond indenter is pressed into a material <sup>[71]</sup>. During the experiment, the applied force is recorded as a function of indentation displacement. Nanoindentation is similar to conventional hardness testing, but performed on a much smaller scale. The forces and displacements recorded are typically in the  $\mu\text{N}$  and nm ranges, respectively. When a nanoindentation test is performed, a load versus displacement curve is obtained. Following the application of the maximum load, the load is progressively removed and the displacement is recorded.

On unloading, if any plastic deformation occurs, the load-displacement data follows a different path than the loading curve, until at zero applied load a residual impression is left in the specimen surface. To analyze the data, classical contact mechanics solutions are commonly used <sup>[71,72]</sup>. The maximum depth of penetration, along with the slope of the unloading curve measured as the tangent to the unloading data at maximum load, gives a measure of both the hardness and elastic modulus of the specimen <sup>[73]</sup>. Nanoindentation experiments have been used to estimate residual stress based on the elastic recovery of indents, and the effect of subsurface quality on indentation results <sup>[74,75]</sup>. Figure 2.6 shows a schematic of the residual impression left during indentation, along with the displacements used in determining elastic properties.

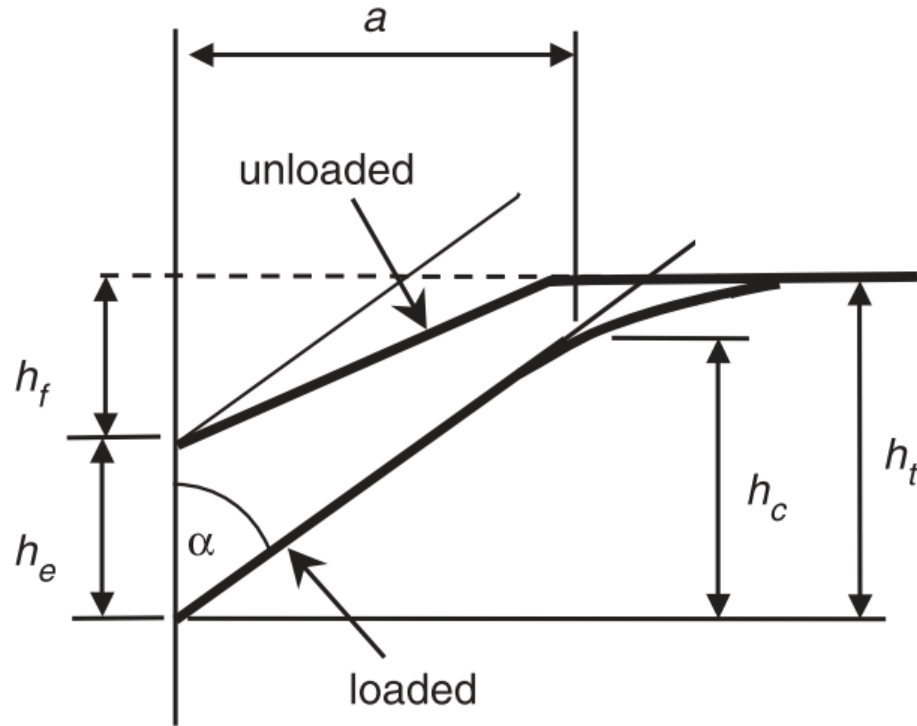


Figure 2.6: Schematic of indenter-sample surface contact during loading and unloading. The values shown are:  $a$  the contact radius,  $\alpha$  the indenter semi-angle,  $h_c$  the contact depth,  $h_f$  the final residual penetration depth and  $h_t$  the total depth of penetration.

#### 2.4.1. Area Function Determination

A particularly meaningful quantity in indentation is the projected area of the contact, defined by a calculated area function. In nanoindentation, the projected area of the contact is estimated from the plastic depth of penetration ( $h_p$ ). The Berkovich indenter that was used in this study consists of a three sided pyramid shape. The projected area of the contacts for an ideal three sided pyramidal tip is given by:

$$A = 3\sqrt{3}h_p^2 \tan^2 \theta$$

for a Berkovich geometry the semi-angle  $\theta=65.27^\circ$ . The depth of penetration,  $h_p$ , is related to the deformation of the material and the shape of the indenter by:



$$h_p = h_{max} - \varepsilon \frac{P_{max}}{S}$$

where  $h_{max}$  and  $P_{max}$  are the maximum tip displacement and load,  $\varepsilon$  is a geometric constant that accounts for the deflection of the surface at the contact perimeter, it is estimated as 0.75 by Oliver and Pharr<sup>[71]</sup> and  $S$ , is the stiffness calculated from the slope ( $dP/dh$ ) of the unloading curve, as seen in figure 2.7.

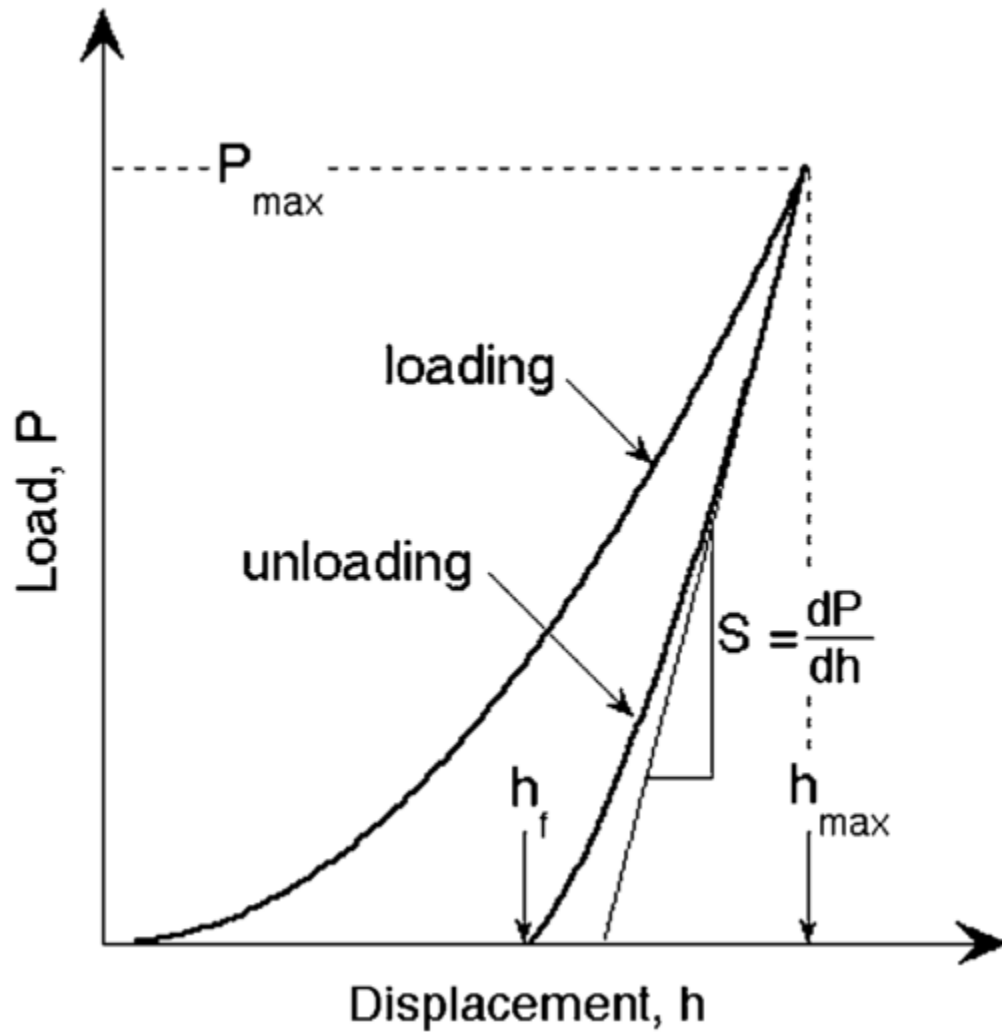


Figure 2.7: Load displacement curve showing the stiffness  $dP/dh$  and maximum load  $P_{max}$  used in calculating the elastic properties from nanoindentation.

However, perfect tip geometry is impossible to achieve. To account for non-ideal geometry of the indenter it is necessary to apply a correction factor that is part of the instrument's calibration. For this tip area calibration a series of indents at various contact depths on a calibration sample (fused quartz) of known elastic modulus are performed to fit a six order polynomial function of the form:

$$A = C_0 h_p^2 + C_1 h_p + C_2 h_p^{1/2} + C_3 h_p^{1/4} + C_4 h_p^{1/8} + C_5 h_p^{1/16}$$

where  $C_0=24.5$  for a berkovich tip and the other constants are determined during calibration. This calibration is typically done on a well studied material, fused quartz, for which the Oliver-Pharr analysis explains the behavior and mechanical properties near perfectly.

## **2.4.2 Analysis Methods**

Described below are several of the most commonly used analysis methods in instrumented indentation. Each has its own use based on the conditions of indentation, and their ability to accurately calculate the properties of interest. All of these analysis methods were used in this thesis work, however the indentation process overall proved advantageous beyond the calculation of elastic properties.

### **2.4.2.1 Oliver and Pharr Method**

There has been extensive work in the analysis and interpretation of instrumented indentation data, as well as the effect of stress on indentation in brittle materials. One of the most accepted methods of indentation analysis was proposed by Warren Oliver and

George Pharr <sup>[71,72]</sup>, in which the mechanical properties are obtained from the slope,  $S$  ( $dP/dh$ ), of the unloading curve. The equations they utilized are defined as follows:

$$H = \frac{P_{max}}{A}$$

$$S = \frac{dP}{dh} = \frac{2}{\sqrt{\pi}} E_r \sqrt{A}$$

where  $A$  is the projected area for a Berkovich indenter,  $h_p$  is the plastic depth of penetration,  $H$  is the hardness,  $P_{max}$  is the maximum applied load, and  $S$  is the contact stiffness during the initial unloading. The reduced elastic modulus accounts for the fact that elastic deformation occurs in both the indenter and the sample and it is related to the modulus of elasticity ( $E$ ) through:

$$\frac{1}{E_r} = \left( \frac{1 - \nu^2}{E} \right)_{sample} + \left( \frac{1 - \nu^2}{E} \right)_{indenter}$$

For a standard diamond indenter tip,  $E_{indenter} = 1140$  GPa and  $\nu_{indenter} = 0.07$ .

#### 2.4.2.2 Work of Indentation

In general, the response to the applied load is divided into an elastic-plastic loading followed by an elastic unloading. The net plastic area enclosed by the load-displacement curve represents the energy lost due to plastic deformation and any stored elastic strain due to residual stresses within the material <sup>[76]</sup>. During unloading, work is then done by the system as the material elastically recovers. Seen below is a schematic of the total work to indent,  $W_{tot}$  and the work that is elastically recovered under the indent  $W_u$ .

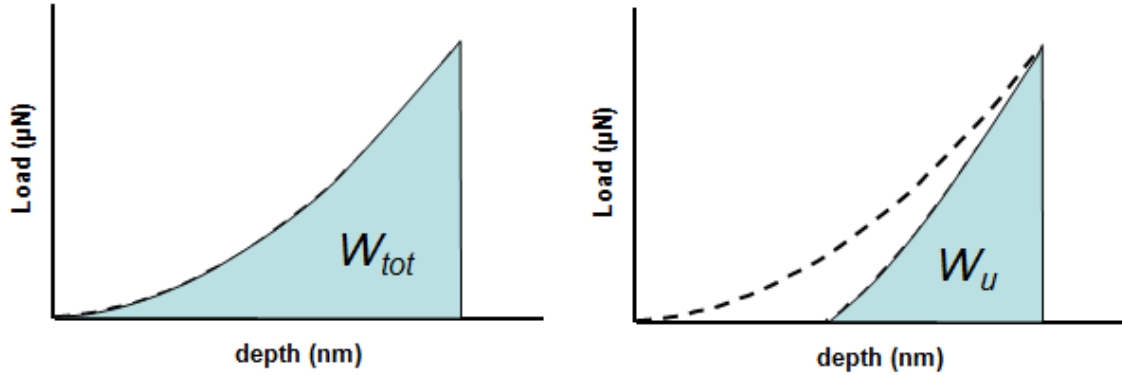


Figure 2.8: Schematic of the total and elastic work descriptions.

The load-displacement curve (sometimes called the load-depth curve) obtained from nanoindentation can be considered equivalent to a force-distance curve and therefore, by integration under the curve, the work of indentation can be found. The total work done by the indenter,  $W_{tot}$ , to cause both elastic and plastic deformation when the indenter reaches maximum depth,  $h_{max}$  is given by:

$$W_{tot} = \int_0^{h_{max}} P \, dh$$

Integration under the load-displacement curves can be numerically found using the trapezoid rule. Basically, the trapezoid rule works by approximating the area under the curve as the sum of very small trapezoids. The plastic ( $W_p$ ), elastic ( $W_u$ ) and total ( $W_{tot}$ ) works of indentation were calculated from all the load-displacement nanoindentation curves. Integration under the loading curve gives  $W_{tot}$ , while integration under the unloading provides  $W_u$ . The difference between  $W_{tot}$  and  $W_u$  is the plastic work ( $W_p$ ) of indentation. This analysis was initially proposed by Cheng and Cheng <sup>[77]</sup>, and

used a method of dimensional analysis to relate this work value to a ratio of hardness to reduced elastic modulus:

$$\frac{H}{E^*} \approx \Pi_{\theta} \left( \frac{W_{tot} - W_u}{W_{tot}} \right)$$

Where the  $\Pi_{\theta}$  term is a dimensionless function based on yield strength, elastic modulus, indenter angle and Poisson's ratio.

### 2.4.2.3 Joslin and Oliver

A parameter that's often looked at to eliminate any dependence of elastic modulus or hardness on contact area was developed by Joslin and Oliver <sup>[78]</sup>. A ratio of the applied load (P) to the contact stiffness squared ( $S^2$ ) is used to directly measure the elastic modulus and hardness independent of the penetration depth or contact area. Given that neither the hardness nor elastic modulus varies with depth, the following equation can be applied <sup>[72,78]</sup>:

$$\frac{P}{S^2} = \frac{\pi}{(2\beta)^2} \frac{H}{E^2}$$

This was first used in an experiment where surface roughness led to uncertainties in the contact area, yet a comparative evaluation of the mechanical properties of several materials was needed <sup>[71]</sup>. Since then, it has proven useful in providing accurate calculations of hardness even when significant pile-up is seen. As this parameter is independent of contact area, and contact area has been shown to be influenced by residual stressing <sup>[72]</sup>, it is a useful tool in relating mechanical properties between like materials with different levels of stress.

### 3. Experimental Procedures

The goal of this thesis was to understand how machining will influence the amount of residual stress and damage present in a machined component. It was determined that the techniques to be used needed to be as non destructive in nature as possible. This was done to avoid causing any significant changes in the stress states at the surfaces of the samples, or impart any uncontrolled deformation into the material. For the majority of this thesis work, this was accomplished mainly through the use of Raman spectroscopy and nanoindentation. The use of XRD stress analysis and Knoop indentation are presented in Chapter 4, as standalone work in metallic systems. The use of x-ray diffraction for stress analysis in silicon carbide ceramics is quite difficult to achieve without the proper setup or x-ray source <sup>[79,80]</sup>.

#### 3.1 Raman Spectrometer

The Raman system used in this work was an inVia Raman Microscope from Renishaw Inc. (New Mills, Wotton-under-Edge Gloucestershire, GL12 8JR UK). Coupled to this system is a Leica microscope with 5x, 20x and 50x objectives attached. Objectives are selected based on the required resolution of the experiment, with spatial resolution increasing with larger apertures, as given by:

$$R = \frac{0.61 \times \lambda}{NA}$$

Where  $\lambda$  is the excitation wavelength and NA is the numerical aperture of the objective. For this thesis work, all spectra were obtained using the 50x objective of the inVia microscope. Laser wavelength is typically selected based on the sample type, with resonance effects taken into consideration. For many inorganic samples with large band

gaps, much of the visible spectrum can be used for Raman excitation. Available on this machine are: 785nm diode laser; 633nm HeNe laser; and 514nm Ar ion laser. The near-infrared 785nm laser is often used for polymer or biological samples, where fluorescence effects may be an issue. The 633nm and 514nm lasers were mainly used throughout this work, as there were actually fluorescence issues with the 785nm wavelength in silicon carbide.

The inVia unit is shown in figures 3.1 and 3.2, with the relevant components labeled. Laser light enters the system unit from the back at the bottom right mirror. This mirror provides the initial alignment of the beam through the system, and is often unchanged once properly set. The light is then passed through a beam expander that allows the user to defocus the beam by any percentage of interest. This is done mainly in imaging modes, where the beam is defocused 100% to saturate the entire CCD at once and obtain Raman images. This mode was not used in this work, and the beam expander was set at 0% to allow the full focus of the beam to interact with the sample.

From here, the laser light hits a second alignment mirror, the bottom left mirror, which is the main adjustment mirror with which users can calibrate and align the beam. This mirror sends the laser up through the vertical section into the top left mirror, which is a Rayleigh filter. This filter, consisting of a wheel of mirrors with one set of mirrors for each excitation wavelength, allows for the excitation light to pass into the inVia podule and filters out the returning elastically scattered light. This is known as a holographic notch filter, and allows only the Raman scattered light to pass back through into the spectrometer.

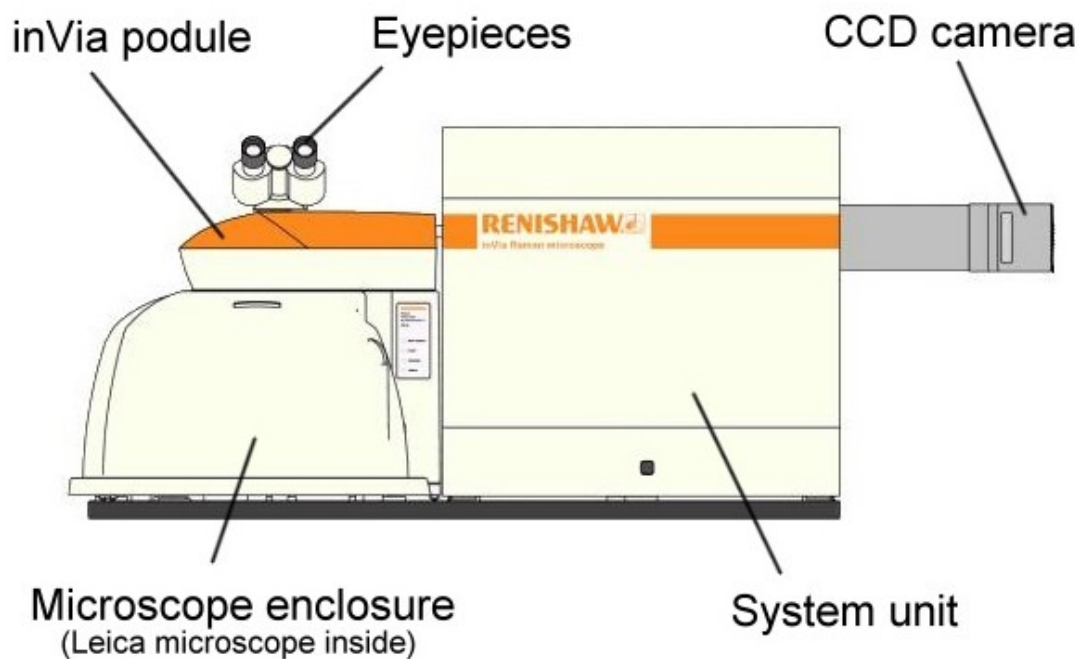


Figure 3.1: External Components of the Raman inVia microscope. Note the unit used in this study did not have a microscope enclosure.

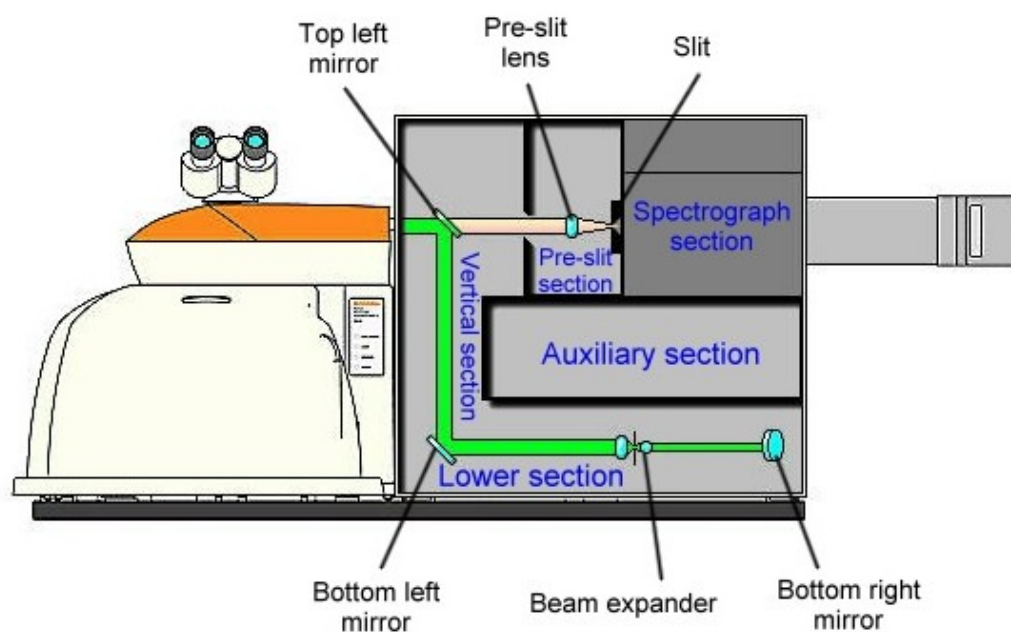


Figure 3.2: Internal Components of the Raman inVia microscope.



Once inside the podule, the laser beam is either directed to the sample through the microscope enclosure, or to a silicon reference sample at the end of the unit. Silicon is used as a reference as it has one strong peak at  $520.5\text{cm}^{-1}$  that is easy to calibrate against. To acquire Raman spectra from samples, the incident light is sent through the microscope objective to strike the sample surface that is in focus below. The Raman scattered light is then collected back up through the objective, this is known as a backscattered geometry and is the one most often used for the Raman collection geometry. The Raman signal is then passed through the filter at the top left mirror, where any incident wavelength light is filtered out, and passes through a pre-slit lens. This lens focuses the Raman signal onto an adjustable slit, set to a specific width to allow optimal signal strength and resolution. The standard slit width is calibrated based on the silicon reference sample, and is set at  $50\mu\text{m}$ .

After passing through the slit, the signal enters the spectrograph section where another series of lenses focuses the light onto a diffraction grating. This grating splits the light into different wavelength components, i.e. the Raman spectrum, so that the CCD at the end of the unit can detect the individual components and create the spectrum. Diffraction gratings are selected based on laser wavelength and have a direct effect on the spectral resolution of the system. This system is equipped with an 1800- and a 1200 l/mm grating, though the 1800 l/mm grating is optimized for the 514 and 633 nm lasers. Once the Raman signal is diffracted and focus onto the CCD, the photons are read and interpreted by the CCD and the result is a Raman spectrum. Figure 3.3 shows a more detailed look at the laser path through the system and the interaction with the gratings.

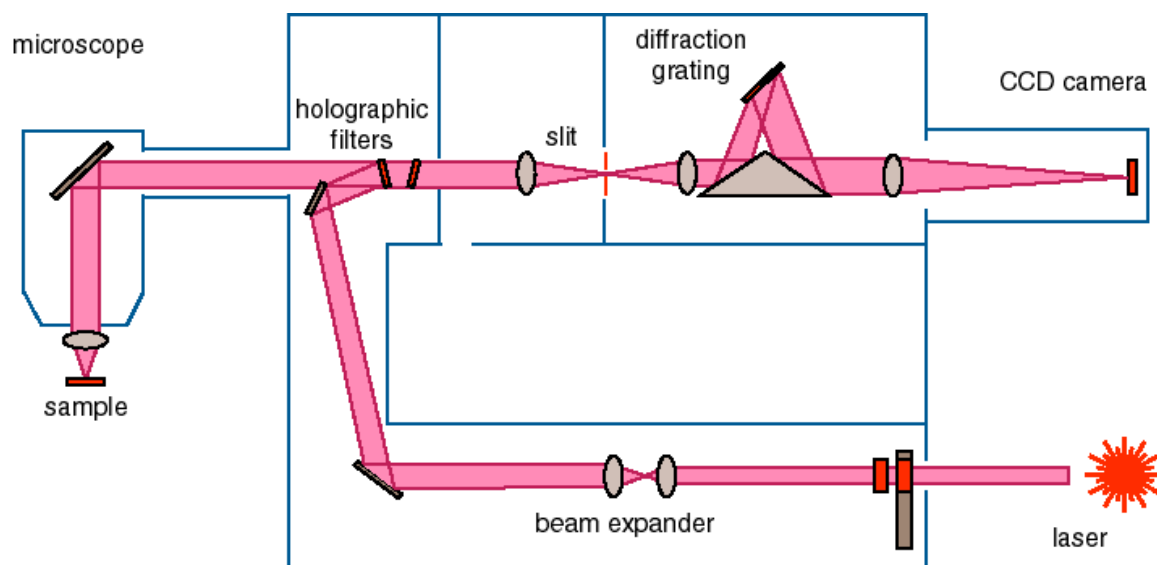


Figure 3.3: Laser path through the Raman spectrometer

### 3.1.2 Raman Mapping

The method of sample analysis used in this work is that of Raman mapping. In this setup, the laser is moved across the surface in a raster pattern and a Raman spectrum is collected at each point on the map. Once the sample is placed under the microscope, and focus at the proper objective is achieved, the mapping can begin. Map scans were performed on each sample over areas of  $40\mu\text{m} \times 40\mu\text{m}$  with  $2\mu\text{m}$  spacing between each map point. Maps were collected at 4 spectrometer settings: 514nm excitation with slit width of  $20\mu\text{m}$  and CCD pixel collection area of 3 pixels (confocal setting), 514nm excitation with slit width  $50\mu\text{m}$  and CCD pixel collection area of 20 pixels (regular setting), 633 nm excitation with “confocal” setting, and 633nm excitation with “regular” setting. For each sample surface, 10 such maps were created in different areas to get an idea of both the local stress variation and overall stress of the sample. Reported values in this thesis are averaged over the entire set of maps for each sample.

### 3.1.3 Curve Fitting

The software provided with the Raman system, known as WiRE 3.2™, was used to analyze the spectra obtained from the mapping procedure. Spectra were corrected for baseline, and normalized to the most intense peak for easier curve fitting. The fitting process was performed using the curve fit tool in the software, in which a set of curves were defined for the 6H-SiC spectra. Figure 3.4 shows the curve fit parameters for the peaks of interest in this work. The “% Gaussian” parameter indicates how much of the curve is fit to a Gaussian distribution, with the remaining percent being a Lorentzian fit. It is important to note that these are starting parameters for the fitting process, based on single crystal spectra, with additional peaks that were found in the machined samples.

Peak Position (cm <sup>-1</sup> )	Center	Width	Height	%Gaussian
767	766.935	7.119	0.1578	35.802
776	775.457	7.792	0.0655	0
789	789.215	7.489	0.939	23.129
797	797.373	7.944	0.374	14.864
970	970.91	12.558	0.408	10.387

Figure 3.4: Fit parameters for the Raman curve fitting software.

With the fitting curves defined, a mapping review could now be performed. This is a software feature that takes the curve fit parameters, and applies them to all of the spectra obtained within a map. This allows for fast analysis of each acquired spectrum, as well as the ability to pick which features: intensity, shift, width, area etc. that the user wants mapped. The resulting map files provide an exportable list of all the values of interest at each mapping point which can be post-processed using another software package (SigmaPlot™, Origin™, Excel™, ... etc.).

Peak information from the TO peak located around  $789.2 \text{ cm}^{-1}$  was used in both stress analysis and deformation analysis using peak shifts and widths, respectively. The following equation was used to determine residual stress and comes from Liu et al. <sup>[81]</sup>. It is derived from experiments applying hydrostatic pressures to single crystal SiC samples and fitting an empirical relation to the change in peak position due to stress.

$$\omega_{TO}(\text{cm}^{-1}) = 789.2 (\text{cm}^{-1}) + 3.11P - 0.009P^2$$

Where,  $P$  is the pressure applied to the system and  $\omega_{TO}$  is the recorded wavenumber shift due to  $P$ . As the pressures that Liu applied were vastly greater than what is expected to be seen here, the quadratic part of the above equation can be ignored, reducing the equation to a linear fit. This equation is modeled after the application of hydrostatic pressure, which is not the same as residual stresses from machining. Residual stresses may be uniaxial, biaxial or triaxial; However, the below equation provides a method to quantify the overall effect of the residual stresses and to qualitatively rank the different machining methods in terms of residual stress generated.

$$\omega_{TO}(\text{cm}^{-1}) = 789.2 (\text{cm}^{-1}) + 3.11P$$

The width analysis uses the peak widths obtained from the TO peak in each sample. These widths are normalized to the single crystal peak width obtained for the scan setting used. Analysis of peak widths, as discussed in Chapter 2 gives an indication of the amount of residual deformation in a crystal, and can be indicative of subsurface damage.

### 3.2 Nanoindentation

Nanoindentation experiments were performed on all samples using a Hysitron Inc., MN55344, USA, Triboindenter™ fitted with a Berkovich diamond indenter tip. The Berkovich tip has a 3-sided pyramidal geometry, and the tip radius for the indenter used was 150nm. Each sample was indented with an array of 441 indents, evenly spaced in a  $40\mu\text{m} \times 40\mu\text{m}$  grid with  $2\mu\text{m}$  spacing. This spacing was set to match the resolution limits of the Raman machine, as well as limiting the effect of prior indents on the next indent. The load functions used can be seen in figures 3.5 and 3.6, and maximum applied loads were set at 10mN and 30mN. These were chosen as they were the maximum loads that the 2 transducers available could apply.

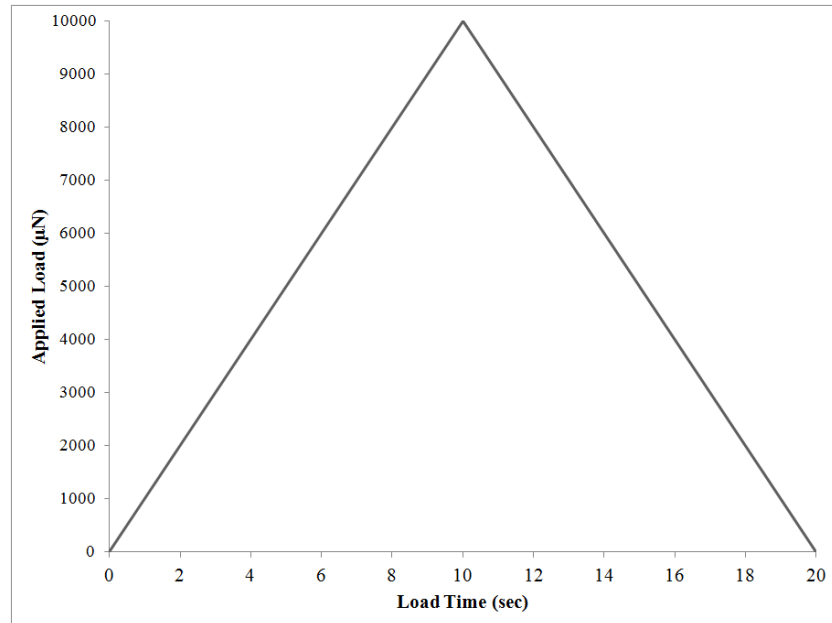


Figure 3.5: Load function used for 10mN maximum load indentation. No hold is set for this function as creep is not assumed to be an issue.

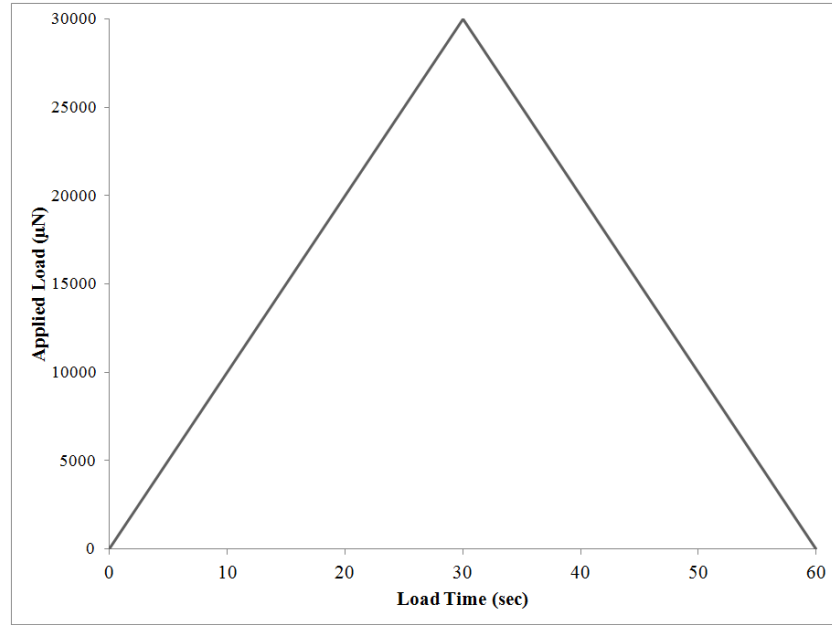


Figure 3.6: Load function used for 30mN maximum load indentation. No hold is set for this function as creep is not assumed to be an issue.

Using the indentation software coupled to the Triboindenter, the elastic modulus and hardness values are determined from the Oliver and Pharr method<sup>[71]</sup>. Load-displacement curves are exported into text files to perform the work analysis proposed by Cheng and Cheng<sup>[76]</sup>. The stiffness and load values recorded for each indent were used for the Joslin and Oliver analysis, which is independent of contact area.

### 3.3 Raman Spectroscopy

Following the indentation experiments, Raman mapping was performed over the indented arrays. This mapping followed the same setup as in the pre-indented samples, using the same processing of spectra and curve fit parameters. Post-indentation maps were used to study the effects of introducing a controlled deformation to the machined surfaces.

#### 4. Study on Stress in Metallic Samples

The work presented below consists of a study wherein the techniques used to quantify residual stress in metallic systems were examined. The goal was to establish whether a simple indentation technique using a Knoop indenter could be used as an alternative to x-ray diffraction as a tool for stress analysis. It was found that, while unable to be used for quantitative residual stress measurements, Knoop indentation could be in a qualitative manner to determine whether a residual stress was present in a metallic sample.

##### 4.1 Identifying changes in residual stress using indentation on machined metallic surfaces

B.P. Groth<sup>a</sup>, A.B. Mann<sup>a,b</sup>

<sup>a</sup>*Materials Science and Engineering Department, Rutgers University, 607 Taylor Road, Piscataway NJ, 08854. USA*

<sup>b</sup>*Biomedical Engineering Department, Rutgers University, 599 Taylor Road, Piscataway NJ, 08854. USA*

Emails: [bengroth@eden.rutgers.edu](mailto:bengroth@eden.rutgers.edu) and [abmann@rci.rutgers.edu](mailto:abmann@rci.rutgers.edu)

**Abstract:** The processing of metals can create residual surface stresses that dramatically impact their performance and may even lead to premature failure. An example is abrasive, mechanical machining of metals to create components with specific dimensions. Knoop indentation and nanoindentation have been used to identify compressive residual stresses produced during surface abrasion of high purity ruthenium and alloys of aluminum, steel and titanium. X-ray stress measurements of residual stresses were used as a control. A larger elastic recovery is seen in the shorter axis of Knoop indentations

and in nanoindentation load-depth curves when comparing metals with a “rough” surface preparation to those with a “standard” polished finish. The degree of elastic recovery mirrors the increased compressive residual stress in the metals. The residual stress does not directly affect the mechanical properties of the metal rather it affects the indentation geometry. All the samples showed a similar effect suggesting that the methods could be used as a quick and easy quality control check for the extent of residual stresses produced by mechanical machining of metals.

**Keywords:** Metal forming and shaping; Indentation and hardness; Metals and alloys; Elastic properties

## **1. Introduction:**

Machining is a harsh process that may cause changes in microstructure (such as twinning, dislocation formation and point defects), increases in residual stresses and the generation of sub-surface flaws.<sup>[1-3]</sup> Quantifying the effects of machining can be difficult, as well as destructive to the end product. When dealing specifically with stress analysis, small samples often need to be cut from larger pieces which must be sacrificed. In order to simplify this process indentation methods have been examined as a tool for assessing the extent of residual stress in machined metals. The study encompassed the testing of residual stresses in a variety of alloys with different crystal structures (FCC, BCC and HCP). The analysis method chosen is based on the approach of Marshall et al.<sup>[4]</sup> who used Knoop indentation to examine the ratio of hardness (H) to elastic modulus (E) for various materials. They developed a simple relationship between H/E and the ratio of the elastic recovery of the short axis of a Knoop indent to the mostly invariant long axis.



Figure 1 shows the axes measured and Marshall et al.'s graph of the short axis to long axis ratio versus  $H/E$ , along with the linear fit they proposed. Marshall et al.'s method does not take into account the stress state of the sample, though others have suggested that stress may influence the shape of a Knoop indent<sup>[5-9]</sup>. If such a dependence between stress and the indent geometry exists it will influence the values of  $H/E$  determined using the Marshall et al. method and give values that do not follow the trend line they developed.

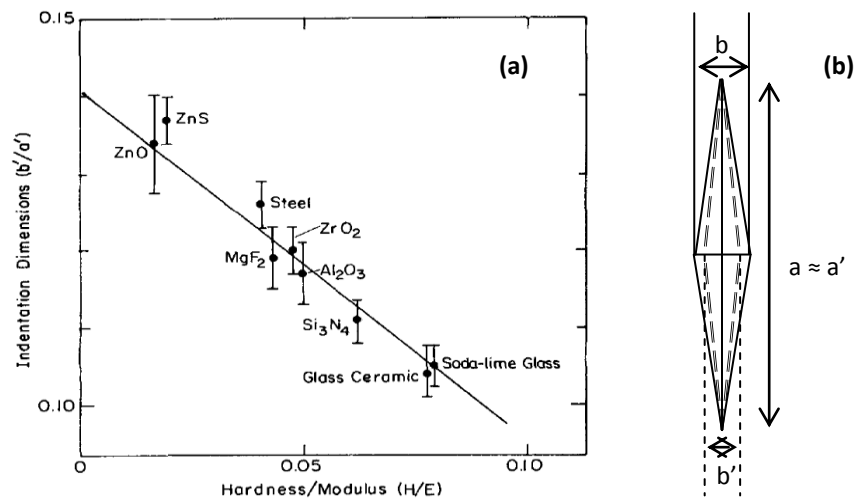


Figure 1: (a) Graph from Marshall et al.<sup>4</sup> showing the relationship between  $H/E$  for various materials (from literature) and (b) the ratio of the residual Knoop impression's axes,  $a'$  and  $b'$ .

## 2. Material and methods:

Seven samples of high purity (>99.95%) ruthenium, Ru, were cut from disc shaped blocks formed via hot-isostatic pressing of Ru starting powders. The pressed Ru blocks had densities >99% of the theoretical density of pure Ru. All the disc shaped

blocks were roughly ground at various machining rates to their final dimensions, before being finished on a diamond wheel, with the exception of one sample which was kept in the rough-polished state. Two samples were polished with decreasing particle size diamond abrasives while one sample was taken from a rough-polish to finished polish with an orbital sanding pad affixed with fine carbide paper. To ensure all seven samples had a uniform finish they were taken from a point midway between the disc's center and its circumference.

In addition to Ru, which has a hexagonal close packed crystal structure, tests were performed on several metal alloys commonly used in engineering applications to examine the generality of the results. These were: face-center cubic 6061-T651 grade aluminum; hexagonal CP-2 titanium; and body-centered cubic 1018 cold rolled steel. Each of these samples were cut from 6.35 mm diameter rods and given a mild polish to remove any burs or large cut marks. These “as received” samples were tested to obtain a baseline value for residual stress. They were then intentionally stressed by a modified shot-peening method to induce a high, compressive, residual surface stress.

Knoop indentation measurements were performed on all the samples, and also on the full-size blocks of Ru to ensure that there was no effect from removing the samples from the full disc. The indentations were made with a 2kg load using a LECO Corporation, MI 49085, USA microhardness tester fitted with a diamond Knoop indenter. The long and short axes (see Fig. 1b) were measured on the instrument using 10x magnification and, subsequently, using a high magnification optical microscope with computer software image analysis. The stress was independently measured using X-ray diffraction (XRD) by the traditional  $\psi^2$  method<sup>[10]</sup> and a refined setup similar to the  $\psi^2$

that yields more accurate data. A Bruker AXS Inc., WI 53711-5373, USA, HiStar™ system with a 2D array detector, and Cu radiation with a 0.05mm diameter collimator was used. The baseline samples were all found to have residual compressive stress, but it was lower in the alloys than in the Ru.

The H and E of the samples was tested by nanoindentation using a Hysitron Inc., MN55344, USA, Triboindenter™ equipped with a Berkovich pyramidal diamond tip. The methods set forth by Oliver and Pharr<sup>[11]</sup> were used to analyze the unloading portion of the load-depth curves.

### **3. Results:**

The ratio of the elastic recovery of the Knoop indent axes on the Ru samples are plotted against residual stress measured with XRD in Figure 2. These samples were found to have compressive stresses averaging 900 MPa and their average elastic recovery was 0.129 with the exception of the sample taken finished with orbital sanding (labeled “G” on Figure 2); had a larger compressive stress (1250 MPa). Nanoindentation (see Figure 3) also gave noticeable differences between sample G and the other Ru samples, with  $E=442$  GPa and  $H=16.2$  GPa for the lower stress samples, which are close to literature values<sup>[12]</sup>, but  $E=525$  GPa and  $H=20$  GPa for sample G.

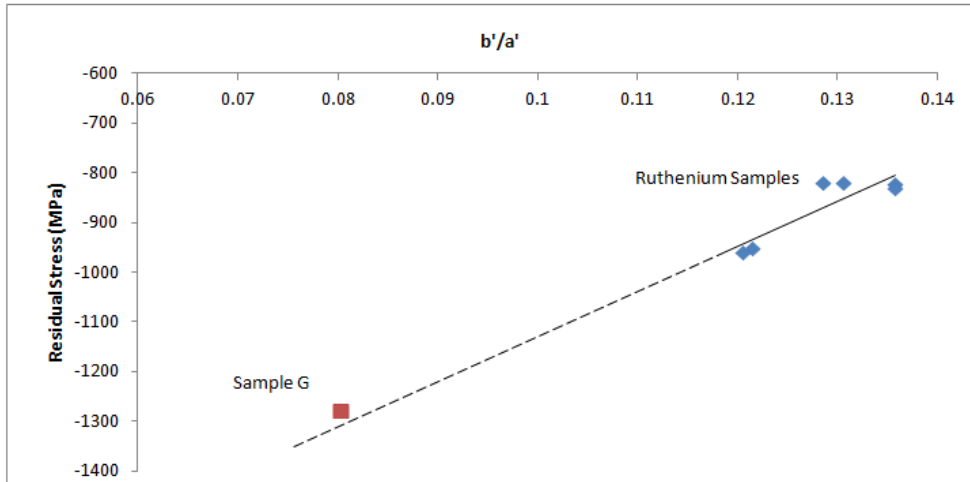


Figure 2: Graph showing the elastic recovery of the Knoop indent in the Ruthenium samples vs. the residual stress values. The solid line is a best fit line for the low stress samples, while the dashed is an extension of this line out to lower recovery values. The higher stressed “sample G” fits well with this trend line.

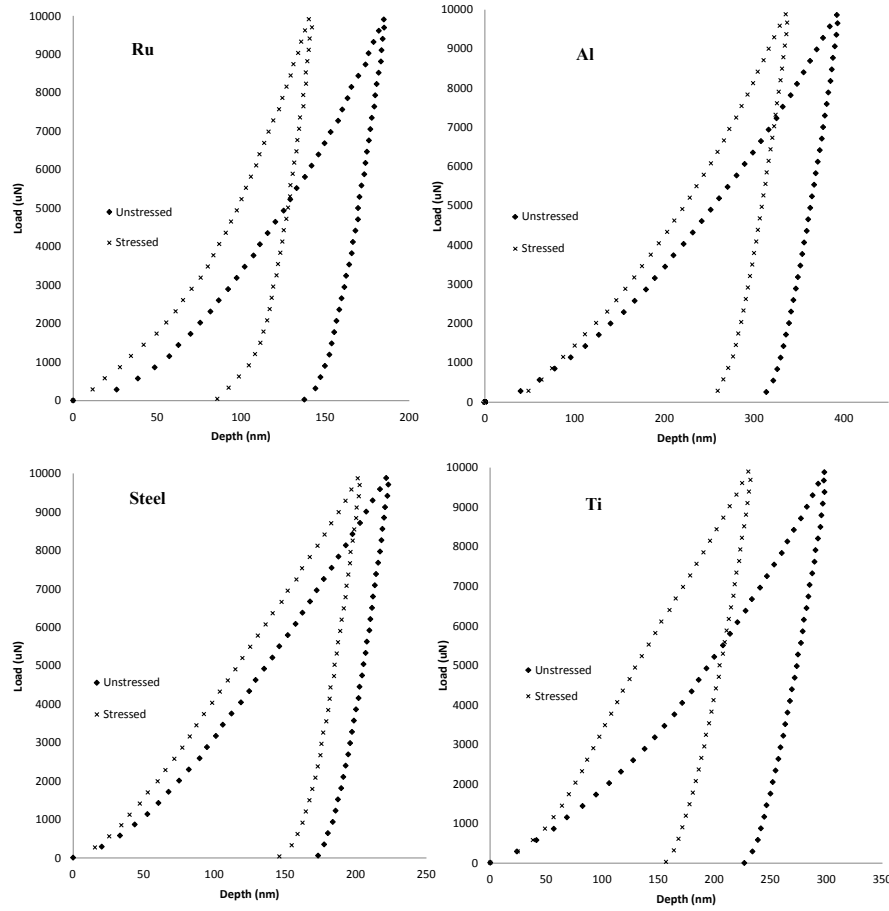


Figure 3: Comparison of load-depth curves obtained from nanoindentation for all samples studied. In all four it can be seen that there is a change in maximum depth due to the presence of stress.

During nanoindentation similar differences to those seen in Ru were observed between low and high stress in the three alloys, as shown in Figure 3 and summarized in Table 1. Knoop indentation also showed the short to long axis ratio was affected by residual stress in a similar manner for all the samples (Figure 4).

	Ruthenium	Aluminum	Steel	Titanium
Unmachined Stress	-900 MPa	-80 MPa	-200 MPa	-150 MPa
Unmachined $E^2/H$	$10571.9 \pm 1644.8$	$2135.53 \pm 230.52$	$7165.55 \pm 780.26$	$2964.63 \pm 312.27$
Machined Stress	-1280 MPa	-230 MPa	-366 MPa	-300 MPa
Machined $E^2/H$	$11230.3 \pm 1544.7$	$2227.25 \pm 250.48$	$7300.30 \pm 820.5$	$2974.50 \pm 325.64$
Yield Stress <sup>1</sup>	-	255 MPa	415 MPa	410 MPa

Table 1: List of data obtained for all metal samples, showing the same value for  $E^2/H$  (within error, values from nanoindentation) of the highly stressed as the lower stressed (values from XRD) samples (Note 1: Values from The Metals Handbook, Desk Edition).

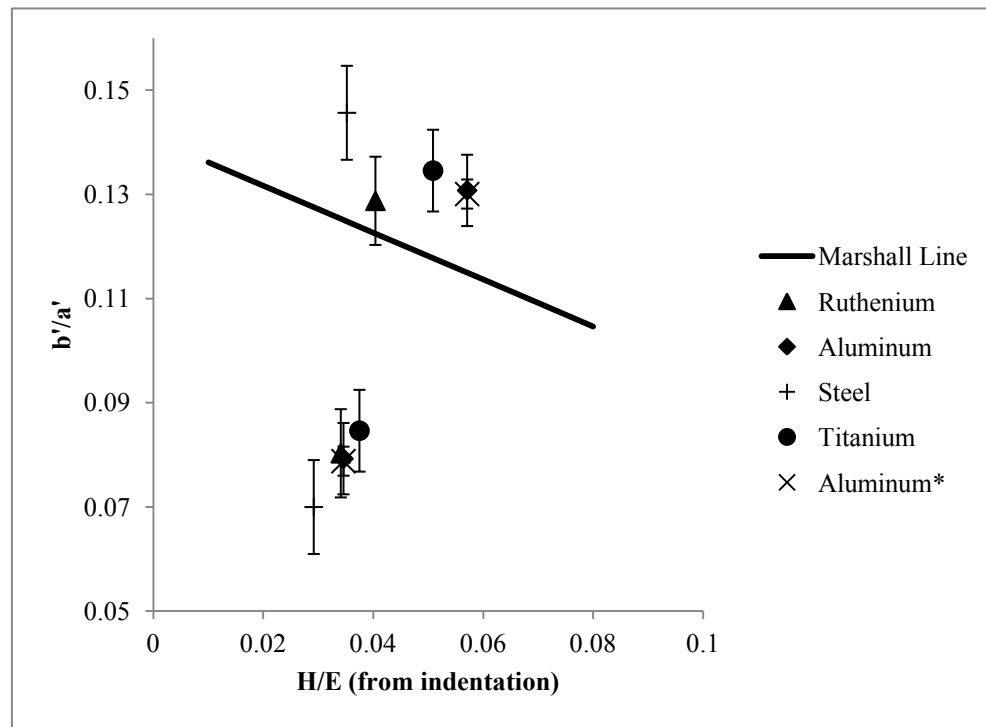


Figure 4: Plot of the  $H/E$  values obtained from nanoindentation vs recovery,  $b'/a'$ , for all tested materials. The Aluminum\* point marks the recovery obtained from lower load Knoop indents (averaged from 100g-1Kg).

#### 4. Discussion:

Using the Marshall et al.<sup>[4]</sup> approach, and based on literature values<sup>[20]</sup> for Ru,  $E=447$  GPa,  $H= 15$  GPa, we get a value of  $H/E$  ratio that is 0.033, which from figure 1 gives an expected recovery ratio for unstressed Ru of  $b'/a' = 0.127$ . This is very close to the value (0.129) obtained by averaging the recovery for the Ru samples with a compressive stress of 900 MPa. For the Ru sample G which has a larger residual stress (1250 MPa) there is a clear drop in the value of  $b'/a'$  to 0.08, indicating that there is a significant recovery in the short axis of the residual Knoop indent. This value falls some distance from the expected value of Marshall et al. and would severely overestimate the ratio  $H/E$  placing it close to that seen for glass, as shown on figure 1.

Using the average nanoindentation values of  $H$  and  $E$  for the low compressive residual stress Ru samples to find the ratio  $H/E$  we find the elastic recovery is again close to the Marshall et al. line of figure 1. For the Ru with large residual stress (sample G) the effects of stress on the nanoindentation load-depth curve are clearly seen in figure 3 (a) . The effects of stress on nanoindentation data have been studied previously<sup>[13-18]</sup> and it has been shown that compressive stresses can cause substantial errors in the calculated contact area. This causes the differences seen in the load-depth data and, consequently, a perceived change in the  $H$  and  $E$ . In reality it is very hard to change  $E$  for a material and the nanoindentation values for  $E$  and  $H$  can be corrected to avoid the errors that occur when calculating the contact area. This is best shown by examining the peak load divided by the unloading stiffness squared (which can be evaluated as  $H/E^2$ ) using a contact area-independent analysis developed by Joslin and Oliver<sup>[19]</sup>. When using this analysis it can

be seen from Table 1 that the high- and low-stressed Ru samples give values for  $H/E^2$  that are the same within the standard error of the data.

The metal alloys studied, like the Ru samples, show a strong dependence between elastic recovery of the Knoop short axis and residual compressive stress. Specifically, low stress results in a recovery close to that predicted by Marshall et al. while high compressive stress gives a lower value of  $b'/a'$ . The nanoindentation load-depth curves (Figure 3) and the standard data analysis values of E and H for the alloys also show the same stress dependence as the Ru samples. Once again correcting for the contact area error by using  $H/E^2$  (see Table 1) it is found that the samples' mechanical properties are unchanged by the residual stress.

## 5. Conclusion:

It has been shown that the elastic recovery of the short axis of a Knoop indent, as measured by  $b'/a'$ , can be used to identify residual compressive stresses in ductile metal samples where  $H/E$  is relatively small. It may also be useful in some ceramic materials provided they have a low  $H/E$ . It is likely to be less useful for materials such as silica based glasses where  $H/E$  is relatively large. Marshall et al.'s analysis indicates that these materials will have an inherently low value of  $b'/a'$ , so using this ratio to quantify stress will have lower sensitivity. In general, using Marshall et al.'s approach in the presence of residual compressive stress would cause an overestimation of the  $H/E$ . The standard analysis for nanoindentation also over-estimates H and E when there is compressive stress acting. However, combining the Marshall et al. analysis and the nanoindentation  $H/E$  ratio gives a fairly good match for the unstressed samples. The use of Knoop



indentation and nanoindentation qualitatively shows the effects of residual compressive stress and may in some cases be a technique for quantitatively measuring these stresses.

**Acknowledgements:** The authors would like to thank Dr. Thomas Emge and Dr. Beda Mohanty of Rutgers University and Dr. Adrish Ganguly, now at Schlumberger, for their help in performing this work. This material is based upon work supported through the Ceramic, Composite and Optical Materials Center supported by the National Science Foundation, Industry & University Cooperative Research Program, under Grant #1034978.

#### References:

- [1] G. A. Ibrahim, C. Che Haron, and J.A. Ghani, "The Effect of Dry Machining on Surface Integrity of Titanium Alloy Ti-6Al-4V ELI," *Journal of Applied Sciences*, vol. 9, no. 1, pp. 121-127, 2009.
- [2] D. G. Morris, C. Garcia Oca, J. Chao, and M. A. Munoz-Morris, "Influence of machining conditions on tensile stress and ductility of a mechanically alloyed Fe – 40Al intermetallic," *Scripta Materialia*, vol. 46, pp. 843-850, 2002.
- [3] G. Quinn, L. Ives, and S. Jahanmir, "Machining Cracks in Finished Ceramics," *Key Engineering Materials*, vol. 290, pp. 1-13, 2005.
- [4] D. B. Marshall, T. Noma, and A. G. Evans, "A simple method for determining elastic-modulus-to-hardness ratios using knoop indentation measurements," *Communications of the American Ceramic Society*, October, pp. 175-176, 1982.
- [5] B. R. Lawn and V.R. Howes, "Elastic recovery at hardness indentations," *Journal of Materials Science*, vol. 16, no. 10, pp. 2745–2752, 1981.
- [6] J. C. Conway, "Determination of hardness to elastic modulus ratios using Knoop indentation measurements and a model based on loading and reloading half-cycles," *Journal of materials science*, vol. 21, no. 7, pp. 2525–2527, 1986.
- [7] A. Shindo, "A theoretical analysis of indentation hardness. VI. Analysis of the influence of the residual stresses on Knoop hardness," *Memoirs of the Faculty of Engineering, Kobe University*, no. 21, pp. 1-17, 1975.
- [8] M.J. Choi, S.K. Kang, I. Kang, and D. Kwon, "Evaluation of nonequibiaxial residual stress using Knoop indenter," *Journal of Materials Research*, vol. 27, no. 1, pp. 121-125, Nov. 2011.
- [9] D. Di Maio and S. G. Roberts †, "Substrate and elastic recovery effects in hardness measurement of CVD WC-based coatings," *Philosophical Magazine*, vol. 85, no. 1, pp. 33-43, Jan. 2005.

- [10] B.D Cullity and S.R. Stock. Elements of X-ray Diffraction. 3<sup>rd</sup> edition. New Jersey. Prentice Hall: 2001.
- [11] W. C. Oliver and G. M. Pharr, "Measurement of hardness and elastic modulus by instrumented indentation: Advances in understanding and refinements to methodology," *Journal of Materials Research*, vol. 19, no. 1, pp. 3-20, Jan. 2004.
- [12] ASM International Handbook Committee, J.R. Davis (ed.). Metals Handbook Desk Edition. 2<sup>nd</sup> Edition. New York: CRC Press; 1998.
- [13] Z.H. Xu and X. Li, "Estimation of residual stresses from elastic recovery of nanoindentation," *Philosophical Magazine*, vol. 86, no. 19, pp. 2835-2846, Jul. 2006.
- [14] A.W. Warren, Y.B. Guo, and M. L. Weaver, "The influence of machining induced residual stress and phase transformation on the measurement of subsurface mechanical behavior using nanoindentation," *Surface and Coatings Technology*, vol. 200, no. 11, pp. 3459-3467, Mar. 2006.
- [15] N. Schwarzer, G.M. Pharr, "On the evaluation of stresses during nanoindentation with sharp indenters," *Thin Solid Films*, vol. 469, SI, pp. 194-200, Dec. 2004.
- [16] T.Y. Tsui, W.C. Oliver, and G.M. Pharr, "Influences of stress on the measurement of mechanical properties using nanoindentation: Part I. Experimental studies in an aluminum alloy," *Journal of Materials Research*, vol. 11, no. 3, pp. 752-759, Jan. 2011.
- [17] A. Bolshakov, W.C. Oliver, and G.M. Pharr, "Influences of stress on the measurement of mechanical properties using nanoindentation: Part II. Finite element simulations," *Journal of Materials Research*, vol. 11, no. 3, pp. 760-768, Jan. 2011.
- [18] Z.H. Xu and X. Li, "Influence of equi-biaxial residual stress on unloading behaviour of nanoindentation," *Acta Materialia*, vol. 53, no. 7, pp. 1913-1919, Apr. 2005.
- [19] D.L. Joslin and W.C. Oliver, "A new method for analyzing data from continuous depth-sensing microindentation tests," *Journal of Materials Research*, vol. 5, no. 1, pp. 123-126, 1990.
- [20] L. Hyukjae, R.A. Coutu, S. Mall, and K.D. Leedy, "Characterization of metal and metal alloy films as contact materials in MEMS switches" *Journal of Micromechanics and Microengineering*, vol. 16, pp. 557-563, 2006.

## 5. Stress Variations in Machined Silicon Carbide

The following chapter is a discussion on the variations in stress states in silicon carbide ceramics that have undergone different levels and types of machining. The data was obtained through the use of Raman spectroscopy, as discussed in Chapter 3.1. The paper presented contains an analysis of the peak shift and peak width data for the TO peak for each machined sample. Further testing and discussion is provided in Section 5.3 that examines the effects of nanoindentation on the measured stress states. Additionally, attempts to map cross-sections of each sample as a means of observing the machining deformation layer are presented in that section.

### 5.1 Using Raman mapping to determine stress variation in machined silicon carbide ceramics

B.P. Groth<sup>a</sup>, A.B. Mann<sup>a,b</sup>

<sup>a</sup>*Materials Science and Engineering Department, Rutgers University, 607 Taylor Road, Piscataway NJ, 08854. USA*

<sup>b</sup>*Biomedical Engineering Department, Rutgers University, 599 Taylor Road, Piscataway NJ, 08854. USA*

Emails: [bengroth@eden.rutgers.edu](mailto:bengroth@eden.rutgers.edu) and [abmann@rci.rutgers.edu](mailto:abmann@rci.rutgers.edu)

**Abstract:** Machined SiC tiles were examined using Raman spectroscopy in order to identify and quantify variations in stress states due to the machining process. Mapping was performed using 514- and 633-nm wavelength excitation, in a standard and confocal setting to allow for depth analysis. These tiles, formed through hot-pressing, were machined on one side to four different surface finishes, each imparting a different amount

of surface deformation. Raman maps were created for each sample, showing the shift in peak position with depth at each point. Obtained spectra were compared to stress free single crystal samples as a reference, as well as single crystal samples that were deformed with micro-Vickers indents. The stress maps of the machined surfaces showed variations between surface finishes, as well as variations with depth. No variation was seen between samples on the un-machined side. Spectra peak widths were also analyzed as a means of determining crystallinity, and showed that a higher stress value, and extensive machining, did not necessarily correspond to a more damaged crystal. These results support the use of Raman as a simple qualitative and quantitative analysis tool for assessing damage in carbide ceramics.

## **Introduction and Background**

### **Silicon Carbide:**

Silicon Carbide is one of the hardest materials known, 4<sup>th</sup> behind diamond, boron carbide and cubic boron nitride<sup>[1]</sup>. As such, machining SiC parts into the required form can be difficult and yield unwanted defects. Whether the pieces are machined by grinding and polishing, laser-assisted techniques, or ultrasonic techniques<sup>[2]</sup>, the potential for residual stresses to form is always present. It is necessary to understand how much stress machining can impart to components, and whether this stress is detrimental (early failure) or advantageous (toughening).

Silicon carbide is made up of tetrahedra of either 4 Si atoms and 1 C atom, or 4C atoms and one Si atom<sup>[10]</sup>. These tetrahedra can be stacked in either parallel or anti-parallel sequences, and this stacking allows for SiC to take on many different polytypes.

The most commonly used polytypes are a cubic structure known as 3C or beta-SiC, or 2 hexagonal phases 4H and 6H, known as alpha-SiC. Each polytype has slightly different mechanical, optical and electronic properties that make them useful for specific applications in both the power electronics industry and abrasives industry<sup>[3]</sup>. As a result of their different structures and properties each form has its own unique Raman spectra that make the technique very useful for characterizing variations in polytype within the material.

In single crystal SiC, stress concentrators take the form of micropipes<sup>[3,4]</sup> and dislocations<sup>[5]</sup>. More detrimental than causing a stress, these features often impinge on the electronic properties and performance for which single crystal materials are used. As electronic properties are less important for bulk polycrystalline samples, machining aims to limit the defects so they are not able to act as stress intensifiers. In bulk, polycrystalline samples, stress points can come from processing inclusions and thermal stresses<sup>[6,7]</sup> caused during hot-pressing or heat treating. If the density is large enough, and the polytype mis-match great enough, stacking faults can also impart a significant stress into the sample<sup>[8,9]</sup>.

### **Raman Spectroscopy:**

Raman spectroscopy is a form of vibrational spectroscopy, that relies on inelastic scattering of monochromatic light to provide vibrational, rotational and other low-frequency mode information about a material system<sup>[11]</sup>. Data obtained from Raman spectroscopy comes in the form of a vibrational spectra. For a given material system, this spectrum will be unique, and contain information related to the elemental bonding within

that system. The theory and fundamentals of Raman have been discussed at great length elsewhere<sup>[11-13]</sup>, as well as the ability to use Raman as a stress measuring tool<sup>[14-17]</sup>. In the case of silicon carbide, the numerous polytypes that can form all have unique Raman spectra. This allows for easy characterization and distinction between polytypes, as seen in figure 1. The use of Raman to measure stress in silicon carbide has been examined quite thoroughly. However, these experiments are often done on the cubic, 3C<sup>[18-25]</sup> polytype, as it is more widely used in the power electronics field. Only a few papers<sup>[26,27]</sup> discuss the use of Raman for stress analysis in 6H-SiC, and this paper focuses on the equations developed by Liu and Vohra<sup>[27]</sup> as these are widely accepted for 6H silicon carbide.

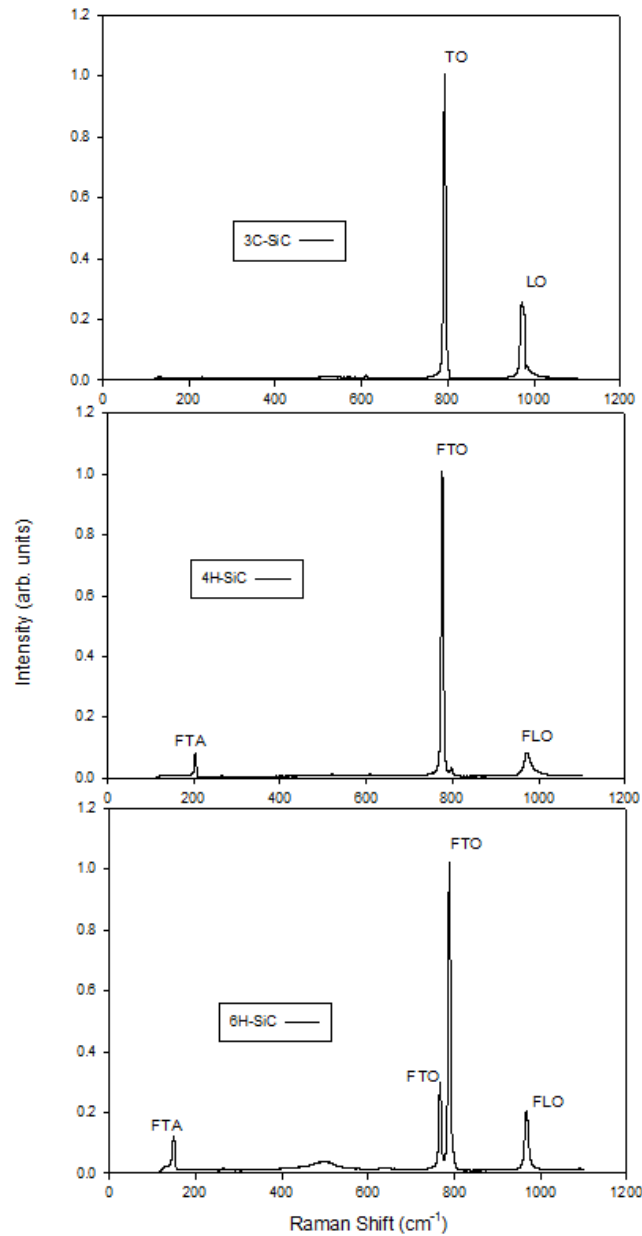


Figure 1: Sample spectra for 3C-, 4H-, and 6H-SiC. The variation in both position of optical phonons and unique acoustic modes allow for characterizing different polytypes. Peaks are designated by their propagation direction, with TO and LO being transverse optical and longitudinal optical, respectively. The ‘F’ before each designation in the hexagonal polytypes indicates a ‘folded mode’, a phonon mode having a reduced wave vector along the basic Brillouin zone of the 3C-SiC system.

The resolution of the system must be considered when analyzing spectra, and creating map images. There are several resolutions that will be taken into account: spatial, spectral, depth sensitivity and instrument precision. The spatial resolution of the scan is limited by the optics and the choice of wavelength, which determines the diffraction limit of the light; with lower wavelength excitation and higher N.A. (numerical aperture) objectives allowing for tighter mapping. The spectral resolution is set by the detector and machine alignment, and defines the system's ability to resolve peaks within a range of wavenumbers (number of wavelengths per cm). For the Renishaw Inc (New Mills, Wotton-under-Edge Gloucestershire, GL12 8JR UK) machine, at 633nm wavelength, this resolution is on the order of 5 wavenumbers. This means that peaks closer than  $5 \text{ cm}^{-1}$  could not be deconvoluted, however for the peaks analyzed in silicon carbide this will not be an issue. The depth from which information is obtained is wavelength dependent, and is also a function of the material being investigated. Penetration depth can be estimated by:

$$D_p = \frac{1}{\alpha(\lambda)}$$

,where shorter wavelengths,  $\lambda$ , and higher absorption coefficients,  $\alpha$ , allow for shallower analysis depths. Finally, the ability to reproduce the data at a given point is important. This is Raman system dependent, and if the machine being used is not very precise, the values obtained can be more readily questioned. For the inVia Renishaw Spectrometer, precision has been quoted as  $0.05 \text{ cm}^{-1}$  and verified by scanning the same point on a silicon calibration wafer several times, allowing for the sample to cool/settle between scans. The accuracy of the machine, or how close to the “real” spectra the



acquired spectra is, should be better than 1 wavenumber, and was checked against a neon lamp and calibrated to within 0.25 wavenumbers.

## **Materials and Methods**

Four hot-pressed silicon carbide tiles, made with alpha-SiC (6H structure) were obtained for this study. Each tile was mechanically machined on one side to a different surface finish: standard finish; grit blast finish; rotary ground; and mirror polish. The unmachined side, termed the reverse surface, acts as the baseline for each tile. The standard finish, figure 2(a) was simply a removal of excess carbon from the tile pressing with a light sand blasting. Optically, the standard finish surface is similar to the unmachined reverse side and can be considered an as-pressed sample. The grit blast samples were impacted with fine steel shot which, as it can be seen from the SEM image in figure 2(b), gives significant deformation on the machined surface of the tile. The rotary ground samples, figure 2(c) were taken from the as-pressed state to its finish through the use of diamond grinding wheels, running on a rotary grinder. The mirror polish samples were taken from the as-pressed state to a mirror-like finish through the use of successive polishing with diamond abrasive wheels. These samples displayed the lowest amount of surface roughness, as shown by figure 2(d). Single crystal samples of 6H-SiC were obtained from MTI Corporation, Richmond, CA 94804, USA, and used as a standard for stress comparison.

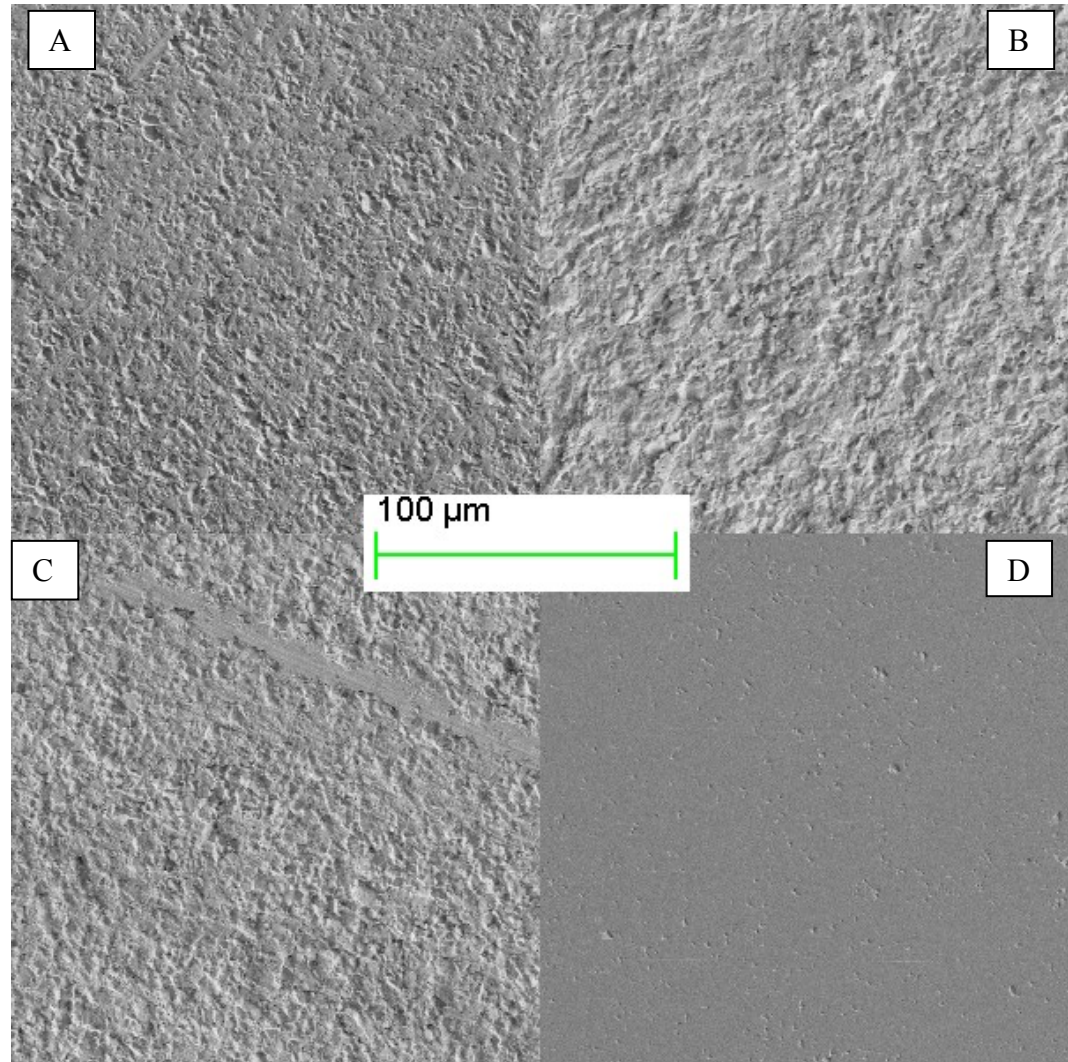


Figure 2: SEM images of the machined surfaces for the a) Standard, b) Grit Blast, c) Rotary Ground, and d) Mirror Finish.

In order to evaluate and quantify the stress in each sample due to machining, Raman maps were created over  $40 \times 40 \mu\text{m}$  areas, with  $2 \mu\text{m}$  spacing between points. This size was set based on the capabilities of the Raman system and to avoid spatial overlap of the Raman signal. The system was equipped with an  $1800 \text{ l/mm}$  diffraction grating for both the Ar ion  $514\text{nm}$  laser and the HeNe  $633\text{nm}$  laser. The maps acquired were point maps where each point was an individual spectra obtained, so as to obtain the full spectral

range of the sample, and not just one peak as examined in a linefocus map. Maps were acquired over several sections of each sample and stress values were averaged over all maps. Sample maps can be seen in the results section, showing the variation in each machined sample, with depth. Along with the machined surfaces, maps were created of the reverse, unmachined, sides of each tile. As all samples were pressed to the same specifications, it was found that the unmachined sides showed little variation between sample sets. The stress values obtained from these maps shows the residual stress due to the forming process alone.

In order to examine depth variations in the samples, a confocal setup was used, along with different excitation wavelengths. The confocal setting uses a virtual pinhole, created by slits in the spectrometer path and a decreased CCD scan area, as opposed to a physical pinhole in the laser path or in the microscope. The slits spacing is decreased from 50  $\mu\text{m}$  in the regular setup, to 20  $\mu\text{m}$  in the confocal, in order to limit the angle of returning light that is analyzed. Similarly, the CCD area is taken from 15 pixels down to only 3 pixels; this allows for greater spatial resolution at a cost of signal-to-noise ratio. In order to achieve intensity counts similar to those in the regular setting, several scan iterations were performed.

Collected maps were processed using the Wire3.2 software available from Renishaw. Spectra intensity were normalized to the largest intensity peak, the transverse-optical (TO) peak at  $789.2\text{cm}^{-1}$ , and corrected for baseline. Curve fitting was performed using the software's curve fit feature, with curve parameters set to allow mixed Gaussian-Lorentzian behavior. These parameters were saved and applied to each spectra in the acquired maps, and peak position and width information for the TO peak was extracted

for each map point. These values were used to create a contour plot of peak shift over the mapped area, and to obtain an average value for the peak width over the mapped area.

Peak shift values were then turned into stress values through:

$$\Delta\nu_{TO} = 3.11P + 789.2$$

,where P is applied pressure,  $\Delta\nu_{TO}$  is the measured TO peak position, and the value 789.2 is the unstressed peak position for the TO peak. This is a modification of the equation developed by Liu and Vohra<sup>[27]</sup>, as they investigate ultrahigh pressures where a quadratic term is needed. The residual stress values here are expected to still be in the linear region of this equation, and therefore only the first pressure dependent term is used.

## Results

### Single Crystal:

Raman maps taken over the unstressed single crystal silicon showed that it was uniformly unstressed. The peak position values obtained were statistically close to the accepted average value of 789.2 cm<sup>-1</sup><sup>[28]</sup> for the TO peak, having deviations less than 0.05cm<sup>-1</sup> from the average over the mapped section. The penetration depth for single crystal 6H-SiC is on the order of 10μm based on absorption coefficients from [12]. The spectra acquired at each map point are an average from the surface to this depth in each sample. Peak width values were also collected and averaged over the map area to provide a baseline peak width for comparison. Once the unstressed peak shift and width values were acquired, stress was intentionally introduced in the single crystal through the use of a Vickers indent.

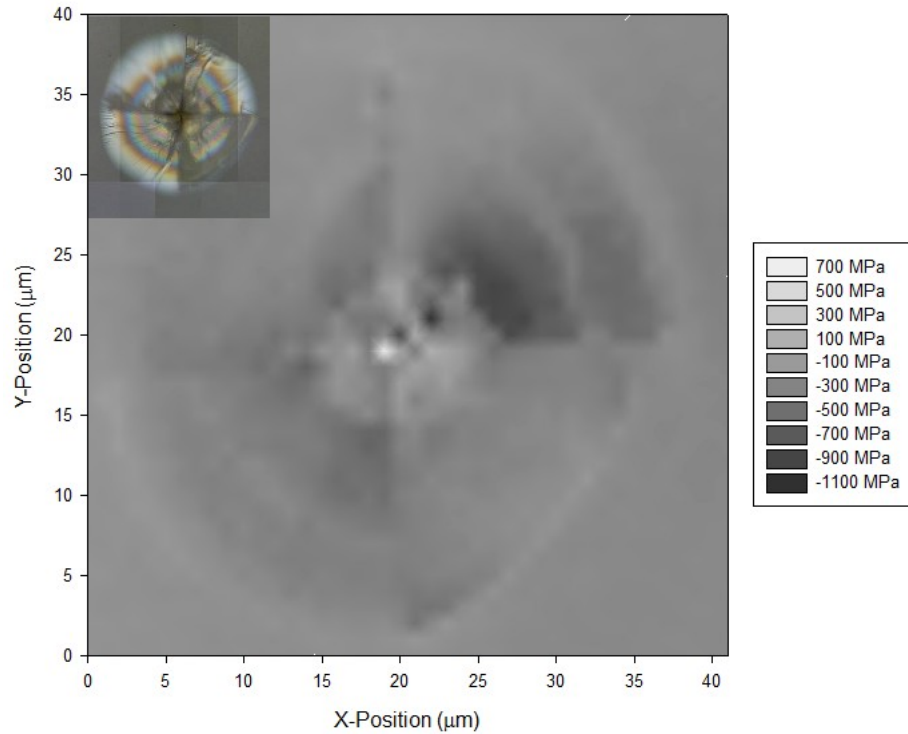


Figure 3: Raman contour map of the peak shift, and thereby the stress variation, of a single crystal 6H-SiC sample indented with a Vickers indenter. The map was collected using the 514nm excitation with a spacing of 1μm. Inlaid is a composite optical image of the indent, taken with the Raman microscope and the Renishaw software.

Indents were made using a diamond Vickers tip, on a Leco Corporation, MI 49085, USA hardness tester at loads of 500g, 1kg and 2kg. Raman maps were made over the most symmetric microindents that also showed the most uniform cracking. The maps were obtained with the smallest spacing between spectra allowable for best resolution. The 514nm, confocal map of TO peak position can be seen in figure 3, where the variation in stress clearly follows the shape of the indent. The very center of the indent gives data that is not readily usable because this was the point of greatest deformation and the peaks were greatly broadened, and in some cases it was even impossible to

deconvolute them through the use of curve fitting. The map shows an average residual compressive stress value of -201.75 MPa, with greatest stress values upwards of -1000 MPa, especially closer to the center of the indent. As the penetration gets deeper into the sample the average stress value decreased over the indent, down to -151.37 MPa at the deepest penetration. A map of the width values shows that the crystal has indeed been deformed, with crystallinity drastically decreasing from the unaffected region towards the center of the indent.

### **Machined Samples:**

The average stress values for the 4 machined samples, as calculated from the Raman maps collected nearest to the surface ranked:  $-220.4 \pm 24.78$  MPa for the Standard finish,  $-370.59 \pm 26.99$  MPa for the grit blast sample,  $-484.8 \pm 32.78$  MPa for the rotary finish, and  $-601.3 \pm 38.37$  MPa for the mirror finish. Raman maps for all 4 samples at each setting are shown in figures 4, 5, 6 and 7. Raman maps of the reverse sides of all samples showed a uniform stress value through the depth of  $-207.8 \pm 20.6$  MPa, the same magnitude as the standard finish sample within margin of error. There were stress variations seen within each map, showing a range of peak shift values, along with an overall decrease in peak shifting with depth. For almost all of the samples, the average stress value dropped by 25-30% between the confocal and regular scan settings suggesting a decrease in stress with depth from the surface. This stress gradient is greatest in the mirror finished sample, and is practically non-existent in the standard finish sample. Figure 8 shows the average stress value of each sample, along with the unstressed and indented single crystal sample, at each depth. The standard sample shows

a consistent stress level throughout the depth, which matches the values for the unmachined sides of all samples.

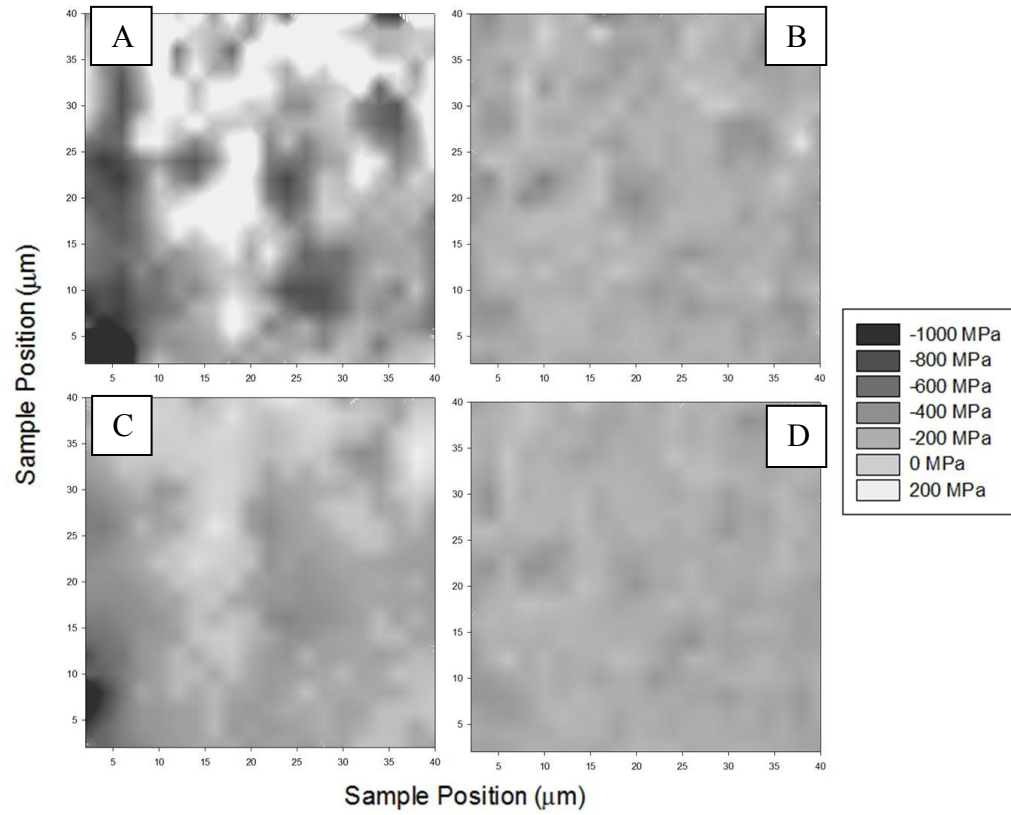


Figure 4: Stress maps of the standard finish sample at a) 514nm confocal, b) 633 confocal, c) 514 regular and d) 633 confocal settings.

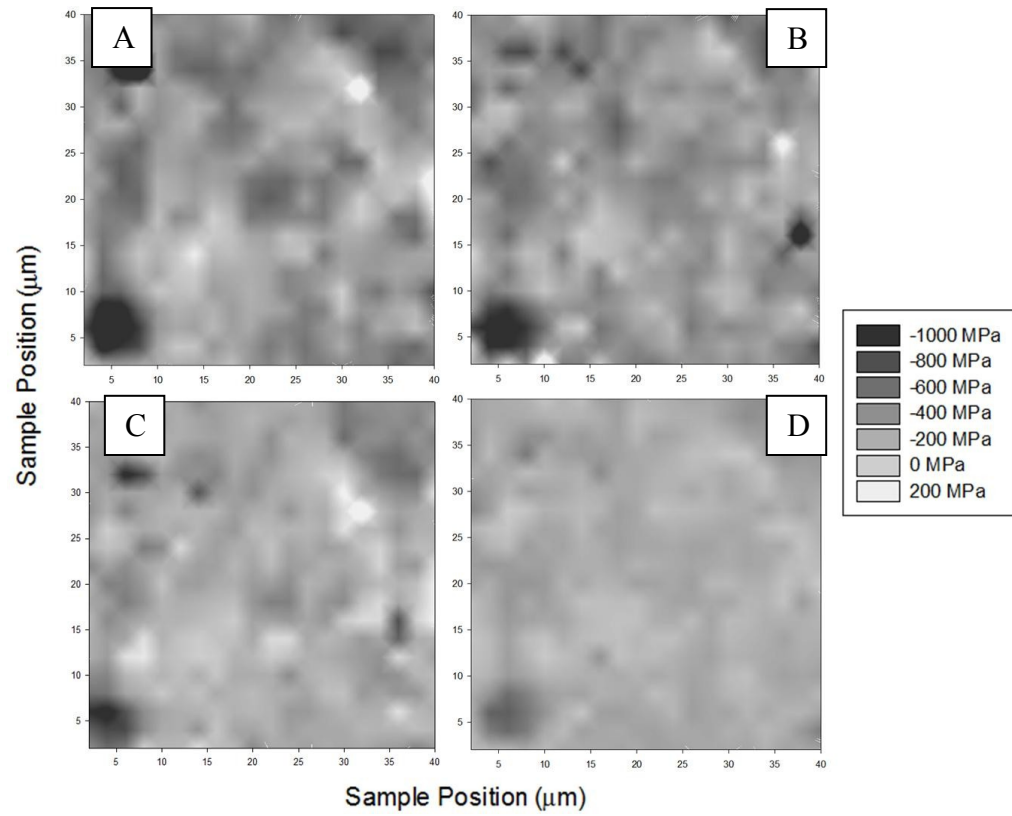


Figure 5: Stress maps of the grit blast sample at a) 514nm confocal, b) 633 confocal, c) 514 regular and d) 633 confocal settings.



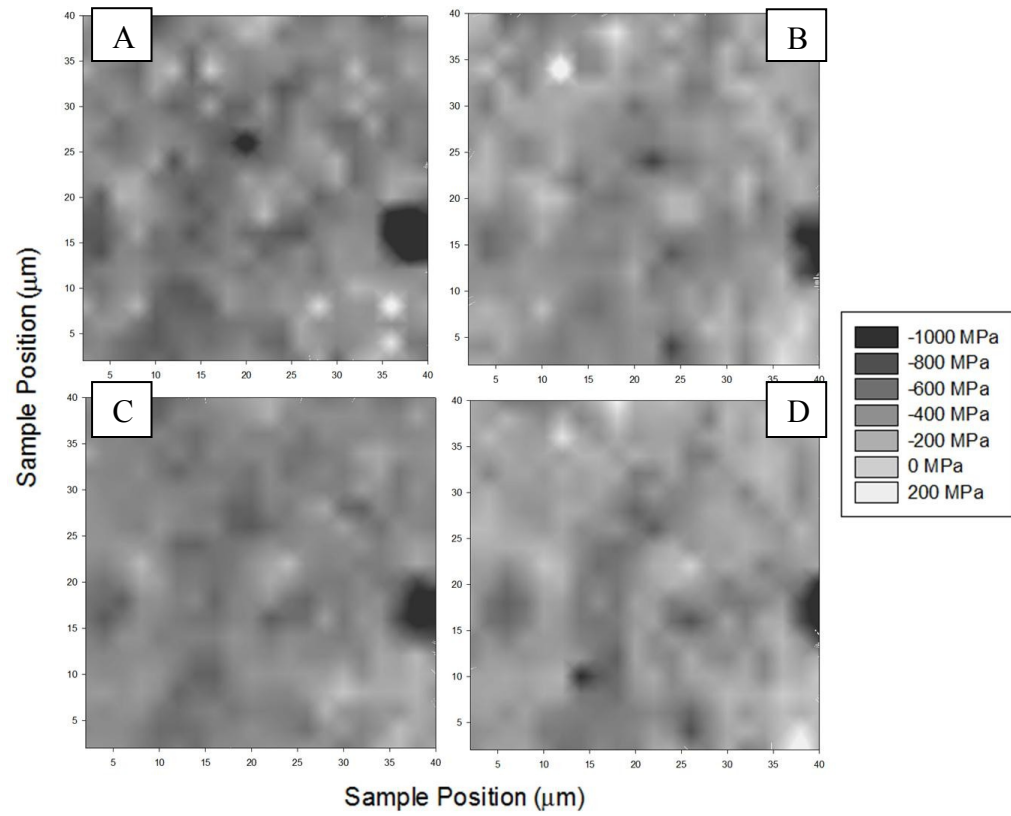


Figure 6: Stress maps of the rotary ground sample at a) 514nm confocal, b) 633 confocal, c) 514 regular and d) 633 confocal settings.

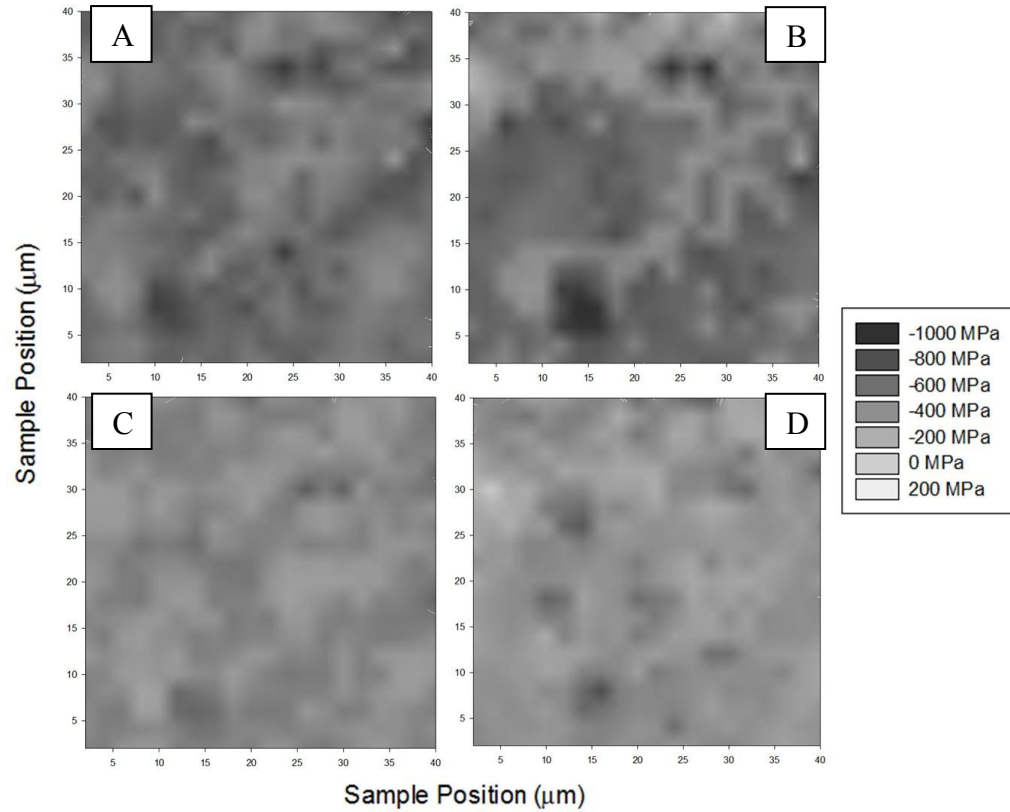


Figure 7: Stress maps of the mirror finish sample at a) 514nm confocal, b) 633 confocal, c) 514 regular and d) 633 confocal settings.

The data collected on the TO peak width showed that the samples split into 2 groups. The grit blast and rotary finish showed similar and higher average relative width values,  $1.8 \text{ cm}^{-1}$  from the near-surface map, compared to the standard and mirror finish samples,  $1.5 \text{ cm}^{-1}$  from the near-surface map. These values were normalized with respect to the average width values of the unstressed single crystal SiC, at the respective scan setting. The width values for all samples with depth can be seen in figure 9. All machined samples tend towards a single relative width value as the penetration depth increases, while the indented single crystal sample tends toward the unstressed single crystal unity

value. A sample Raman spectrum showing the variation in width, as well as peak position can be seen in figure 10.

For both the stress and width analysis, the values obtained from map scans are an average over the depth of penetration. The average values given at each penetration depth are derived from a weighted average based on the penetration of the laser. For example, the values presented for the 514nm confocal setting, having a penetration of 1.5  $\mu\text{m}$ , are an average of the first 1.5  $\mu\text{m}$ . In the 514 regular setting, with penetration depth of  $\sim 3$   $\mu\text{m}$ , the values are obtained by accounting for the contribution from the first 2  $\mu\text{m}$  obtained from the 514nm and 633nm confocal settings. The result is an average value over the sample depth between 2 and 3  $\mu\text{m}$ . This is given as the value at 3  $\mu\text{m}$  penetration.

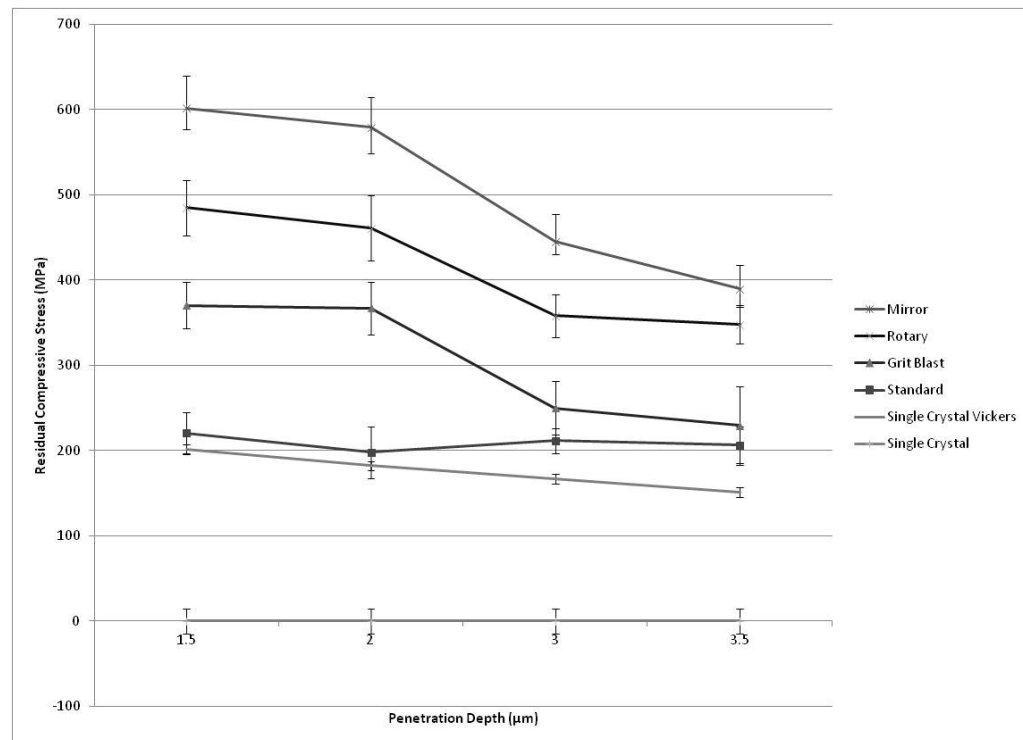


Figure 8: Plot of residual stress values in all samples as they vary with depth.

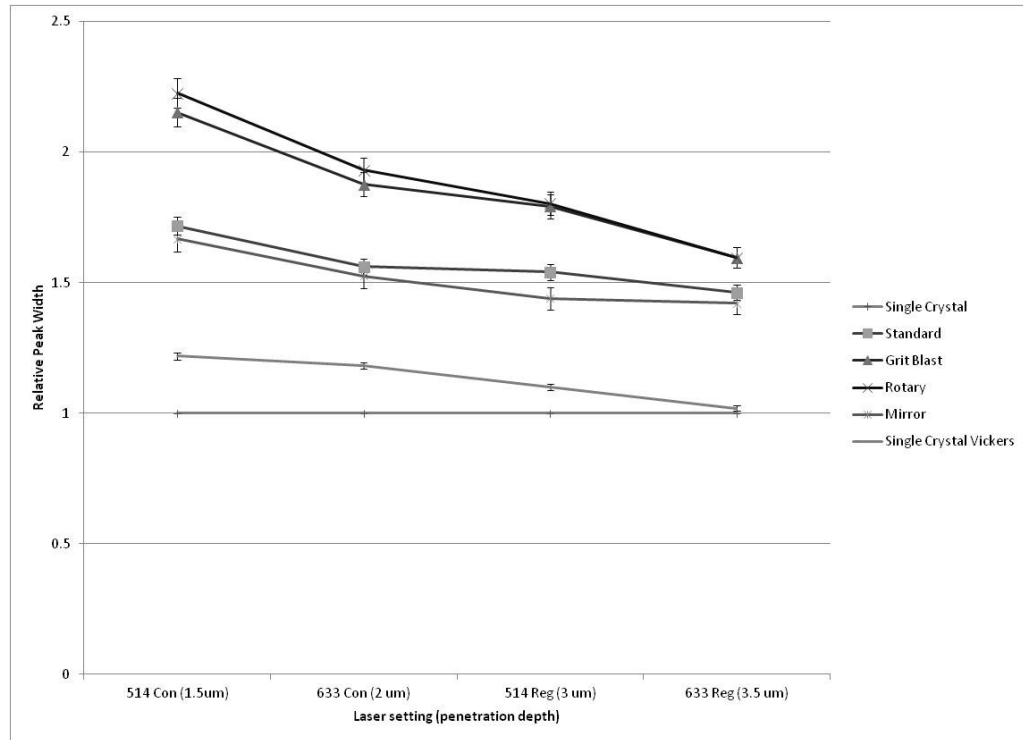


Figure 9: Plot of relative peak widths for all samples as they vary with depth.

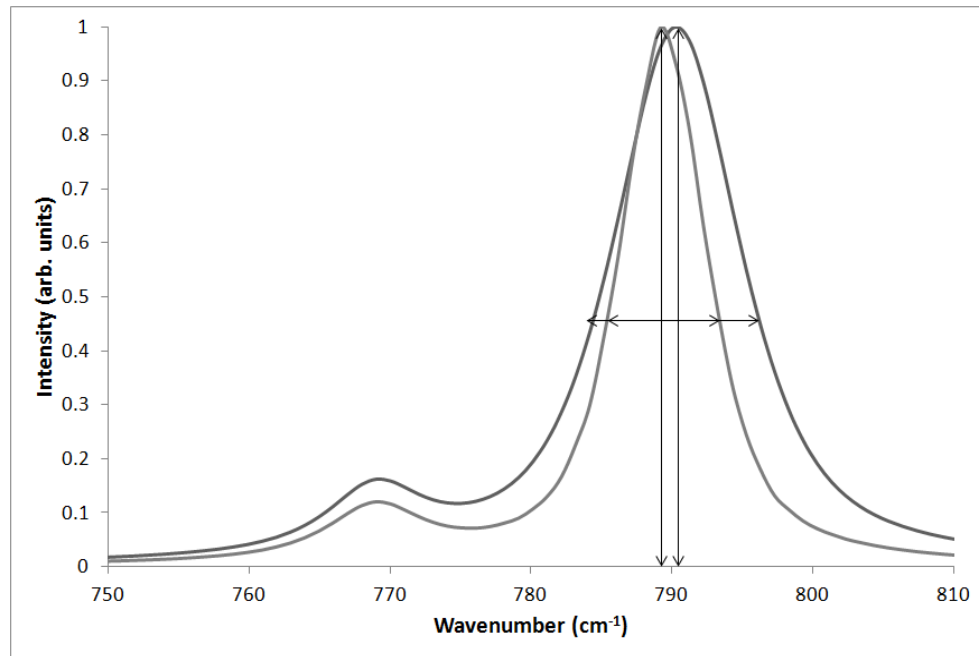


Figure 10: Typical spectra showing peak position and peak width variations seen.

The peaks located at  $\sim 768\text{cm}^{-1}$  are mostly invariant, while the TO peak at  $789.2\text{cm}^{-1}$  can both broaden and shift.

## Discussion

When making stress measurements using Raman a number of assumptions are made, notably the equations used assume a hydrostatic stress is acting on the sample, and that the peaks shift according to this stress alone. In all the samples studied this is an oversimplification, though in the single crystal sample, where the deformation and stress is introduced by an indent, it may be the closest to the introduction of hydrostatic stress. The equations will more accurately represent the peak position shifts in this sample. For the machined surfaces, more complex stress states are likely to be present. In this case, the same stress per wavenumber shift ( $\text{GPa}/\text{cm}^{-1}$ ) may not hold, and actual stress values may be different than evaluated. However, within each sample, the change in average peak shift value with depth shows that there is a stress gradient in the sample.

The machined stress values in each sample show a linear trend towards a baseline residual stress value, which is that of the unmachined reverse sides. The intercept of the trendline with the baseline residual stress value gives an approximate depth at which the machining process has affected the sample. For the higher stressed mirror finish and rotary ground samples, this value is  $6.6 \pm 0.5\mu\text{m}$  and  $6.45 \pm 0.74\mu\text{m}$ , respectively. In the grit blast sample, this value was lower, at  $4.43 \pm 0.43\mu\text{m}$ , indicating that the deformation and stress concentration was much nearer to the surface. In shot peened or grit blasted samples the deformation generally tends to be nearer the surface as the intent is to apply residual compressive surface stresses from densification in the impacted regions. For the single crystal samples it should be noted that given the absorption coefficient of 6H-SiC, and the wavelength dependence of this coefficient, there is no wavelength that could be used to analyze this depth with Raman spectroscopy, without sectioning the sample.

There are z-scan techniques that utilize through-focus scanning to get depth resolution, but the depth estimation falls off quickly even with small below-focus step sizes<sup>[13]</sup>.

A similar analysis of the peak width data shows that all 4 samples will reach the baseline width value, set by the unmachined side, by a depth of  $4.51 \pm 0.33\mu\text{m}$ . Presented with only the width data to predict sample damage would show that employing a mirror finish has little effect on the quality of the sample, with no subsurface damage, and would be less likely to fail versus the grit blast or rotary finished samples. Similarly, looking solely at the stress data would lead to the assumption that the grit blast procedure simply adds to the residual compressive stress of the sample without much crystal deformation.

## Conclusions

Mechanically machined SiC samples were investigated using Raman spectroscopy to determine the effects of machining on near-surface stress states. All samples analyzed contained residual compressive stresses within the surface to a depth of  $3.5\mu\text{m}$ . The nature of the stress, whether hydrostatic, biaxial or triaxial cannot be determined readily from the analysis, yet due to the nature of machining it is necessary to assume complex stress states. As the level and quality of machining increased, so too did the magnitude of the residual stress, especially near the surface of the sample with a mirror finish. However, it was found that this alone is not an indicator of sample damage, as analysis of peak widths revealed larger deformation in less stressed samples. The depth of this deformation could be estimated from the intercept of relative values with baseline values. These results showed that it is necessary to look at more than just one factor in assessing sample quality and damage from machining when using Raman spectroscopy.

The utility of the Raman technique in assessing the importance of machining damage will come from correlating these factors with results from failure and performance testing.

## References

- [1] Schwetz, K.A., *Silicon Carbide Based Hard Materials*, in *Handbook of Ceramic Hard Materials*. 2008, Wiley-VCH Verlag GmbH. p. 683-748.
- [2] Marinescu, I.D., *Handbook of Advanced Ceramic Machining*. 2007, Taylor & Francis Group, Boca Raton
- [3] Sadow, S., Agarwal, A., *Advances in Silicon Carbide Processing and Applications*. 2004, Artech House, Inc, Massachusetts.
- [4] Sasaki, M. et al. "Defect Formation Mechanism of Bulk SiC" *Materials Science Forum* **264-268** (1998) pp 41-44
- [5] Tuominen, M. et al. "Defect Analysis in Lely-grown 6H SiC" *Journal of Crystal Growth* **165** (1996) pp 233-244
- [6] Hundhausen, M. et al. "Characterization of defects in silicon carbide by Raman spectroscopy," *physica status solidi (b)*, **245**, no. 7, pp. 1356-1368, Jul. 2008.
- [7] Wesch, W., "Silicon carbide: synthesis and processing," *Nuclear Instruments and Methods in Physics Research Section B: Beam Interactions with Materials and Atoms*, **116**, no. 1, pp. 305–321, 1996.
- [8] Zhu, J. et al., "Raman study on residual strains in thin 3C-SiC epitaxial layers grown on Si(001)," *Thin Solid Films*, **368**, no. 2, pp. 307-311, Jun. 2000.
- [9] Genzel, C. et al., "Residual stress fields in surface-treated silicon carbide for space industry—comparison of biaxial and triaxial analysis using different X-ray methods," *Materials Science and Engineering: A* **390**, no. 1-2, pp. 376-384, Jan. 2005.
- [10] Lundquist, D., On the Crystal Structure of Silicon Carbide and its Content of Impurities. *Acta Crystallographica Section B*, 1948. 2: p. 177-191.
- [11] Ferraro, John R., Kazuo Nakamoto, and Chris W. Brown. *Introductory Raman Spectroscopy*. 2nd ed. San Diego: Academic Press, 2003.
- [12] Werheit, H. and Schwetz, K.A., "Comparative optical investigations of sintered and monocrystalline black and green silicon carbide (SiC)," *Journal of Solid State Chemistry* **177** (2004) pp. 580-585.
- [13] Bruneel, J.L., Lassegues, J.C., and C. Sourisseau, "In-depth analyses by confocal Raman microspectrometry: experimental features and modeling of the refraction effects," *Journal of Raman Spectroscopy* **33** (2002) pp. 815-828.
- [14] Dietrich, B. & Dombrowski, K. Experimental challenges of stress measurements with resonant micro-Raman spectroscopy. *Journal of Raman spectroscopy* **30**, 893–897 (1999).



- [15] Colomban, P. Analysis of Strain and Stress in Ceramic, Polymer and Metal Matrix Composites by Raman Spectroscopy. *Advanced Engineering Materials* **4**, 535-542 (2002).
- [16] Falkovsky, L. a., Bluet, J.M. & Camassel, J. Strain-fluctuation effect on Raman spectra. *Physical Review B* **55**, R14697-R14700 (1997).
- [17] Gouadec, G. & Colomban, P. Raman Spectroscopy of nanomaterials: How spectra relate to disorder, particle size and mechanical properties. *Progress in Crystal Growth and Characterization of Materials* **53**, 1-56 (2007).
- [18] Debernardi, A., Ulrich, C., Syassen, K. & Cardona, M. Raman linewidths of optical phonons in 3C-SiC under pressure: First-principles calculations and experimental results. *Physical Review B* **59**, 6774 (1999).
- [19] Feng, Z., Choyke, W. & Powell, J. Raman determination of layer stresses and strains for heterostructures and its application to the cubic SiC/Si system. *Journal of applied physics* **64**, 6827–6835 (1988).
- [20] Genzel, C., Klaus, M., Denks, I. & Wulz, H.G. Residual stress fields in surface-treated silicon carbide for space industry—comparison of biaxial and triaxial analysis using different X-ray methods. *Materials Science and Engineering: A* **390**, 376-384 (2005).
- [21] Ghosh, D., Subhash, G. & Orlovskaya, N. Measurement of scratch-induced residual stress within SiC grains in ZrB<sub>2</sub>-SiC composite using micro-Raman spectroscopy. *Acta Materialia* **56**, 5345-5354 (2008).
- [22] Lee, C. Raman microprobe mapping of residual microstresses in 3C-SiC film epitaxial lateral grown on patterned Si(1 1 1). *Applied Surface Science* **228**, 10-16 (2004).
- [23] Olego, D. & Cardona, M. Pressure dependence of Raman phonons of Ge and 3C-SiC. *Physical Review B* **25**, 1151-1160 (1982).
- [24] Mukaida, H. *et al.* Raman scattering of SiC: Estimation of the internal stress in 3C-SiC on Si. *Journal of applied physics* **62**, 254–257 (1987).
- [25] Matsuoka, D. *et al.* Raman Scattering Study of Stress Distribution around Dislocation in SiC. *Materials Science Forum* **600-603**, 337-340 (2009).
- [26] Grodecki, K. *et al.* Raman Piezospectroscopy of Phonons in Bulk 6H-SiC. *Acta Physica Polonica A* **116**, 6-9 (2009).
- [27] Liu, J. & Vohra, Y.K. Raman modes of 6H polytype of silicon carbide to ultrahigh pressures: A comparison with silicon and diamond. *Physical review letters* **72**, 4105–4108 (1994).
- [28] Nakashima, S. & Harima, H. Raman investigation of SiC polytypes. *physica status solidi (a)* **162**, 39–64 (1997).

## **5.2 Further Discussion**

Presented in this section is a discussion of the Raman maps acquired over indented areas of the machined surfaces and Raman maps taken at the edge of fracture surfaces with the goal of visualizing a deformation layer. The expectation of the indentation process was to see an increase in either measurable residual stress, surface deformation, or both. With the Raman maps over the tile cross-sections, the same stress and deformation gradient was expected to be seen.

### **5.2.1 Effects of Indentation on Measured Stress**

Following the Raman mapping analysis of machining induced residual stressing, sample surfaces were indented according to the experimental setup discussed in Chapter 3.2. Maximum loads of 10mN and 30mN were applied over the same areas mapped with Raman spectroscopy as a means of introducing stresses and surface damage. Typical indents in single crystal silicon carbide can be seen in figures 5.1 and 5.2 for the 10mN and 30mN loads, respectively. Re-mapping of these indented surfaces, and the analysis of peak shifts and peak widths was conducted in the same manner as in the paper.

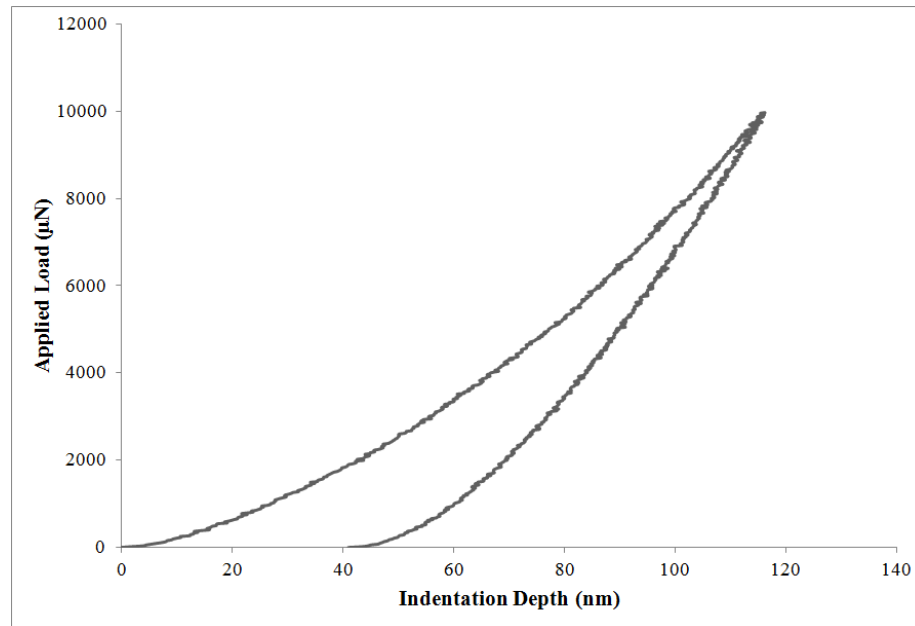


Figure 5.1: Typical indent in single crystal SiC with maximum load of 10mN.

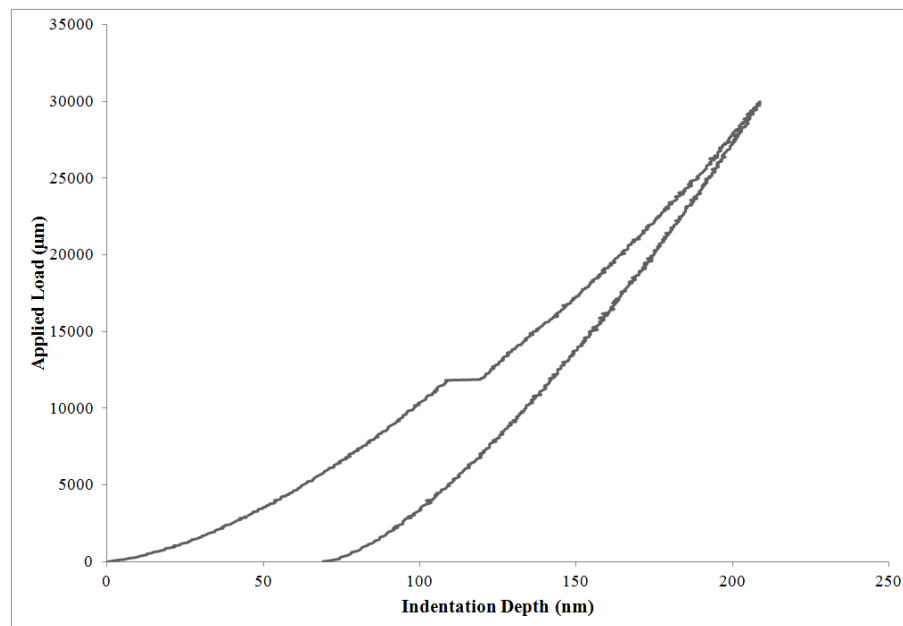


Figure 5.2: Typical indent in single crystal SiC with maximum load of 30mN.

The jump in depth around 12000 $\mu$ N is known as a pop-in and indicates fracture of material beneath the indenter tip.

### 5.2.1.1 Indentation at 10 mN

The 10mN load indents did not reveal any change in the average stress values over any of the machined samples. In comparing the pre- and post-indented Raman maps, the local stress states appear to have changed for each of the maps however. This can be seen in the set of figures 5.3-5.10. For each set, the maps on the left side, marked (a) and (c), correspond to the pre-indented 514nm and 633nm wavelengths, respectively. The right side marked (b) and (d) correspond to the post-indented 514nm and 633nm wavelengths, respectively. The type of machined surface and the confocal setting is indicated in the figure captions.

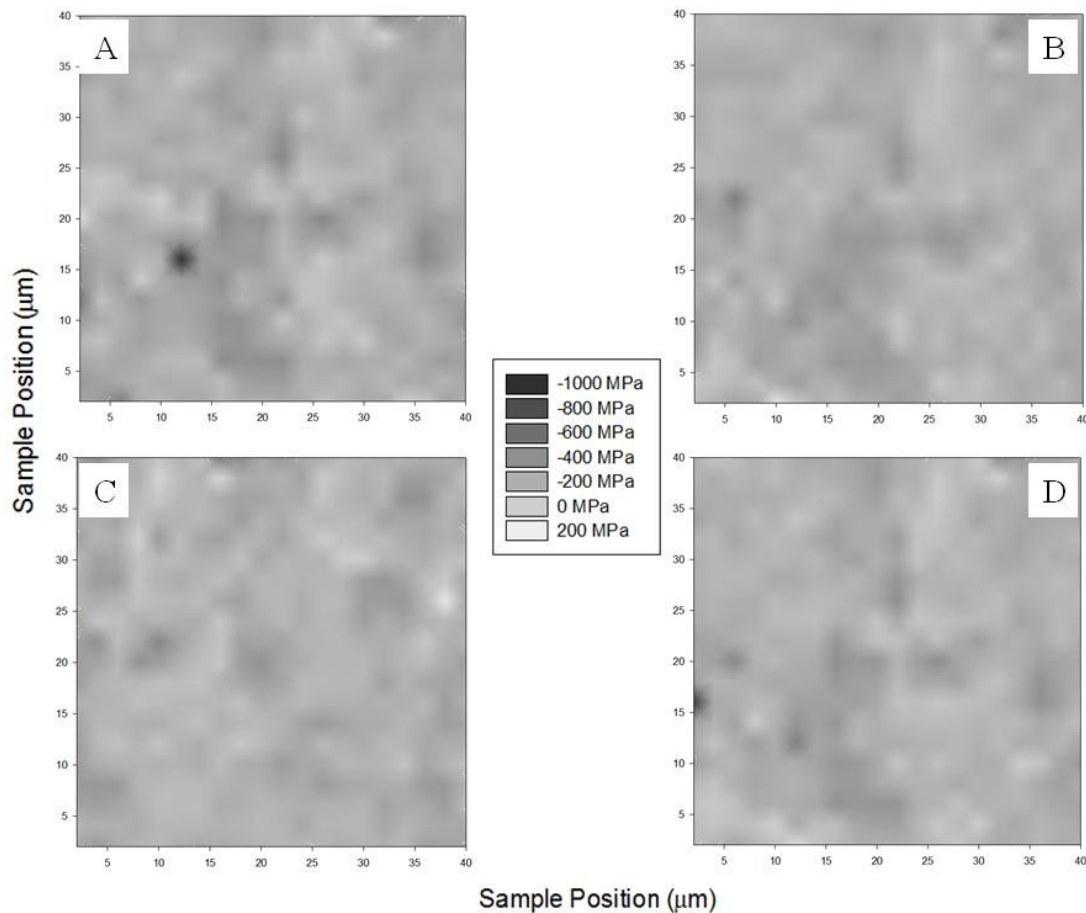


Figure 5.3: Stress maps of the standard surface finish obtained using the confocal setting.

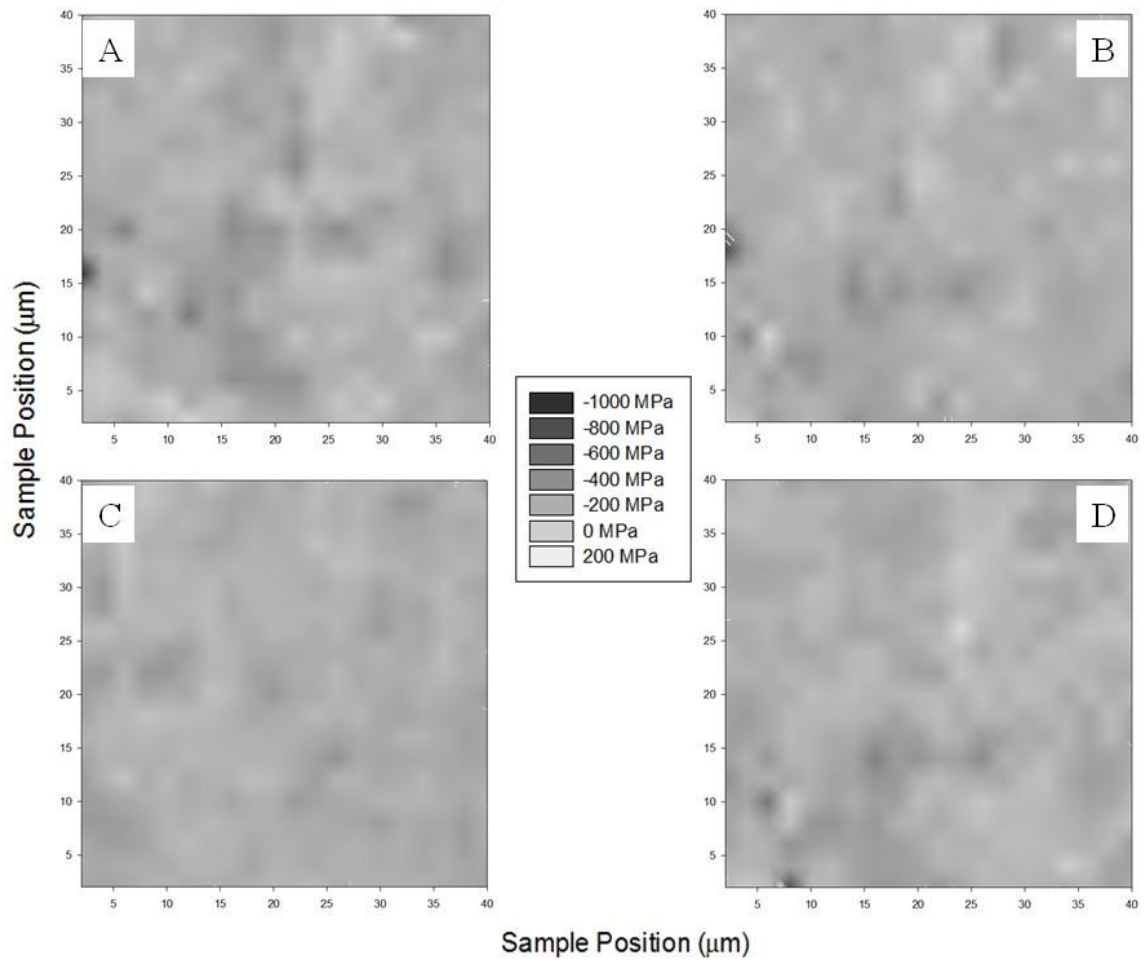


Figure 5.4: Stress maps of the standard surface finish obtained using the regular scan setting.

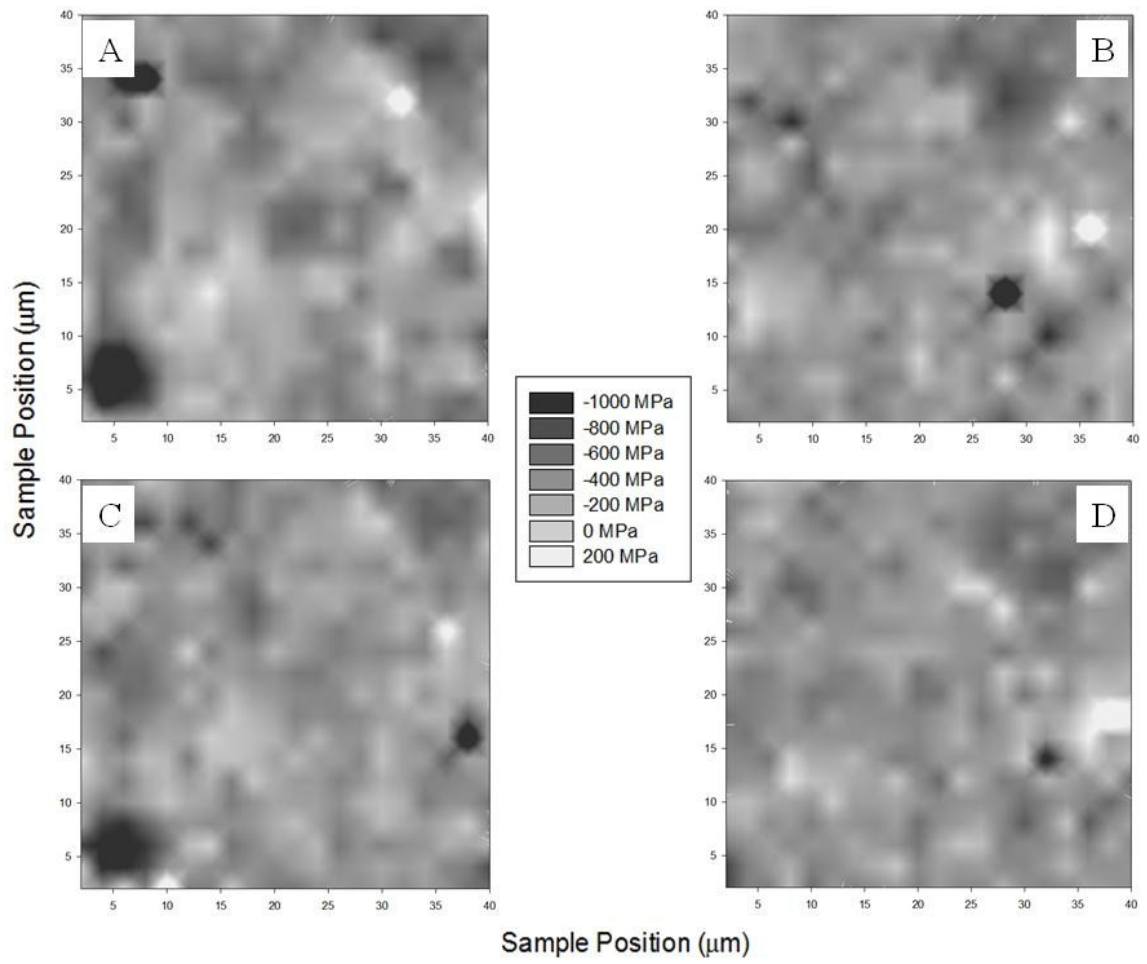


Figure 5.5: Stress maps of the grit blast surface finish obtained using the confocal scan setting.

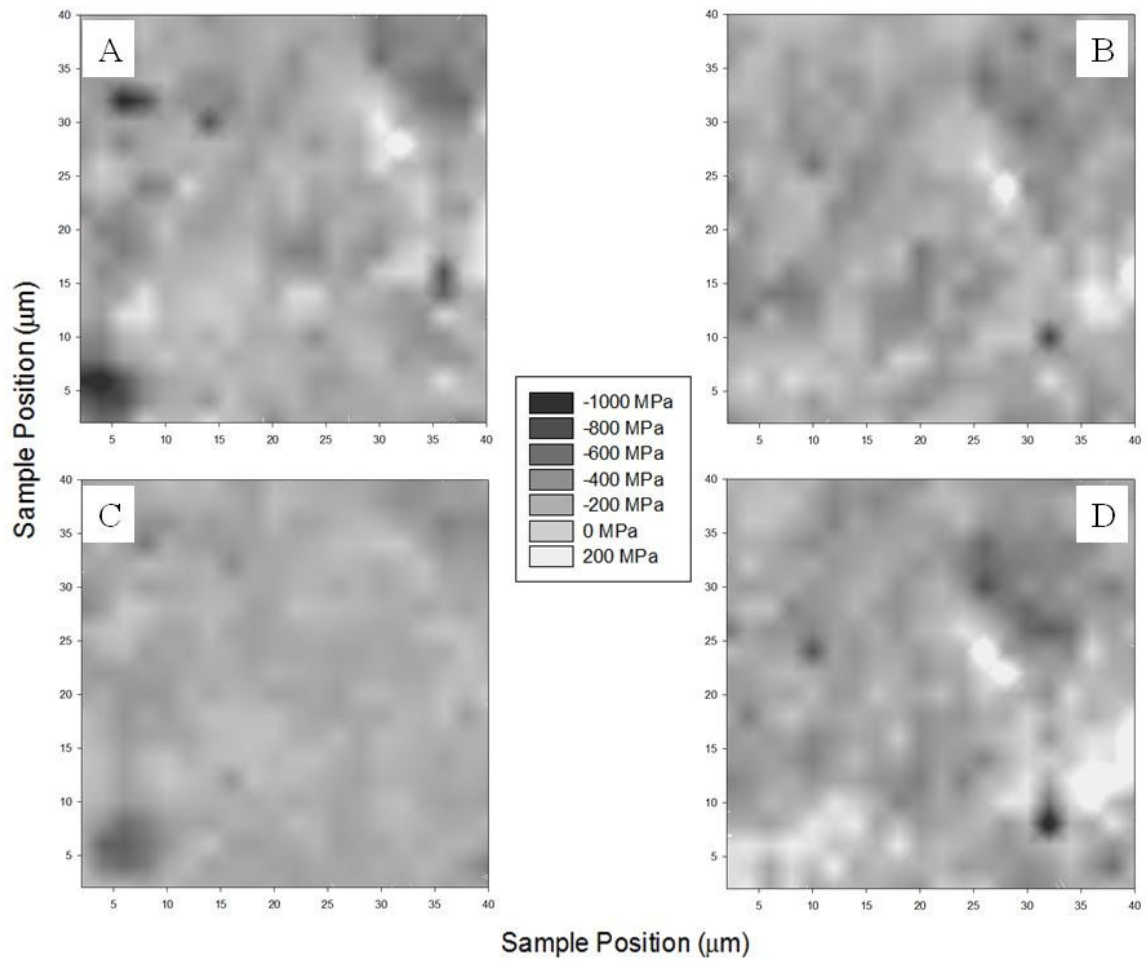


Figure 5.6: Stress maps of the grit blast surface finish obtained using the regular scan setting.

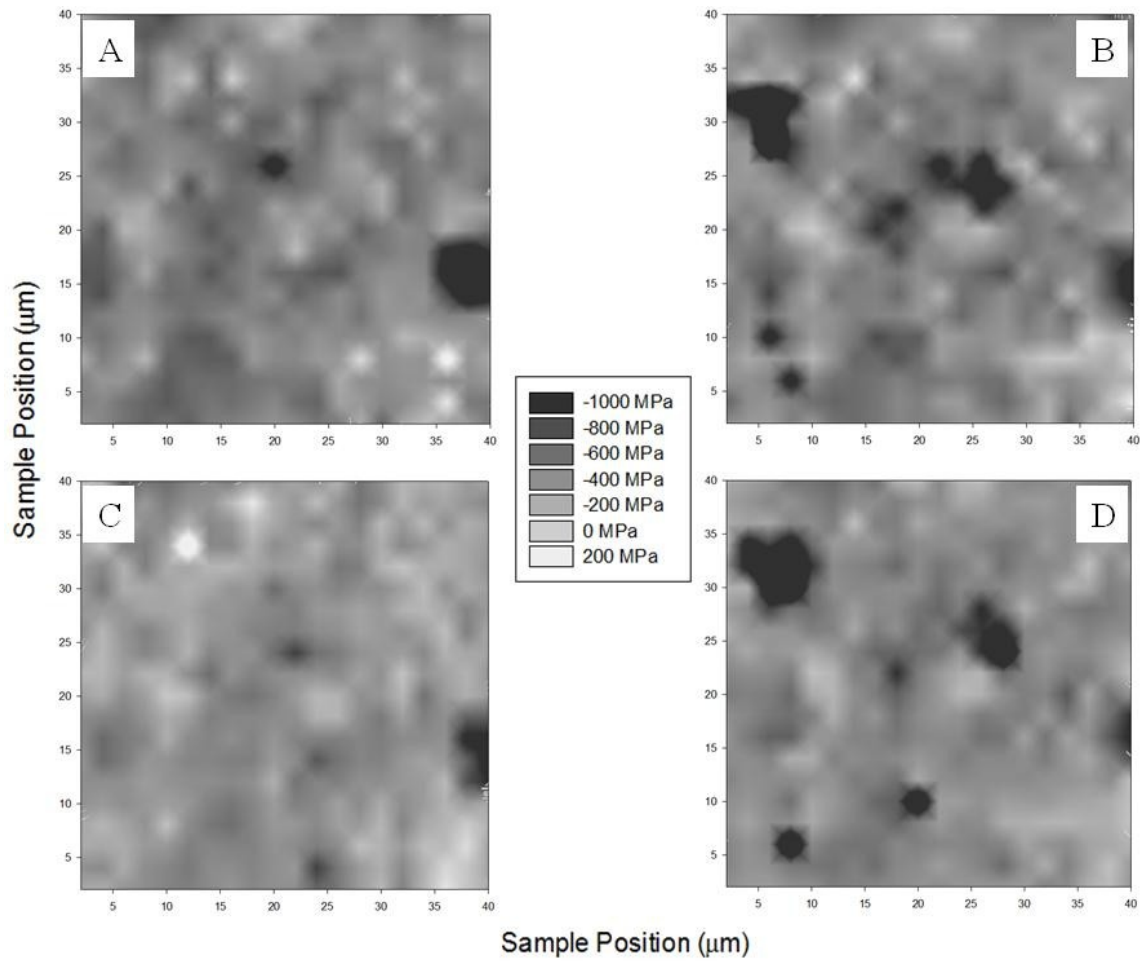


Figure 5.7: Stress maps of the rotary ground surface finish obtained using the confocal scan setting.



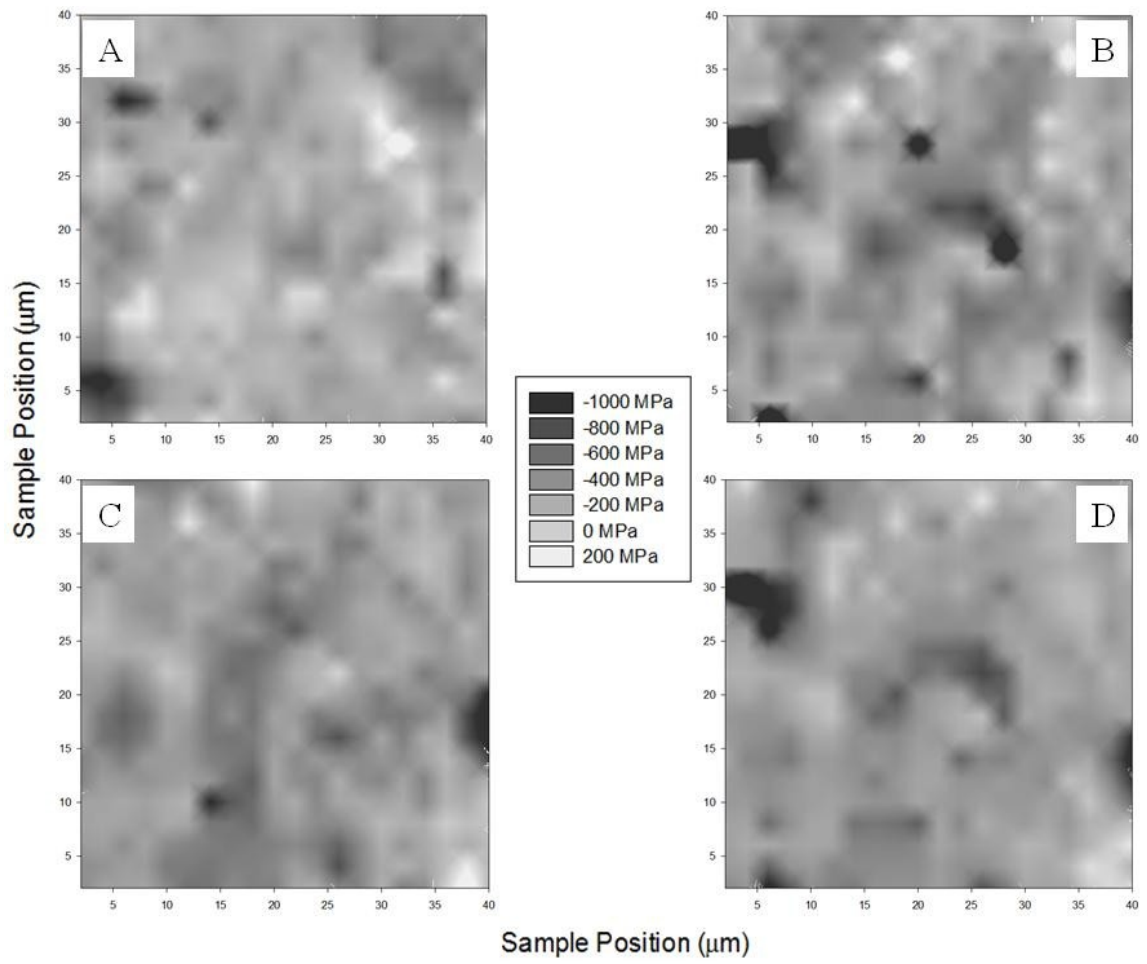


Figure 5.8: Stress maps of the rotary ground surface finish obtained using the regular scan setting.

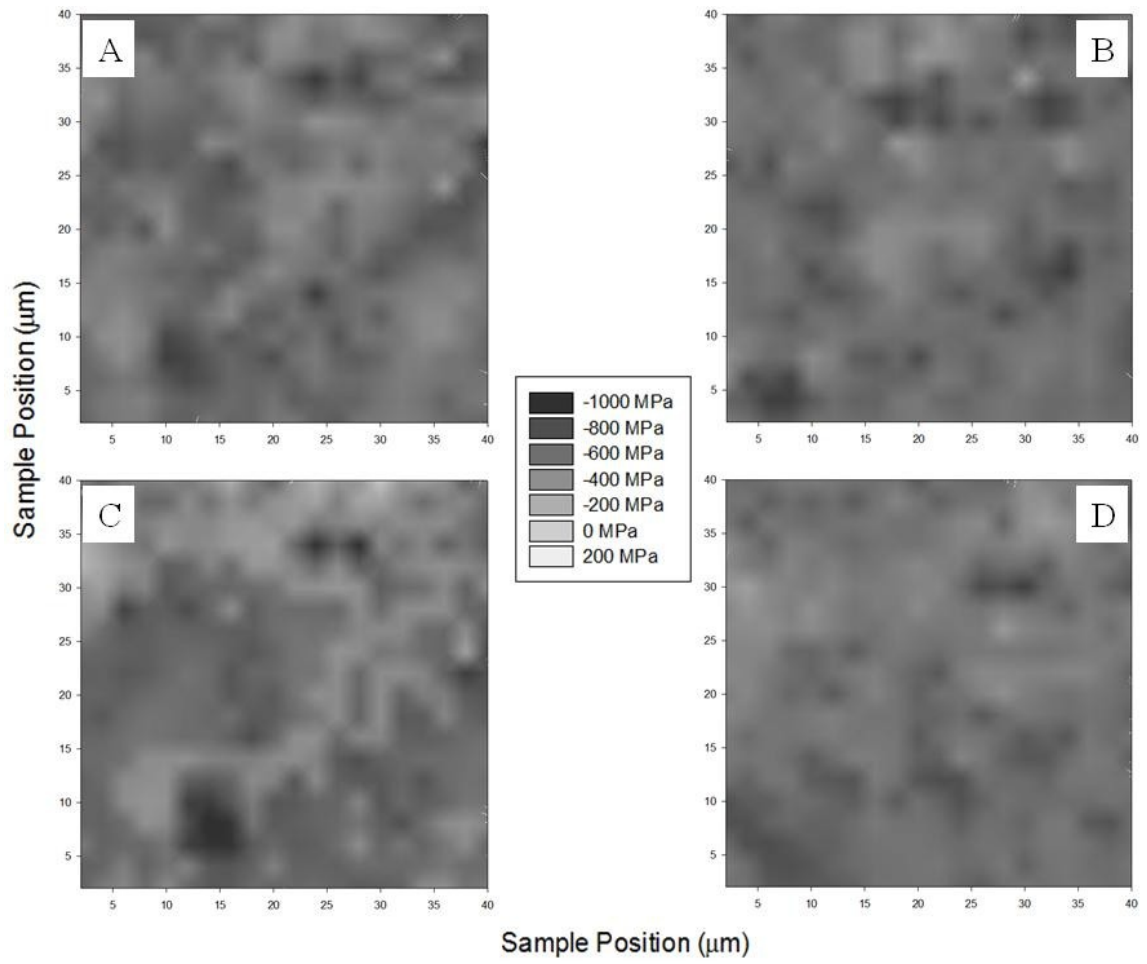


Figure 5.9: Stress maps of the mirror polish surface finish obtained using the confocal scan setting.

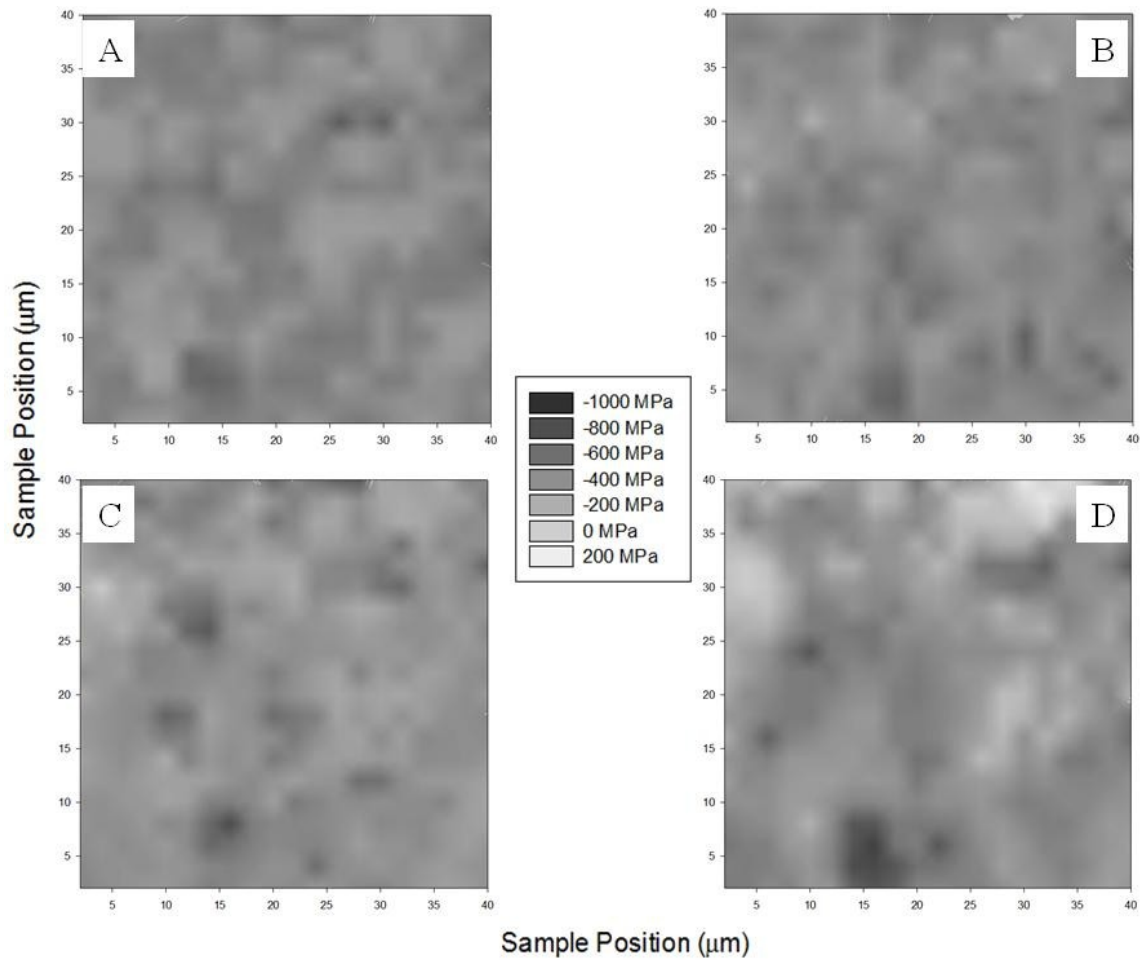


Figure 5.10: Stress maps of the mirror polish surface finish obtained using the regular scan setting.

The work done by Chen and Bull<sup>[82]</sup> has shown the relationship between maximum penetration depth of nanoindentation to the residual plastic zone under the indent. Their analysis shows that for materials with elastic modulus to hardness ratios of  $\sim 10$ , as in Silicon Carbide, the resulting plastic zone from indentation would be 10 times the indentation depth. At 10mN, the indentation depth is on average 150nm, giving a plastic zone radius of 1.5μm. For the 514nm confocal setting, this is the estimated penetration depth in silicon carbide. The variations seen in the stress states at this scan

setting can thereby be explained by the presences of this plastic zone. The stress caused by indentation has either relieved or intensified the stresses present in the sample surfaces, but in such a way that the overall values have gone unchanged. The variations seen within other scan settings that probe deeper into the sample can be assumed to be affected by the volume averaging within Raman spectroscopy. The following width maps show similar redistribution post-indentation while not showing any changes in the average width value due to the 10mN indentation.

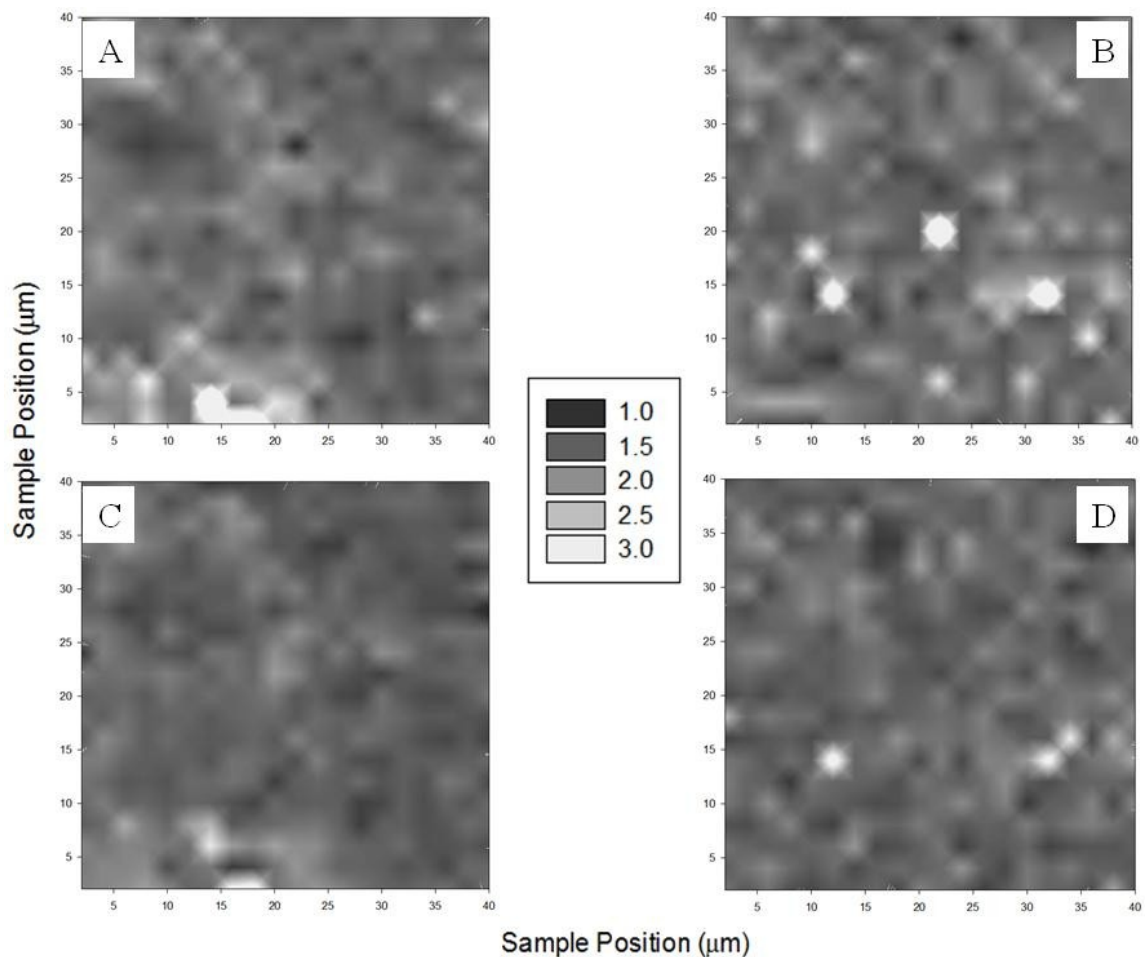


Figure 95.11: Relative width maps of the standard surface finish obtained using the confocal scan setting.

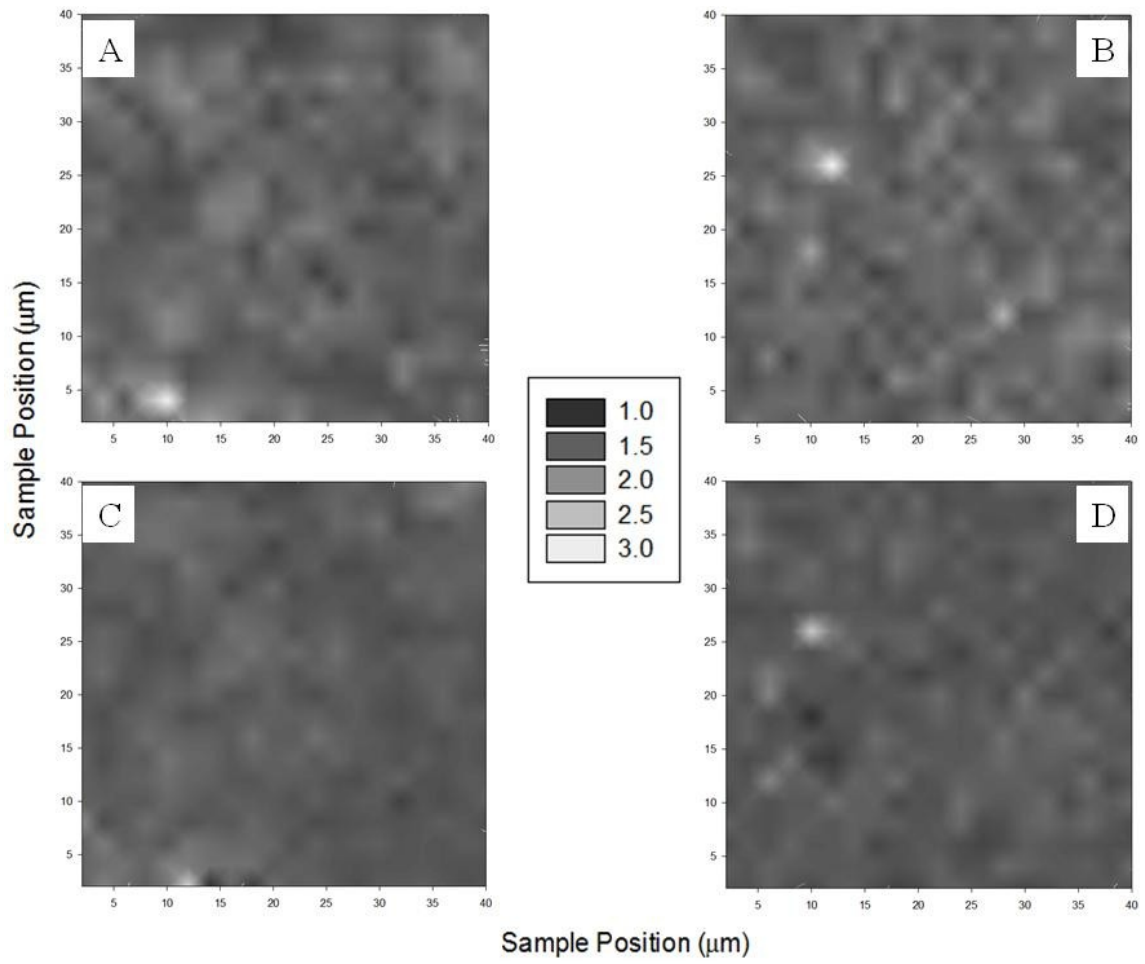


Figure 5.12: Relative width maps of the standard surface finish obtained using the regular scan setting.

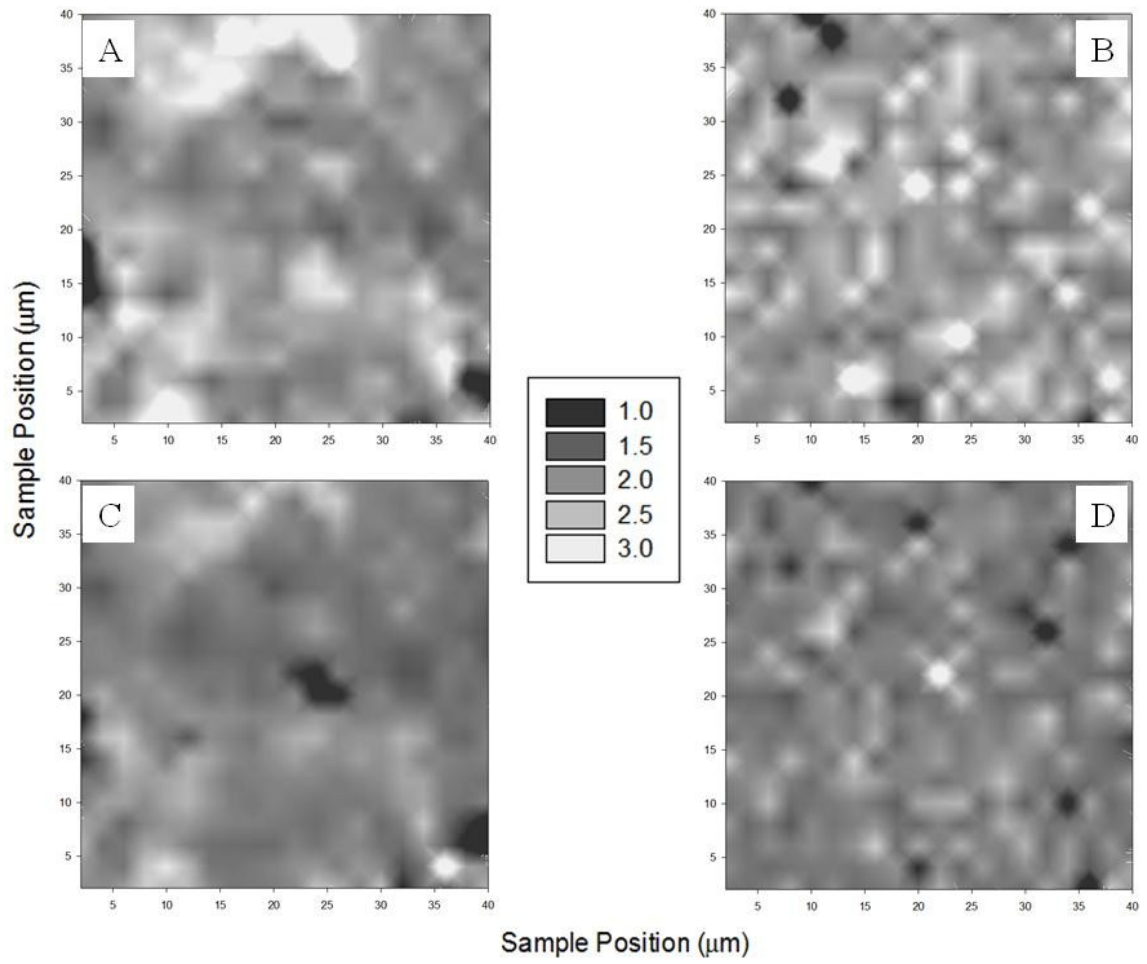


Figure 5.13: Relative width maps of the grit blast surface finish obtained using the confocal scan setting.

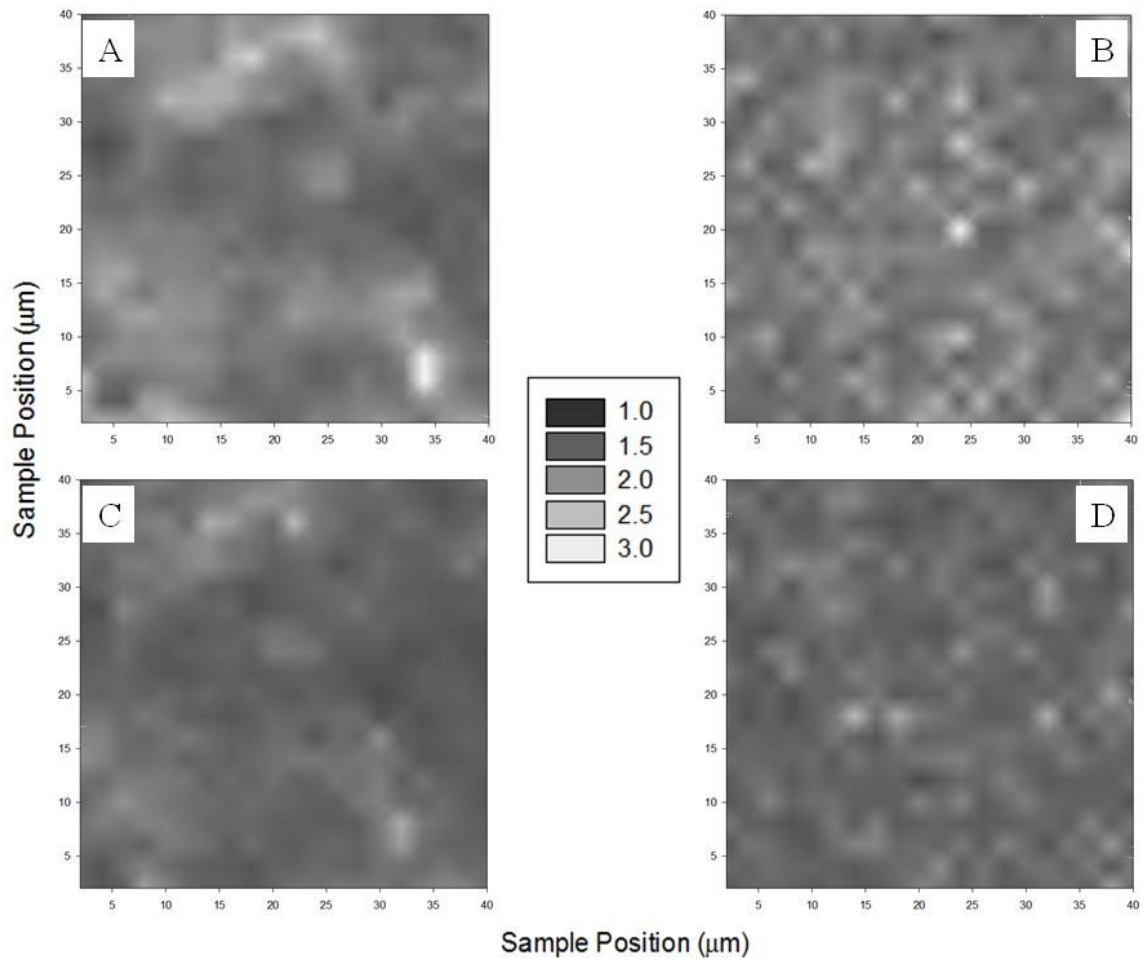


Figure 5.14: Relative width maps of the grit blast surface finish obtained using the regular scan setting.

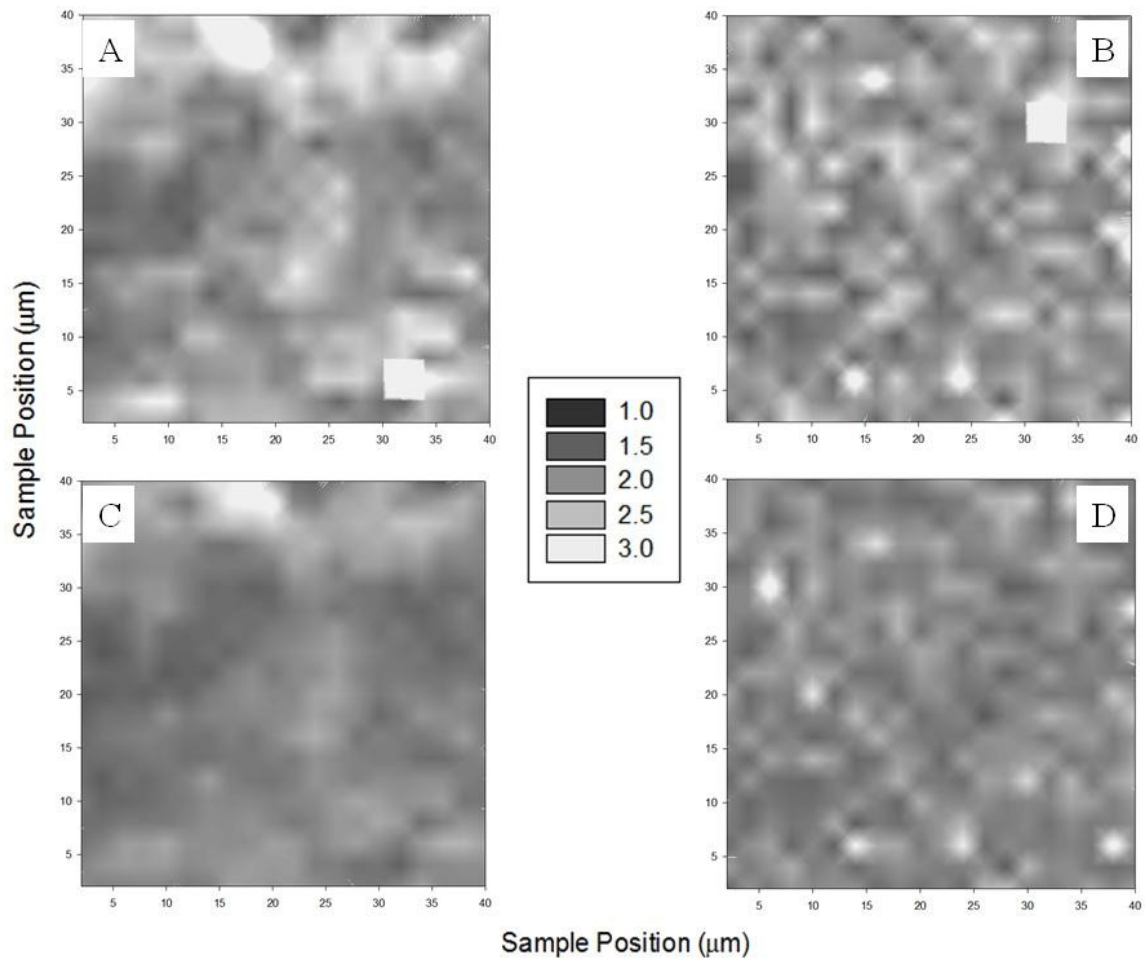


Figure 5.15: Relative width maps of the rotary ground surface finish obtained using the confocal scan setting.



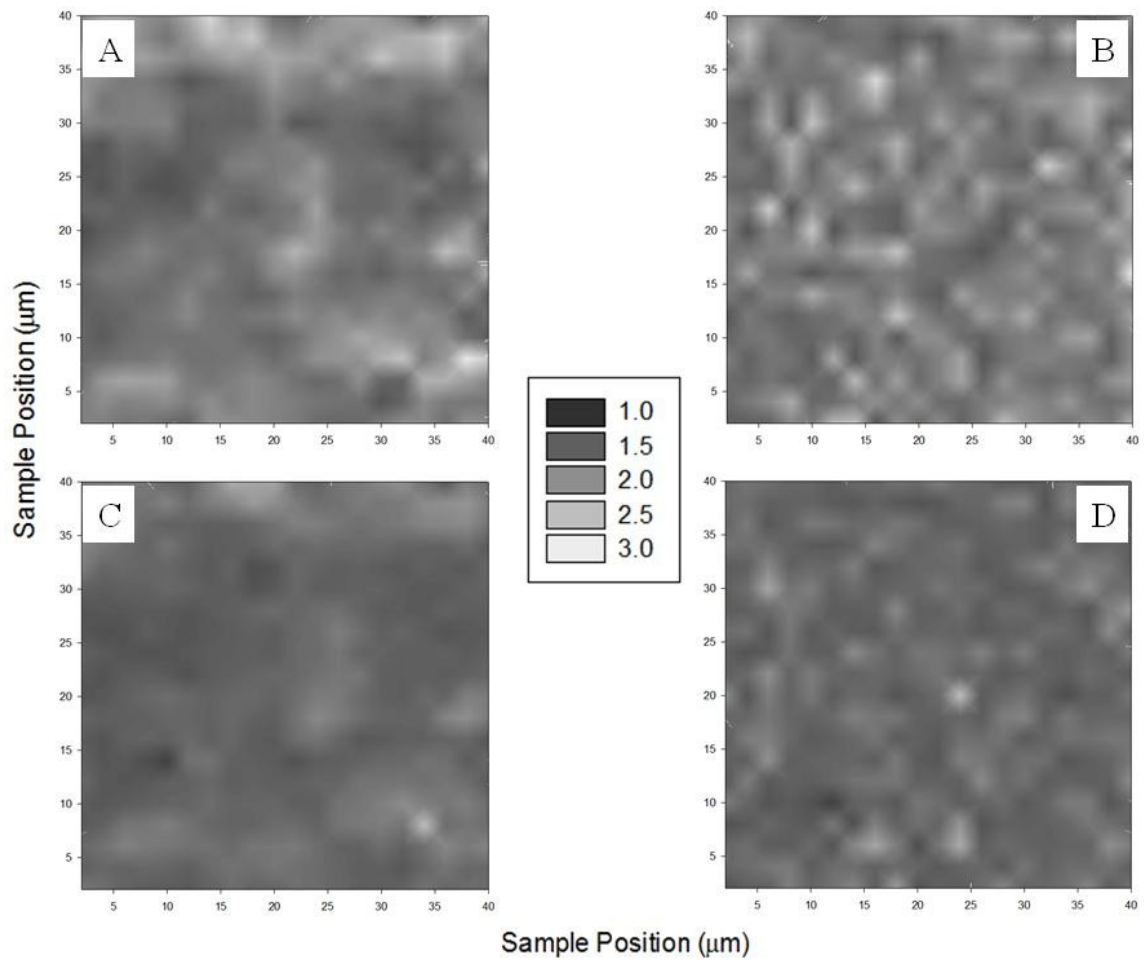


Figure 5.16: Relative width maps of the rotary ground surface finish obtained using the regular scan setting.

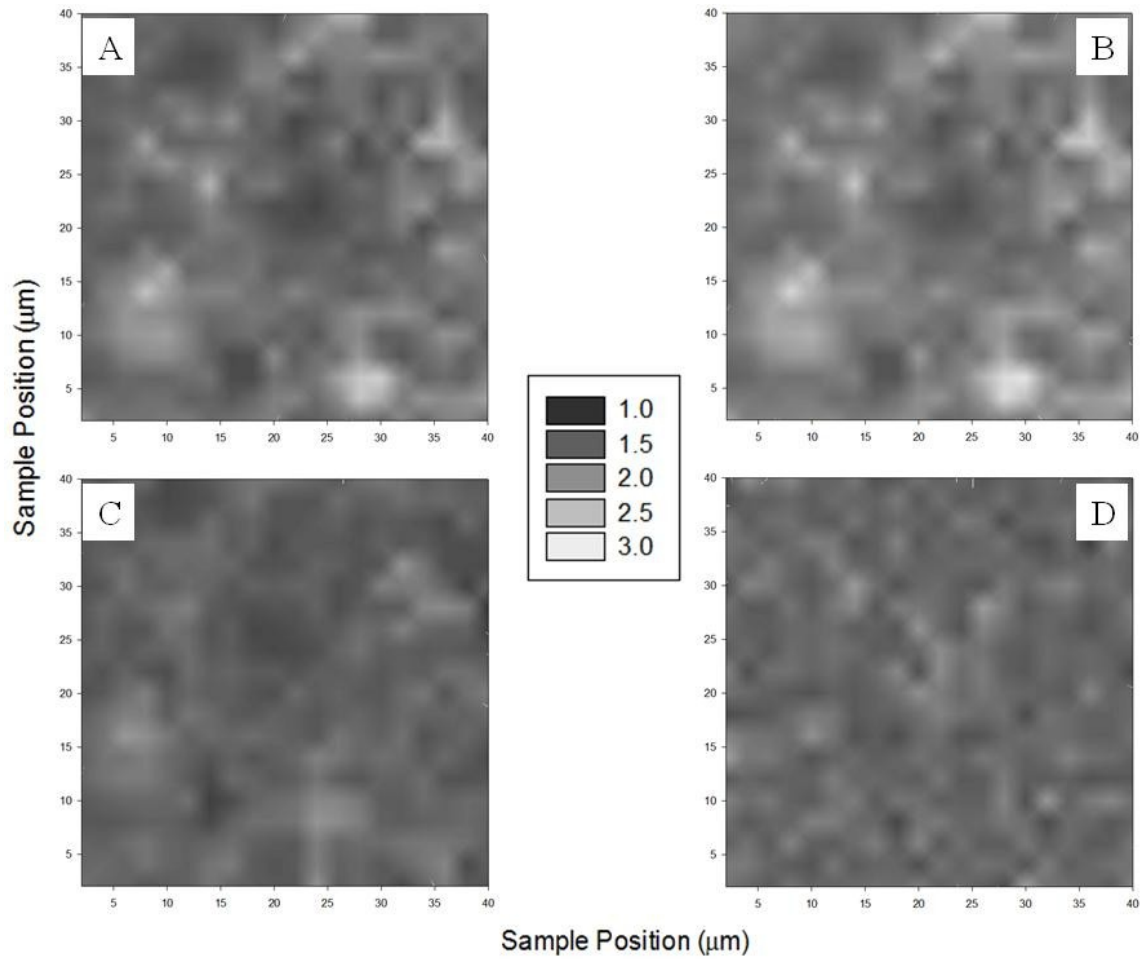


Figure 5.17: Relative width maps of the mirror polish surface finish obtained using the confocal scan setting.

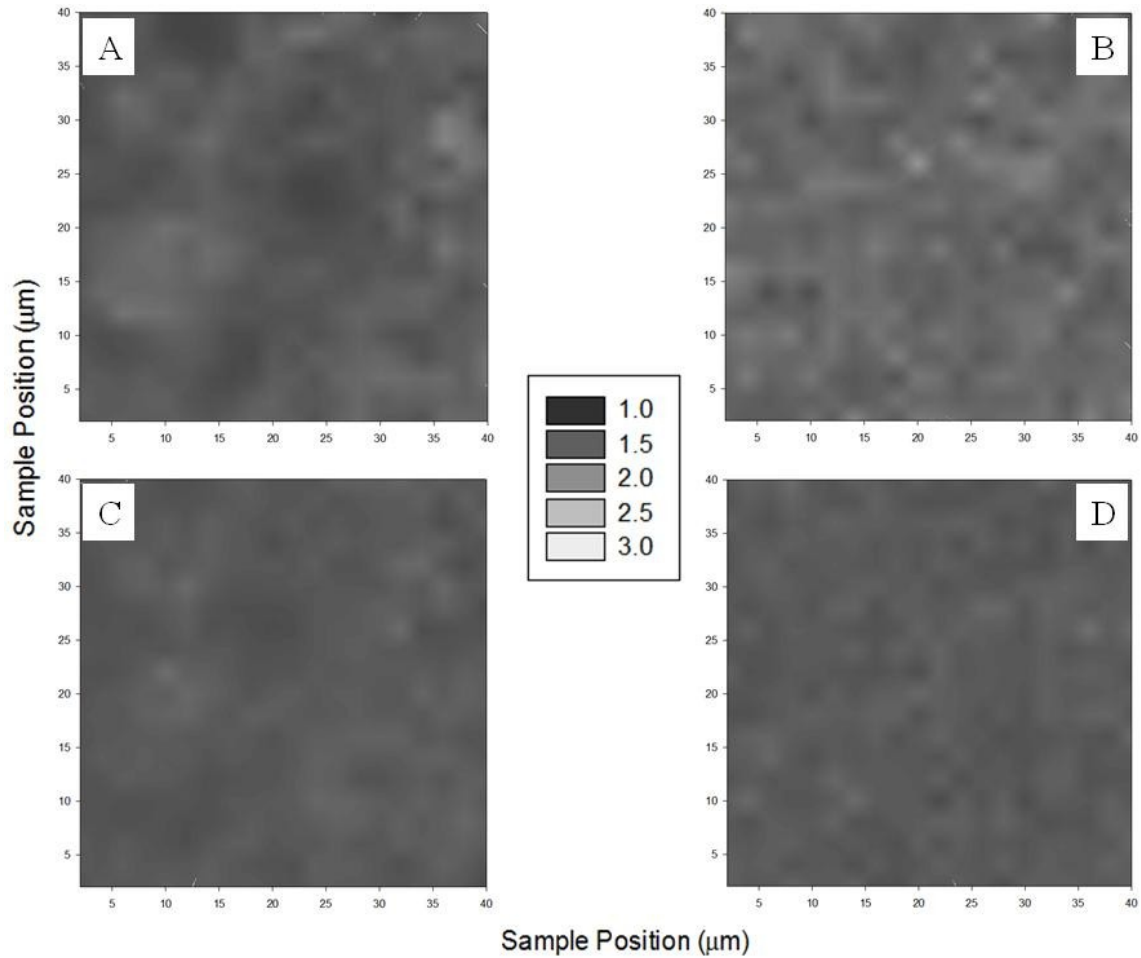


Figure 5.18: Relative width maps of the mirror polish surface finish obtained using the regular scan setting.

The changes in the width of a Raman peak are attributed to plastic deformation in a sample, but also can represent the amount of amorphization in a crystal structure. While there have been studies on amorphization in silicon carbide at low loads<sup>[62]</sup>, true amorphization does not occur in silicon carbide until much higher loads are applied. The large redistribution of relative widths at the surfaces shows the localized effects of indentation that is partially seen in the bulk. This redistribution is greater in the grit blast and rotary ground, where the deformation was already larger than either the standard or

mirror finish sample. This could be attributed to material under the indenter tip being transformed slightly, or the material under the indenter is being forced into a more ordered structure under the indentation pressure.

#### **5.2.1.2 Indentation at 30 mN**

The 30mN load indents did not reveal any change in the average stress values over the standard, grit blast, or rotary finish samples. In the mirror finish sample however, the average stress at the surface increased beyond the standard deviation of the pre-indented average stress value. Similarly, only in the mirror sample did the width analysis show an increase in deformation. Figure 5.19 shows a plot of the average stress values for each sample as they change with depth, before and after 30mN maximum load indentation. The width variations for each sample before and after indentation can be seen in figure 5.20.

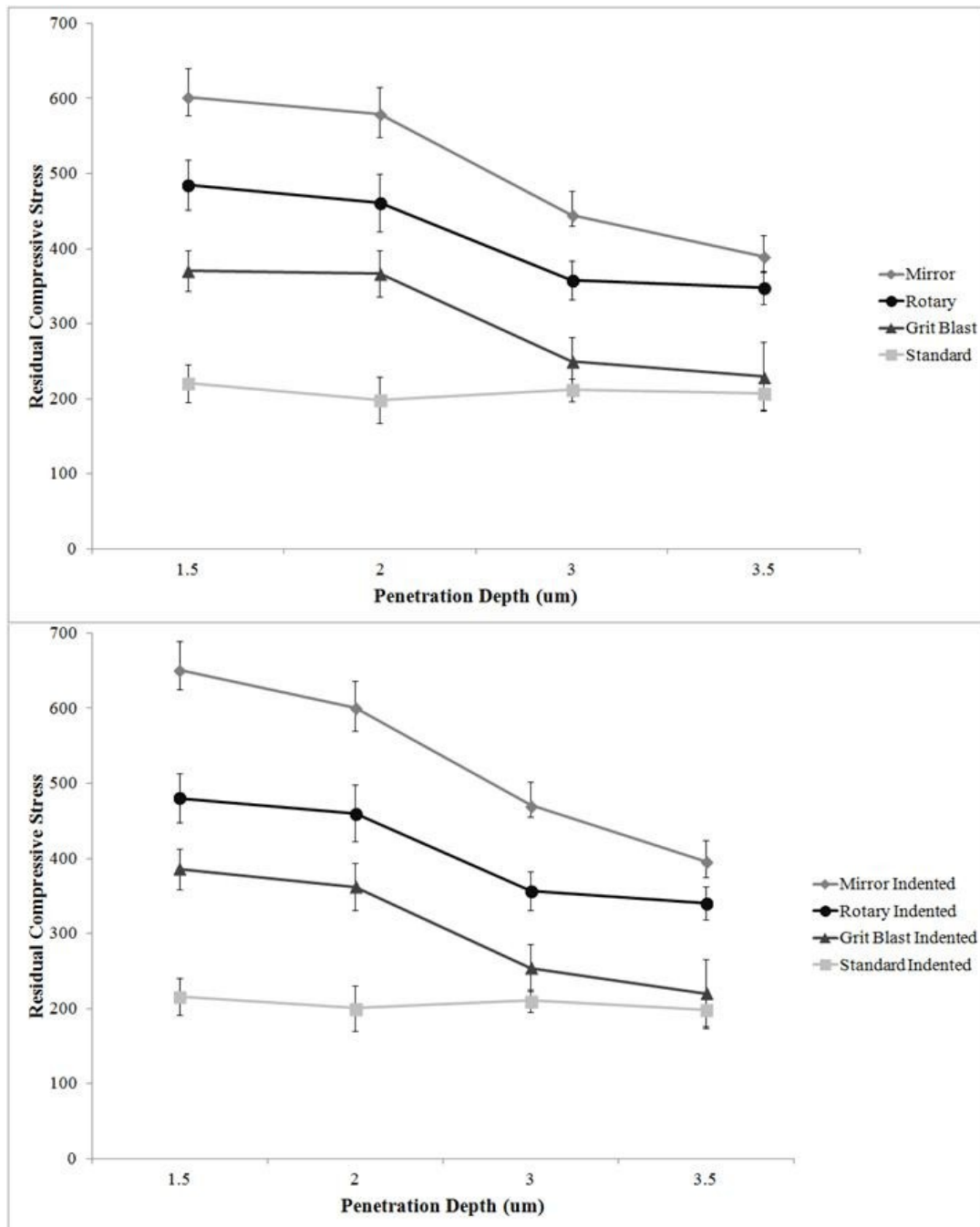


Figure 5.19: Average stress value plots (a) pre- and (b) post-indentation. The increase in average value of the mirror finish is seen at the near surface.

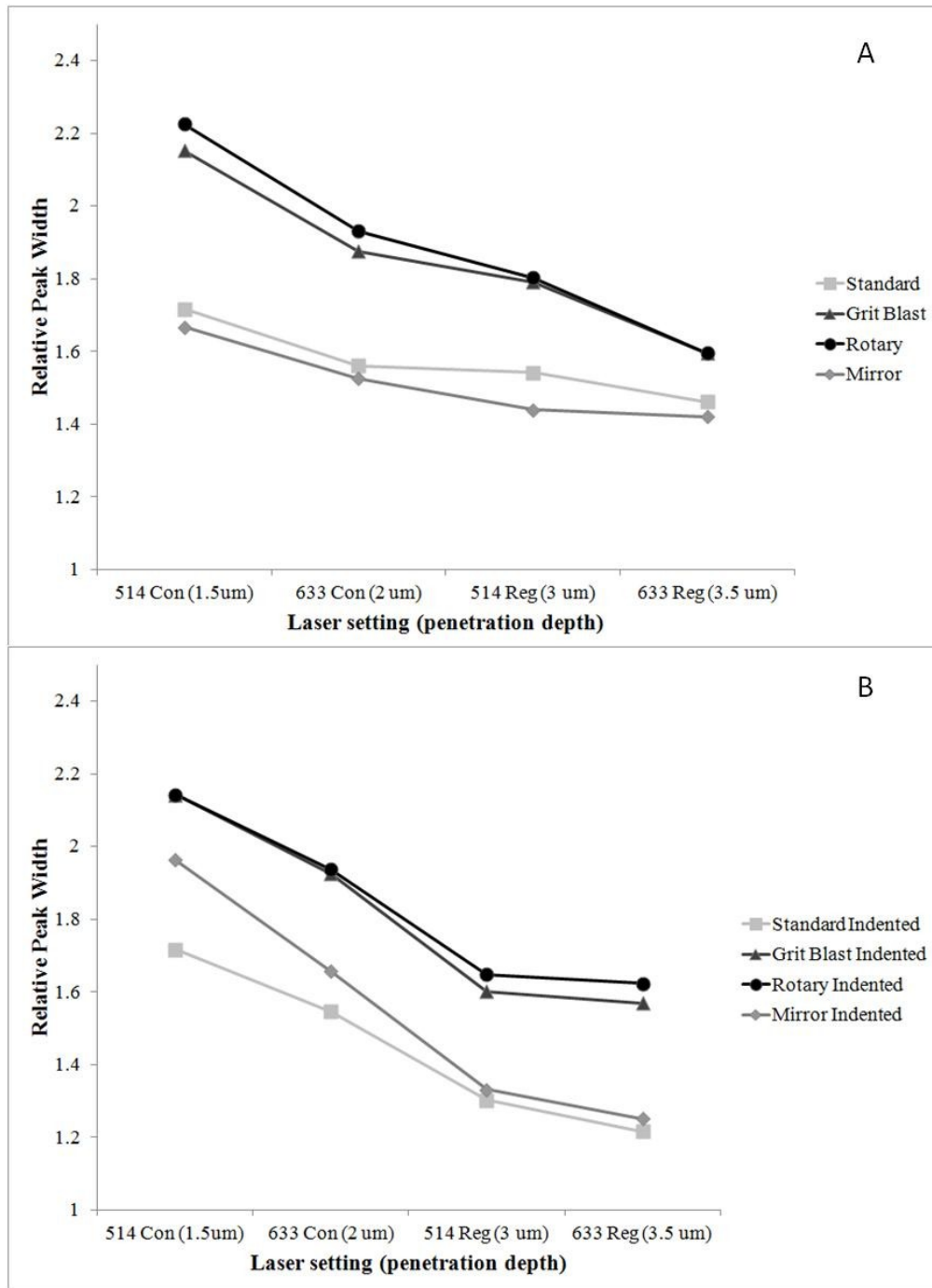


Figure 5.20: Average relative width value plots (a) pre- and (b) post-indentation.

As with the average measured stress in the mirror sample, the peak width at the surface has increased as well.

At 30mN, the stress under the indenter tip coupled with the high residual stress at the surface of the mirror finish sample cause a slightly higher residual post-indentation. This is most likely not seen in the other samples at this load, as the stress value near surface was not high enough to elicit a lasting change. This can also partially explain the higher relative width value near surface. The roughness of mirror finish sample was much lower than any of the other samples. This means that the contact between tip and sample was greater, and that the full load was applied to the surface. With the rougher surface finishes, the tip may only come in partial contact with the surface and not properly indent. As a reference, both the stress and width maps for the 30mN indentation can be found in Appendix 1.

## 6. Variations in Raman Spectra of Silicon Carbide

The Raman spectra collected from mapping showed variations beyond peak shifting and broadening that were thought to provide further information on machining induced deformation. These variations included the appearance of several peaks associated with polytypes other than the 6H-SiC structure, relative intensity changes of the TO and LO peaks, and shifting of the LO peak with the presence of the new peaks. The following paper is a study on these spectral features and how they link to machining induced subsurface damage.

### 6.1 Variations in the Raman spectral profile of 6H-silicon carbide ceramics due to machining

B.P. Groth<sup>a</sup>, A.B. Mann<sup>a,b</sup>

<sup>a</sup>*Materials Science and Engineering Department, Rutgers University, 607 Taylor Road, Piscataway NJ, 08854. USA*

<sup>b</sup>*Biomedical Engineering Department, Rutgers University, 599 Taylor Road, Piscataway NJ, 08854. USA*

Emails: [bengroth@eden.rutgers.edu](mailto:bengroth@eden.rutgers.edu) and [abmann@rci.rutgers.edu](mailto:abmann@rci.rutgers.edu)

#### Abstract

Raman spectroscopy was performed on hot-pressed, machined SiC tiles in order to determine the effect of different surface finishes on the acquired Raman spectra. Tiles were machined on one side to four different surface finishes, each imparting a different amount of surface deformation. Experiments were performed using 514- and 633-nm wavelength excitation, in a standard and confocal setting to allow for depth analysis. Differences in the Raman spectra were scrutinized and compared to single crystal



profiles, including: variations in the ratio of characteristic peaks, peak intensities versus peak positions, and the presence of additional Raman peaks from stacking faults and new phases. Nanoindentation experiments were performed on each sample, to 10mN and 30mN peak loads, to introduce deformation to the surfaces. Subsequent Raman over the indents showed a statistical increase in the number of stacking faults as well as new phases from the pre-indented surfaces.

## **Introduction**

Silicon carbide is known to exist in many polytypes, each differing by the stacking sequence of the silicon-carbon tetrahedron <sup>[1]</sup>. The ability to differentiate each polytype using Raman spectroscopy has been studied and used in characterizing silicon carbide ceramics <sup>[2]</sup>. The inherent nature of polytype formation allows for the presence of stacking faults within manufactured silicon carbide. This stacking fault presence greatly influences the performance and properties of silicon carbide semiconductors, acting much like a defect. As such, the focus of Raman spectroscopy for stacking fault and other defect detection has been on single crystal wafers <sup>[3-11]</sup>. In polycrystalline and bulk sintered samples where electronic performance is not as essential, the role that stacking faults play is less understood.

The work of Li and Liao <sup>[12]</sup> has shown that machining of ceramics can produce subsurface damage that is not easily identifiable and is detrimental to the strength and performance of the machined component <sup>[13,14]</sup>. Raman spectroscopy has proven useful in examining damage caused by various machining processes <sup>[15]</sup>; however the influence of damage on stacking faults has yet to be examined. Presented in this work is an analysis of

Raman maps over silicon carbide ceramics that have undergone various machining regimens. The effect of this machining on the presence of stacking faults is examined, and used as an estimator of subsurface damage.

## **Materials and Methods**

### **Silicon Carbide**

Four hot-pressed silicon carbide tiles made with alpha-SiC (6H structure) were obtained for this study. Each tile was mechanically machined on one side to a different surface finish: standard finish; grit blast finish; rotary ground; and mirror polish. The unmachined side, termed the reverse surface, acts as the baseline for each tile. The standard finish, figure 1(a) was simply a removal of excess carbon from the tile pressing with a light sand blasting. Optically, the standard finish surface is similar to the unmachined reverse side and can be considered an as-pressed sample. The grit blast samples were impacted with fine steel shot which, as it can be seen from the SEM image in figure 1(b), gives significant deformation on the machined surface of the tile. The rotary ground samples, figure 1(c) were taken from the as-pressed state to its finish through the use of diamond grinding wheels, running on a rotary grinder. The mirror polish samples were taken from the as-pressed state to a mirror-like finish through the use of successively finer polishing with diamond abrasive wheels. These samples displayed the lowest amount of surface roughness, as shown by figure 1(d). Single crystal samples of 4H- and 6H-SiC were obtained from MTI Corporation, Richmond, CA 94804, USA, and used as a standard for comparison. Baseline spectra for the single crystal samples can be seen in figure 2.

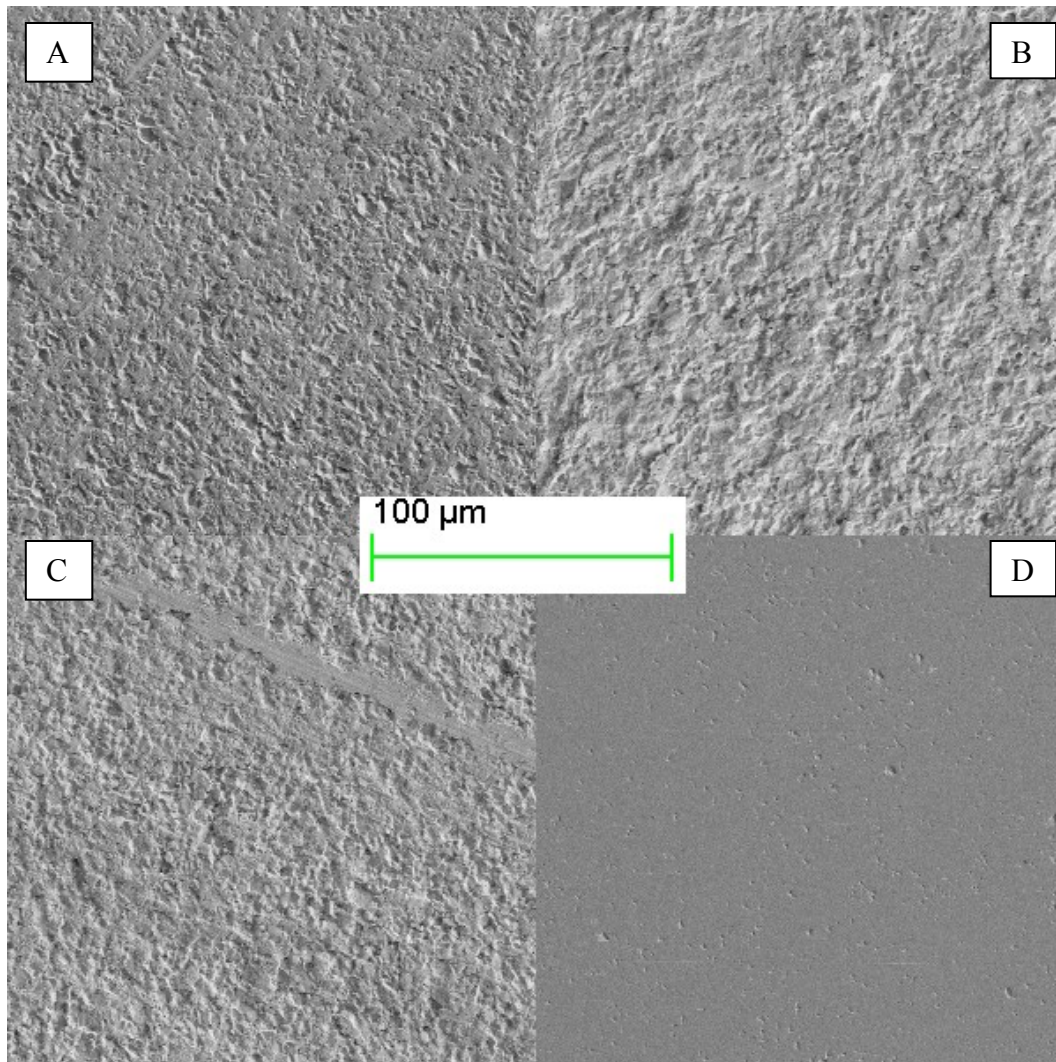


Figure 1: SEM images of the machined surfaces for the a) Standard, b) Grit Blast, c) Rotary Ground, and d) Mirror Finish.

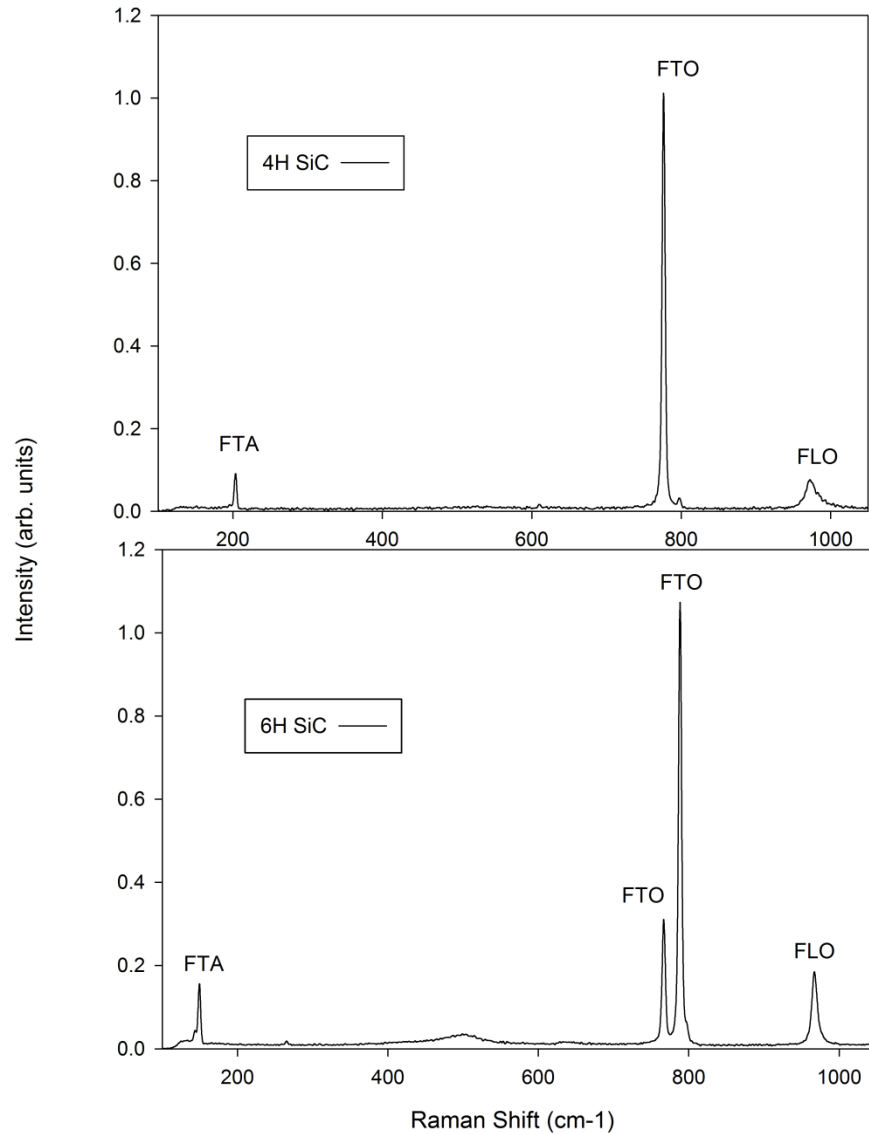


Figure 2: Typical Raman spectra profile for 4H- and 6H-SiC. Labeled are the unique transverse and longitudinal optical phonons, as well as the acoustic phonons. FLO peaks overlap indicating that the component peaks would need to be deconvoluted to see the contribution from either polytype. The “F” indicates a folded mode, a term used to indicate that these peaks are obtained by folding the first Brillouin zone of the hexagonal structures, such that they represent the same spacing as in the cubic 3C structure.

### **Raman Spectroscopy**

Raman mapping was conducted over a 40x40 $\mu\text{m}$  area, with 2 $\mu\text{m}$  spacing between points for each surface finish. This size was set based on the capabilities of the Raman system and to avoid spatial overlap of the Raman signal. The system was equipped with an 1800 1/mm diffraction grating for both the Ar ion 514nm laser and the HeNe 633nm laser. In order to scan through the depth of each sample, both a confocal and non-confocal setup was used. The confocal setting uses a virtual pinhole, created by slits in the spectrometer path and a decreased CCD scan area, as opposed to a physical pinhole in the laser path or in the microscope. The slit spacing was decreased from 50 $\mu\text{m}$  in the regular setup, to 20 $\mu\text{m}$  in the confocal, in order to limit the angle of returning light that was analyzed. Similarly, the CCD area was taken from 15 pixels down to only 3 pixels; this allows for greater spatial resolution at a cost of signal-to-noise ratio. In order to achieve intensity counts similar to those in the regular setting, several scan iterations were performed.

Each point of the acquired maps was an individual spectrum, so as to obtain the full spectral range of the sample, and not just one peak as examined in a linefocus map. Collecting the full spectrum at each point allowed for complete analysis of every peak feature in the silicon carbide system. Collected maps were processed using the WiRE3.2 software available from Renishaw. Spectra intensity were normalized to the largest intensity peak, the TO peak at 789.2 $\text{cm}^{-1}$ , and corrected for baseline. Curve fitting was performed using the WiRE 3.2 software's curve fit feature, with curve parameters set to allow mixed Gaussian-Lorentzian behavior. These parameters were saved and applied to each spectrum in the acquired maps.

The relative intensities of the  $789.2\text{cm}^{-1}$  TO peak and the  $968.4\text{cm}^{-1}$  LO peak for each sample was analyzed. This was done to understand the orientation of the grains within each machined sample. Along with the relative intensities of the TO and LO peaks, the intensity of the stacking fault peak at  $797\text{cm}^{-1}$ , associated with both the 3C- and 4H-SiC polytype, was analyzed. The SF peak intensities were compared to the LO peak positions, as well as to the ratio of TO-to-LO peak intensities. Also investigated was the appearance of the 4H TO peak located at  $776\text{cm}^{-1}$ , and its relation to the SF peak. Lower wavenumber acoustic peaks were recorded in each scan, and qualitatively assessed by noting the appearance of any peaks unique to 4H-SiC.

The values obtained from map scans are an average over the depth of penetration, which is inversely proportional to the absorption coefficient of the analyzed material. The average values given at each penetration depth are derived from a weighted average based on the penetration of the laser. For example, the values presented for the 514nm confocal setting, having a penetration of  $1.5\text{ }\mu\text{m}$ , are an average of the first  $1.5\text{ }\mu\text{m}$ . In the 514 regular setting, with penetration depth of  $\sim 3\text{ }\mu\text{m}$ , the values are obtained by accounting for the contribution from the first  $2\text{ }\mu\text{m}$  obtained from the 514nm and 633nm confocal settings. The result is an average value over the sample depth between 2 and  $3\text{ }\mu\text{m}$ . This is given as the value at  $3\text{ }\mu\text{m}$  penetration.

### **Nanoindentation**

Instrumented indentation was conducted on all samples using a Triboindenter™, Hysitron, Minneapolis, MN, equipped with a 10mN and 30mN transducer head and a diamond Berkovich tip. Loads were applied to each sample at a rate of  $1\text{mN/sec}$  to a maximum load of 10mN, followed by unloading at the same rate with no hold time.

Regions of each sample that were analyzed with Raman spectroscopy were indented in this manner, in a  $40\mu\text{m} \times 40\mu\text{m}$  area with  $2\mu\text{m}$  indent spacing, to match the Raman maps. This process was repeated at a maximum applied load of 30mN, at the same loading rate, over different regions than the 10mN indents.

Following indentation, samples were remapped using Raman spectroscopy to study the effects of indentation. Spectra were acquired using the same wavelengths and scan settings as previously, with mapping points coinciding with the indented area. Scans were processed as before, using the normalization and curve fitting tools in the WiRE 3.2 software. Changes in the average values of relevant peak information were analyzed, as well as changes to the map images post-indentation.

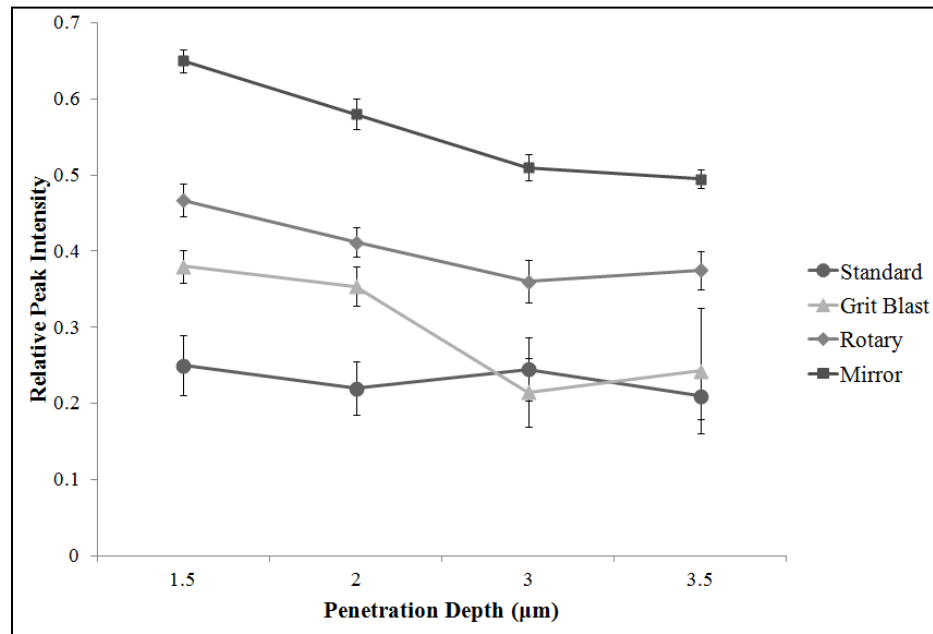


Figure 3: Plot of the peak intensity of the SF peak, relative to the TO peaks, as it changes with depth for each machined surface. The threshold intensity below which a peak appeared as a shoulder was roughly 35% of the TO peak. Error bars indicate standard deviation of the values obtained.

## Results

### Stacking Fault Peak

Average relative peak intensities as they change with depth can be seen for each machined sample in figure 3. These values are averaged over the collected map image, and represent a qualitative look at the density of SF, with higher values representing larger SF density. The standard finish sample showed the smallest density of stacking faults, with the fewest SF peaks having large enough intensity to appear as more than a shoulder on the  $789\text{cm}^{-1}$  peak. The concentration was uniform throughout the probed depth of the sample, and were randomly scattered across the Raman map. Peak intensities for the grit blast sample showed a higher concentration of SF closer to the surface of the sample, with density decreasing into the bulk of the sample. The two confocal settings, with nearer surface penetration, showed a uniform distribution over the first  $1.5\mu\text{m}$  and  $2\mu\text{m}$ , respectively, of the sample. Figure 4 shows the collected intensity map under the confocal settings, with values relative to the TO peak, for the grit blast surface as compared to the standard finish.

The rotary ground sample showed a higher SF density than both the standard and grit blast samples, with almost every  $797\text{cm}^{-1}$  peak appearing as more than a shoulder on the TO peak. The average stacking fault density remained high into the bulk of the sample, decreasing only at the largest penetration depth that could be analyzed. The mirror finish sample showed the highest SF concentration, having relative peak intensities of no less than 50% of the  $789\text{cm}^{-1}$  peak. This concentration held into the bulk of the sample, with relative intensity values remaining within 10% over mapped points



with depth as seen in figure 5. Typical Raman spectra obtained for each sample between 700cm<sup>-1</sup> and 1050cm<sup>-1</sup> showing differences in the SF peak intensity can be seen in figure 6.

Following indentation at 10mN, the average SF density did not change beyond the standard deviation for any machined sample. The distribution over the mapped areas did not change greatly either, with higher peak intensities remaining static at each point from the un-indented map. Following the 30mN indentation, the average SF peak intensity increased at the surface for all samples. This was more apparent in the standard and grit blast samples, where peak intensities had been low enough in the un-indented surfaces to appear only as shoulders in the TO peak.

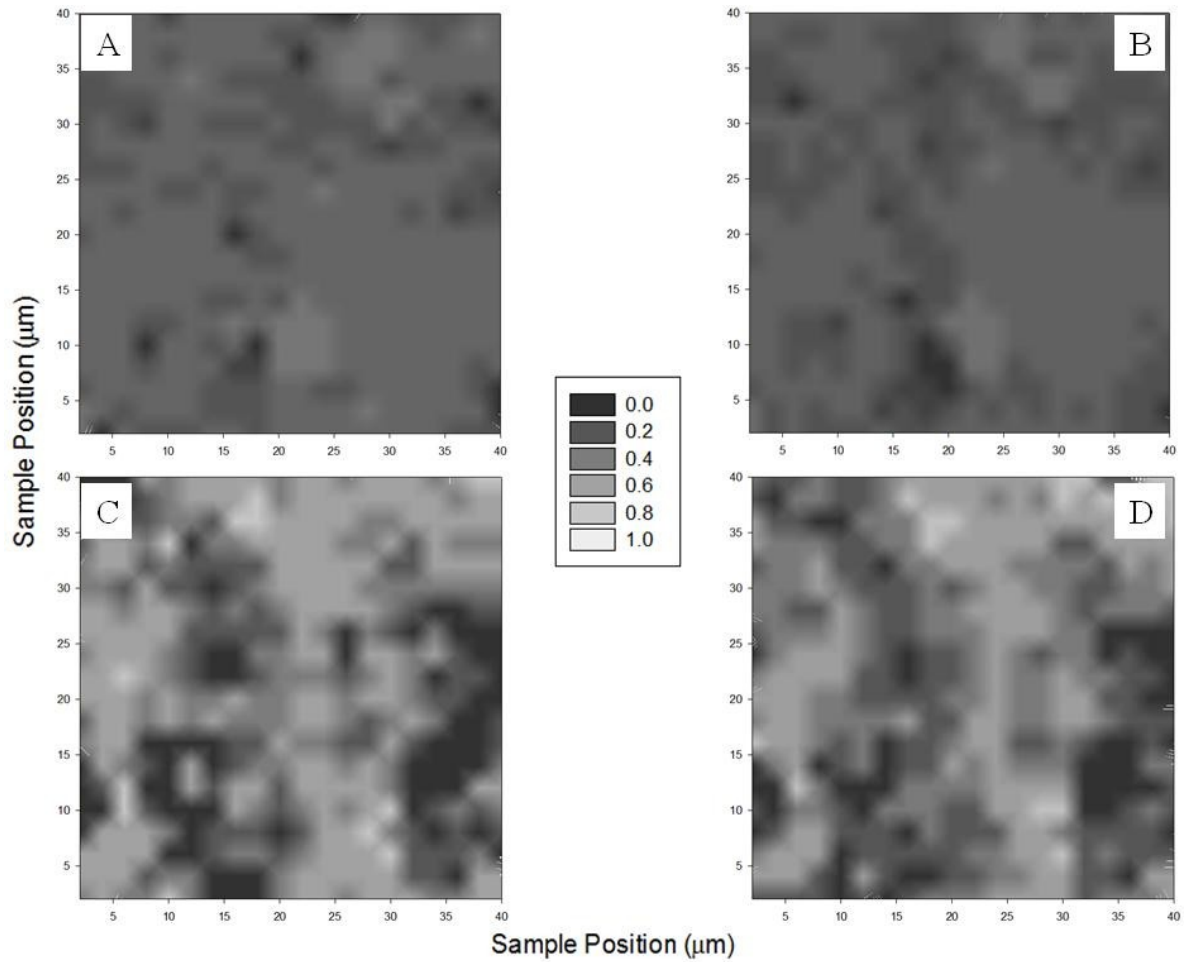


Figure 4: Raman maps of the relative peak intensity for the stacking fault peak, normalized to the 6H transverse optical peak are shown. The a) 514nm confocal and b) 633nm confocal maps for the standard sample represent the baseline stacking fault density. There is a noticeable increase in intensity, and therefore SF density, as well as distribution in the c) 514nm confocal and d) 633nm confocal grit blast maps.

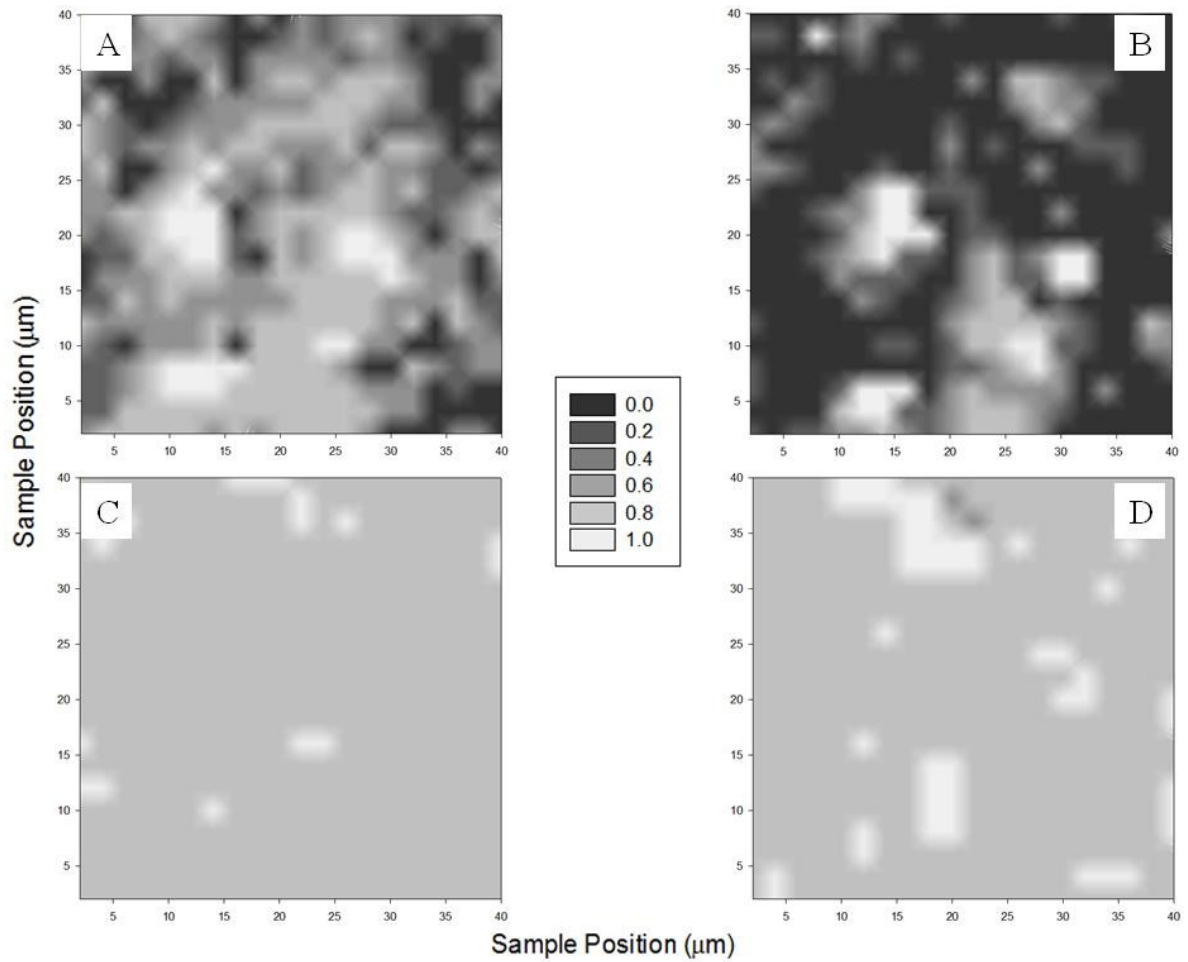


Figure 5: Pre-indentation Raman maps of the SF peak relative intensity for the a) 514 confocal and b) 633 regular scan settings on the rotary ground sample and c) 514 confocal and d) 633 regular scan settings on the mirror finish sample. The rotary ground sample displayed stacking fault peaks with high intensity near the surface that diminished into the bulk. The saturation in the mirror finish map shows the large density of stacking faults throughout the analyzed depth of the sample.

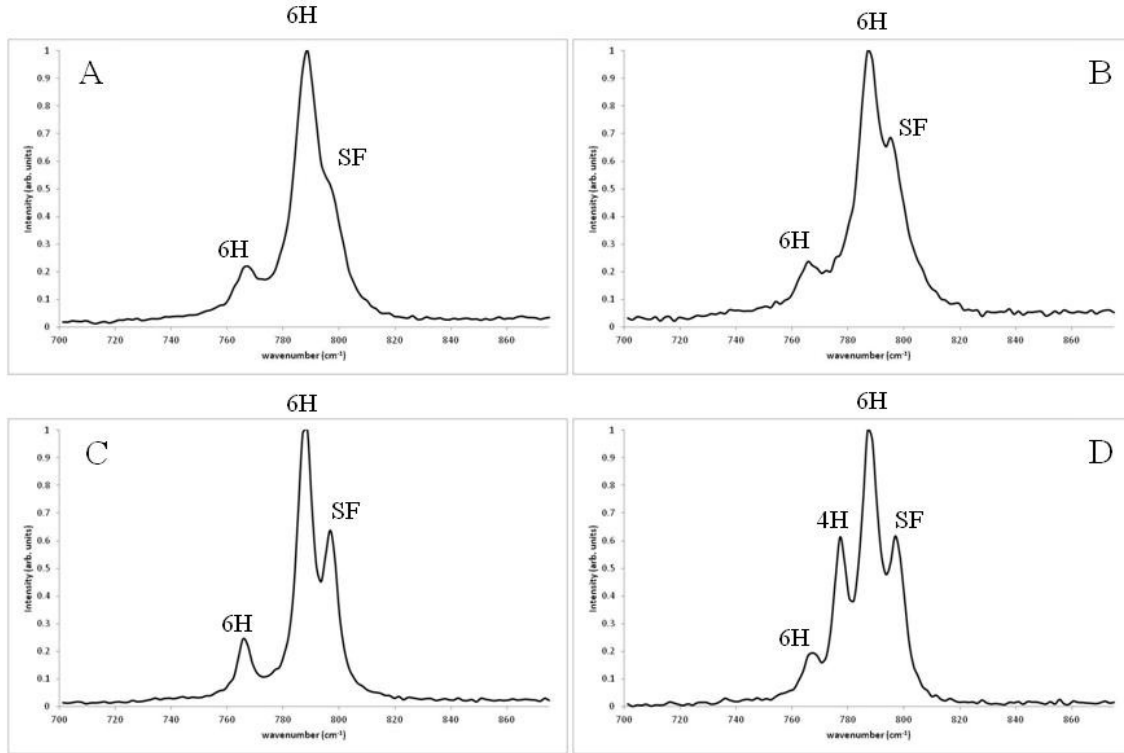


Figure 6: Typical Raman spectra showing the differences in intensity of the stacking fault peak, located at  $\sim 797\text{cm}^{-1}$ . The shoulder-like appearance in (a) is seen mostly in the standard finish sample, and in the bulk of the grit blast and rotary ground samples. (b) and (c) are seen at the surface of the grit blast and rotary ground samples, while the mirror finish displayed Raman spectra similar to (c) throughout the entire analyzed depth. (d) is a spectra found mostly in the mirror finish sample, corresponding to map points with values of 1.0, where the TO peak of the 4H-SiC system appeared.

### Peak Ratios

Analysis of the relative intensity ratios of the TO and LO peaks showed the LO peak intensity ranged from 19.13% to 98.89% of the TO peak for all machined surfaces. Studies have indicated that this ratio can be used to qualitatively identify grain orientations as grains are rotated from the c-axis (LO/TO intensity ratio of ~20%) towards the a-axis (LO/TO intensity ratio increases)<sup>[8]</sup>. Each surface showed similar distribution over the mapped surfaces of these same intensity ranges, with groups of like intensities in 4-12 $\mu\text{m}^2$  areas of the map scan. These groups varied only slightly with depth in each sample, with groups either growing or shrinking through the 3.5 $\mu\text{m}$  probed. The peak ratio in the single crystal 6H sample was a constant 19% for the (0001) orientation.

In comparing the LO/TO intensity ratio to that of the SF peak intensity, it was found that the intensity of stacking fault peaks was not dependent on the LO/TO intensity, i.e. grain orientation. This is shown in figure 7, where the average SF intensity values are plotted against the intensity value of the LO/TO ratio. Note that the LO/TO axis is divided in such a way that the major unit includes information from the  $\pm 0.05$  relative intensity values. This same trend was seen in each of the machined sample sets. Indentation at both 10mN and 30mN loads did not significantly alter this trend. The increased density of stacking faults over all maps skewed the data slightly, but the same trend as in figure 7 could be assumed after indentation. This suggests that indentation increases the apparent formation of stacking faults.

However, when looking at the relative intensity of the stacking fault peak with respect to the position of the longitudinal optical peak shift, there was a noticeable trend to the data. As seen in figure 8, as the relative intensity of the SF peak intensity with respect to the TO peak intensity increased, the LO peak position shifted from the 6H position ( $968.4\text{cm}^{-1}$ ) towards the higher wavenumber 4H position ( $973.6\text{cm}^{-1}$ ). This held true for all surfaces investigated, regardless of overall density of SF seen. It should be noted that the largest LO shift recorded, at  $972.2\text{cm}^{-1}$  in the mirror finish sample, was still below the position of the 4H-SiC LO peak. The transverse optical peak of the 4H-SiC polytype, appearing at  $776\text{cm}^{-1}$ , was seen in map spectra for each sample, but only at points containing the highest SF peak intensities and largest LO peak shifts.

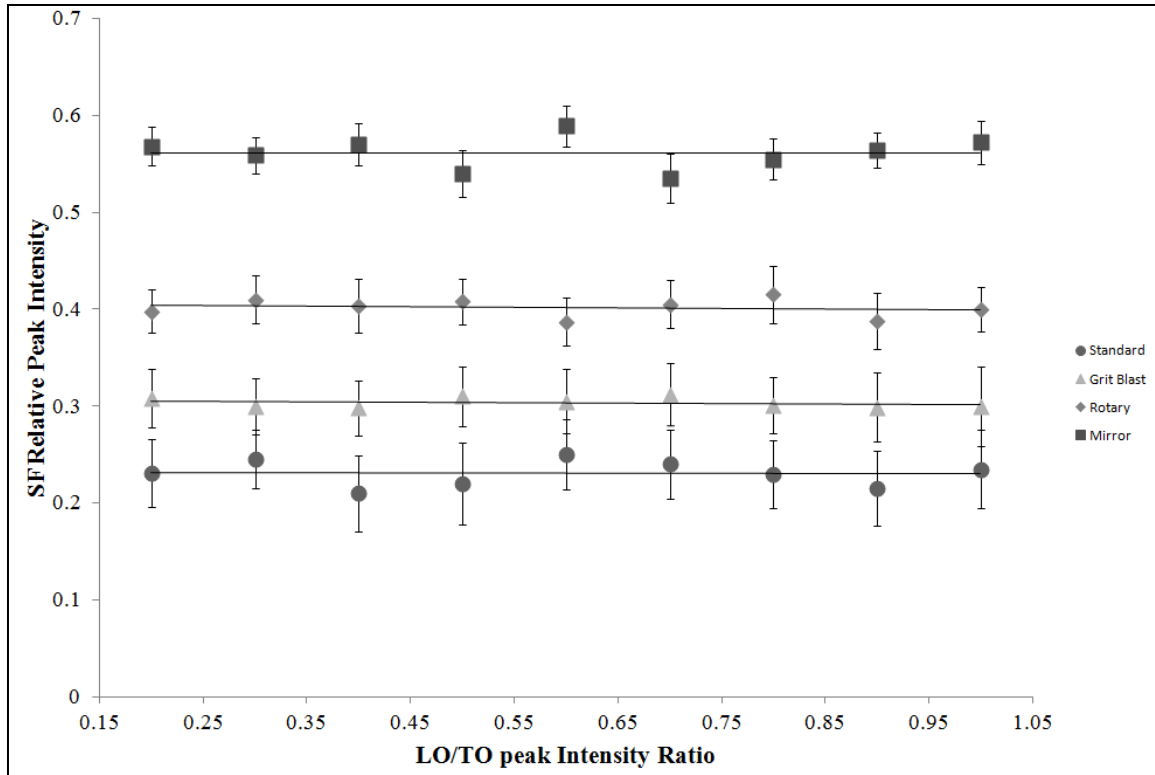


Figure 7: Plot of the LO/TO peak intensity ratio versus the relative peak intensity of the stacking fault peak for each sample. The average value varies between samples, but each sample exhibits the same SF intensity invariant to the LO/TO ratio. This result shows that there is an independence of the stacking fault peak to grain orientation, while other studies have estimated that some dependence should exist.

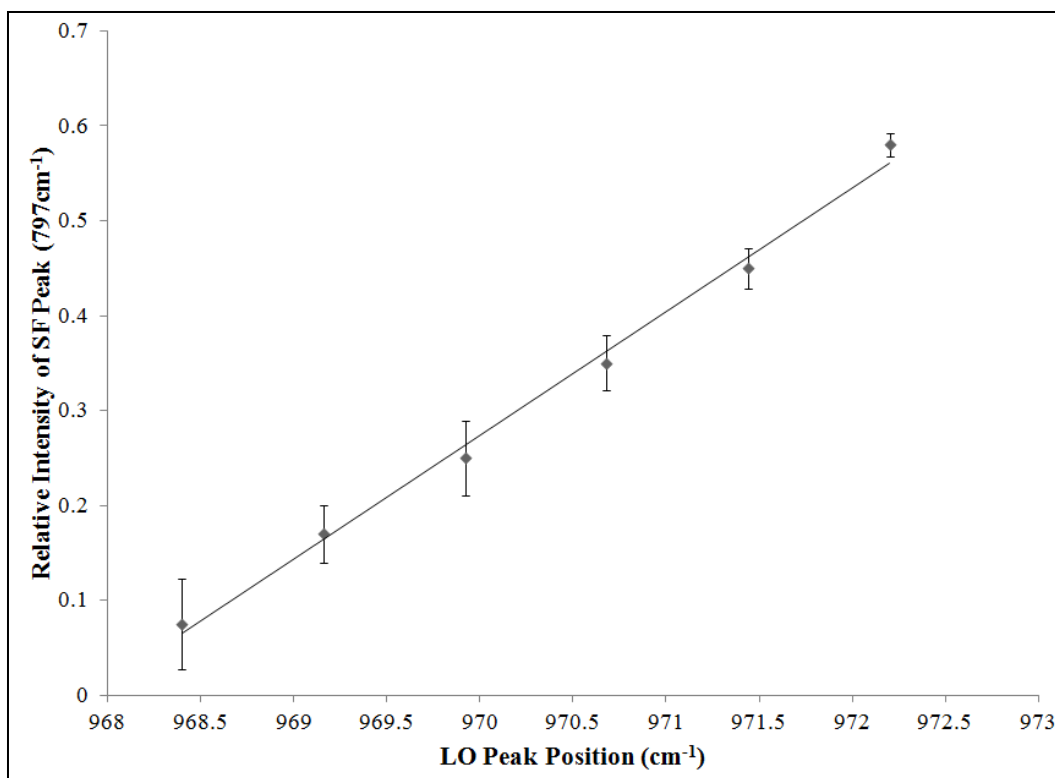


Figure 8: Plot of LO peak position vs SF peak intensity relative to the TO peak. There is a clear linear relationship between the shift in the LO peak position and the intensity of the stacking fault peak.

## Discussion

### Stacking Faults

The presence of stacking faults in the standard sample is caused by deformation of the 6H starting powders from the compaction and forming part of the tile making process. Grains have been shown to preferentially shear along planes such that the stacking of other polytypes could be observed <sup>[16-19]</sup>. The uniformity throughout the analysis volume implies an equal pressure was applied to the entire body, which is expected from an isostatically pressed sample. Previous studies <sup>[15]</sup> have shown through



analysis of peak widths that the deformation throughout the standard finish sample is uniform. This same analysis reveals that the grit blast sample contained a larger amount of deformation at the surface that remained into the probe-able depths of the sample. The stacking fault analysis from figure 3 however shows that there was an increase in density only in the first  $2\mu\text{m}$  of the sample. This indicates that the initial impact of steel shot caused cleaving of the surface grains, while the distributed force below caused the sample to deform without altering the apparent stacking of the material.

The increase in stacking fault density in the rotary ground sample over the standard and grit blast can be attributed to the nature of the rotary grinding process. In an intense rotary grinding procedure, a large cutting disc coated with diamond abrasive is swept across the sample in a raster pattern in order to remove material. This aggressive removal of material will take place at weaker points or along preferential cleavage planes. The depth of the damage will be related to the size of the diamond coating grit, and is why the apparent density of stacking faults is increased even into the bulk of the sample. In the mirror finish sample, the density of stacking faults was greatest of the machined samples over the  $3.5\mu\text{m}$  depth probed. The width analysis from previous work showed that the crystallinity of this sample was not altered greatly by the machining process. This suggests that even with successive polishing with decreasing size diamond grit, there remains subsurface damage left from the larger grit that is not polished. Rather than deforming the grains in such a way as to appear amorphous, the damage takes the form of material being sheared causing the appearance of stacking fault peaks in the Raman spectra.

The increase in stacking fault density following the 30mN indentation, and not the 10mN load, at the surface of each sample suggests that the higher load caused some form of crystal shearing or deformation. This could also be attributed to the lack of depth sensitivity of the wavelengths used in this study. Ultraviolet excitation can allow for nanometer depth penetration, potentially revealing effects due to the 10mN peak load indentation. The pop-in, or pop-out, events typically seen in indentation and associated with phenomena like fracture and dislocation generation were not present in any of the load-depth curves at the 10mN load. However, for the maximum load 30mN load, these were seen throughout the load-depth curves and all occurred between 12mN and 25mN. At a maximum load of 30mN, the highest indentation depth recorded was 223.1nm. The depth through which the Raman signal is obtained and averaged at the 514nm wavelength confocal setting is  $\sim 1.5\mu\text{m}$ . This implies that the 30mN loading causes a subsurface change to occur that is large enough to affect the volume of material analyzed with the Raman configuration.

### **Peak Ratios**

The ratio between the transverse optical and longitudinal optical peak intensities has been shown to correlate to the crystal orientation of the 6H-SiC structure <sup>[20]</sup>. The sizes of the groupings with similar intensity ratios is consistent with the average grain size of the silicon carbide starting powders and processing technique used to form the tiles tested. While the actual grain orientation was not determined, the Raman maps show that there is a range of different orientations being scanned, given by the LO/TO intensity

ranging from ~20% to ~98%. The plot in figure 7 shows that there is no dependence of the stacking fault peak intensity on the perceived grain orientation. In the work by Nakashima et al. <sup>[8]</sup> they suggest a possible orientation dependence of this SF peak, while none is seen here. Indenting the samples at both 10mN and 30mN loads did not appear to change this trend; however the distribution of SF relative intensity values shifted up, due to the greater frequency of more intense peaks.

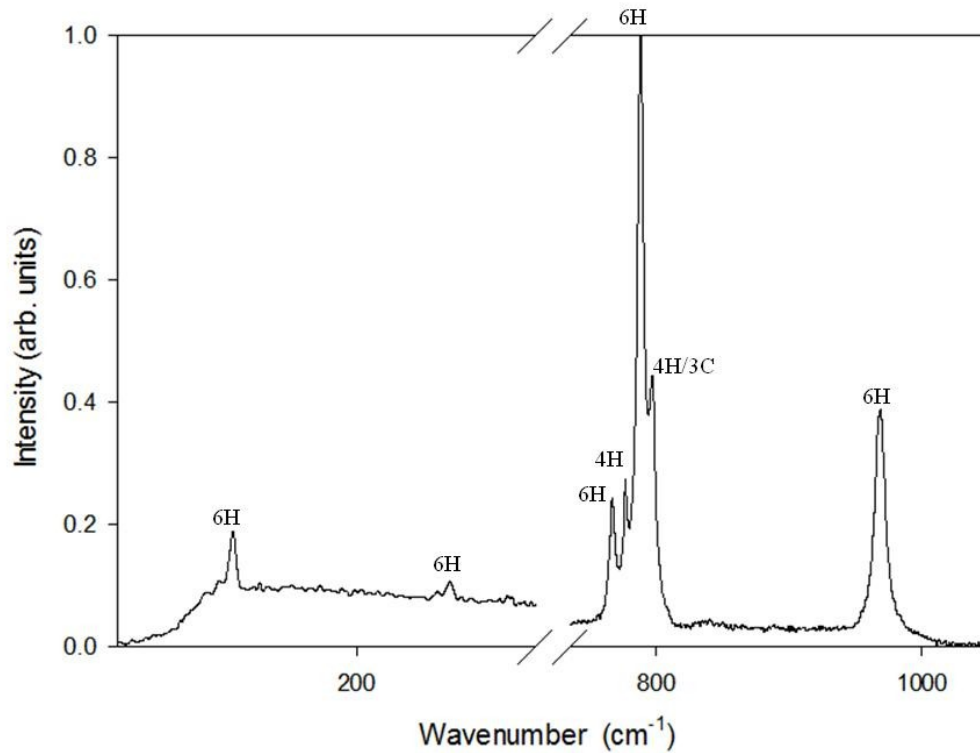


Figure 9: Raman spectra containing the TO peak of the 4H-SiC structure, without the corresponding acoustic peaks of that structure.

The relationship between the stacking fault intensity and LO peak position indicates that a polytype other than the nominal 6H is present. The appearance of the 4H transverse optical peak at the greatest LO peak shift and highest SF relative intensity suggests that this is due to the presence of 4H-SiC. While the appearance of this peak does indicate a higher presence of the 4H polytype, none of the acoustic peaks unique to 4H were seen in any of the spectra obtained, as seen in figure 9. The 3C-SiC structure shares similar TO and LO peak positions to the 4H stacking, and does not have any acoustic peaks attributed to its unique Raman spectra. This suggests that either the 4H formation is local, having no long-range order that acoustic peaks tend to represent, or that the formation is actually 3C-SiC.

## **Conclusions**

Silicon carbide tiles with 4 different machined surface finishes were examined in this study. It was found that as the level of machining increased the density of stacking faults within the surfaces increased. For the more aggressive machining conditions, stacking faults were present further into the sample, suggesting machining induced sub-surface deformation. The presence of stacking faults is typically more detrimental for applications involving single crystal silicon carbide; however this study has shown that the same Raman technique can be used to characterize bulk, polycrystalline samples whose performance may be influenced by the presence of stacking faults. The orientation of the grains in each sample were found to not influence the distribution of stacking faults, while the position of the longitudinal optical phonon peak coupled with the relative intensity of the stacking fault peak proved useful in detecting the presence of alternate polytypes.

## References

- [1] Wesch, W. "Silicon carbide: synthesis and processing". Nuclear Instruments and Methods in Physics Research Section B: Beam Interactions with Materials and Atoms 116, 305–321 (1996).
- [2] Nakashima, S., Higashihira, M., and K. Maeda. "Raman Scattering Characterization of Polytype in Silicon Carbide Ceramics: Comparison with X-ray Diffraction". Journal of the American Ceramic Society 86, No. 5, 823-829 (2003)
- [3] Rohmfeld, S., Hundhausen, M. and L. Ley. "Influence of Stacking Disorder on the Raman Spectrum of 3C-SiC". Phys. Stat. Sol. (b) 215, 115-119 (1999)
- [4] Rohmfeld, S. Hundhausen, M. and L. Ley. "Raman scattering in polycrystalline 3C-SiC: Influence of stacking faults". Physical Review B 58, No. 15, 9858-9862 (1998)
- [5] Ward, Y., Young, R.J., and R.A. Shatwell. "Application of Raman microscopy to the analysis of silicon carbide monofilaments". Journal of Materials Science 39, 6781-6790 (2004)
- [6] Hundhausen, M, Pusche, R., Rohrl, J. and L. Ley. "Characterization of defects in silicon carbide by Raman spectroscopy". Phys. Stat. Sol. (b) 245, No. 7, 1356-1368 (2008)
- [7] Rohmfeld, S. Hundhausen, M. and L. Ley. "Raman scattering in polycrystalline 3C-SiC: Influence of stacking faults". Physical Review B 58, No. 15, 9858-9862 (1998)
- [8] Nakashima, S and H. Harima "Detection of stacking faults in 6H-SiC by Raman scattering". Applied Physics Letters 77, No. 22, 3612-3614 (2000)

- [9] Nakashima, S. Kisoda, K., Niizuma, H., and H. Harima. "Raman scattering of disorderd SiC". *Physica B* 219 & 220, 371-373 (1996)
- [10] Martin, E., Jimenez, J., and M. Chafai. "Microraman Study of Crystallographic Defects in SiC Crystals". *Solid-State Electronics* 42, No. 12, 2309-2314 (1998)
- [11] Nakashima, S, Nakatake, Y., Ishida, Y., Takahashi, T., and H. Okumura. "Sensitive Detection of Defects in alpha and beta SiC by Raman Scattering". *Materials Science Forum* 389-393, 629-632 (2002)
- [12] Li, K., and W. Liao. "Surface/subsurface damage and the fracture strength of ground ceramics". *Journal of Materials Processing Technology* 517, Nos. 3-4, 207-220 (1996)
- [13] Jahanmir, S. "Machining of Advanced Materials". *Proceedings of the International Conference on Machining of Advanced Materials* 847 (1993)
- [14] Xu, H.H.K and S. Jahanmir. "Effect of Microstructure on Abrasive Machining of Advanced Ceramics". *Ceram. Eng. Sci. Proc.* 16, 295-314 (1995)
- [15] Groth, B.P. and A.B. Mann. "Using Raman mapping to determine stress variation in machined silicon carbide ceramics".
- [16] Ghosh, D., Subhash, G. and N. Orlovskaya. "Measurement of scratch-induced residual stress within SiC grains in ZrB<sub>2</sub>-SiC composite using micro-Raman spectroscopy". *Acta Materialia* 56, 5345-5354 (2008)
- [17] Nakashima, S., Kato, T., Nishizawa, S., Mitani, T., Okumura, H., and T. Yamamoto. "Deep Ultraviolet Raman Microspectroscopic Characterization of Polishing-Induced Surface Damage in SiC Crystals". *Journal of the Electrochemical Society* 153, No. 4, G319-G323 (2006)
- [18] Capano, M.A. and B.C. Kim. "Residual strains in cubic silicon carbide measured by Raman spectroscopy correlated with x-ray diffraction and transmission electron microscopy". *Journal of Applied Physics* 100,083514-1 (2006)
- [19] Danishevskii, A.M., Tregubova, A.S., and A.A. Lebedev. "Characterization of macrodefects in pure silicon carbide films using X-ray topography and Raman scattering". *Semiconductors* 31, No. 10, 1025-1029 (1997)
- [20] Halac, E., Burgos, E. and H. Bonadeo. "Static and dynamical properties of SiC polytypes". *Physical Review B* 65, 125202 (2002)

## 7. Mechanical Properties from Indentation

At the start of this thesis work, as the objectives were still being defined, there was an attempt to link the variations between machined surfaces and the elastic properties obtained from indentation. The intent was to be able to show a correlation between some Raman features: whether it was the level of residual stress, any amorphization caused by the machining process, or the estimation of subsurface damage via stacking fault peaks, and the properties that could be gleaned from indentation: elastic modulus, hardness, plastic work of indentation, and a calibration/error correction in the estimate of the contact area given by the ratio  $E^2/H$ . As it turned out, the ability to correlate these sets of data was not straight forward and proved difficult to make a decisive connection. For completeness however, the information obtained from the indentation tests along with a discussion on the variation seen is presented below, with maps of the data given in appendix 2. The values in the discussion are referenced in the table below, showing the relevant properties for each sample, as well as the ideal single crystal sample. Typical indents can be seen in figure 7.2 and 7.3, showing both ideal load-depth curves and the effects of a rough surface on the obtained curves.

	Modulus	Hardness	$E^2/H$	Work
Standard	$279.13 \pm 133.02$	$19.48 \pm 14.85$	$4842.54 \pm 2407.74$	$0.507 \pm 0.0123$
Grit Blast	$237.96 \pm 136.67$	$15.92 \pm 15.92$	$5063.15 \pm 2942.80$	$0.521 \pm 0.139$
Rotary Ground	$231.37 \pm 107.20$	$16.99 \pm 13.76$	$3833.07 \pm 1609.28$	$0.507 \pm 0.117$
Mirror Finish	$367.82 \pm 37.82$	$39.20 \pm 6.46$	$3499.09 \pm 522.72$	$0.351 \pm 0.043$
Single Crystal	$420.15 \pm 6.59$	$40.72 \pm 0.944$	$4334.39 \pm 50.49$	$0.294 \pm 0.013$

Figure 7.1: Mechanical properties obtained from indentation experiments.

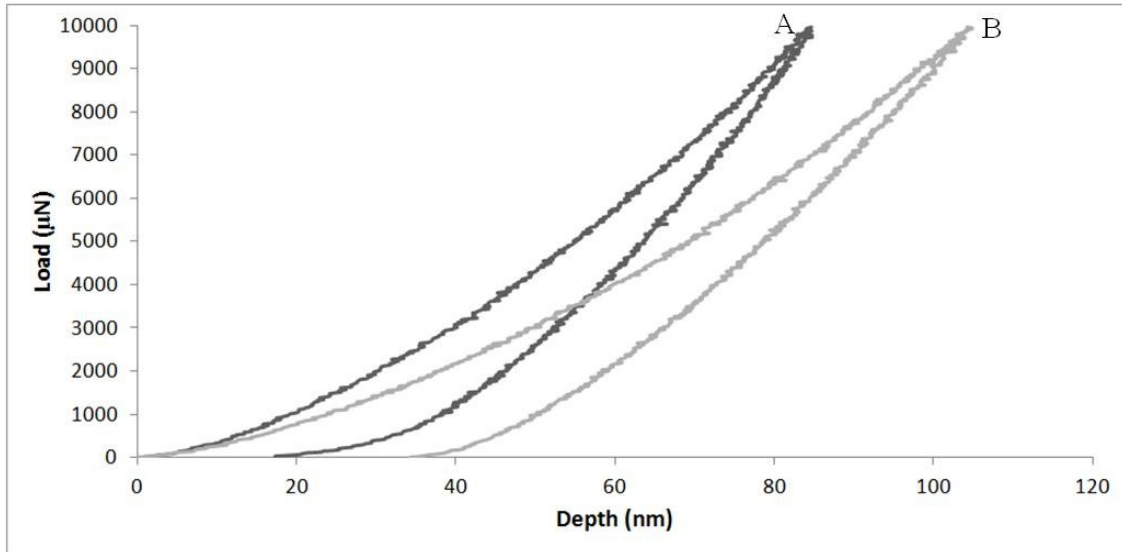


Figure 7.2: Typical load-depth curve obtained from indentation up to a peak load of 10mN. Curves similar to (a) yield values from the Oliver & Pharr analysis in the machined samples that are similar to single crystal SiC. Load-depth curves resembling (b) yield values similar to the average calculated values in the mirror finish sample.



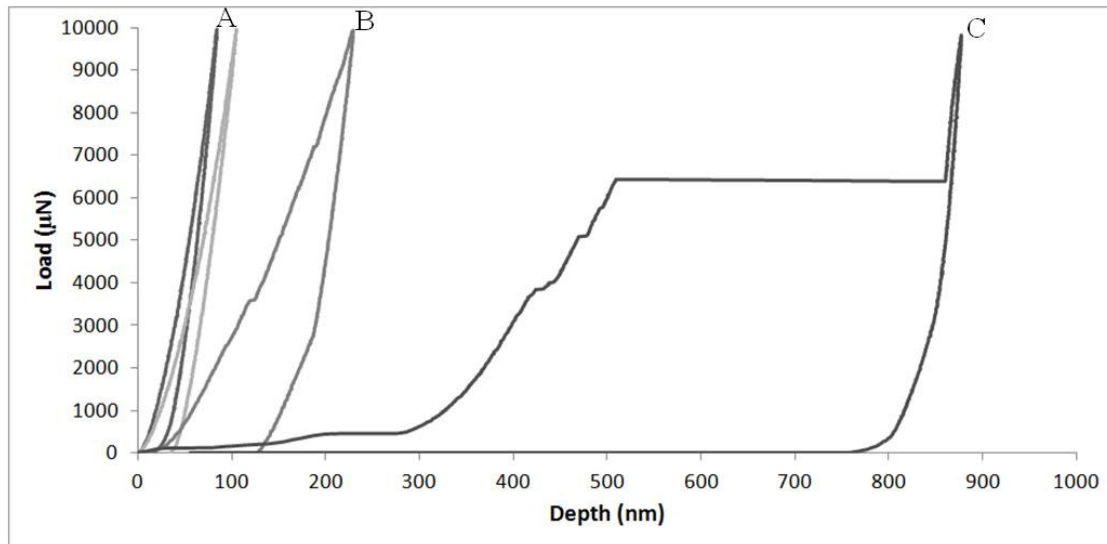


Figure 7.3: Load-depth curves obtained at 10mN peak load indentation. The curves in (a) are similar to those discussed in figure 7.2, while curves in (b) and (c) are the result of poor contact between the indenter tip and the sample surface. With a rough sample, the indenter can make initial contact with the side of a rough feature and then slide down that feature as load is applied. This can be seen in (c) where the depth “jumps” quite drastically for no change in applied load. These curves will provide incorrect property data and are not usable for any statistical measurements.

## 7.1 Elastic Modulus

The elastic modulus was determined using the method set forth by Oliver and Pharr, as calculated with the indentation software. A material’s elastic modulus is difficult to change. The drastic variation seen in the elastic modulus of the rougher standard, grit blast, and rotary samples is much greater than should be seen from a normal deviation of values. The differences seen can be attributed to two main factors: the

surface roughness of the sample, and for a similar reason, the contact area. When performing instrumented indentation and the accompanying analysis, assumptions are made about the contact between indenter tip and sample surface. The foremost of which is that the two are fully in contact and this does not change greatly during the indentation. For rough samples, where the indenter tip can come in contact with the edge of a grain, or indent into a valley, the tip will not fully contact the surface. Similarly the tip can contact a feature and deflect, representing an over estimation of the penetration depth. For the former, the machine does not know the tip is only contacting part of the sample, and therefore uses the entire area function for calculating the contact area. In the latter case, the deeper penetration will overestimate the contact and give a false modulus value. In the case of the mirror sample, which has notable higher modulus values than the rough samples, the decrease from the ideal is a compliance issue. This is theoretically compensated by the  $E^2/H$  analysis.

## **7.2 Hardness**

The hardness for each sample was determined by dividing the maximum load by the contact area, and was calculated by the indentation software. Unlike the elastic modulus of a material, there are certain factors that can change the measured hardness. Grain size, toughening mechanisms, fracture, and even the applied load can affect the hardness of a material. While these are factors, most of them would not cause as large a variation as seen here within samples with similar processing parameters (i.e. grain size). The main reason for such a large disparity between hardness values comes from the surface roughness of the indented sample. In the case of the mirror polish however, where the surface was by far the least rough, the deviation from the ideal can be seen as an

effect from the grain structure. In the single crystal, the load is applied over essentially one grain without interaction with surround material. For the mirror polish, there are grains and grain boundaries that effect how the load is distributed over the indented area.

### **7.3 Plastic Work of Indentation**

The plastic work of indentation was calculated using the method developed by Cheng and Cheng. The area under the load-depth curves was computed using the trapezoidal rule, and the resulting value is an estimation of the ratio of hardness to modulus. The closer to unity the value, the more plastic deformation imparted to the sample and the less elastic recovery once the indenter is removed. The baseline set by the single crystal sample shows what the maximum deformation at any applied load could be. The work analysis is a way of looking at the hardness-to-modulus ratio without needing to account for the machine compliance. However it is greatly affected by the perceived indentation depth. With a rough sample, where the tip can deflect or slide against the side of the material, there is an overestimation of the indentation depth and thereby an exaggeration of the plastic deformation. In the mirror finish sample, the fuller contact between tip and surface are what bring the work value closer to the ideal single crystal value.

### **7.4 Elastic Modulus squared divided by Hardness ( $E^2/H$ )**

The ratio of elastic modulus squared to hardness, developed by Joslin and Oliver, is used as a way of eliminating any error in measuring the contact area. Errors in measuring the contact area will result in errors in the determination of the elastic modulus and hardness. Even if the contact area is defined correctly for the indenter tip, any stresses in the indented sample will either over- or under-estimate this area. This analysis

is used to adjust mainly for the effects of stress in the samples. The table of values shows that the  $E^2/H$  ratios for each sample are all within the standard deviation of each other. This would suggest that absent the presence of stress, and accounting for the roughness of the surfaces, the elastic properties between samples are really not as different as the numbers suggest. In reality the overwhelming roughness of the samples still prevents any decisive analysis without knowing what percentage of the indenter tip is not in contact with the sample.

## 8. Conclusions

This thesis sought to characterize machining induced damage in silicon carbide ceramics using a combination of Raman spectroscopy and nanoindentation. Raman spectroscopy was selected as an analysis tool for its ability to evaluate a broad range of features in samples non-destructively, while nanoindentation could provide mechanical property data that could give insight into the deformation process.

Four samples were examined that had undergone different machining methods. Samples examined also included ideal single crystal silicon carbide, obtained from a manufacturer of pristine semiconductor grade wafers. The four machined samples were processed from the same batch powder, and hot-pressed under the same conditions. Variations could then be attributed solely to the machining process. Machining methods included: grit blasting with abrasive shot, intensive rotary grinding using diamond cutting wheels, and successive polishing with fine diamond grit polishing wheels until a mirror finish was achieved. A baseline “machined” surface consisted of the as-pressed silicon carbide tile that was abraded with sand to remove excess carbon left from the pressing process.

Each machined tile was examined using Raman spectroscopy at 2 different wavelengths: 514nm and 633nm excitation, with 2 scanning modes: a regular mode that is set to optimize resolution and signal-to-noise ratio, and a highly confocal setting that sacrifices signal intensity for higher spectral and depth resolution. The results of the Raman analysis showed variations in stress across sample surfaces, with the depth of penetration and between machined finishes. The standard sample set the baseline for

stress at compressive residual stress of 210MPa, with the average stress increasing as the amount of machining increased, up to 600MPa in the mirror finish sample.

Further analysis of the Raman spectra indicated an increase in the density of stacking faults present in machined samples. A density value could not be determined; however spectral features indicated the mirror finish sample had the largest density of faults through the depth. This was attributed to damage caused by the large diamond grit used to perform the initial polish that was not removed with further polishing under smaller grit size. Grain orientation analysis from Raman showed no effect of orientation on the presence of stacking faults

Analysis using instrumented indentation showed large variations in mechanical properties between machined samples. The machining process is known to cause decrease in strength of ceramic materials, however this was determined to not be the cause for these variations. The most valid explanation for the differences seen is the large surface roughness of each sample. While the mechanical data proved to not provide an adequate correlation to Raman data, it did allow for the introduction of controlled deformations to each surface. Additional Raman analysis over samples indented at 30mN showed a marked increase in the measured values in the mirror finish sample. Residual stress values increased to a compressive 650MPa, while the average peak width increased by a factor of roughly 1.5.

## 9. Future Work

This thesis has shown that Raman spectroscopy could be used as an effective tool in characterizing silicon carbide that has undergone different machining conditions. What is not as clear is exactly how the features seen in Raman spectra evolve through the machining process. It was assumed in this work that sample damage could be classified through a mix of the residual stress and subsurface damage introduced through stacking faults. However, an understanding of the machining conditions is necessary to fully understand which of these is truly represented by the Raman data.

This work relied heavily on samples that were provided having already been machined. As they were commercially graded, the assumption is that beyond the surface finish, there were little to no differences between samples. However, because they were already machined, the machining parameters were not readily available. This limits the ability to link a specific machining parameter to a Raman spectral feature. Future experiments can be done, using the standard samples as a starting point to recreate the machining conditions in an effort to obtain similar results.

Studies have been done on analyzing the effects of polishing load and rate, as well as grit size on surface features in ceramics <sup>[38]</sup>. The technique used in this reference involves a simple automated polishing device, readily available at the university, with controlled polishing parameters. It was estimated in this thesis work that in the mirror polish sample, extensive subsurface damage remained from larger grit polishing that was not removed after moving to smaller diamond grit. This can be examined by doing a step-by-step polishing technique and analyzing the surface between each successive polish

with Raman spectroscopy. The same Raman scan settings can be used to once again analyze the sample with depth.

Speaking to the penetration depth, this value falls greatly with decreasing laser wavelength. Because of this fact, many Raman users seek to utilize excitation wavelengths in the low visible and UV range for very near-surface analysis. In single crystal silicon carbide, the penetration depth drops from  $\sim 10\mu\text{m}$  at 514nm down to only  $\sim 200\text{nm}$  at 244nm excitation <sup>[83]</sup>. This change by almost two orders of magnitude would allow examination of the very near-surface of machined samples. At this depth, the data obtained from nanoindentation may be much more relevant, as the maximum indentation depth at 30mN is just beyond this analysis depth. Indentation has proven to show an increase in the surface stress and deformation in the mirror finish sample. This increase can be more closely studied if the Raman penetration is decreased.

The indentation performed in this work was done at very low loads when compared to what is possible with instrumented indentation systems on the market. The loads are also quite low compared with the modulus-to-hardness ratio of silicon carbide. Higher load indents in the 100mN-10N range would allow for deeper deformation, while still providing the benefits of a load-depth curve for extracting mechanical properties<sup>[84,85]</sup>. The issues with surface roughness would still exist for these loads however. But if the samples examined are those discussed at the beginning of this future work section, then better correlations could be made between the machining process, indentation and Raman spectroscopy.



### Appendix 1 – Raman Maps of Indented Samples

Given below are the Raman stress and width maps collected on samples that have been indented at 30mN maximum applied load. As in Chapter 5, the images on the left are pre-indented surfaces, and the images on the right are the indented surfaces. Similarly, the top images are from 514nm wavelength and the bottom from 633nm wavelength. Confocal setting and sample is indicated in the figure caption.

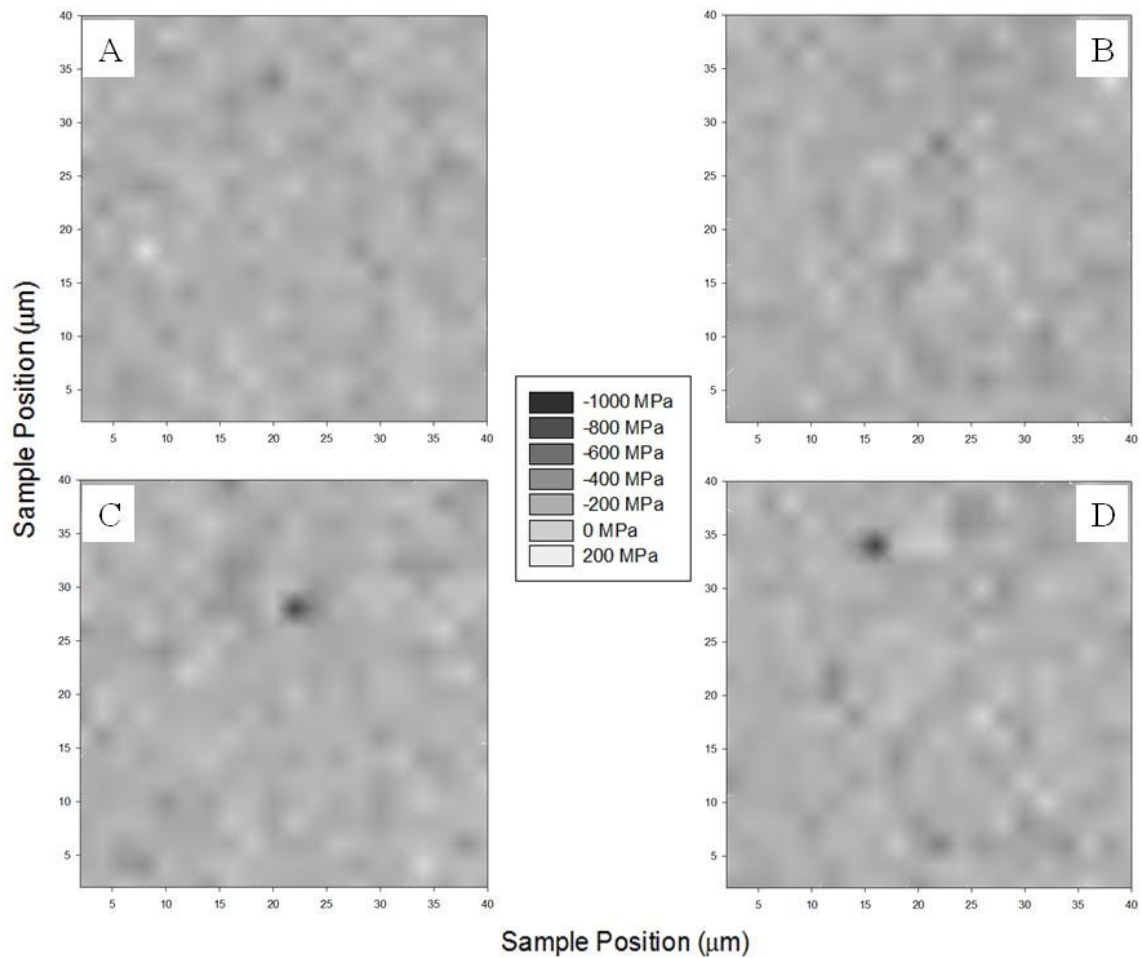


Figure A1.1: Stress maps of the standard surface finish obtained using the confocal scan setting.

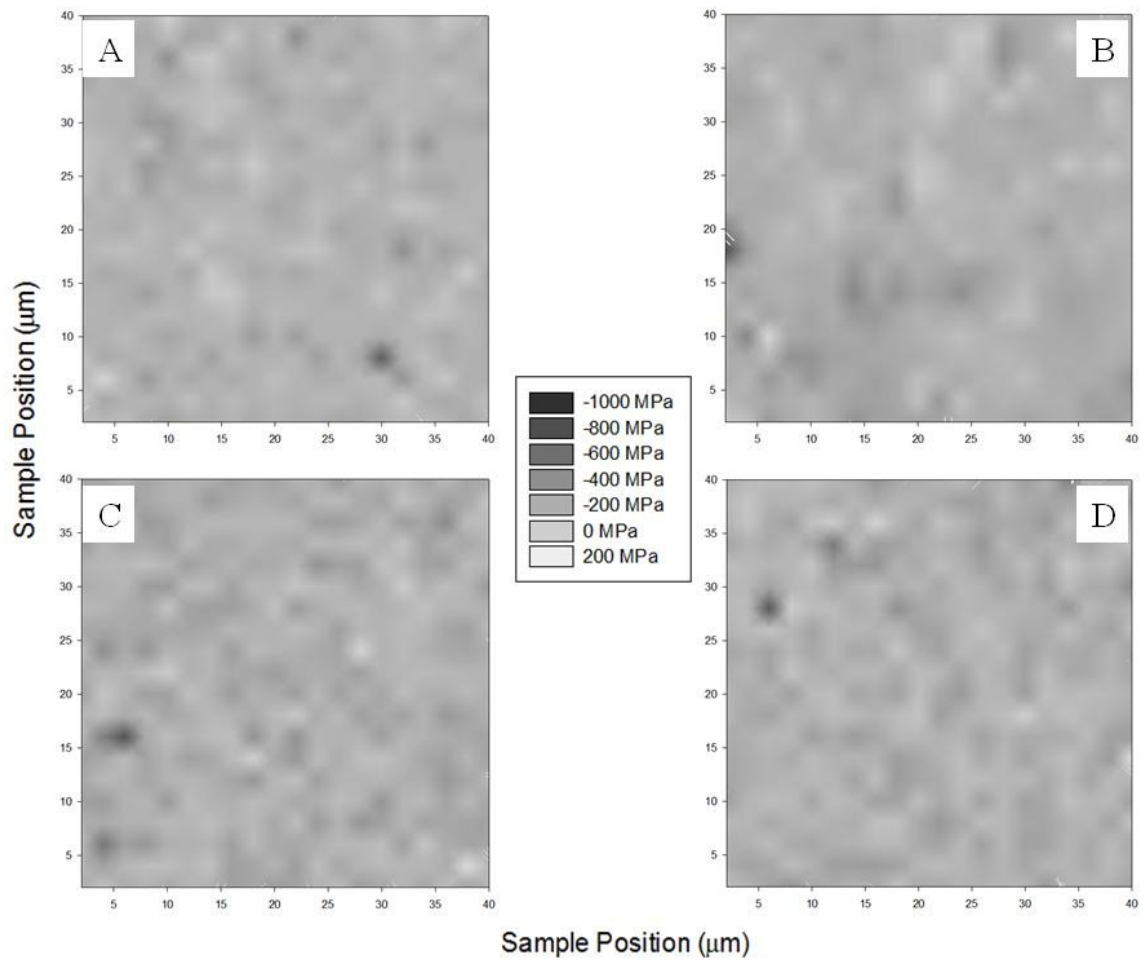


Figure A1.2: Stress maps of the standard surface finish obtained using the regular scan setting.

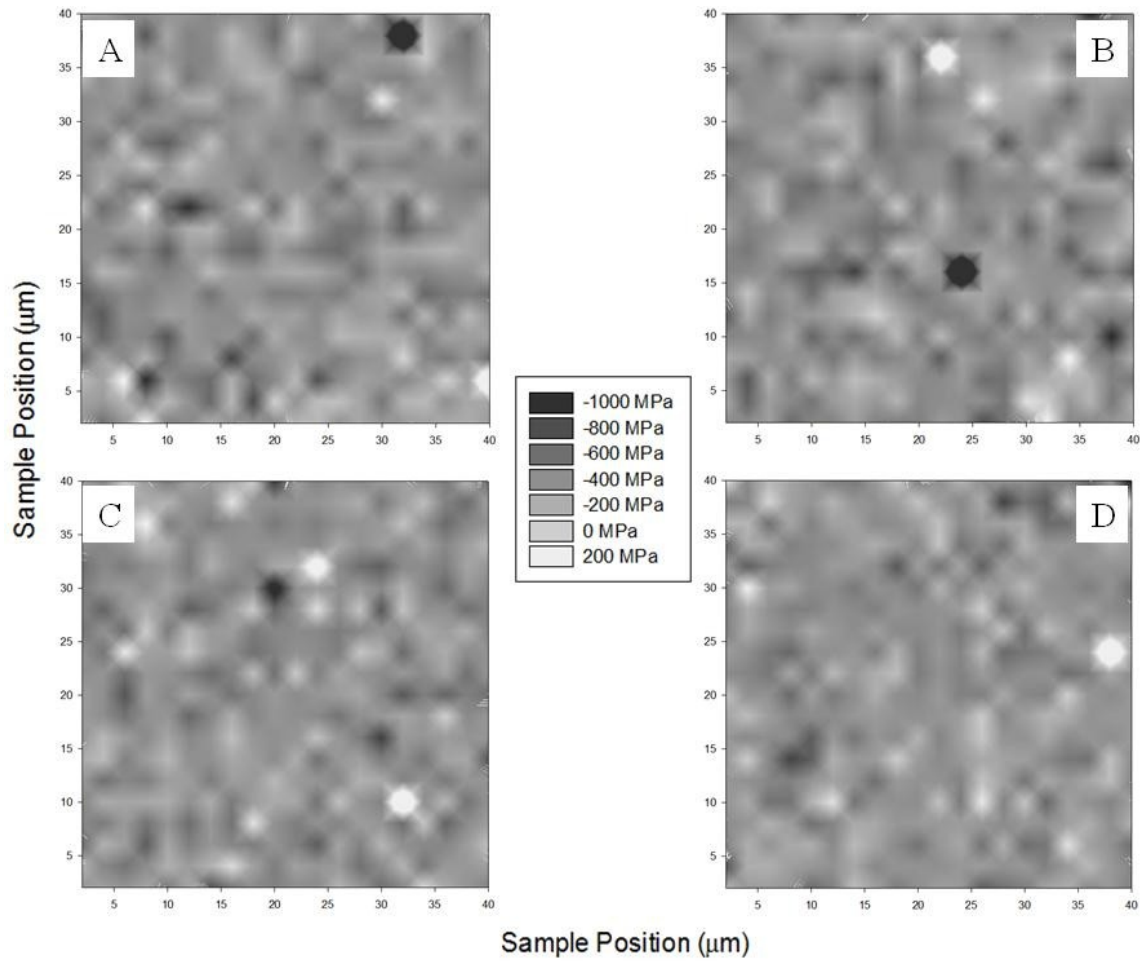


Figure A1.3: Stress maps of the grit blast surface finish obtained using the confocal scan setting.

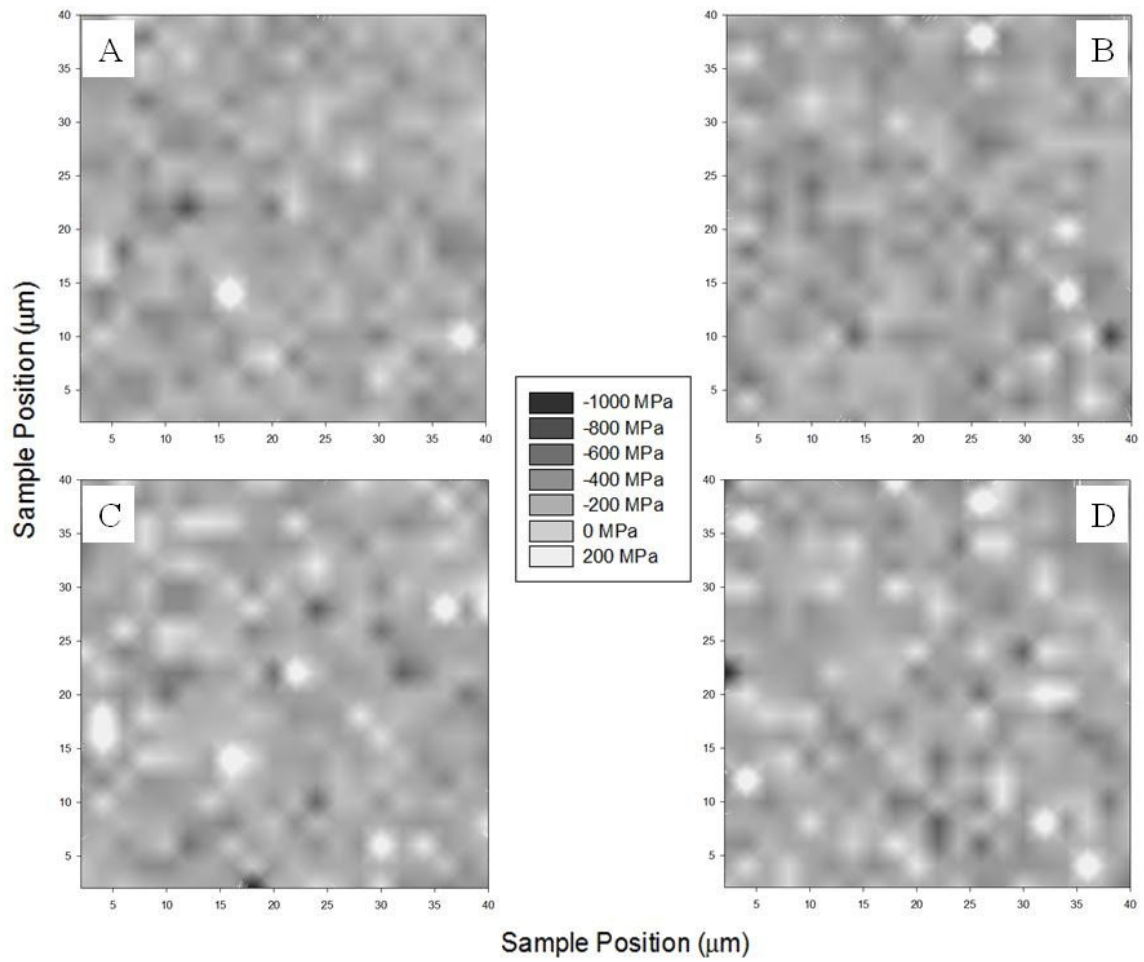


Figure A1.4: Stress maps of the grit blast surface finish obtained using the regular scan setting.

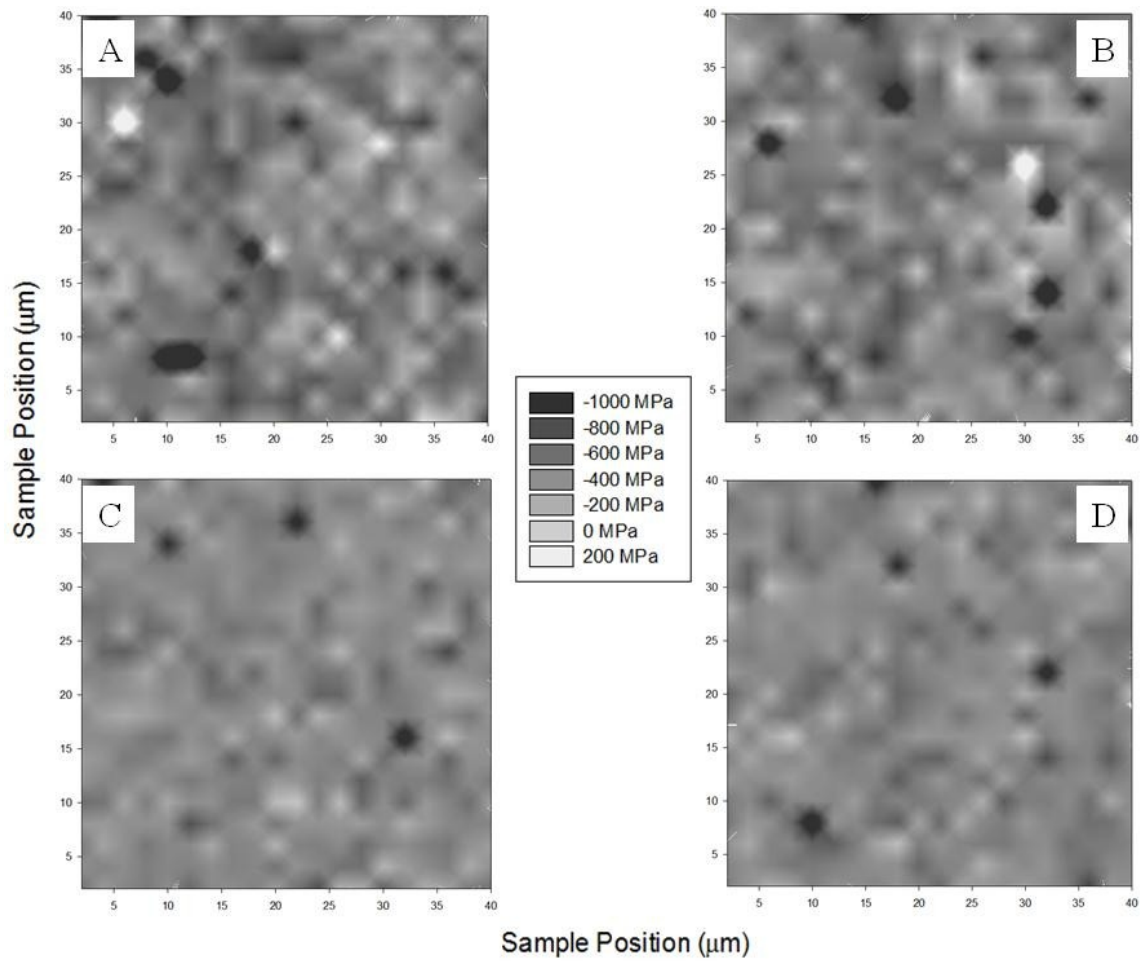


Figure A1.5: Stress maps of the rotary ground surface finish obtained using the confocal scan setting.

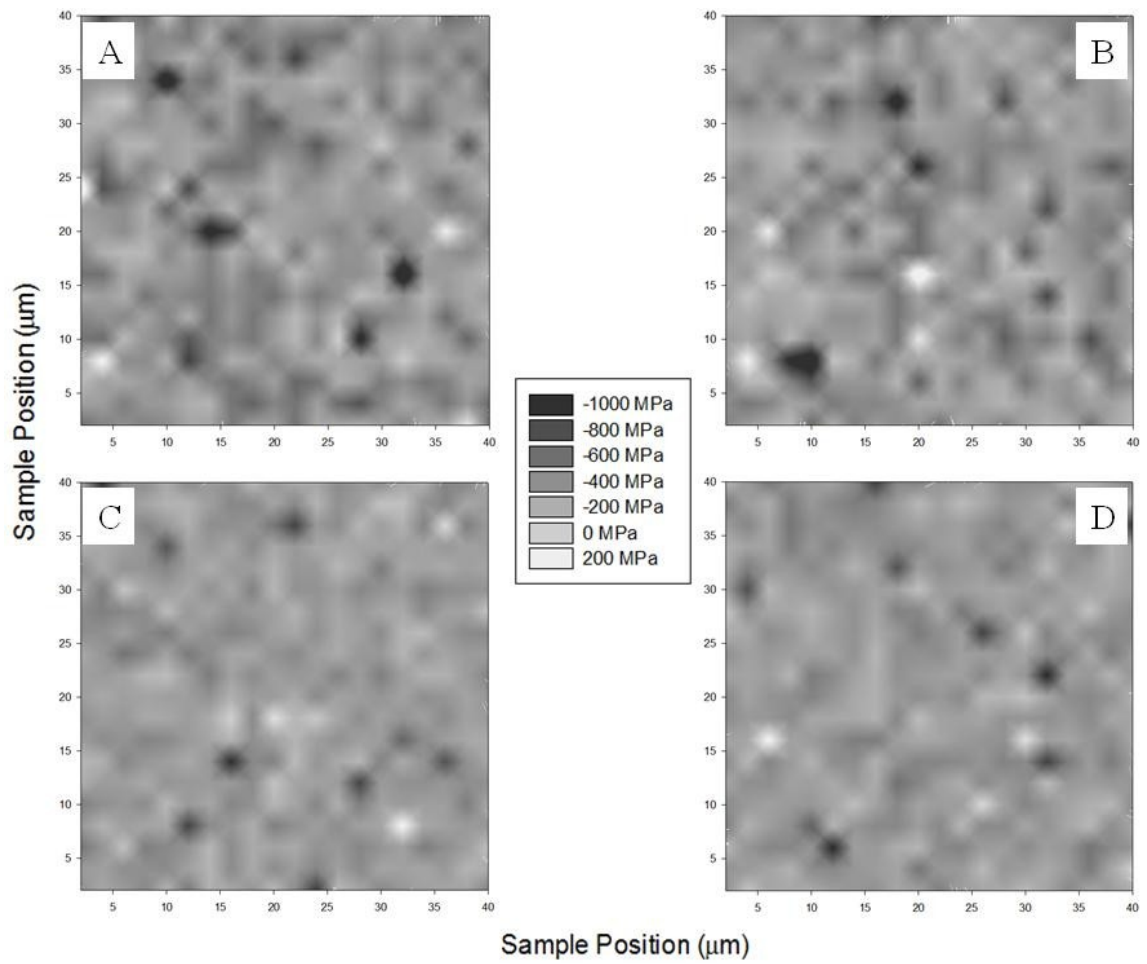


Figure A1.6: Stress maps of the rotary ground surface finish obtained using the regular scan setting.

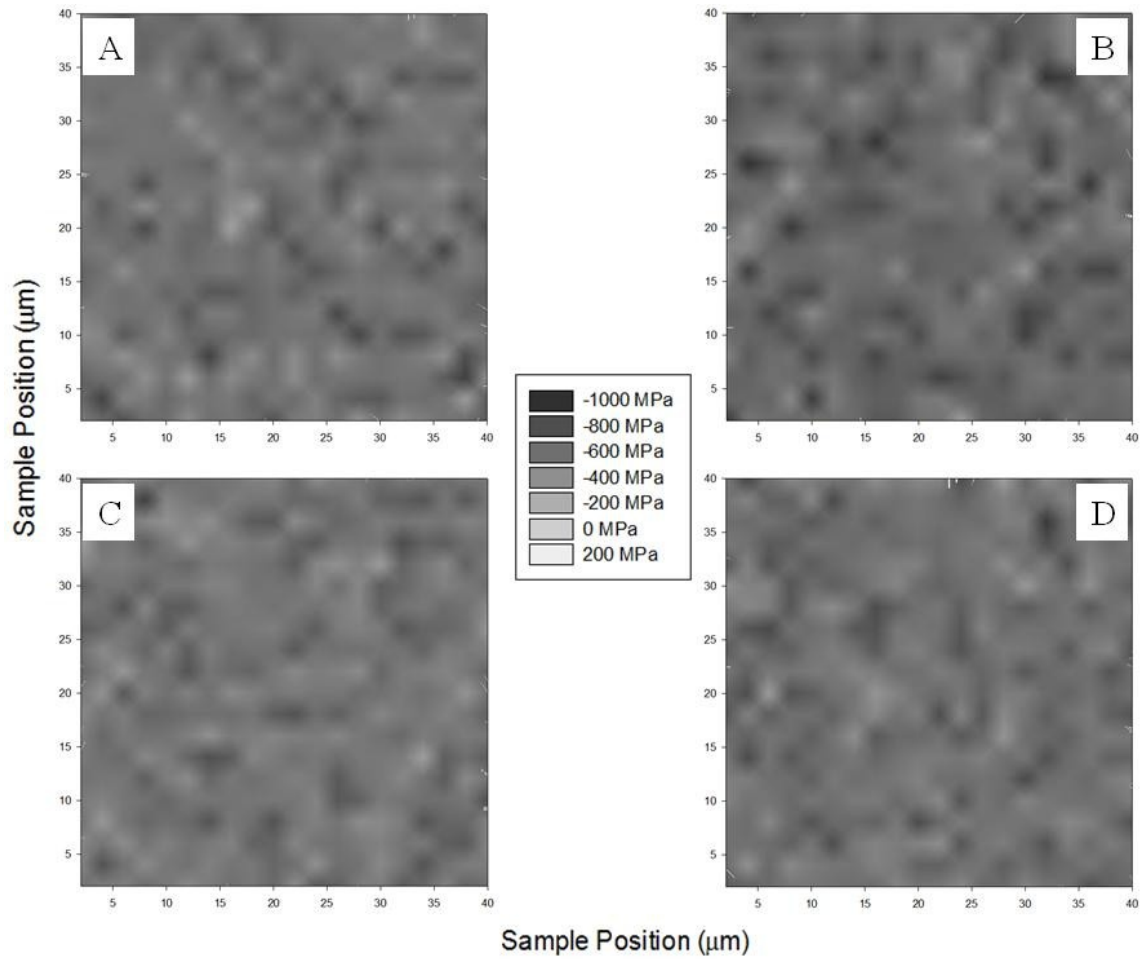


Figure A1.7: Stress maps of the mirror polish surface finish obtained using the confocal scan setting.

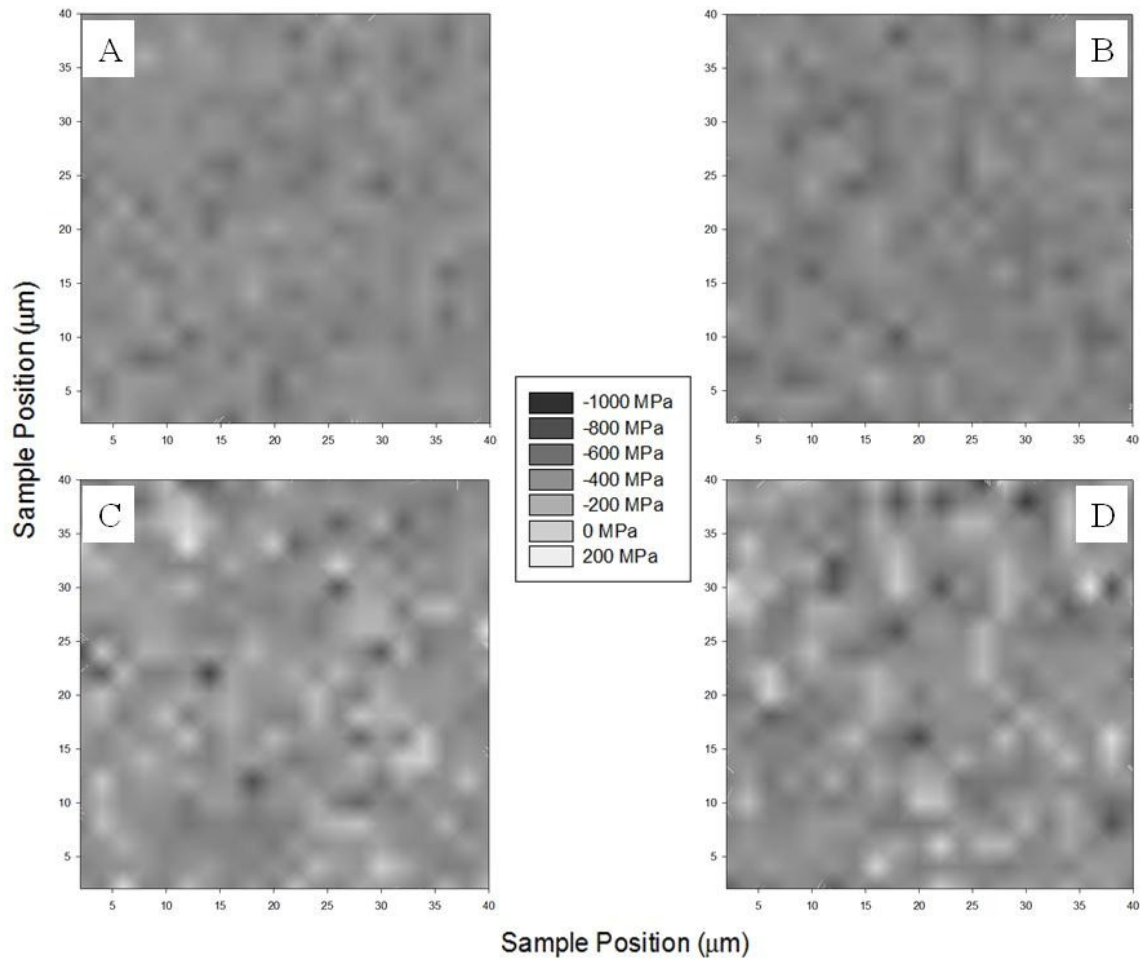


Figure A1.8: Stress maps of the mirror polish surface finish obtained using the regular scan setting.



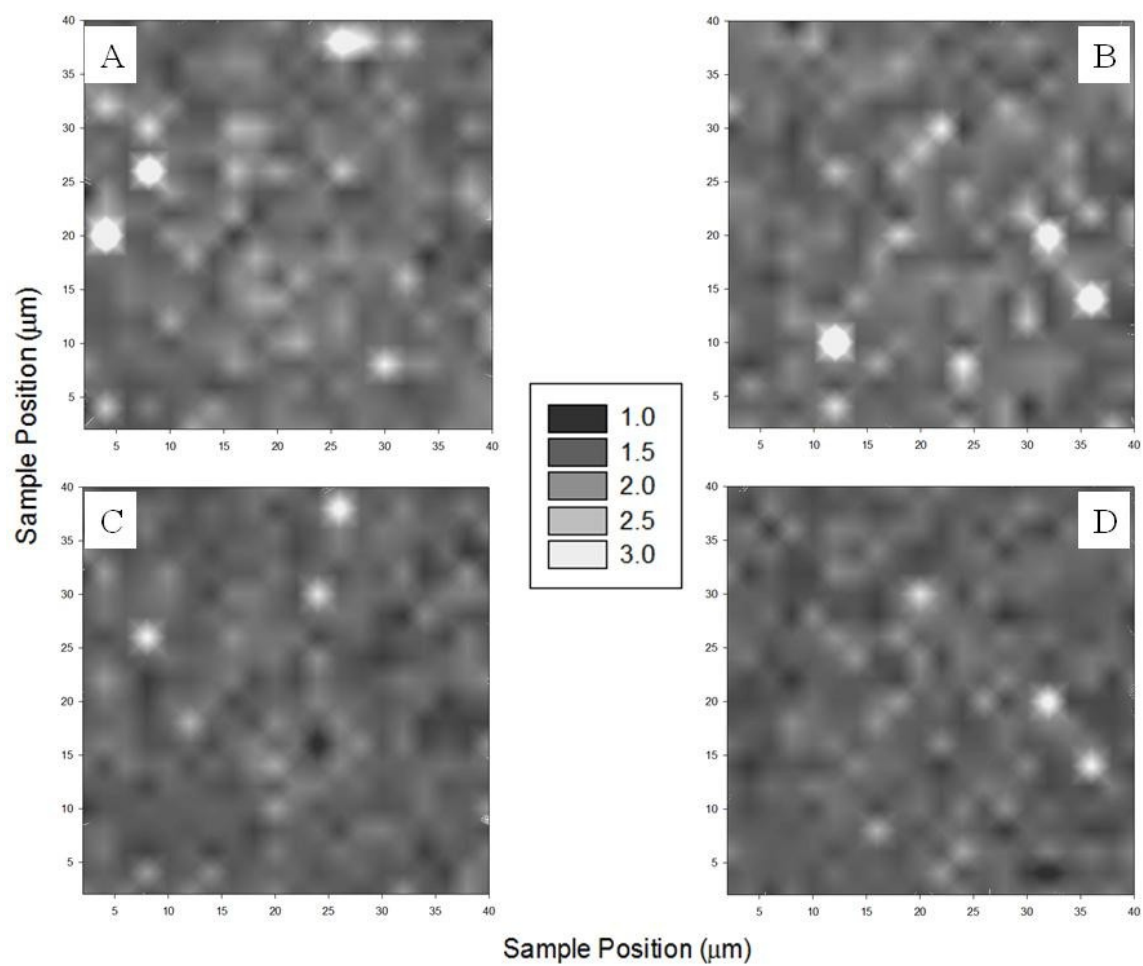


Figure A1.9: Relative width maps of the standard surface finish obtained using the confocal scan setting.

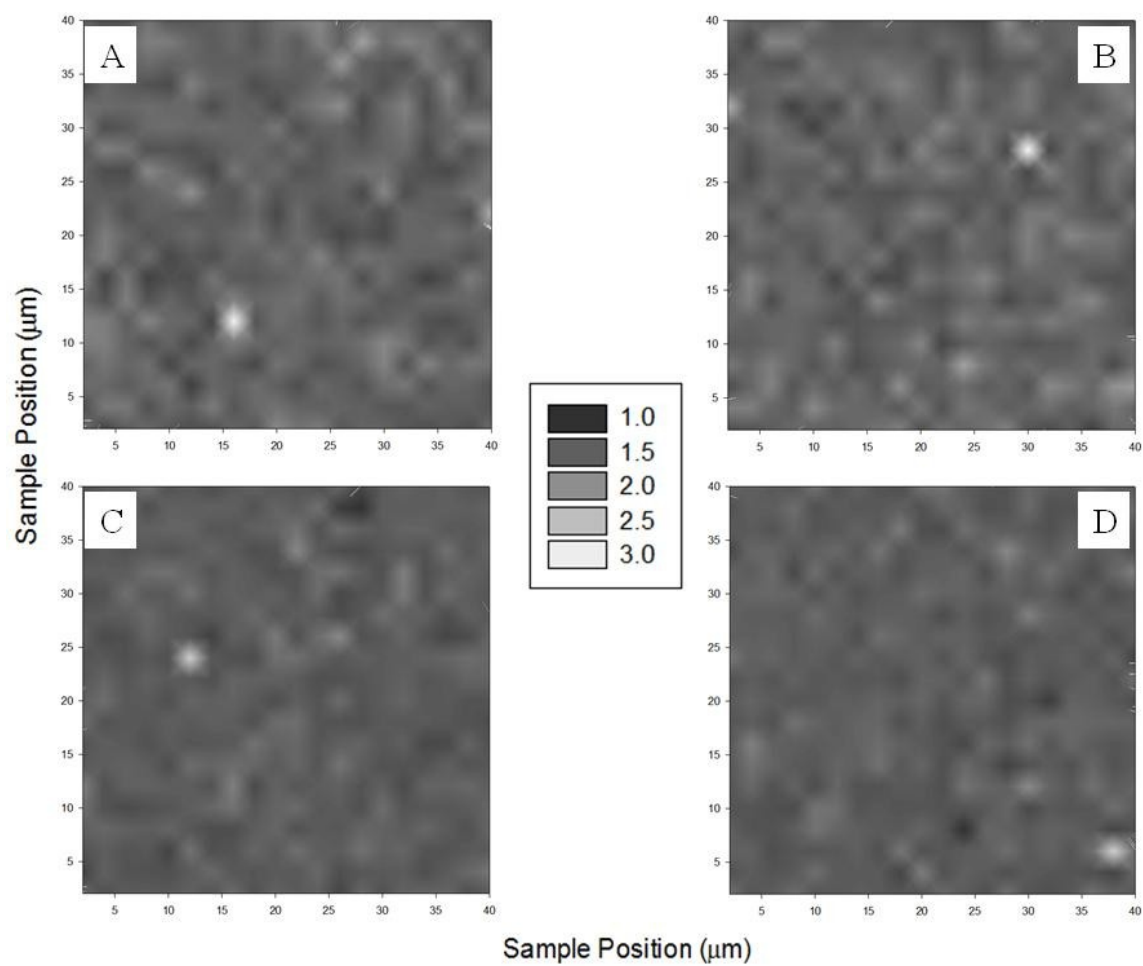


Figure A1.10: Relative width maps of the standard surface finish obtained using the regular scan setting.

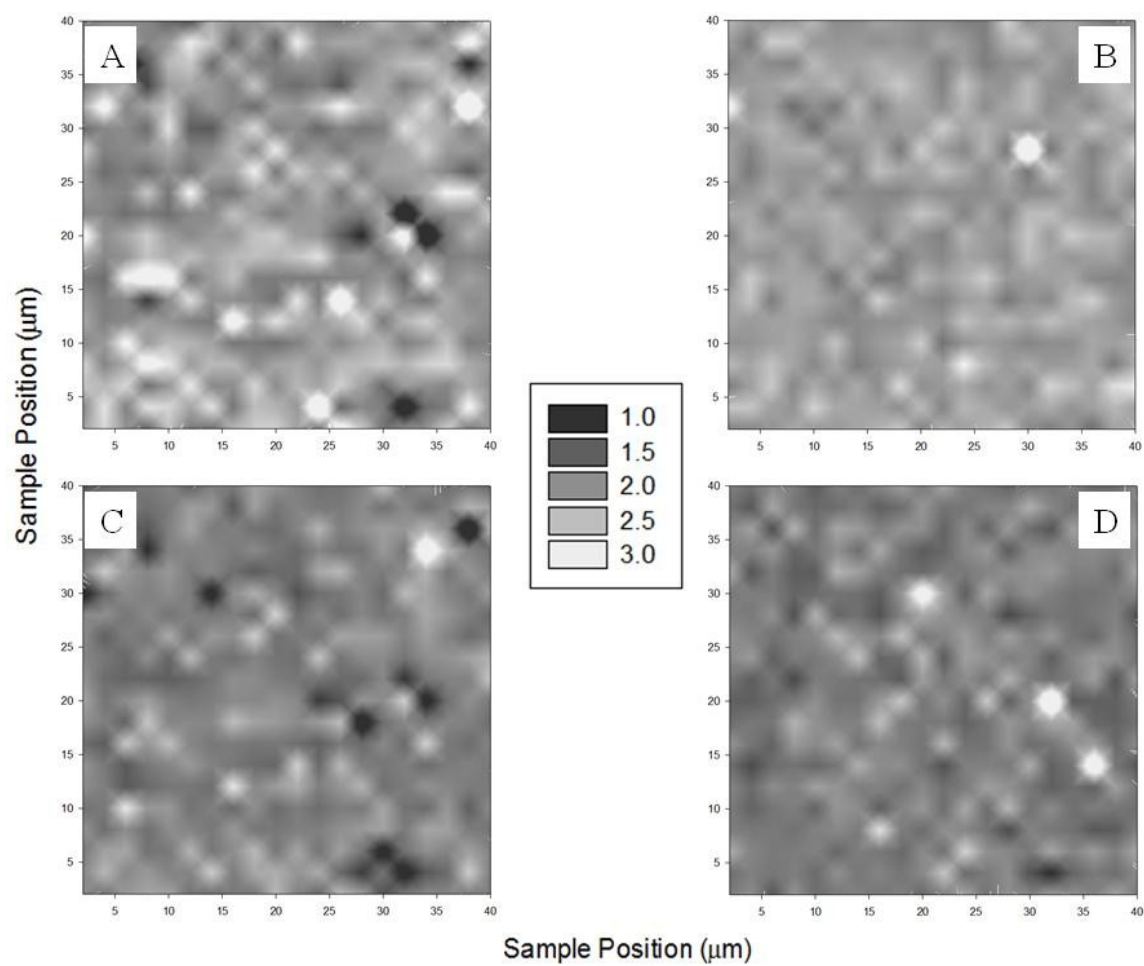


Figure A1.11: Relative width maps of the grit blast surface finish obtained using the confocal scan setting.

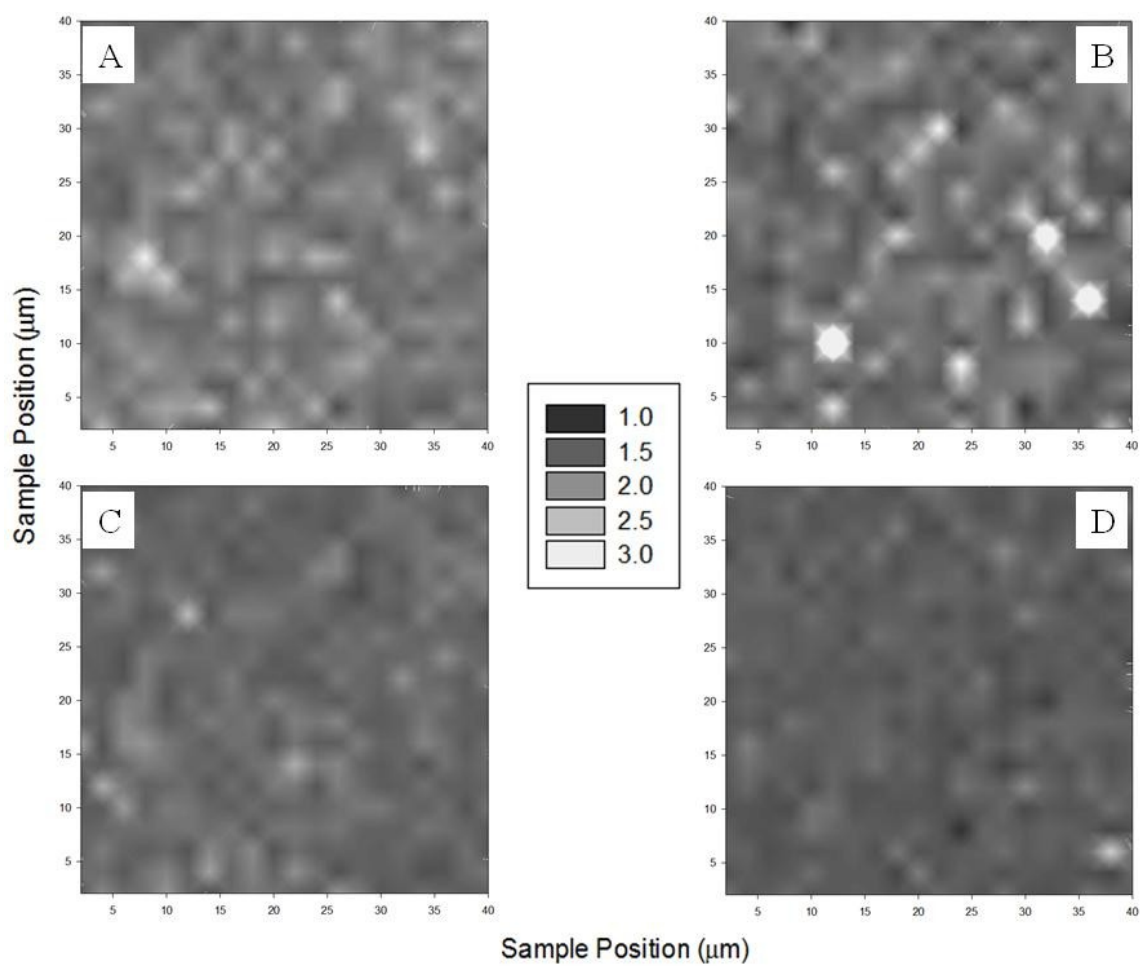


Figure A1.12: Relative width maps of the grit blast surface finish obtained using the regular scan setting.

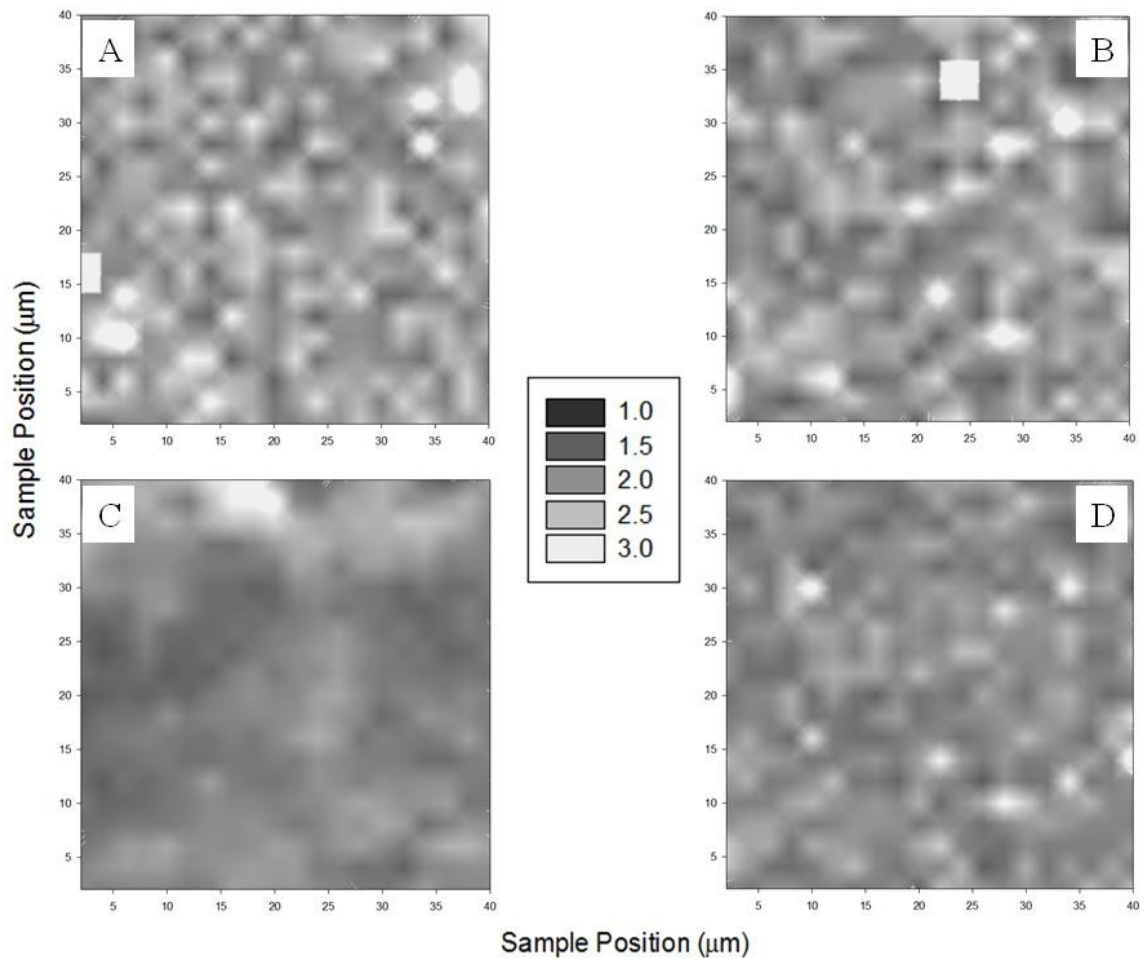


Figure A1.13: Relative width maps of the rotary ground surface finish obtained using the confocal scan setting.

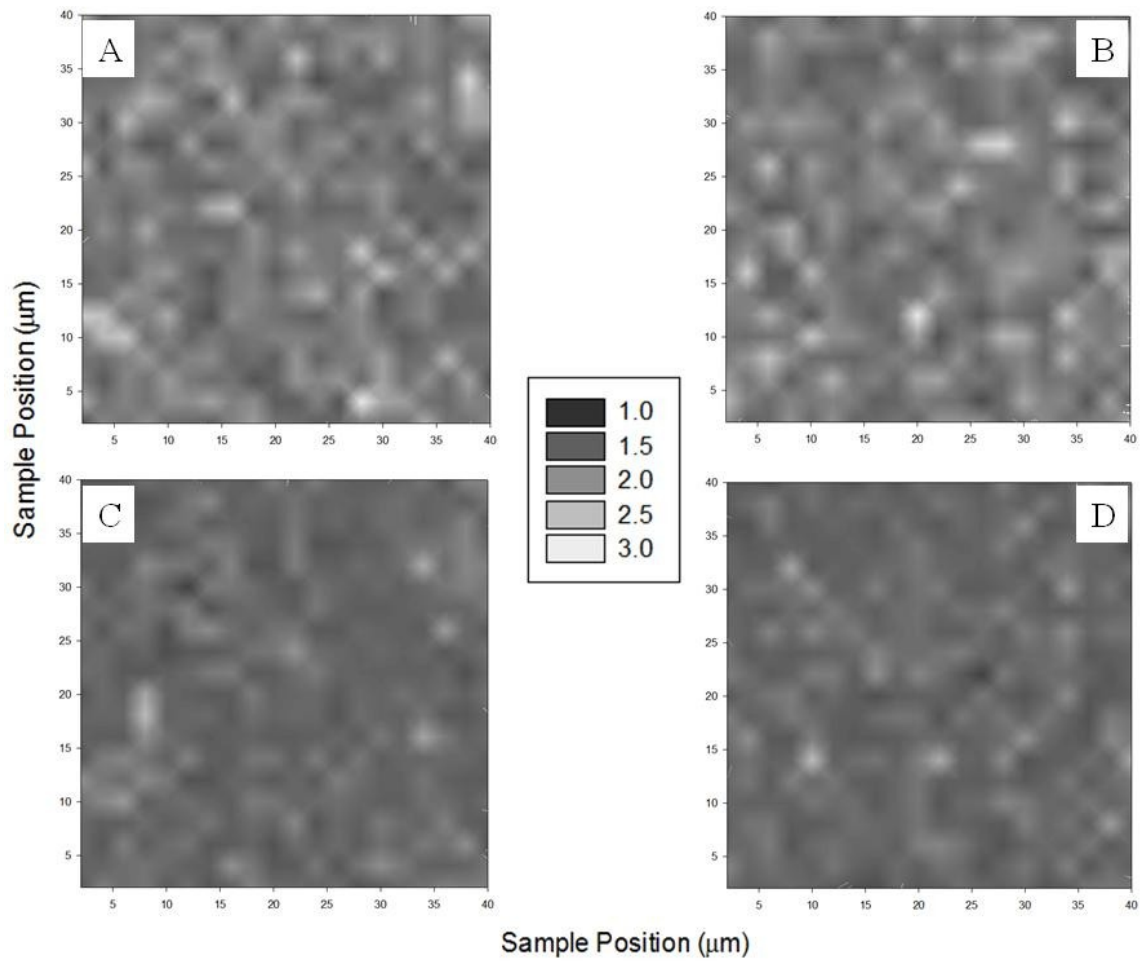


Figure A1.14: Relative width maps of the rotary ground surface finish obtained using the regular scan setting.

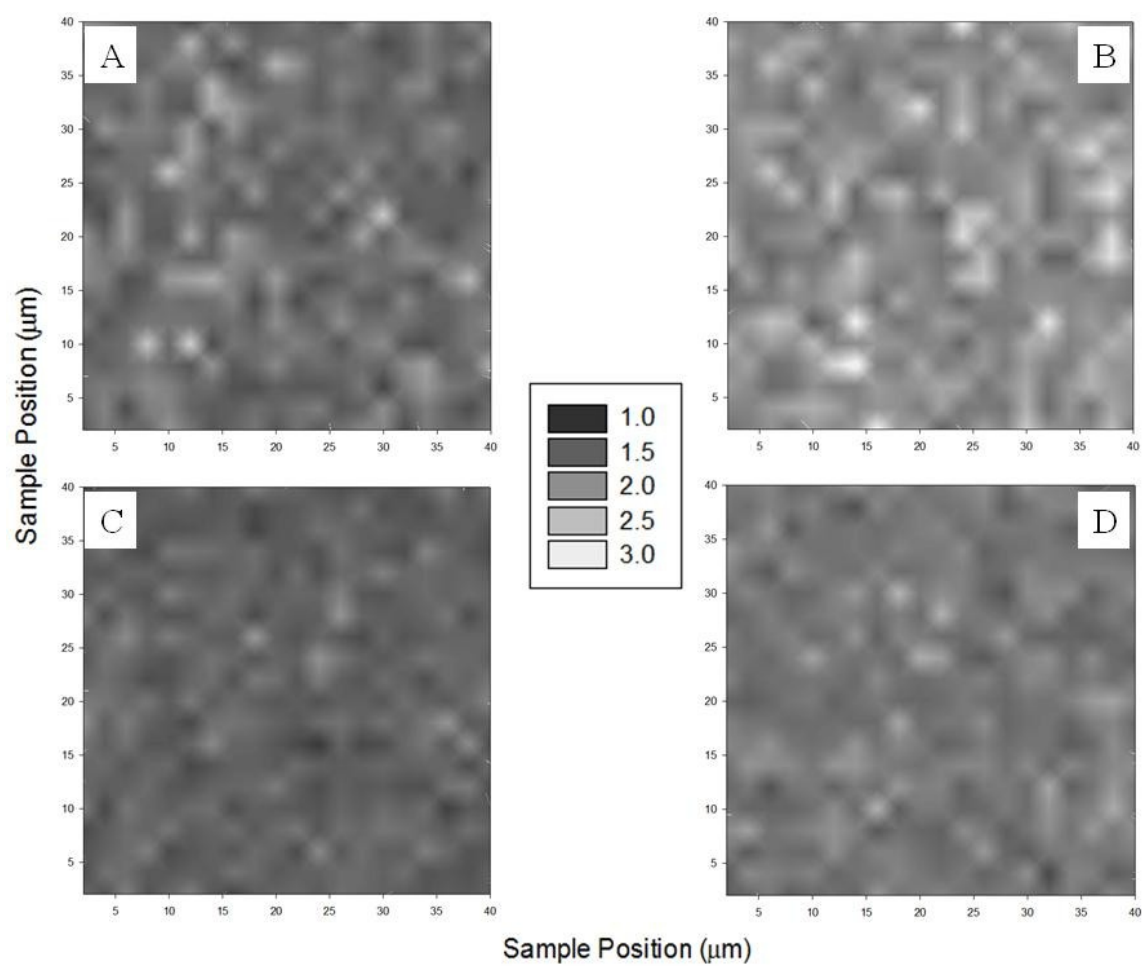


Figure A1.15: Relative width maps of the mirror polish surface finish obtained using the regular scan setting.

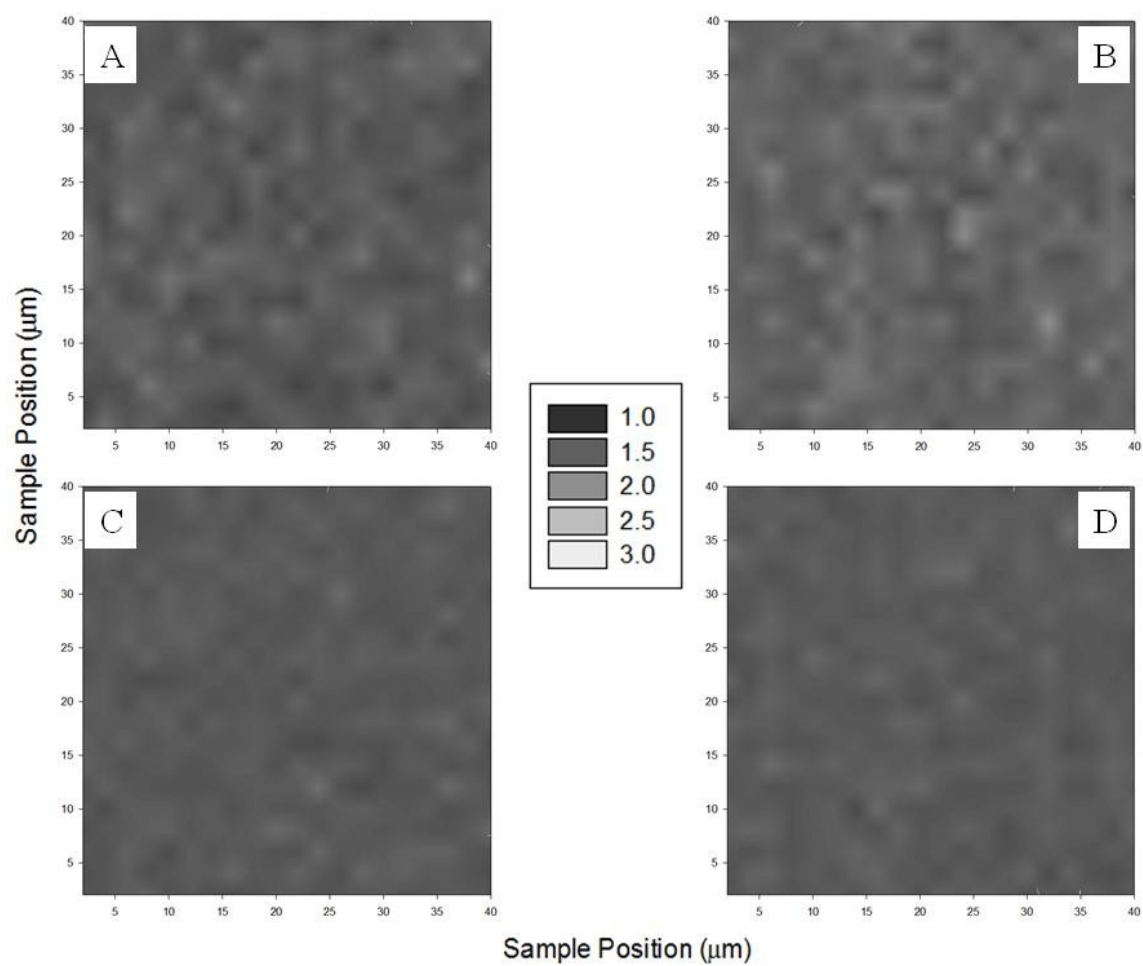


Figure A1.16: Relative width maps of the mirror polish surface finish obtained using the regular scan setting.



## Appendix 2 – Mechanical Properties Maps

Given in this appendix are the mechanical property maps obtained from indentation at both 10mN and 30mN loads for all samples. Figures are split into groups of four for each sample with: a) Elastic Modulus, b) Hardness, c) Work of indentation, and d)  $E^2/H$ . Machining finish and indentation load are listed in the caption for each figure.

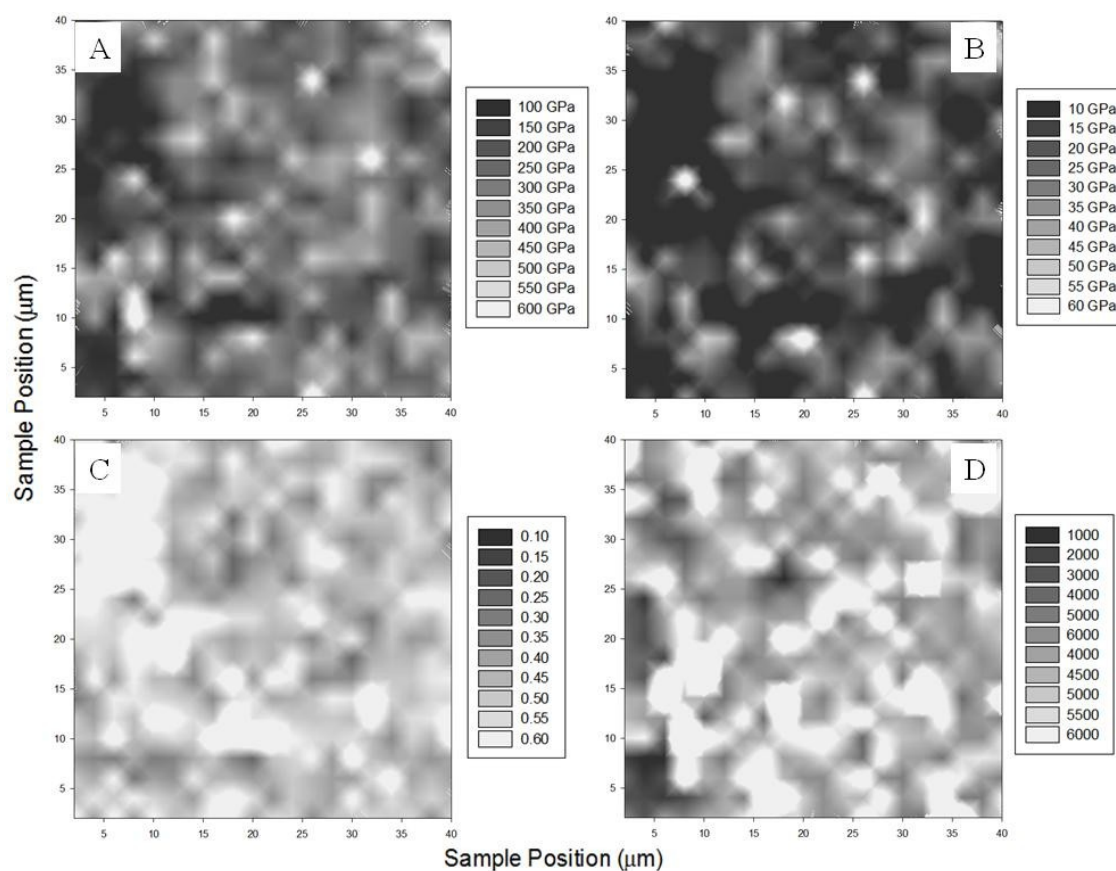


Figure A2.1: Indentation data for the standard surface finish sample at 10mN.

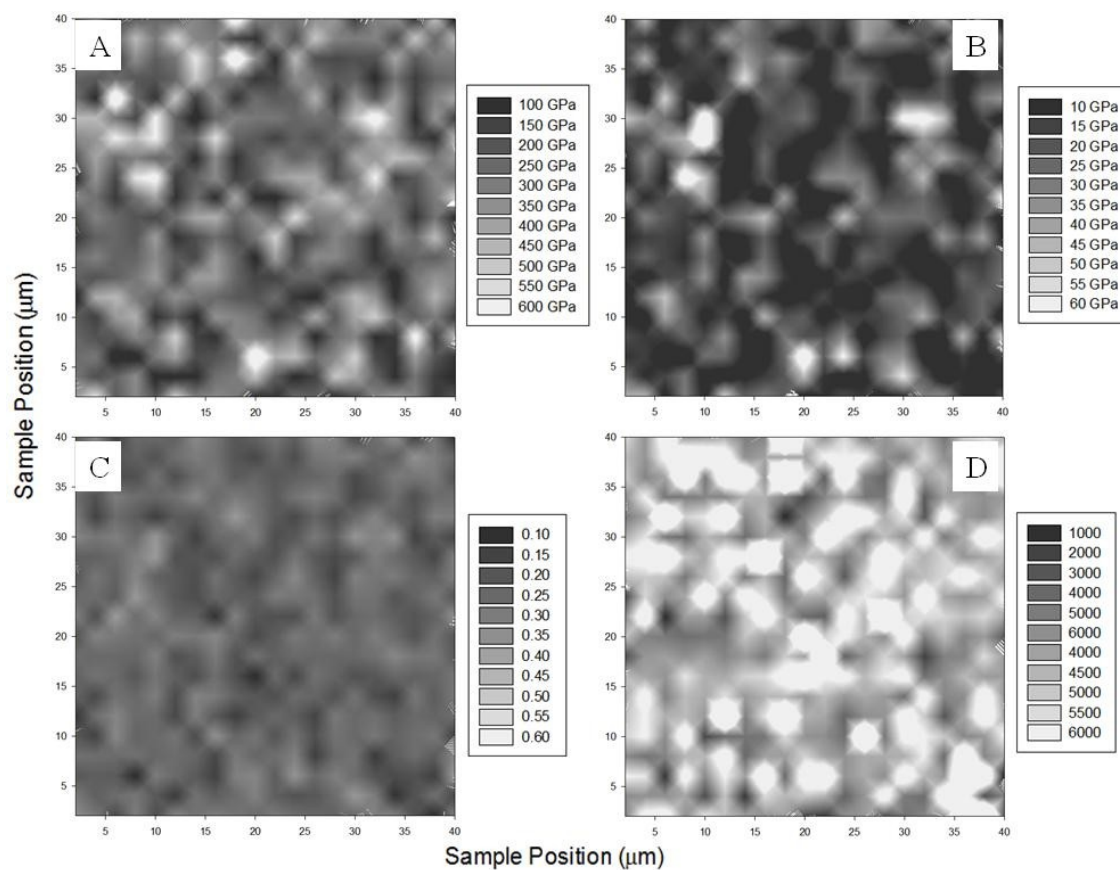


Figure A2.2: Indentation data for the standard surface finish sample at 30mN.

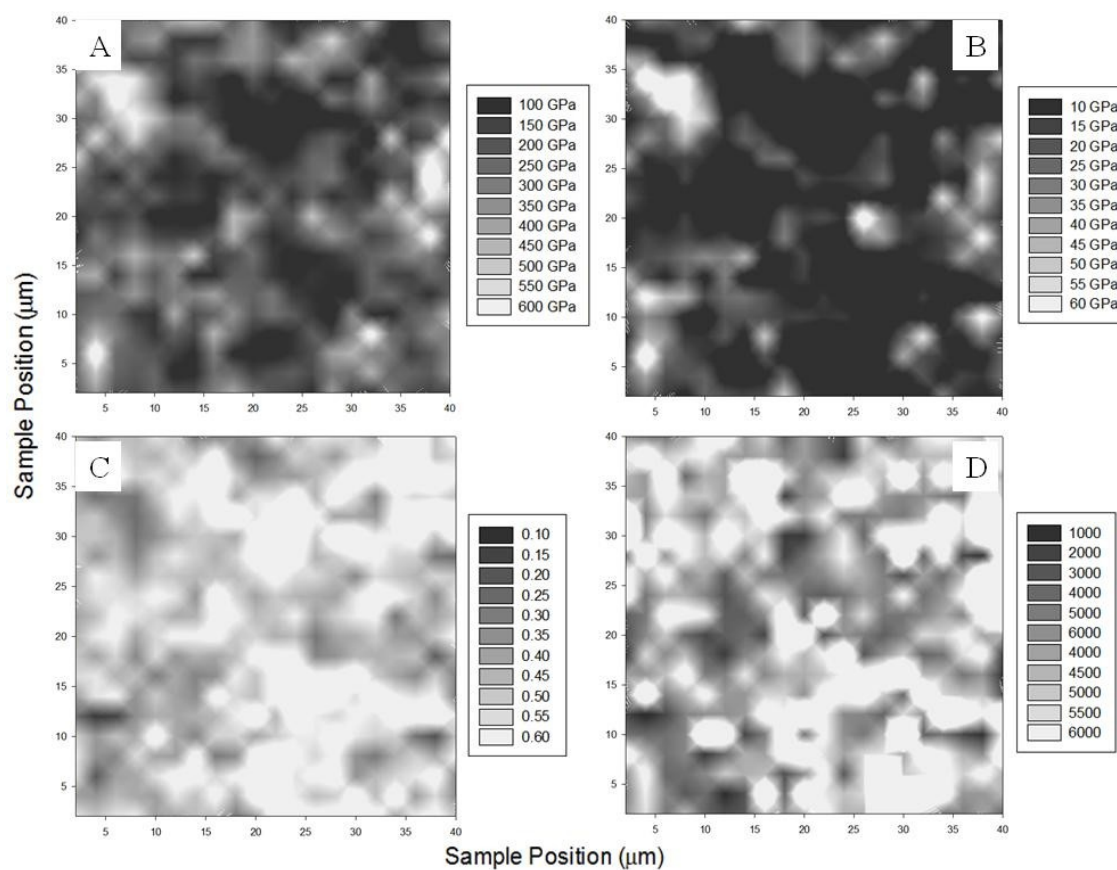


Figure A2.3: Indentation data for the grit blast surface finish sample at 10mN.

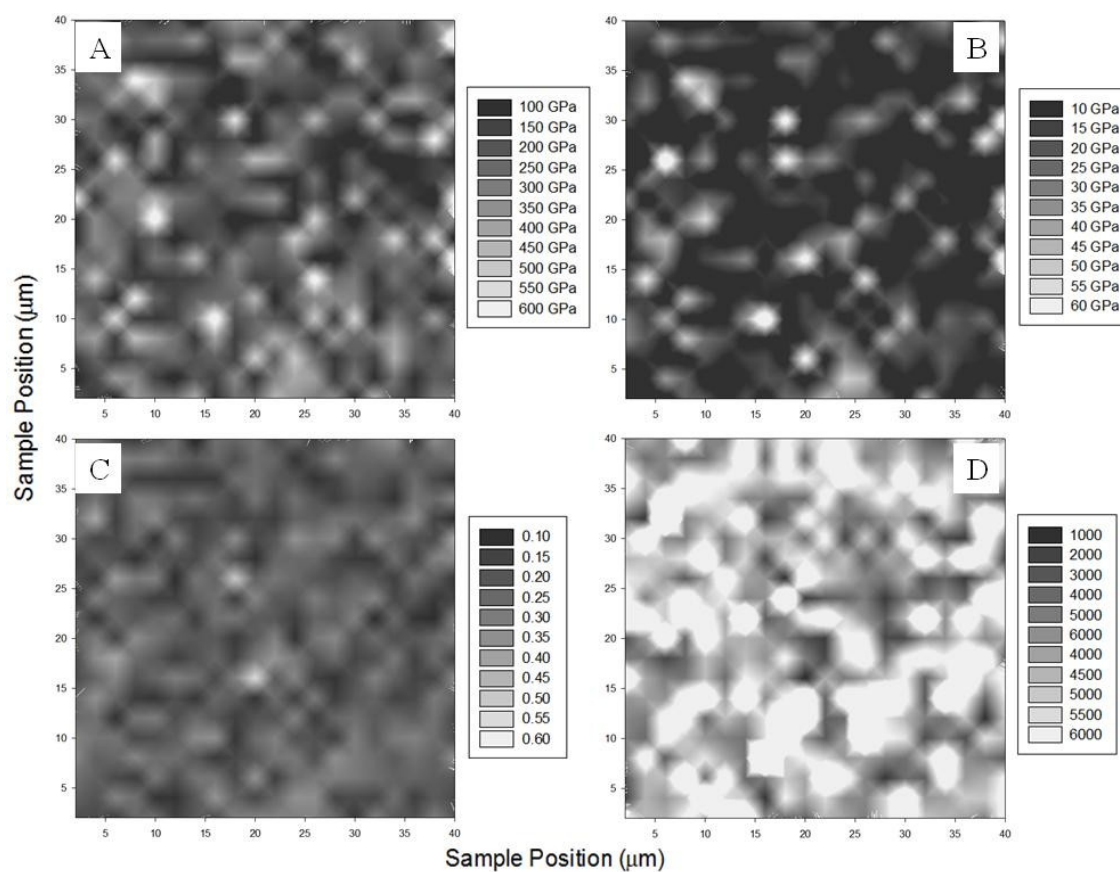


Figure A2.4: Indentation data for the grit blast surface finish sample at 30mN.

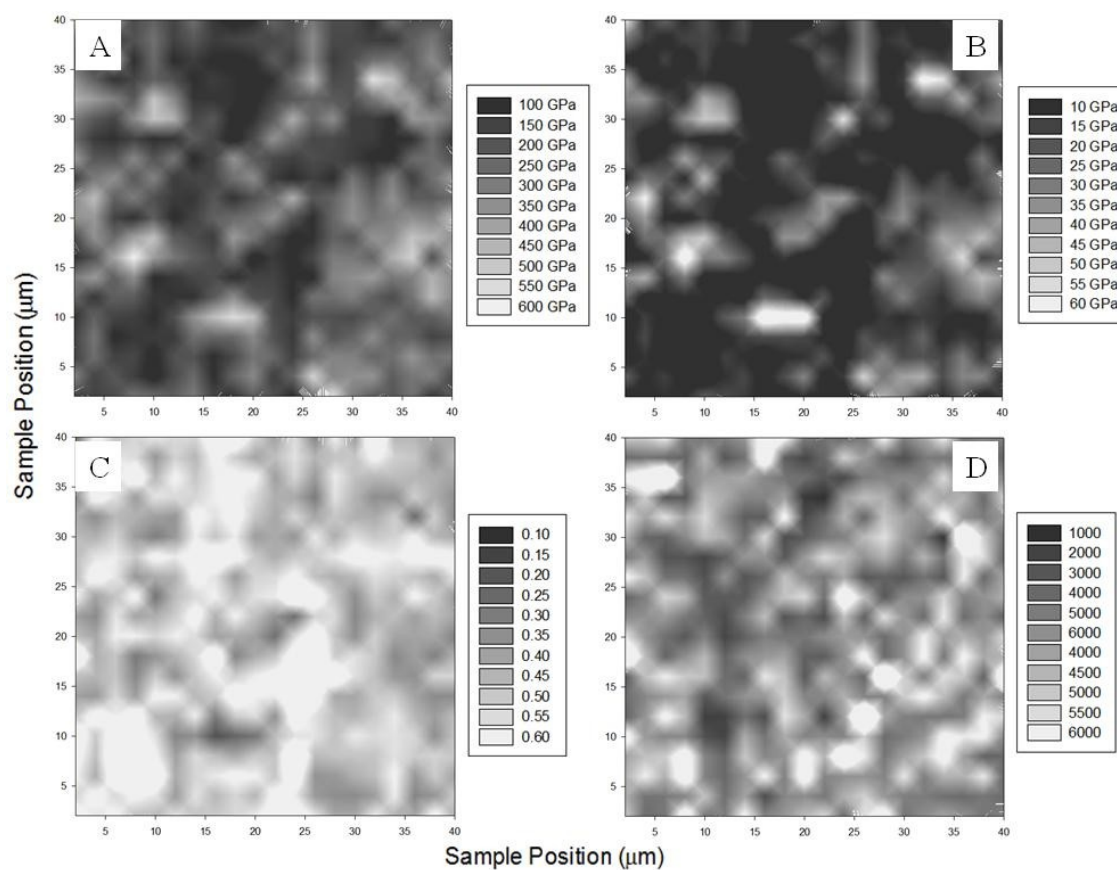


Figure A2.5: Indentation data for the rotary ground finish sample at 10mN.

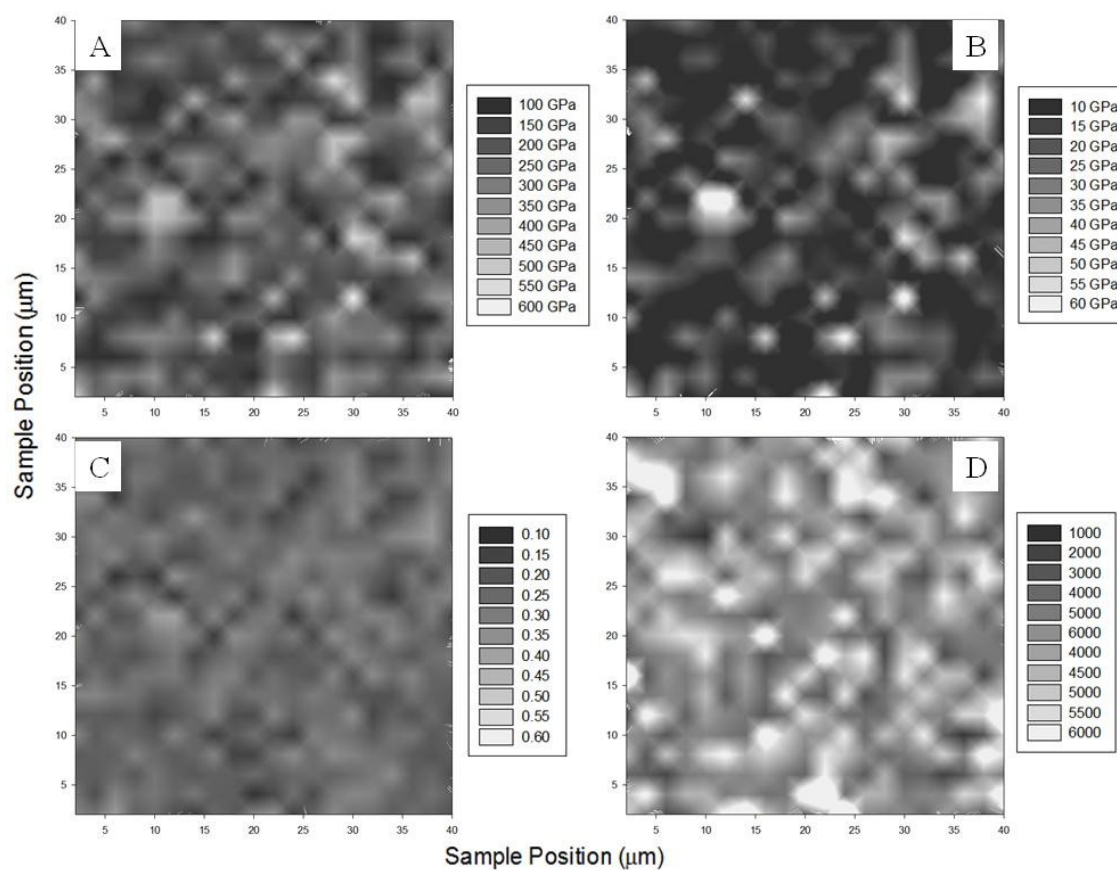


Figure A2.6: Indentation data for the rotary ground finish sample at 30mN.

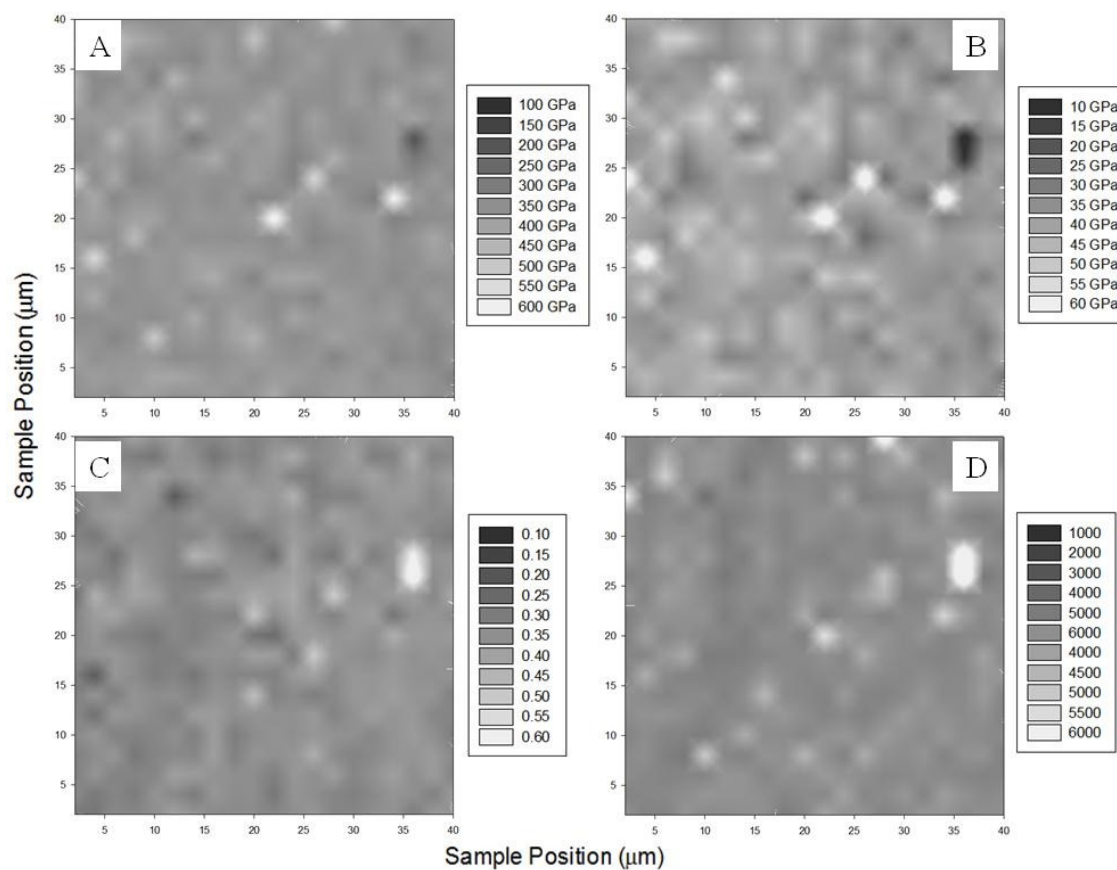


Figure A2.7: Indentation data for mirror polish surface finish sample at 10mN.



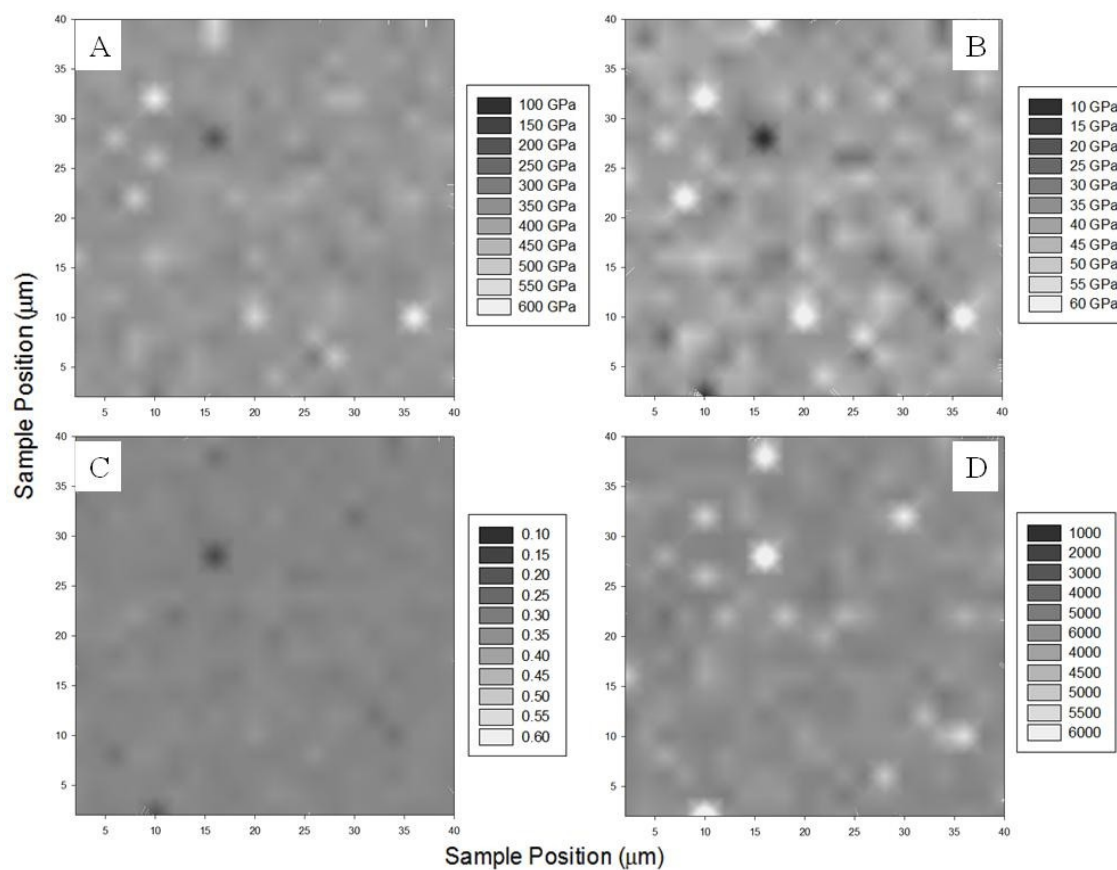


Figure A2.8: Indentation data for the mirror polish surface finish sample at 30mN.



### Appendix 3 – Additional Raman Spectra

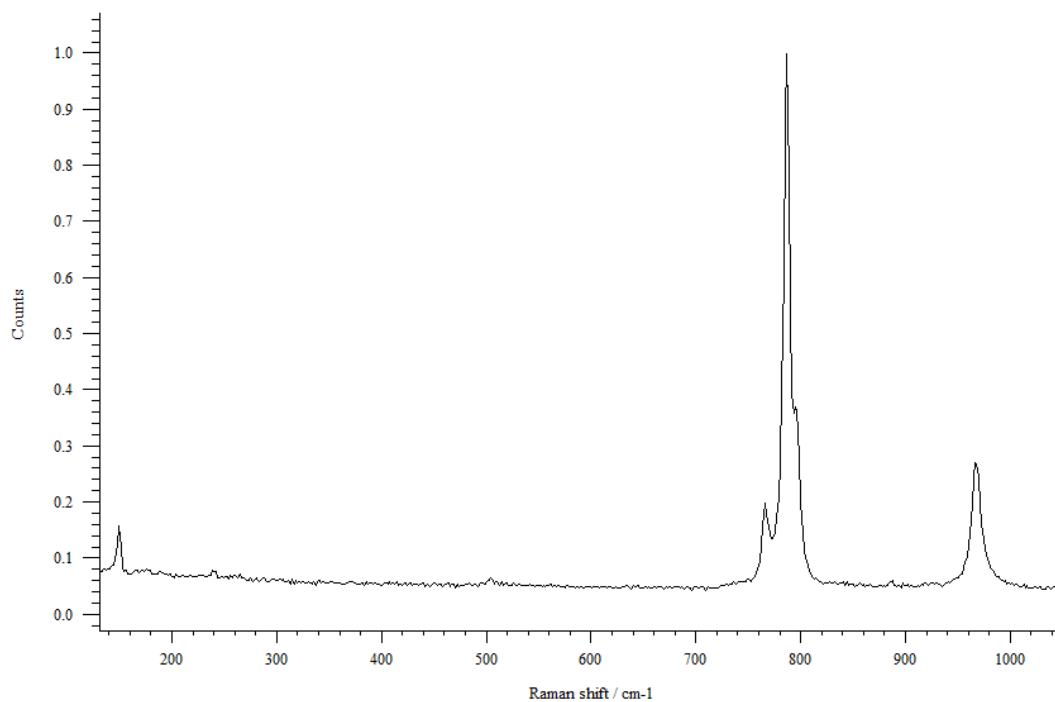


Figure A3.1: Typical Raman spectra for standard finish 514nm confocal setting.

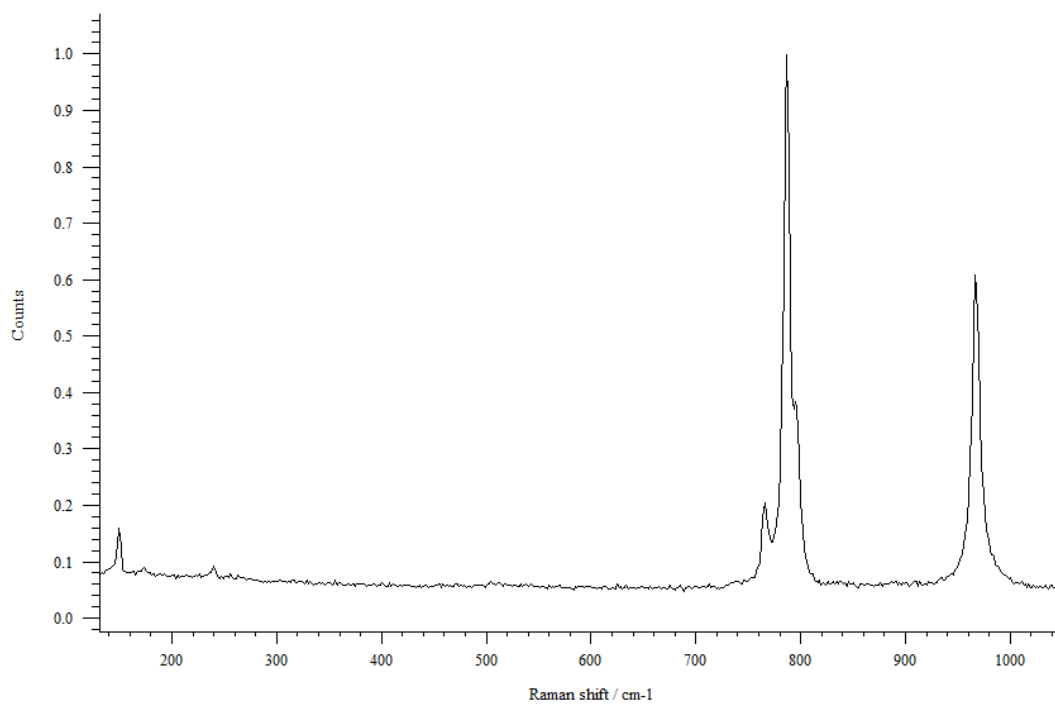


Figure A3.2: Typical Raman spectra for standard finish 633nm confocal setting.

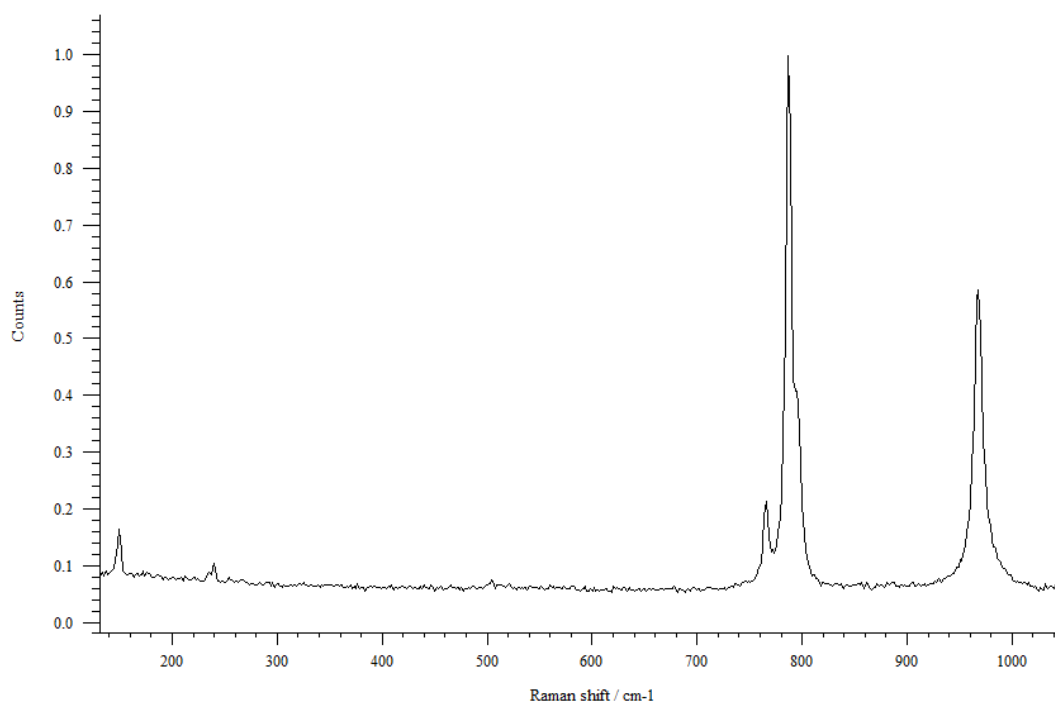


Figure A3.3: Typical Raman spectra for standard finish 514nm regular setting.

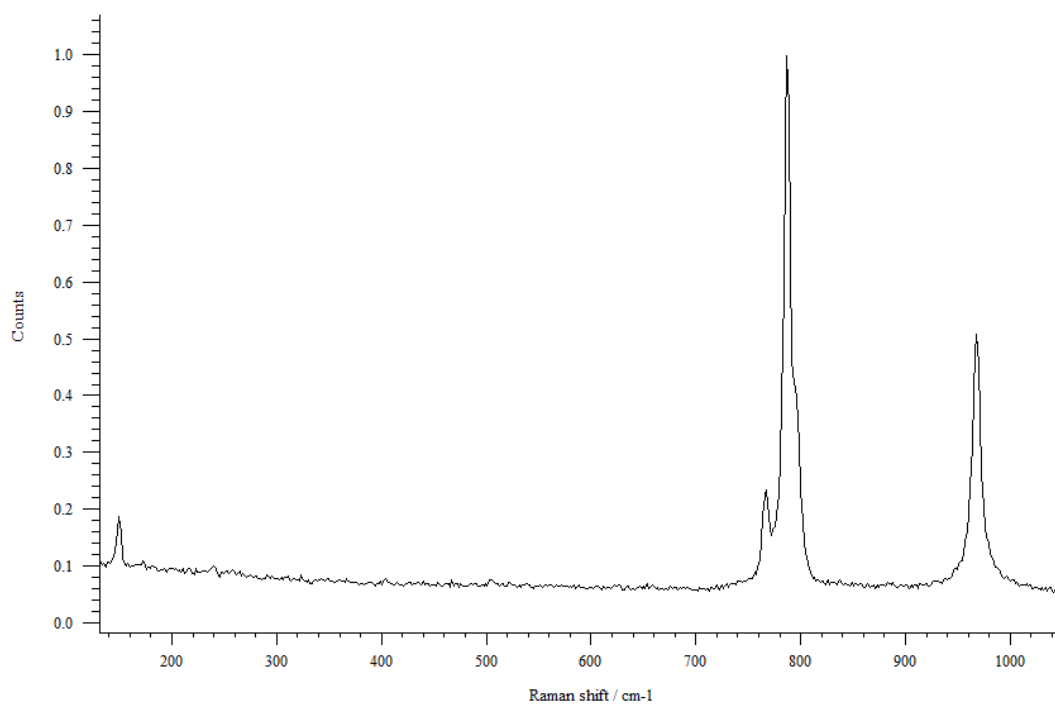


Figure A3.4: Typical Raman spectra for standard finish 633nm regular setting.

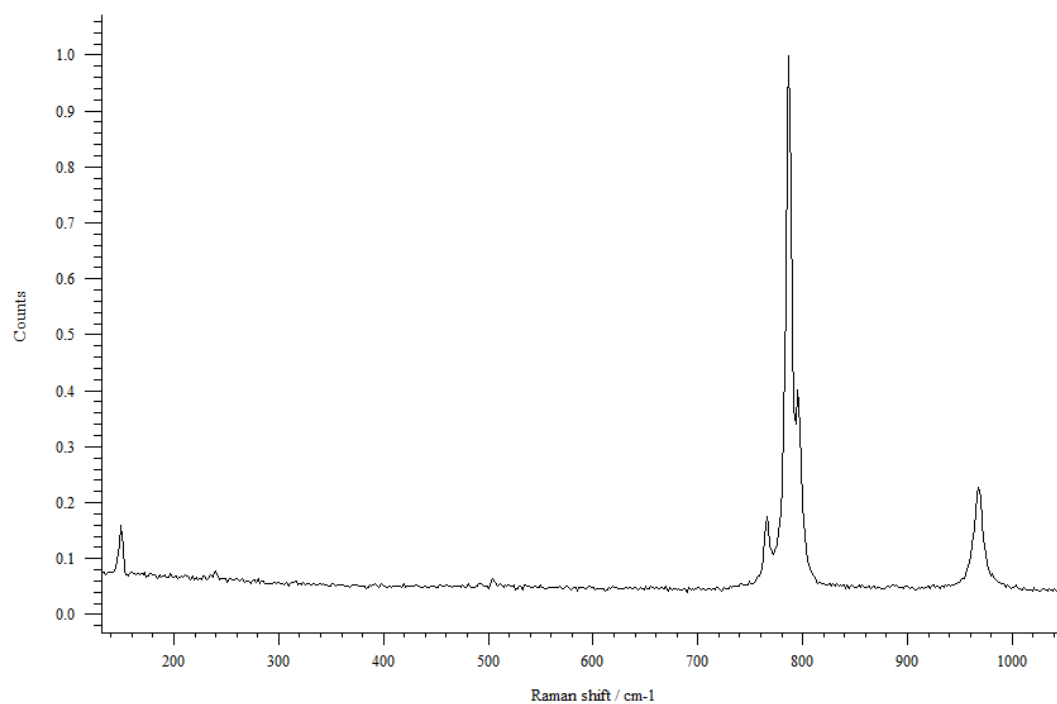


Figure A3.5: Typical Raman spectra for grit blast finish 514nm confocal setting.

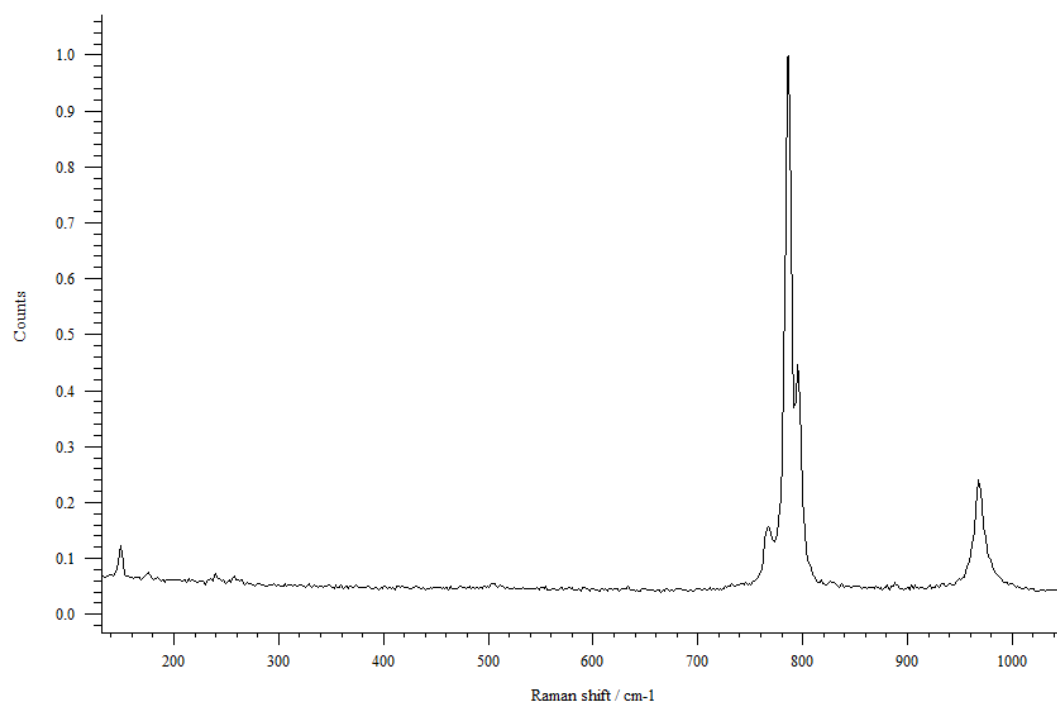


Figure A3.6: Typical Raman spectra for grit blast finish 633nm confocal setting.

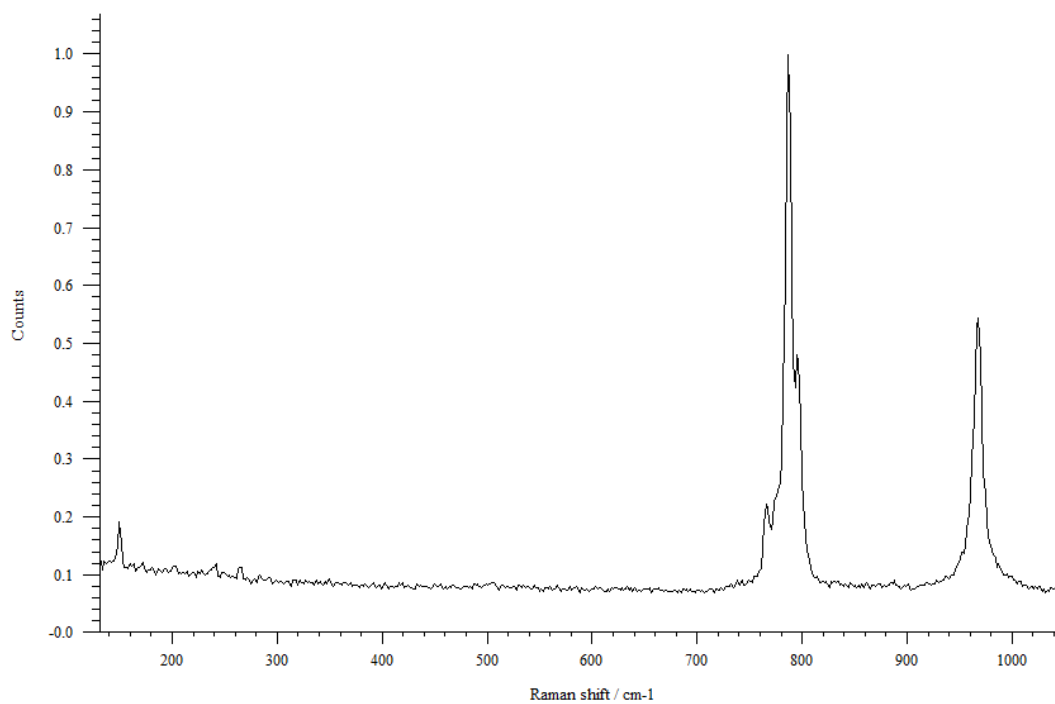


Figure A3.7: Typical Raman spectra for grit blast finish 514nm regular setting.

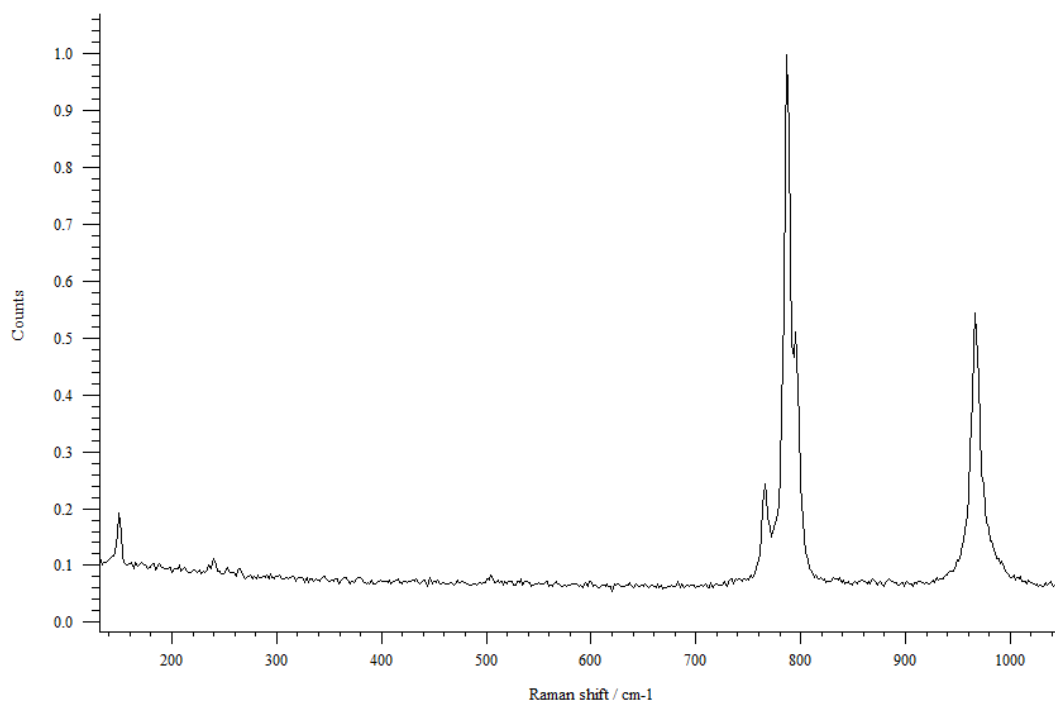


Figure A3.8: Typical Raman spectra for grit blast finish 633nm regular setting.

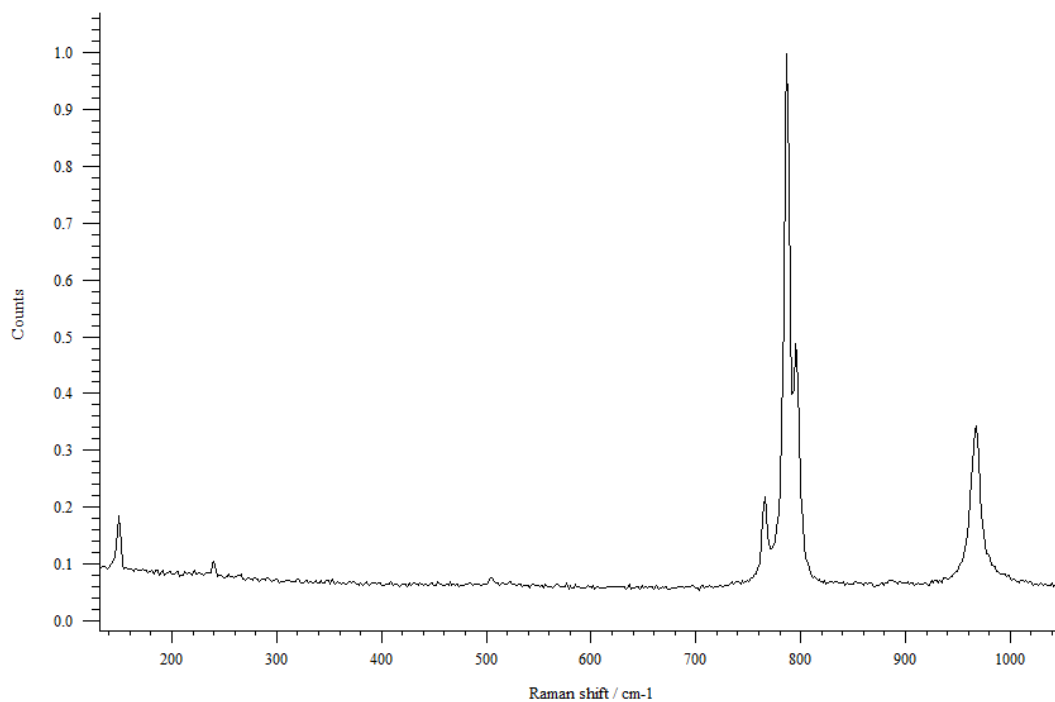


Figure A3.9: Typical Raman spectra for rotary ground finish 514nm confocal setting.

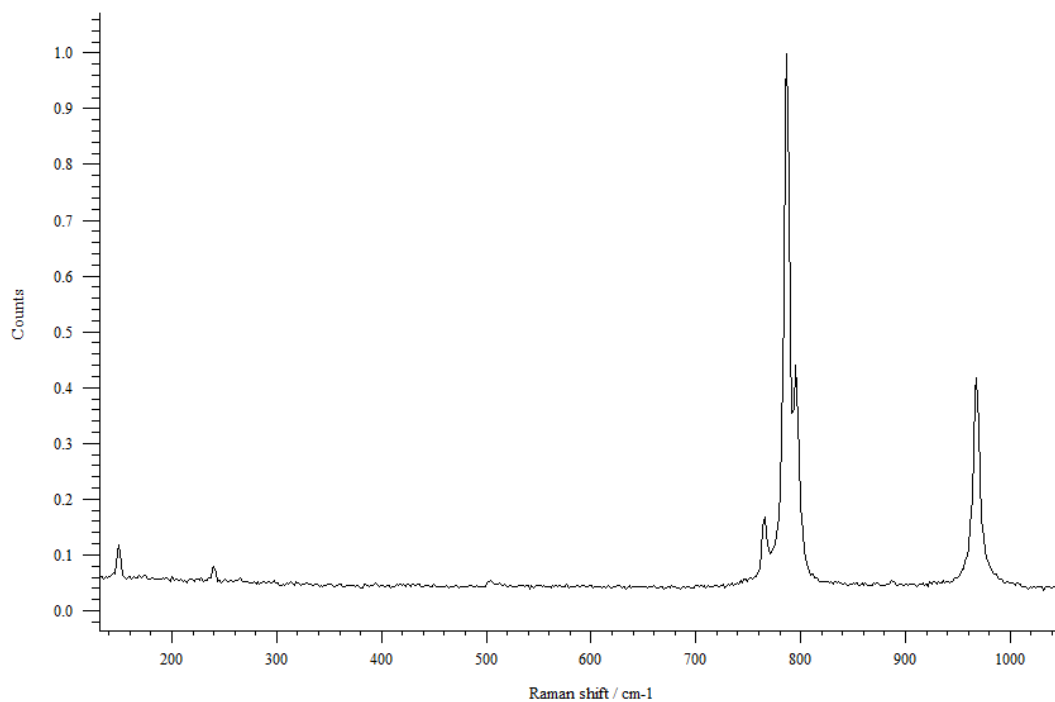


Figure A3.10: Typical Raman spectra for rotary ground finish 633nm confocal setting.

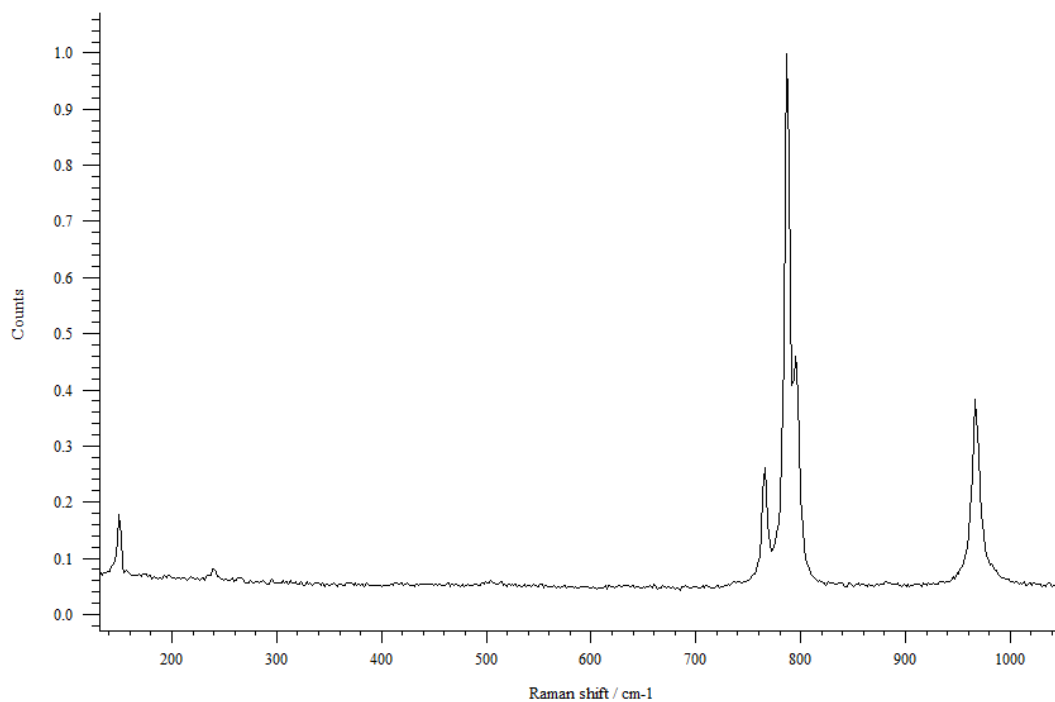


Figure A3.11: Typical Raman spectra for rotary ground finish 514nm regular setting.

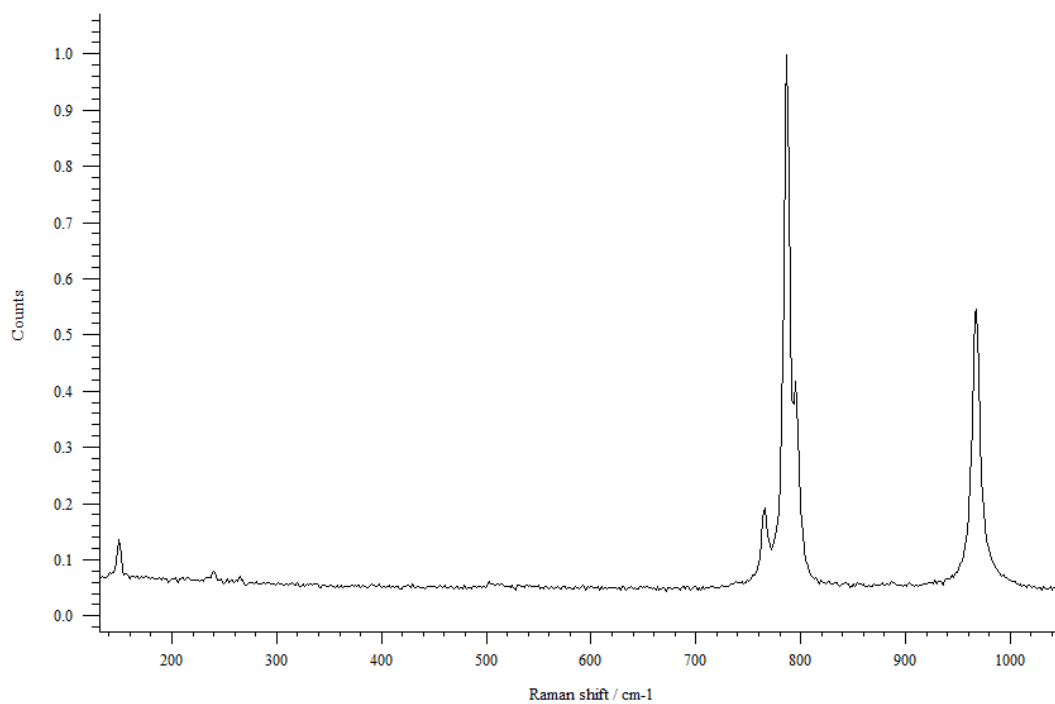


Figure A3.12: Typical Raman spectra for rotary ground finish 633nm regular setting.

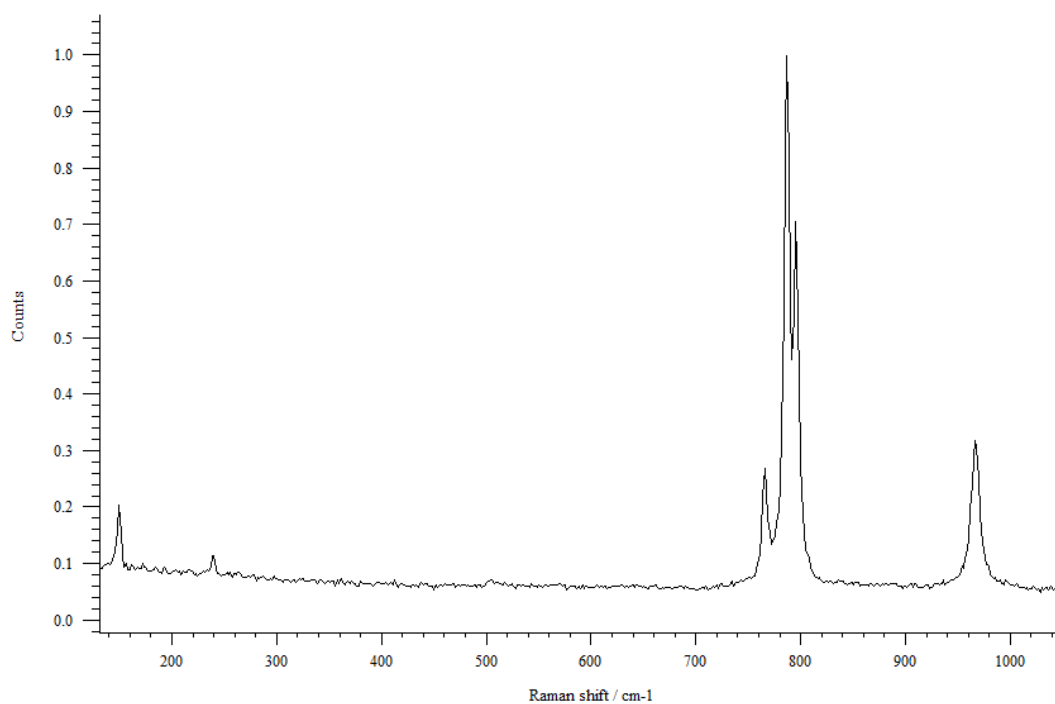


Figure A3.13: Typical Raman spectra for mirror finish 514nm confocal setting.

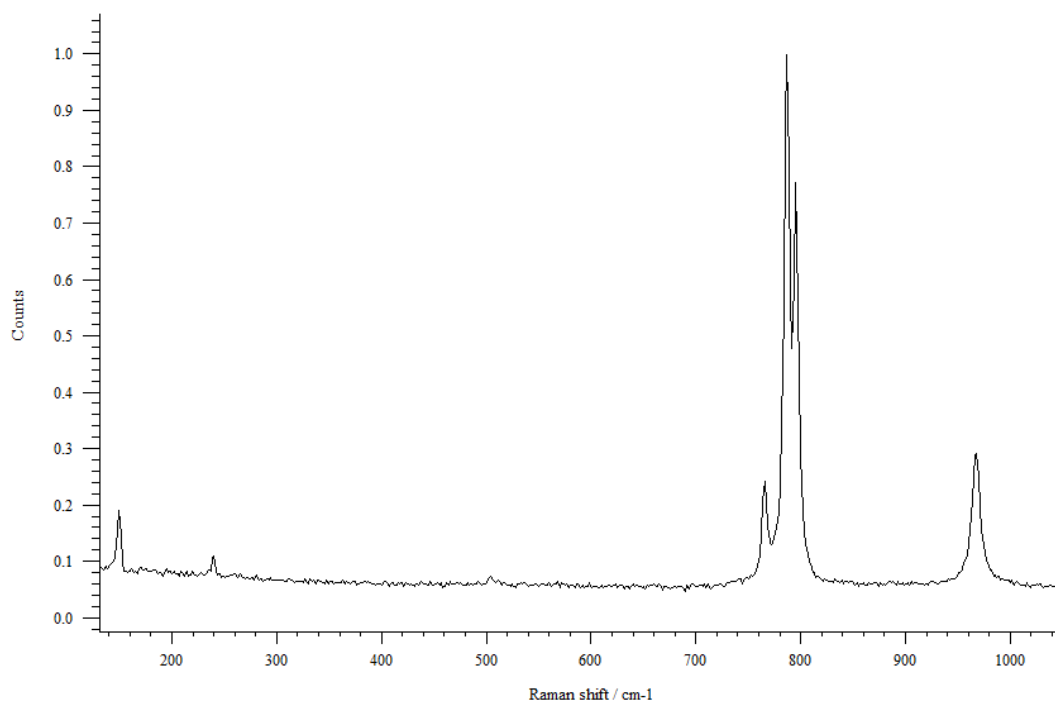


Figure A3.14: Typical Raman spectra for mirror finish 633nm confocal setting.

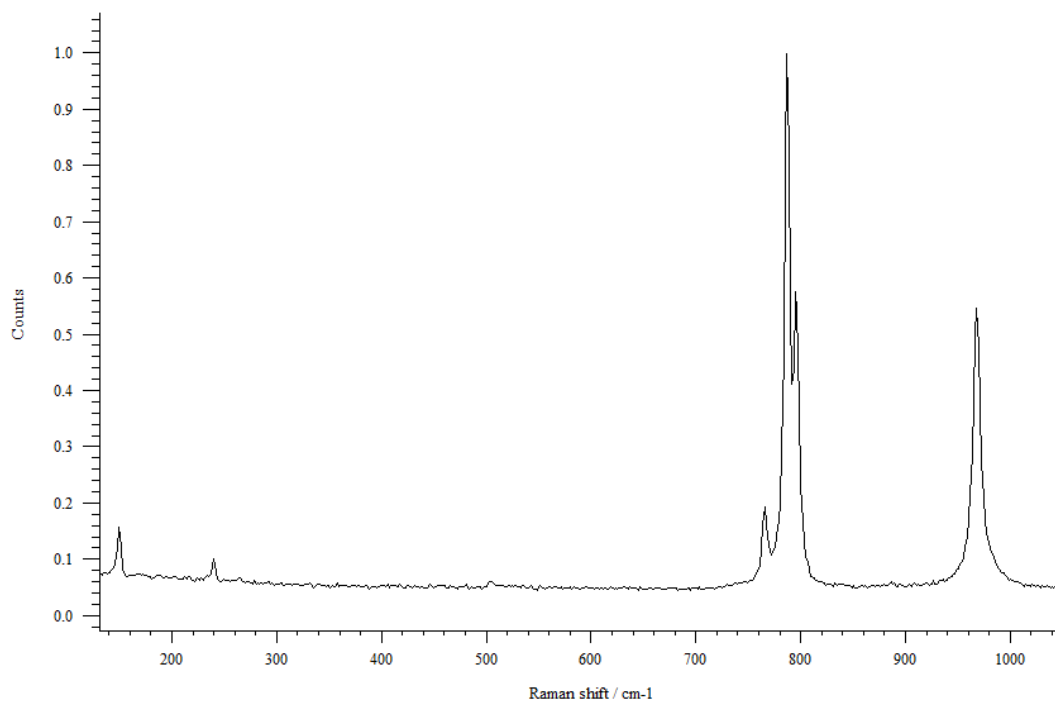


Figure A3.15: Typical Raman spectra for mirror finish 514nm regular setting.

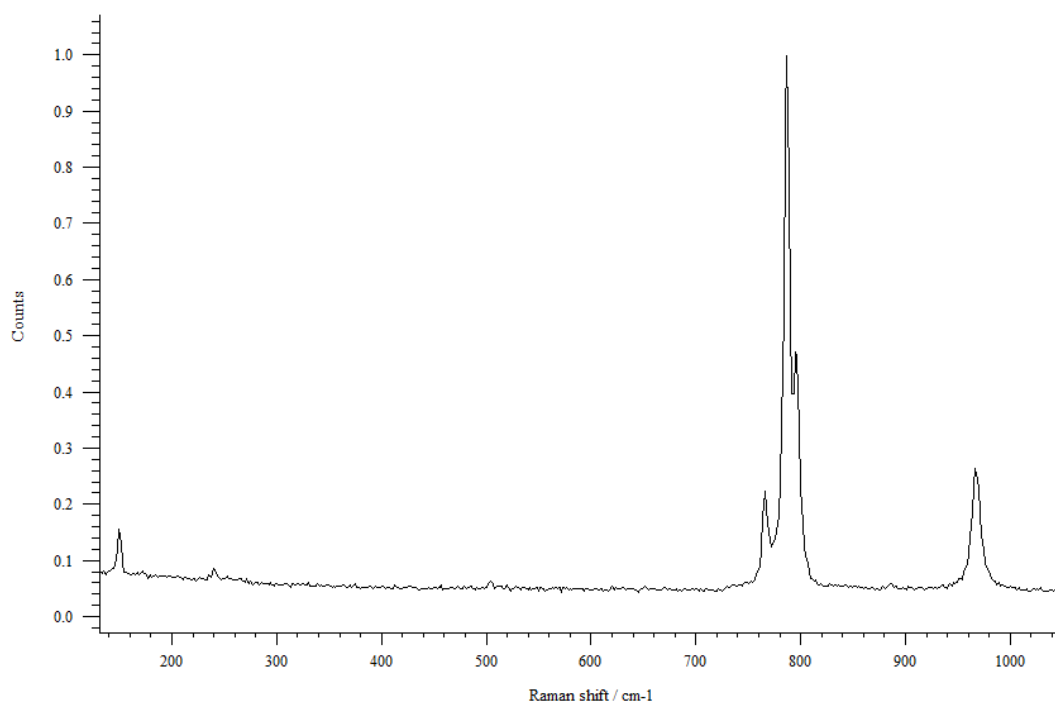


Figure A3.16: Typical Raman spectra for mirror finish 633nm regular setting.



#### Appendix 4 – Additional Load-Depth Curves

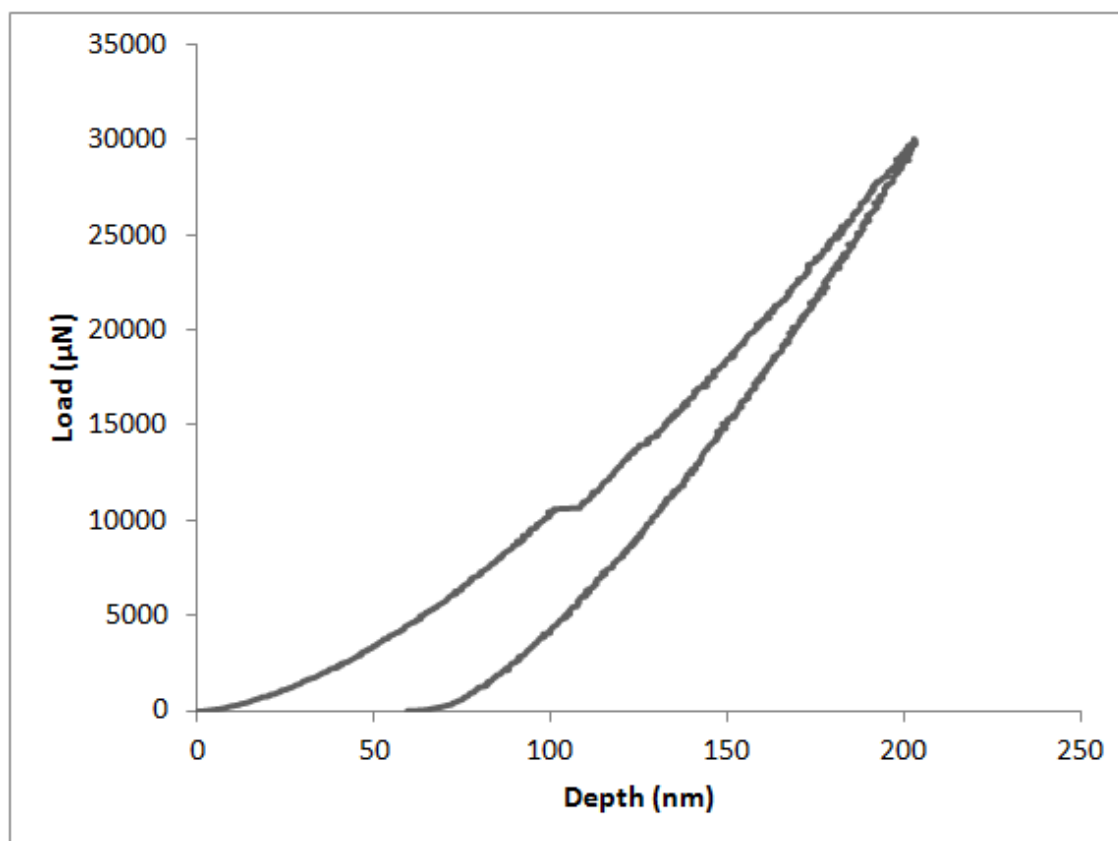


Figure A4.1: Typical Load-Depth curve for single crystal 6H-SiC at a maximum applied load of 30mN.

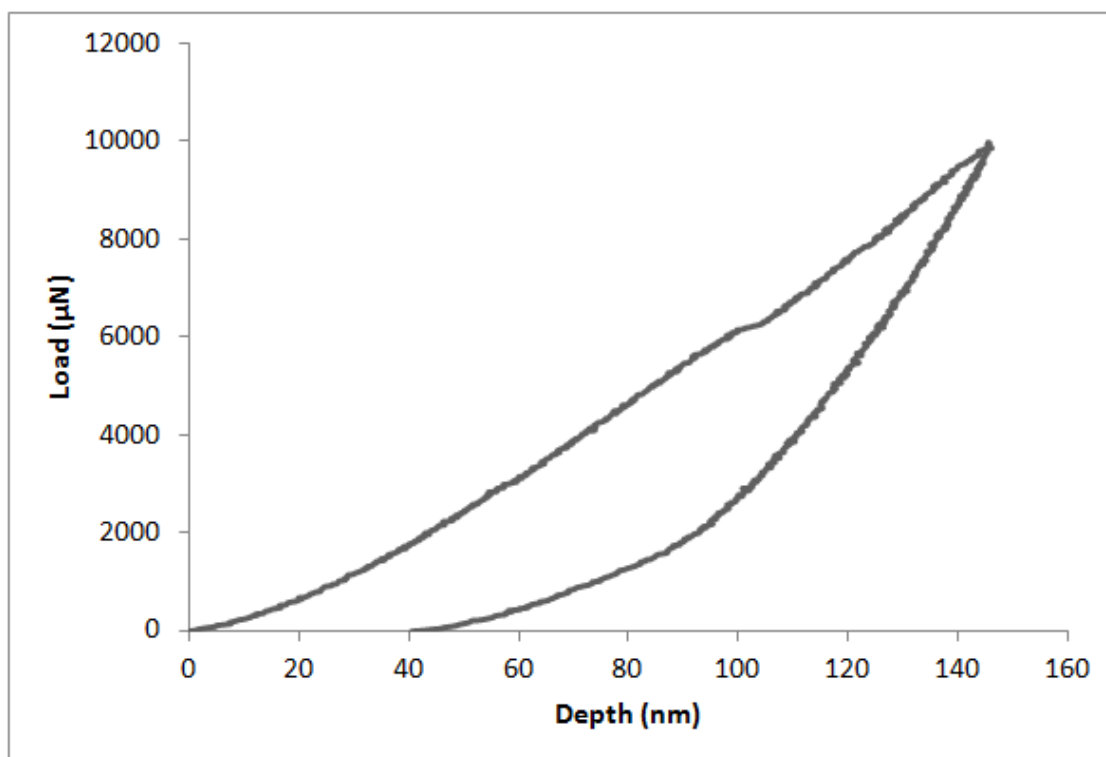


Figure A4.2: Typical Load-Depth curve for standard finish 6H-SiC at a maximum applied load of 10mN.

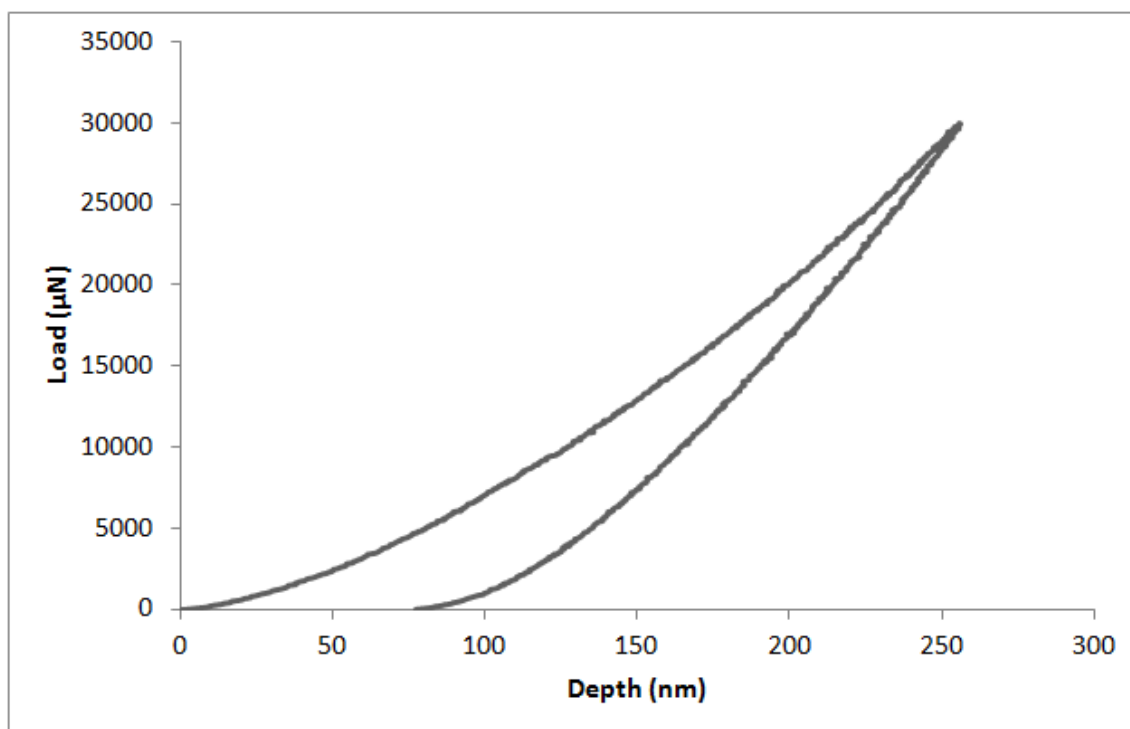


Figure A4.3: Typical Load-Depth curve for standard finish 6H-SiC at a maximum applied load of 30mN.

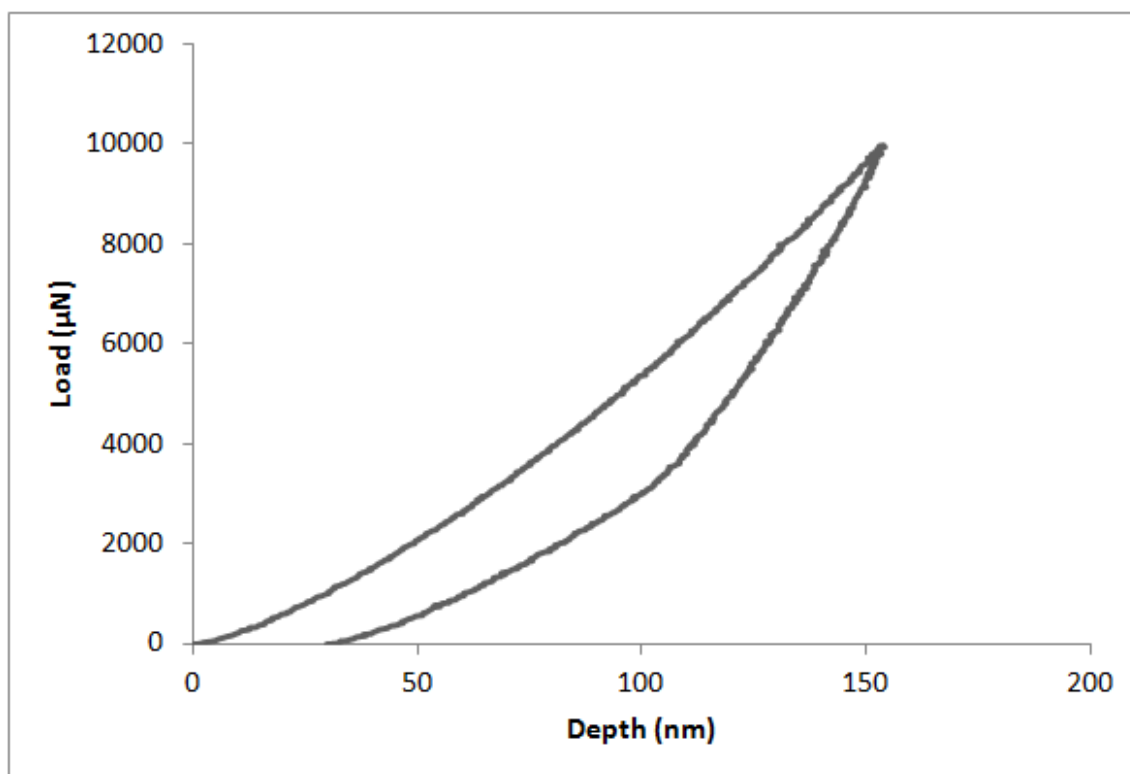


Figure A4.4: Typical Load-Depth curve for grit blast 6H-SiC at a maximum applied load of 10mN.

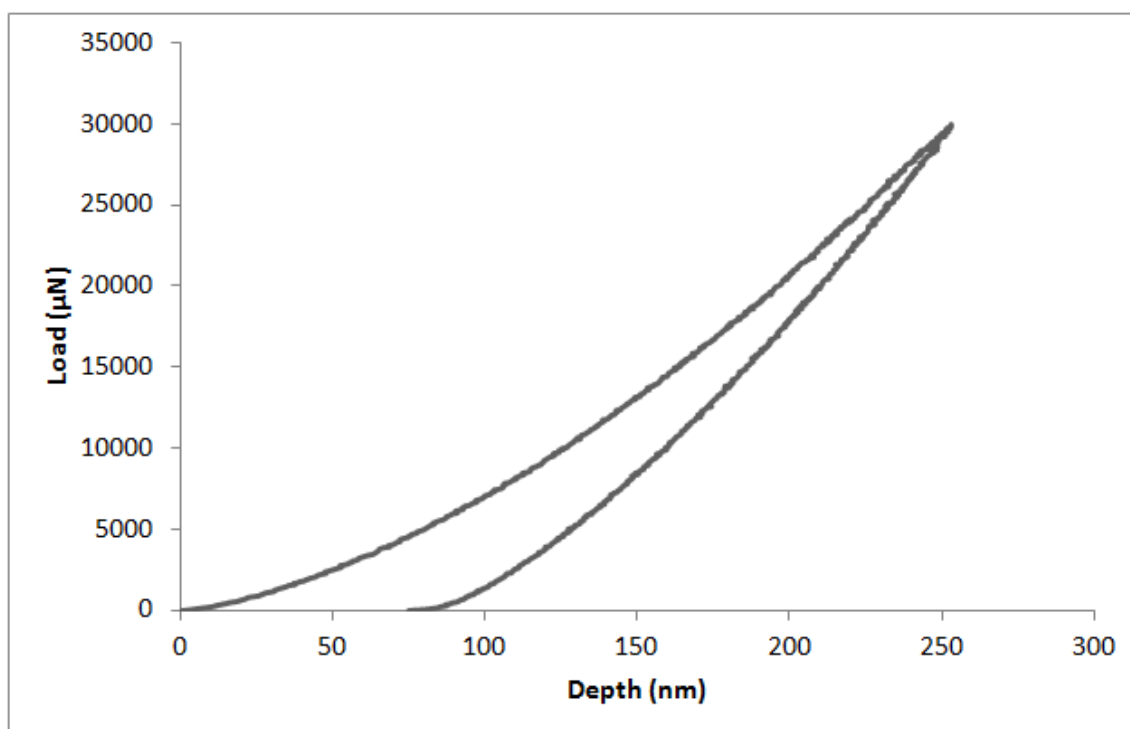


Figure A4.5: Typical Load-Depth curve for grit blast 6H-SiC at a maximum applied load of 30mN.

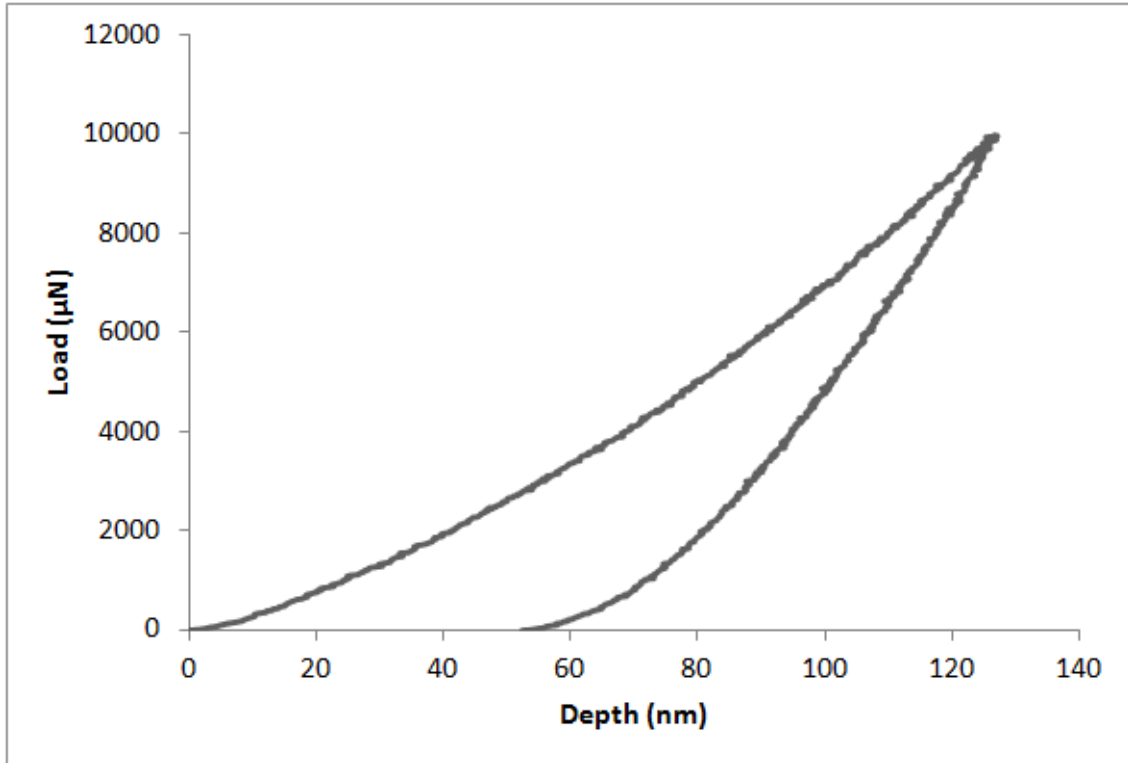


Figure A4.6: Typical Load-Depth curve for rotary ground 6H-SiC at a maximum applied load of 10mN.

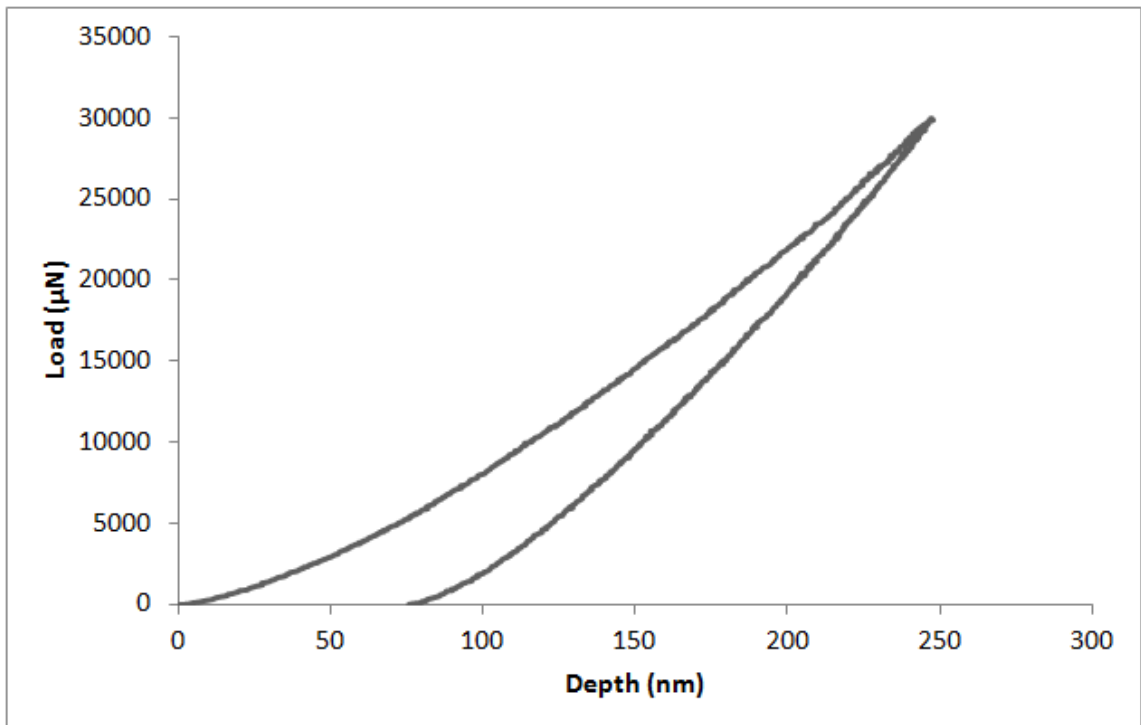


Figure A4.7: Typical Load-Depth curve for rotary ground 6H-SiC at a maximum applied load of 30mN.

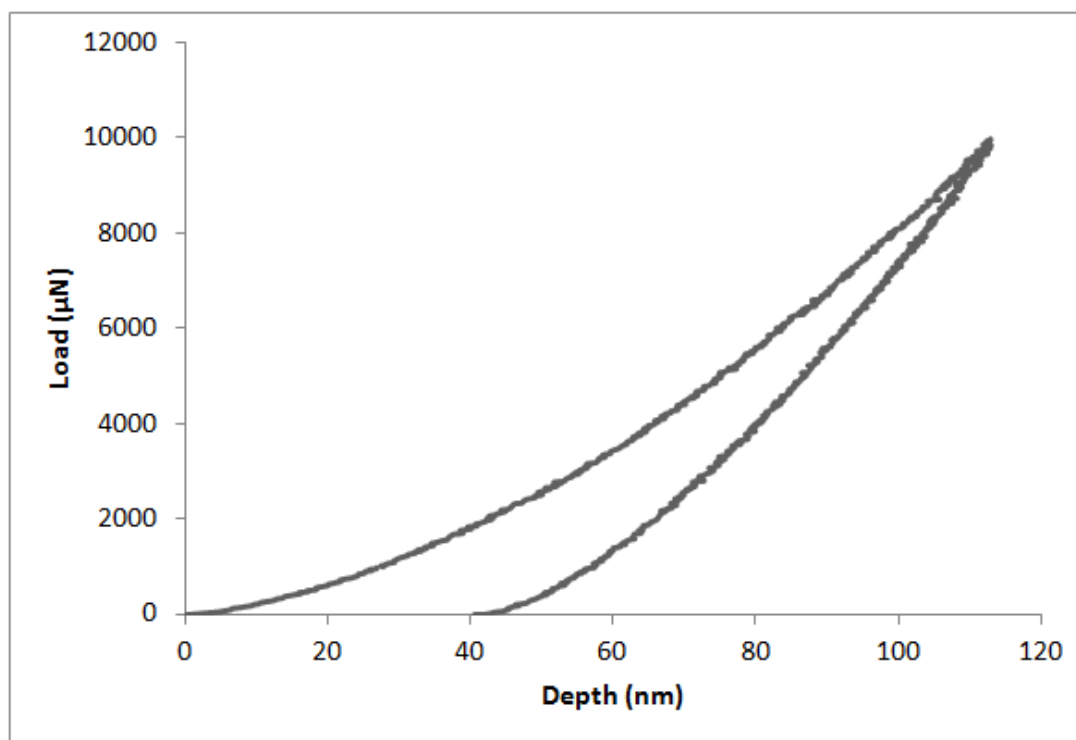


Figure A4.8: Typical Load-Depth curve for mirror finish 6H-SiC at a maximum applied load of 10mN.

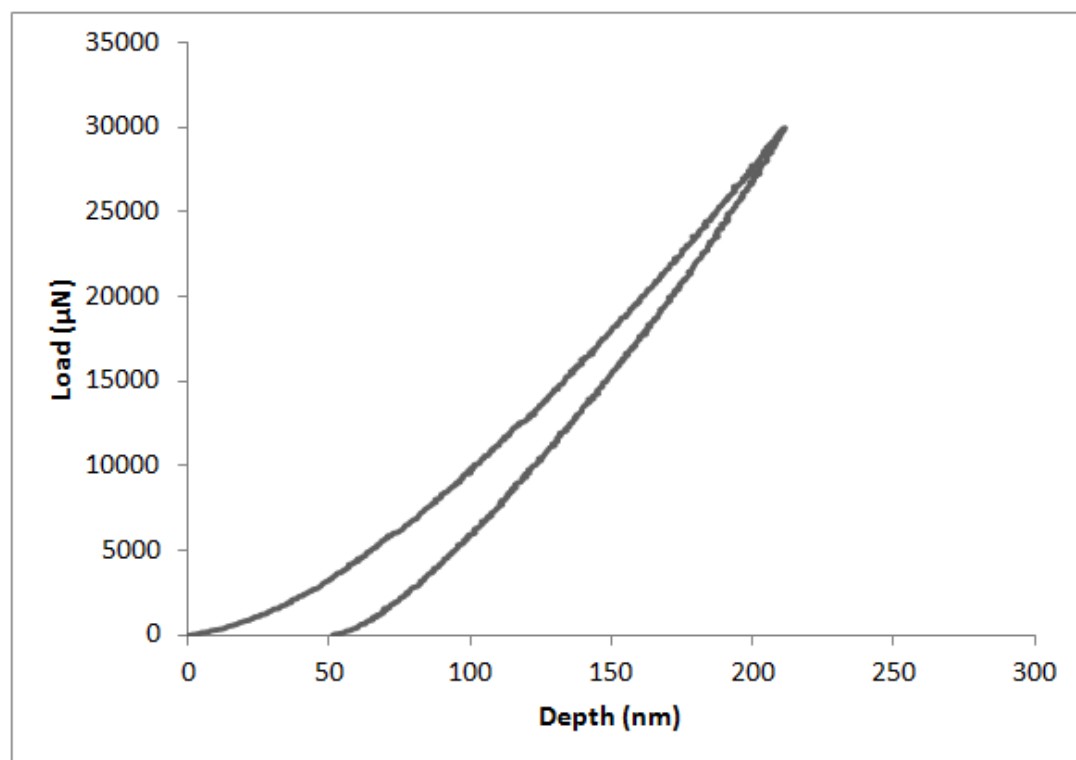


Figure A4.9: Typical Load-Depth curve for mirror finish 6H-SiC at a maximum applied load of 30mN.

## References

- [1] L. Sheppard, "Machining of Advanced Ceramics," *Advanced Materials & Process inc. Metal progress*, pp. 40-48, 1987.
- [2] B. Eigenmann, B. Scholtes, and E. Macherauch. "Determination of residual stresses in ceramics and ceramic-metal composites by X-ray diffraction methods". *Materials Science and Engineering A*, vol. 118, pp. 1-17, 1987.
- [3] J. Watts, G. Hilmas, W. G. Fahrenholtz, D. Brown, and B. Clausen, "Stress measurements in ZrB<sub>2</sub>-SiC composites using Raman spectroscopy and neutron diffraction," *Journal of the European Ceramic Society*, vol. 30, no. 11, pp. 2165-2171, Aug. 2010.
- [4] H. Wu, S. G. Roberts, and B. Derby, "Residual Stress and Subsurface Damage in Machined Alumina and Alumina / Silicon Carbide Nanocomposite Ceramics," *Materials Science*, vol. 49, pp. 507-517, 2001.
- [5] R. Samule et al. "Effect of residual stresses on the fracture of ground ceramics". *Journal of the American Ceramic Society*, vol. 72 no. 10, pp. 1960-1966 1989.
- [6] D.J. Green, F.F. Lange, and M.R. James. "Factors influencing residual surface stresses due to a stress-induced phase transformation". *Journal of the American Ceramic Society* vol. 66 no. 90, pp. 623-629, 1983.
- [7] K. Li and T. Warren Liao, "Surface/subsurface damage and the fracture strength of ground ceramics," *Journal of Materials Processing Technology*, vol. 57, no. 3-4, pp. 207-220, Feb. 1996.
- [8] J.E. Shemilt, A.A. Siddiqui, and S.C. Bradwell. "Investigation of the influence of machining on the fracture of engineering ceramics". *Journal of Materials Science Letters* vol. 13, pp. 1546-1550, 1994
- [9] W. Pfeiffer, T. Hollstein, and E. Sommer. "Strength properties of surface machined components of structural ceramics". *Fracture Mechanics*, vol. 25, 1994.
- [10] M.A. Capano, B. C. Kim, a. R. Smith, E. P. Kvam, S. Tsoi, and a. K. Ramdas, "Residual strains in cubic silicon carbide measured by Raman spectroscopy correlated with x-ray diffraction and transmission electron microscopy," *Journal of Applied Physics*, vol. 100, no. 8, p. 083514, 2006.
- [11] F. Cerdeira, C. Buchenauer, F. Pollak, and M. Cardona, "Stress-induced shifts of first-order Raman frequencies of diamond-and zinc-blende-type semiconductors," *Physical Review B*, vol. 5, no. 2, p. 580, 1972.
- [12] M. Yamaguchi, M. Fujitsuka, S. Ueno, I. Miura, W. Erikawa, and T. Tomita, "Study of Indentation Damage in Single Crystal Silicon Carbide by Using Micro Raman Spectroscopy," *Materials Science Forum*, vol. 645-648, pp. 551-554, Apr. 2010.

- [13] K. Kese and D. J. Rowcliffe, "Nanoindentation method for measuring residual stress in brittle materials," *Journal of the American Ceramic Society*, vol. 86, no. 5, pp. 811–816, 2003.
- [14] X. Chen, J. Yan, and a Karlsson, "On the determination of residual stress and mechanical properties by indentation," *Materials Science and Engineering: A*, vol. 416, no. 1-2, pp. 139-149, Jan. 2006.
- [15] Z.-H. Xu and X. Li, "Estimation of residual stresses from elastic recovery of nanoindentation," *Philosophical Magazine*, vol. 86, no. 19, pp. 2835-2846, Jul. 2006.
- [16] V. Domnich and Y. Gogotsi, "High-Pressure Surface Science," *Experimental Methods in the Physical Sciences*, Vol. 38, Academic Press, New York, 2001.
- [17] W. Wesch, "Silicon carbide: synthesis and processing," *Nuclear Instruments and Methods in Physics Research Section B: Beam Interactions with Materials and Atoms*, vol. 116, no. 1, pp. 305–321, 1996.
- [18] D. Lundquist., "On the Crystal Structure of Silicon Carbide and its Content of Impurities," *Acta Crystallographica Section B*, vol. 2, pp. 177-191, 1948.
- [19] L.S. Ramsdell, "Studies on silicon carbide," *Mineralogical Society of America*, 1947.
- [20] N.W. Jepps and T.F. Page, "Polytypic transformations in silicon carbide," *Progress in Crystal Growth and Characterization*, vol. 7, pp. 259-307, 1983.
- [21] E. Halac, E. Burgos, and H. Bonadeo, "Static and dynamical properties of SiC polytypes," *Physical Review B*, vol. 65, no. 12, pp. 19-22, Mar. 2002.
- [22] G. Brezeanu, "Silicon Carbide (SiC): A Short History and an Analytical Approach for SiC Power Device Design," *Proceedings of the 2005 International Semiconductor Conference*, vol. 2, pp. 345-348, 2005.
- [23] R. Madar, "Materials Science: Silicon carbide in contention," *Nature* , vol. 34 no. 7003, pp. 974-975, 2004.
- [24] S.E. Saddow and A. Agarwal. *Advances in Silicon Carbide Processing and Applications*. Artech House, Inc. Norwood, MA, 2004.
- [25] J.A. Lely, *Berichte der Deutschen Keramischen Gesellschaft*, vol 32. pp. 229, 1978.
- [26] H. Sone, T. Kaneko, and N. Miyakawa, "In situ measurements and growth kinetics of silicon carbide chemical vapor deposition from methyltrichlorosilane," *Journal of Crystal Growth*, vol. 219 no. 3, pp. 245-252, 2000.
- [27] A. Hoerner, J. Vierhaus, and E.P. Burte, "Chemically vapor-deposited silicon carbide films for surface protection," *Surface and Coatings Technology*, vols. 100-101, p. 149-152, 1998.

- [28] R.A., Alliegro, L.B. Coffin, and J.R. Tinklepaugh, "Pressure-Sintered Silicon Carbide," *Journal of the American Ceramic Society*, vol. 39 no. 11, pp. 386-389, 1956.
- [29] R. L. Coble and J.E. Burke, "Sintering in Ceramics," *Progress in Ceramic Science*, ed. J.E. Burke, vol 3, New York: Pergamon Press. 1963.
- [30] F. Guillard et al., "Densification of SiC by SPS: Effects of time, temperature and pressure," *Journal of the European Ceramic Society*, vol. 27 no. 7, pp. 2725-2728, 2007.
- [31] M. Tokita, "Mechanism of Spark Plasma Sintering," Sumitomo Coal Mining Company, Ltd. Tokyo, Japan. P. 13, 1999.
- [32] W. Pfeiffer, "Influence of machining-induced residual stresses on the strength of ceramics." *Proceedings of the 9<sup>th</sup> International Conferrence on Experimental Mechanics*, pp. 1237-1245, 1990.
- [33] T.M.A. Maksoud et al. "Grinding of ceramics: the effect on their strength properties". *Journal of Materials Processing Technology*, vol. 43, pp. 65-75, 1994.
- [34] R. Allor and S. Jahanmir, "Current Problems and Future Directions for Ceramic Machining," *The American Ceramic Society Builletin*, vol. 75, no. 7, pp. 40-43, 1996.
- [35] S. Amada and A. Satoh, "Fractal analysis of surfaces roughened by grit blasting," *Journal of Adhesion Science and Technology*, vol. 14 no. 1, pp 27-41, 2000.
- [36] D.F. Wang, J.H. She and Z.Y. Ma, "Effect of microstructure on erosive wear behavior of SiC ceramics," *Wear*, vol 180 nos. 1-2, pp. 35-41, 1995.
- [37] D.J. Varacalle Jr et al, "Effect of grit-blasting on substrate roughness and coating adhesion," *Journal of Thermal Spray Technology*, vol. 15 no. 3, pp. 348-355, 2006.
- [38] M.F. Huang, T.R. Lin, and H.-C. Chiu, "Effect of machining characteristics on polishing ceramic blocks," *International Journal*, vol. 26, pp. 999-1005, 2005.
- [39] S. Malking and J.E. Ritter. "Grinding mechanism and strength degradation for ceramics". *Journal of Engineering for Industry*, vol. 111 no. 5, pp. 165-174
- [40] R.W. Rice, J.J. Mecholsky Jr, and P.F. Becher. "The effect of grinding direction on flaw character and strength of single crystal polycrystalline ceramics". *Journal of Materials Science*, vol. 16, pp. 853-862, 1951.
- [41] Z.H. Xie et al., "Role of microstructure in the grinding and polishing of alpha-sialon ceramics," *Journal of the European Ceramic Society*, vol. 23 no. 13, pp. 2351-2360, 2003.
- [42] S. Jiang, Y. Tan, G. Zhang, and R. Peng, "DEM simulation and experimental investigation of silicon carbide on pre-stressed machining," *Materials Research*, vol. 128, pp. 241-245, 2010.
- [43] K. Kurosawa et al., "Super-polished silicon carbide mirror for high-power operation of excimer lasers in a vacuum ultraviolet spectral range," *Review of Scientific Instruments*, vol. 61 no. 2, pp. 728-731, 1990.



- [44] Y. Ogita, K. Kobayashi, and H. Daio, "PCA Characterization of residual subsurface damage after silicon wafer mirror polishing and its removal," *Materials Research Society Symposium Proceedings*, vol. 566, pp. 261-266, 2000.
- [45] O.S. Han et al., "The characterization of process induced damage of silicon wafering process-mechanical damage," *Proceedings of the Third International Symposium on Defects in Silicon (Electrochemical Society Proceedings)*, vol. 99, pp. 100-108, 1999.
- [46] J. Patten, W. Gao, and K. Yasuto, "Ductile Regime Nanomachining of Single-Crystal Silicon Carbide," *Journal of Manufacturing Science and Engineering*, vol. 127, no. 3, p. 522, 2005.
- [47] B. Zhang and G. Michael, "Machining FGM: Residual Stresses Redistribution," *Materials Science Forum*, vol. 493, pp. 415-420, 2005.
- [48] T. Kato, T. Noro, H. Takahashi, S. Yamaguchi, and K. Arai, "Characterization of Electric Discharge Machining for Silicon Carbide Single Crystal," *Materials Science Forum*, vol. 603, pp. 855-858, 2009.
- [49] W. Zeng, X. Xu, and Z. Pei, "Rotary Ultrasonic Machining of Advanced Ceramics," *Materials Science Forum*, vol. 533, pp. 361-364, 2006.
- [50] N. Churi, Z. J. Pei, and D. Shorter, "Rotary ultrasonic machining of silicon carbide: designed experiments," *International journal of manufacturing technology and management*, vol. 12, no. 1, pp. 284-298, 2007.
- [51] C.V. Raman and K.S. Krishnan, *Nature* 121, 711 (1928)
- [52] G. Gouadec and P. Colomban, "Raman Spectroscopy of nanomaterials: How spectra relate to disorder, particle size and mechanical properties," *Progress in Crystal Growth and Characterization of Materials*, vol. 53, no. 1, pp. 1-56, Mar. 2007.
- [53] P. Colomban, "Analysis of Strain and Stress in Ceramic, Polymer and Metal Matrix Composites by Raman Spectroscopy," *Advanced Engineering Materials*, vol. 4, no. 8, pp. 535-542, Aug. 2002.
- [54] W. Zhu, J. Zhu, S. Nishino, and G. Pezzotti, "Spatially resolved Raman spectroscopy evaluation of residual stresses in 3C-SiC layer deposited on Si substrates with different crystallographic orientations," *Applied Surface Science*, vol. 252, no. 6, pp. 2346-2354, Jan. 2006.
- [55] D. Ghosh, G. Subhash, and N. Orlovskaya, "Measurement of scratch-induced residual stress within SiC grains in ZrB<sub>2</sub>-SiC composite using micro-Raman spectroscopy," *Acta Materialia*, vol. 56, no. 18, pp. 5345-5354, Oct. 2008.
- [56] M. Yamamoto et al., "Raman Spectroscopic Stress Evaluation of Femtosecond-Laser-Modified Region Inside 4H-SiC," *Applied Physics Express*, vol. 3, no. 1, p. 016603, Jan. 2010.

- [57] J. DiGregorio and T. Furtak, "Analysis of Residual Stress in 6H-SiC Particles within Al<sub>2</sub>O<sub>3</sub>/SiC Composites through Raman Spectroscopy," *Journal of the American Ceramic Society*, vol. 75, pp. 1854-57, 1992.
- [58] K. Grodecki et al., "Raman Piezospectroscopy of Phonons in Bulk 6H-SiC," *Acta Physica Polonica A*, vol. 116, no. 5, pp. 6-9, 2009.
- [59] D. Olego and M. Cardona, "Pressure dependence of Raman phonons of Ge and 3C-SiC," *Physical Review B*, vol. 25, no. 2, pp. 1151-1160, Jan. 1982.
- [60] B. Dietrich and K. Dombrowski, "Experimental challenges of stress measurements with resonant micro-Raman spectroscopy," *Journal of Raman spectroscopy*, vol. 30, no. 10, pp. 893-897, 1999.
- [61] S. Nakashima and M. T., "Characterization of SiC Crystals by Using Deep UV Excitation Raman Spectroscopy S. Nakashima," *Materials Science Forum*, vol. 529, pp. 333-338, 2006.
- [62] H. Werheit and K.A. Schwetz, "Comparative optical investigations of sintered and monocrystalline black and green silicon carbide (SiC)," *Journal of Solid State Chemistry*, vol. 177, pp. 580-585, 2004.
- [63] M. Moskovits, "Surface-enhanced Raman spectroscopy: a brief retrospective," *Online*, pp. 485-496, 2005.
- [64] B. Pettinger, "Single-molecule surface- and tip-enhanced raman spectroscopy," *Molecular Physics*, vol. 108, no. 16, pp. 2039-2059, 2010.
- [65] A. Kudelski, "Surface Science Raman spectroscopy of surfaces," *Surface Science*, vol. 603, no. 10-12, pp. 1328-1334, 2009.
- [66] H. Nienhaus, T. Kampen, and W. Mönch, "Phonons in 3C-, 4H-, and 6H-SiC," *Surface science*, vol. 324, no. 1, p. L328-L332, 1995.
- [67] S. Nakashima, M. Higashihira, K. Maeda, and H. Tanaka, "Raman Scattering Characterization of Polytype in Silicon Carbide Ceramics: Comparison with X-ray Diffraction," *Journal of the American Ceramic Society*, vol. 86, no. 5, pp. 823-829, 2003.
- [68] D.W. Feldman, J.H. Parker Jr, W.J. Choyke, and L. Patrick, "Raman Scattering in 6H SiC," *Physical Review*, vol. 170 no. 3, pp. 698-704, 1968.
- [69] S. Nakashima and H. Harima, "Raman investigation of SiC polytypes," *physica status solidi (a)*, vol. 162, no. 1, pp. 39-64, 1997.
- [70] S. Nakashima, H. Harima, T. Tomita, and T. Suemoto, "Raman intensity profiles of folded longitudinal phonon modes in SiC polytypes," *Physical Review B*, vol. 62, no. 24, p. 16605, 2000.

- [71] W. C. Oliver and G. M. Pharr, "Measurement of hardness and elastic modulus by instrumented indentation: Advances in understanding and refinements to methodology," *Journal of Materials Research*, vol. 19, no. 1, pp. 3-20, Jan. 2004.
- [72] A.C. Fischer-Cripps, "Critical review of analysis and interpretation of nanoindentation test data," *Surface and Coatings Technology*, vol. 200, no. 14-15, pp. 4153-4165, Apr. 2006.
- [73] J. Woirgard, C. Tromas, J. Girard, and V. Audurier, "Study of the mechanical properties of ceramic materials by the nanoindentation technique," *Journal of the European Ceramic Society*, vol. 18, no. 15, pp. 2297-2305, 1998.
- [74] S. Suresh and A. Giannakopoulos, "A new method for estimating residual stresses by instrumented sharp indentation," *Acta Materialia*, vol. 46, no. 16, pp. 5755-5767, 1998.
- [75] W. Warren, Y. B. Guo, and M. L. Weaver, "The influence of machining induced residual stress and phase transformation on the measurement of subsurface mechanical behavior using nanoindentation," *Surface and Coatings Technology*, vol. 200, no. 11, pp. 3459-3467, Mar. 2006.
- [76] Y.T. Cheng and C.-M. Cheng, "Scaling, dimensional analysis, and indentation measurements," *Materials Science and Engineering: R: Reports*, vol. 44, no. 4-5, pp. 91-149, Aug. 2004.
- [77] Y. T. Cheng and C. M. Cheng, "Relationships between hardness, elastic modulus, and the work of indentation," *Applied physics letters*, vol. 73, no. 5, p. 614, 1998.
- [78] D. Joslin, "A new method for analyzing data from continuous depth-sensing microindentation tests," *Journal of Materials Research*, vol. 5, no. 1, pp. 123-126, 1990.
- [79] S. Chowdhury, M. Laugier, and J. Henry, "XRD stress analysis of CVD diamond coatings on SiC substrates," *International Journal of Refractory Metals and Hard Materials*, vol. 25, no. 1, pp. 39-45, Jan. 2007.
- [80] C. Genzel, M. Klaus, I. Denks, and H. G. Wulz, "Residual stress fields in surface-treated silicon carbide for space industry—comparison of biaxial and triaxial analysis using different X-ray methods," *Materials Science and Engineering: A*, vol. 390, no. 1-2, pp. 376-384, Jan. 2005.
- [81] J. Liu and Y. K. Vohra, "Raman modes of 6H polytype of silicon carbide to ultrahigh pressures: A comparison with silicon and diamond," *Physical review letters*, vol. 72, no. 26, pp. 4105-4108, 1994.
- [82] J. Chen and S.J. Bull, "On the relationship between plastic zone radius and maximum depth during nanoindentation," *Surface & Coatings Technology*, vol. 201, pp. 4289-4293, 2006.
- [83] S. Nakashima et al., "Deep Ultraviolet Raman Microspectroscopic Characterization of Polishing-Induced Surface Damage in SiC Crystals service of

Polishing-Induced Surface Damage in SiC Crystals,” *Journal of the Electrochemical Society*, vol. 153, no. 4, 2006.

[84] T. F. Page, W. C. Oliver, and C. J. McHargue, “The deformation behavior of ceramic crystals subjected to very low load (nano)indentations,” *Journal of Materials Research*, vol. 7, no. 2, pp. 450-473, Jan. 2011.

[85] S. Guicciardi, A. Balbo, D. Sciti, C. Melandri, and G. Pezzotti, “Nanoindentation characterization of SiC-based ceramics,” *Journal of the European Ceramic Society*, vol. 27, no. 2-3, pp. 1399-1404, 2007.

## **Curriculum Vitae**

### **Education**

Ph.D. Materials Science and Engineering – Rutgers University, 2013

M.S. Materials Science and Engineering – Rutgers University, 2010

B.S. Materials Science and Engineering – University of Pittsburgh, 2008

### **Work History:**

Rutgers University – Piscataway, NJ, Graduate Research Assistant, 2008-2012

University of Pittsburgh – Pittsburgh, PA, Undergraduate Researcher, 2007-2008

University of Pittsburgh – Pittsburgh, PA, Mascaro Sustainability Initiative  
Fellow, summer 2007

Lawrence Gordon Architects – Larchmont, NY, Paid Intern, 2003-2006

### **Publications/Presentations:**

Groth, B. Mann, A.B. “Variations in the Raman spectral profile of 6H-silicon carbide ceramics due to machining” submitted to Journal of the American Ceramic Society, January 2013

Groth, B. Mann, A.B. “Using Raman mapping to determine stress variation in machined silicon carbide ceramics” submitted to Journal of the American Ceramic Society, January 2013

Groth, B. Mann, A.B. “Identifying changes in residual stress using indentation on machined metallic surfaces” Materials Letters, vol. 89, pp287-290, 2012

Pekor, C. Groth, B. Nettleship, I. "The effect of polyvinyl alcohol on the microstructure and permeability of freeze-cast alumina" Journal of the American Ceramic Society, v93, n1, p115-20, Jan 2010